

---

# Enhancement cavities for attosecond physics

Simon Holzberger

---



München 2015



---

# Enhancement cavities for attosecond physics

Simon Holzberger

---

Dissertation  
an der Fakultät für Physik  
der Ludwig–Maximilians–Universität  
München

vorgelegt von  
Simon Holzberger  
aus Neustadt a. d. Aisch

München, den 22.09.2015

Erstgutachter: Prof. Dr. Ferenc Krausz  
Zweitgutachter: PD Dr. Thomas Udem  
Tag der mündlichen Prüfung: 07.12.2015

## Abstract

The work presented in this thesis was aimed at developing a high-repetition rate source of coherent radiation in the extreme ultra-violet (XUV) spectral region, envisaging applications in attosecond physics or precision metrology in the XUV. Due to the lack of laser oscillators operating in the XUV, the method of choice was the frequency upconversion of a near-infrared laser via the nonlinear process of high-order harmonic generation. Obtaining sufficient XUV photon flux per pulse at repetition rates of several tens of MHz, despite the inherently low conversion efficiency, requires a powerful driving source. To date, passive enhancement of ultrashort pulses in an external resonator has been the most successful strategy in meeting this demand. In this thesis four main achievements towards extending this technique and understanding its limitations are presented.

A first experiment was dedicated to obtaining shorter intracavity pulses without compromising the high average power available from Yb-based laser technology. To this end, we spectrally broadened and temporally compressed the pulses prior to the enhancement in a broadband resonator. Aside from being a prerequisite for time-domain applications, shorter intracavity pulses led to improved conditions for the harmonic generation process.

Furthermore, we addressed the task of extracting the intracavity generated XUV light. We established two methods for geometrical XUV output coupling, one employing the fundamental mode of the cavity, and the other a tailored transverse mode, which offers additional degrees of freedom to shape the harmonic emission. Both techniques are particularly suited for the intracavity generation of attosecond pulses, because they afford an unparalleled flexibility for the resonator design, and exhibit a broadband output coupling efficiency approaching unity for short-wavelength radiation. This enabled a significant improvement of the crucial parameters, photon flux and photon energy.

In a combined experimental and theoretical study, we investigated the ionization-related intensity limitations observed in state-of-the-art enhancement cavities. The quantitative modeling of the nonlinear interaction allows for an estimation of the achievable intracavity parameters and for a global optimization of the XUV photon flux. Based on this model, we proposed a strategy to mitigate this limitation by using the nonlinearity in combination with customized cavity optics for a further spectral broadening and temporal compression of the pulse in the resonator. More importantly, this work establishes enhancement cavities as a tool to investigate nonlinear light-matter interactions with the increased sensitivity provided by the resonator.

The last study was dedicated to the technological challenge of building a resonator in which the electric field of the circulating pulse is reproduced at each round-trip. This is an essential prerequisite to generate identical XUV emission with each driving pulse. By tailoring the spectral phase of the cavity mirrors we succeeded in enhancing pulses of less than 30 fs (less than nine cycles of the driving field) to a few kilowatts of average power with zero pulse-to-pulse carrier-to-envelope phase slip. At similar pulse durations, the generation of isolated attosecond pulses has already been demonstrated in single-pass geometries.

In conclusion, the results presented in this thesis are milestones on the way to a powerful, compact and coherent source of ultrashort XUV radiation. The unique property of the source, that is, its high repetition rate lays the foundation for advancing attosecond physics and precision spectroscopy in the XUV region.

## Zusammenfassung

Ziel dieser Arbeit war die Entwicklung einer Quelle die kohärentes Licht im extrem-ultravioletten (XUV) Spektralbereich mit sehr hohen Repetitionsraten liefert und neue Forschungsfelder in der Attosekundenphysik oder der Präzisionsmetrologie im XUV ermöglicht. Aufgrund des Nichtvorhandenseins an Laseroszillatoren in diesem Spektralbereich beruht die Quelle auf der Erzeugung hoher Harmonischer von Laserlicht im nahen Infrarot. Um trotz inhärent niedriger Konversionseffizienz ausreichend XUV Photonen pro Puls bei Wiederholraten von mehreren 10 MHz zu erhalten, sind hohe treibende Leistungen nötig. Vom heutigen Standpunkt ist dafür die passive Überhöhung von Laserpulsen in einem externen Resonator der vielversprechendste Ansatz. Mit der vorliegenden Arbeit werden vier Beiträge zur Erweiterung dieser Technik geleistet und neue Limitierungen aufgezeigt.

Das erste Experiment befasste sich damit, kürzere Pulsdauern im Resonator zu erzielen, ohne auf die hohen Durchschnittsleistungen der Yb-Lasersysteme zu verzichten. Dies gelang durch spektrale Verbreiterung und anschließender zeitlicher Kompression der Pulse vor der Überhöhung in einem breitbandigen Resonator. Neben der Notwendigkeit kürzerer treibender Laserpulse für die angestrebten Anwendungen im Zeitbereich konnte gezeigt werden, dass sich mit kürzerer Pulsdauer auch die Bedingungen für die XUV Erzeugung verbessern.

Außerdem wurden zwei neue geometrische Verfahren zur Auskopplung der XUV Strahlung aus dem Resonator demonstriert. Beim ersten Verfahren wird der Resonator mit der fundamentalen transversalen Mode betrieben. Das Zweite basiert auf einer speziell angepassten Feldverteilung im Resonator, wodurch neue Freiheitsgrade für die Erzeugung der Harmonischen ermöglicht werden. Beide Methoden eignen sich ideal für die Auskopplung von Attosekundenpulsen, da sie mit einer großen Flexibilität des Resonatordesigns einhergehen und eine Auskopplungseffizienz bieten, die für kurzweilige Strahlung gegen 100 % tendiert. So konnten die beiden wichtigsten Parameter, die Photonenenergie und der Photonenfluss, deutlich erweitert bzw. gesteigert werden.

In einer weiteren Studie wurden ionisationsbedingte Intensitätslimitierungen im Resonator in Theorie und Experiment untersucht. Die Modellierung der nichtlinearen Wechselwirkung im Resonator erlaubt erstmals eine Abschätzung der erreichbaren Pulsparameter und damit eine vollständige Optimierung des XUV Photonenflusses. Darauf aufbauend wurde eine Strategie vorgeschlagen, um die Beschränkung der Intensität zu entschärfen: Diese nutzt die Nichtlinearität in Verbindung mit speziellen Resonatorspiegeln, um eine weitere spektrale Verbreiterung und Pulskompression im Resonator zu erreichen. Darüber hinaus etabliert dieser Forschungsbeitrag Überhöhungsresonatoren als Messinstrumente zur präzisen Charakterisierung von nichtlinearen Wechselwirkungen.

Der letzte Teil der Arbeit widmet sich der technologischen Herausforderung den Resonator so auszulegen, dass sich das elektrische Feld des Pulses von Umlauf zu Umlauf am Interaktionspunkt reproduziert. Dies ist eine notwendige Voraussetzung für identische XUV Erzeugung bei jedem treibenden Puls. Durch Optimierung der spektralen Phase der Resonatorspiegel konnte ein umlaufender Puls von weniger als 30 fs (weniger als neun Zyklen des

elektrischen Feldes) bei einigen Kilowatt mittlerer Leistung erreicht werden, dessen elektrisches Feld konstant bleibt. Für vergleichbare treibende Pulsdauern wurde bereits in Experimenten ohne Resonator die Erzeugung isolierter XUV Pulse mit Pulsdauern im Attosekundenbereich gezeigt.

Zusammenfassend stellen diese Ergebnisse Meilensteine auf dem Weg zu einer kompakten, leistungsstarken Quelle von kohärenter, gepulster XUV Strahlung dar, deren Alleinstellungsmerkmal die hohe Repetitionsrate, weitere Fortschritte in der Attosekundenphysik und der Frequenzkammspektroskopie ermöglicht.

# Contents

<b>Abstract</b>	<b>v</b>
<b>Zusammenfassung</b>	<b>vii</b>
<b>1 Introduction</b>	<b>1</b>
1.1 Motivation . . . . .	1
1.2 Research objectives . . . . .	2
1.3 Outline of the thesis . . . . .	4
<b>2 Theoretical background</b>	<b>5</b>
2.1 Passive enhancement in optical cavities . . . . .	5
2.1.1 Frequency filtering . . . . .	5
2.1.2 Spatial filtering . . . . .	7
2.2 Intracavity nonlinearities . . . . .	9
2.2.1 General aspects . . . . .	10
2.2.2 Intracavity ionization . . . . .	10
2.3 High-order harmonic generation . . . . .	16
2.3.1 Single-atom dipole response . . . . .	16
2.3.2 Macroscopic response . . . . .	20
<b>3 Experimental apparatus</b>	<b>23</b>
3.1 Oscillator and CPA . . . . .	23
3.2 Nonlinear spectral broadening and compression . . . . .	24
3.3 Dynamics of broadband pulse enhancement . . . . .	27
3.4 CEO detection and stabilization . . . . .	28
3.5 Enhancement cavity and comb-cavity stabilization . . . . .	31
<b>4 Cavity-enhanced HHG with geometrical output coupling</b>	<b>33</b>
4.1 Geometrical output coupling of XUV radiation . . . . .	33
4.1.1 Motivation . . . . .	33
4.1.2 Fabrication of output coupling mirrors . . . . .	35
4.2 Experimental setup . . . . .	36
4.3 HHG with the fundamental mode and pierced mirror OC . . . . .	40
4.3.1 Performance considerations . . . . .	40
4.3.2 Cavity performance . . . . .	41
4.3.3 XUV output . . . . .	42
4.3.4 Limitations . . . . .	45
4.4 HHG with tailored driving field in a degenerate resonator . . . . .	47
4.4.1 Properties of the tailored driving field and expected XUV output . . . . .	48

4.4.2	Cavity performance . . . . .	52
4.4.3	XUV Output . . . . .	52
4.5	Conclusions . . . . .	53
<b>5</b>	<b>Quantitative description of enhancement cavities in the nonlinear regime</b>	<b>55</b>
5.1	Modeling the cavity response . . . . .	56
5.1.1	Nonlinear pulse propagation in cavities . . . . .	56
5.1.2	Comparison to simulations in 4D . . . . .	59
5.1.3	Plasma recombination . . . . .	62
5.2	Experimental methodology . . . . .	65
5.2.1	Experimental apparatus . . . . .	65
5.2.2	Phase measurement and phase retrieval . . . . .	67
5.3	Experimental results and comparison with the model . . . . .	68
5.3.1	Linear cavity in the steady state . . . . .	68
5.3.2	Nonlinear cavity in the steady state . . . . .	70
5.4	Implications . . . . .	72
5.4.1	Empirical scaling law for standard-approach cavities . . . . .	72
5.4.2	Wavelength scaling . . . . .	73
5.4.3	Repetition rate scaling . . . . .	74
5.4.4	Beyond standard-approach ECs . . . . .	75
5.5	Conclusions . . . . .	78
<b>6</b>	<b>Cavities for zero phase slip pulse trains</b>	<b>81</b>
6.1	Optimal offset frequency . . . . .	81
6.1.1	Determination of the OOF . . . . .	82
6.1.2	Tuning the optimal offset frequency . . . . .	83
6.2	Experimental setup . . . . .	84
6.2.1	Overview of the experimental apparatus . . . . .	84
6.2.2	Broadband coatings with controlled CEP-shift . . . . .	85
6.3	Experimental findings . . . . .	87
6.3.1	Controlling the optimal offset frequency . . . . .	87
6.3.2	Power and bandwidth scaling . . . . .	90
6.4	Conclusions and outlook . . . . .	92
<b>7</b>	<b>Outlook</b>	<b>95</b>
	<b>List of Acronyms</b>	<b>99</b>
	<b>Bibliography</b>	<b>101</b>
	<b>Appendix</b>	
<b>A</b>	<b>Definitions</b>	<b>117</b>
<b>B</b>	<b>Dynamic response of enhancement cavities in the linear regime</b>	<b>119</b>
<b>C</b>	<b>Cavity enhancement using a single degree of freedom</b>	<b>125</b>

<b>D Algorithm for phase retrieval</b>	<b>129</b>
<b>E Gas expansion with an end-fire nozzle</b>	<b>133</b>
<b>F Data archiving</b>	<b>137</b>
<b>List of scientific publications</b>	<b>139</b>
<b>Danksagung</b>	<b>143</b>



# 1 Introduction

## 1.1 Motivation

Cavities, and the discrete modes of the electromagnetic field inside this bounded space, have played a central role in modern physics and technology. In 1900, Max Planck derived the quantum theory of black-body radiation [1, 2] by postulating that the exchange of energy between the harmonic oscillators and the radiation modes contained in the cavity (“*Vacuum, das rings von festen spiegelnden Wänden umschlossen ist*”) can only occur in quanta of energy  $h\nu$ . Nowadays, this is seen as the birth of quantum mechanics [3]. The theoretical concept of a resonator for electromagnetic fields first gained technological relevance for filtering purposes, for instance in radar applications [4]. Later it was applied as a feedback mechanism to increase the rate of stimulated emission—an essential prerequisite for building laser oscillators [5–7]. Without doubt this invention has revolutionized numerous fields of physics and every day life.

The coherent light emitted by a laser can be used to excite a passive optical resonator. If the field injected in the resonator interferes constructively with the intracavity field, the energy stored in the resonator can exceed the input energy by several orders of magnitude. Used in this configuration, the resonator is termed an *enhancement cavity* (EC). The field enhancement and its sensitivity with respect to the resonance condition have enabled manifold applications in optics. One example is frequency filtering much like in Fabry–Pérot-type interferometers, which applied to frequency combs can be used for absolute wavelength calibration of astronomical spectrographs [8, 9]. Various cavity-based schemes have been implemented to measure absorption [10–12] or dispersion [13–15] with tremendously enhanced sensitivity and with Hz-level resolution, when used in combination with frequency combs [16, 17]. Taking these ideas to the quantum limit has enabled fascinating experiments in millimeter to micrometer-scale optical resonators in which a single photon is coupled to a two level system (such as an atom) [18], or where it is entangled with the mechanical oscillations of one of the cavity end mirrors [19–21]. Looking at the other end of the length scale, that is, to kilometer-long resonators, the enhanced sensitivity in conjunction with the increased intracavity power renders ECs a key technology in the ongoing efforts to detect gravitational waves [22–24].

The prospect of boosting both the average and the peak power of a laser by orders of magnitude makes ECs an attractive means to drive frequency conversion processes, whose efficiency depends strongly on the driving intensity. In this way, frequency doubling of continuous-wave lasers has been achieved with efficiencies approaching unity [25]. About a decade ago, passive optical resonators were first used to enhance ultrashort pulses emitted by mode-locked oscillators [26]. This laid the foundation for combining the boost in peak power in an EC with the nonlinear process of high-order harmonic generation (HHG) in a gas target, which suffers from inherently low conversion efficiency [27]. First demonstrated

in 2005 [28, 29], intracavity HHG seemed to be a perfect match: the resonator enables peak intensities exceeding the  $10^{13}$  W/cm<sup>2</sup> required to rival the intra-atomic field strengths in combination with significant pulse energy by recycling nonconverted fundamental light—all of this with a repetition rate on the order of 100 MHz.

HHG allows for a transfer of the excellent spatial *and* temporal coherence properties of infrared or visible driving sources into the extreme ultra-violet (XUV) spectral region [30, 31] in a table-top source—a property yet unparalleled by other techniques such as free-electron lasers. In addition, the emitted XUV pulses are much shorter than the fundamental pulses, reaching record values as short as 80 as [32]. This has opened the door to the exploration of physics on the attosecond time scale [33–35] with intriguing experiments ranging from the direct measurement of lightwaves [36], to time-resolved studies of photo-induced ionization [37, 38], emission [39, 40], or dissociation [41], and the steering of electronic wave packets in atoms [42], molecules [43], or solids [44, 45]. With the advent of cavity-assisted HHG sources, many of these experiments could become possible with a repetition rate that is increased by 3–5 orders of magnitude compared to typical single-pass systems. As a consequence, acquisition times in pump-probe-type experiments would be dramatically decreased, enabling hitherto unfeasible experiments with simultaneous spatial and temporal resolution<sup>1</sup>. Space charge effects in photo-electron detection systems which currently limit the input XUV flux (e.g., in time and/or angle-resolved photoemission spectroscopy [47, 48], or in coincidence spectroscopy [49, 50]) are avoided by distributing the XUV photons and thus the electrons onto many pulses in time. Shorter acquisition times are in general also beneficial for the overall system stability. Experiments in the spectral domain, that exploit the frequency comb structure of the harmonic spectrum, require a certain minimum comb line spacing (equal to the repetition rate) to resolve individual atomic absorption lines. Such measurements would enable more precise tests of bound-state quantum electrodynamics using fundamental transition lines of hydrogen-like (He<sup>+</sup>, Li<sup>++</sup>) atomic systems lying in the XUV spectral region [51–53]. With the XUV-to-radio-frequency link provided by the frequency comb, optical clocks exploiting nuclear transitions come within reach (e.g., based on thorium [54, 55] or uranium [56]). In summary, tapping the full potential of cavity-assisted HHG would afford table-top sources for a multitude of experiments requiring narrow linewidth or ultrashort (sub-fs) coherent radiation in the XUV with repetition rates ranging from a few tens to several hundreds of MHz.

### 1.2 Research objectives

To realize such a radiation source, several prerequisites need to be fulfilled.

- (i) The seed laser must provide pulses of high energy and short duration with a repetition rate on the order of several tens of MHz.
- (ii) The resonator must provide significant enhancement for the broadband pulses and the optics must withstand the high average power and peak intensity. For the ultimate goal

---

<sup>1</sup>The acquisition time of a single spatially resolved image as presented in [46] using a standard 1-kHz-HHG system amounts to 1.5 h. This renders simultaneous temporal resolution via a pump-probe scheme unpractical.

of isolated attosecond pulses, the intracavity pulses must be at least short enough that methods gating the harmonic emission can be applied.

- (iii) The resonator needs an XUV output coupler that is suitable for the targeted photon energies and that preferably does not impose additional constraints to the intracavity pulse. For the envisaged time-domain applications, the output coupler should provide a non-dispersed XUV beam propagating collinear with the infrared (IR) beam.
- (iv) For experiments requiring sub-fs timing resolution (e.g., as provided by isolated attosecond pulse), the EC must support a driving pulse train with vanishing pulse-to-pulse carrier-envelope phase (CEP) slip, such that the shape of the electric field is the same for every driving pulse.

Despite considerable developments of cavity-based HHG sources since their initial demonstrations, at the onset of this thesis in 2011 there were still major challenges to be overcome and the limitations of intracavity HHG were yet to be explored. Record values in terms of average powers (18 kW) had been achieved with Yb-based laser systems providing a pulse duration of about 180 fs [57], while considerably shorter pulses (28 fs) were only reached at much lower average powers ( $< 40$  W) limited by the seeding titanium-sapphire lasers and the low power-enhancement factors ( $\sim 50$ ) [28]. The demonstrated output coupling mechanisms were either based on diffraction or reflection [28, 29, 58–60], and thus, did not fulfill the requirements mentioned above. For all of these reasons the XUV radiation delivered by cavity-based sources covered only the spectral region above 40 nm [31, 61–64]. Furthermore, the seeding pulse trains were set to match the pulse-to-pulse CEP slip imposed by the EC, and the limitations for the enhancement were still believed to be set primarily by the cavity optics [15, 28, 57, 65].

In this work, we addressed several of these technological challenges and research gaps. First, a new strategy was pursued to obtain high energy (40  $\mu$ J), broadband pulses ( $\Delta\nu/\nu_c \approx 0.1$ ) in the resonator by using nonlinearly compressed seed pulses in combination with broadband cavity mirrors. Second, geometrical output coupling was established as an efficient technique that is particularly suited for applications requiring broadband XUV radiation without imposing other restrictions on the polarization or bandwidth of the driving field [66]. We also demonstrated that the use of a tailored driving field distribution results in comparable XUV flux but offers increased flexibility for shaping the harmonic emission [67]. Third, the ionization-induced intensity limitation in the cavity was modeled, providing a framework for the layout and optimization of a cavity in the nonlinear regime [68]. For these investigations, high-power, high-finesse resonators were combined with spatial-spectral interferometry to access nonlinearly-induced phase shifts with increased sensitivity. Fourth, we demonstrated control over the net pulse-to-pulse CEP slip induced by the resonator without compromising its suitability for HHG (in terms of damage threshold, polarization insensitivity, or bandwidth) [69].

While every point represents an accomplished research objective in its own, they all tie in to advance the development of cavity-based HHG sources for applications ranging from coherent diffractive imaging [70, 71] through metrology in the XUV spectral region [52, 53, 61] to attosecond physics [72–74]. Both the technological developments that were triggered in the course of this work and the methodology used to characterize nonlinear light-matter

interactions will have significant impact beyond cavity-enhanced HHG, for example on intracavity difference-frequency generation [75], or the enhancement of frequency combs in the mid-infrared.

### 1.3 Outline of the thesis

The structure of the thesis reflects the aforementioned research objectives. **Chapter 2** provides a theoretical background on ECs and gives a basic understanding of how nonlinear interactions can change the cavity behavior, in particular, for the case of intracavity ionization. Furthermore, principles of HHG are summarized. Further theoretical aspects that were developed in the course of this thesis are presented in the corresponding chapters. **Chapter 3** gives an overview of the experimental apparatus and discusses the challenges imposed by the enhancement of high-power broadband pulses. Technical details that are only relevant for specific experimental studies are conveyed in the corresponding chapters. In **Chapter 4** we present two proof-of-principle experiments on intracavity HHG, which establishes two distinct methods for geometrical output coupling of the harmonic radiation: the first study uses the fundamental transverse mode of the resonator, while the second is performed with a tailored transverse mode. Furthermore, the measurements show that temporally compressed pulses are a viable way for achieving higher intracavity intensities in the presence of an ionizing gas target. The experimental study presented in **Chapter 5** uses spatially and spectrally resolved interferometry to investigate the nonlinear phase of the intracavity pulse originating from the laser-induced plasma. Besides establishing this technique as a sensitive tool for the investigation of nonlinear interactions, the experimental data allowed for the validation of a quantitative model of the ionization induced limitations in the cavity. The model opens new possibilities in the layout of an EC optimized for driving nonlinear interactions. In **Chapter 6** we describe an approach to overcome the challenge of building a resonator that supports a pulse train with vanishing pulse-to-pulse carrier-to-envelope phase slippage. We demonstrate the production and characterization of mirrors designed to shift the CEP of a pulse in a controlled way. **Chapter 7** concludes the thesis and provides an outlook on the significance of the achieved results for the future prospects of cavity-enhanced experiments.

## 2 Theoretical background

This chapter provides the theoretical background necessary to understand the addressed research objectives and the methodology used in this thesis. For a more comprehensive treatise and for a strict derivation of the stated formulas, further literature is suggested. Section 2.1 discusses the principles of passive enhancement in external cavities. Section 2.2 outlines the multitude of effects that occur when driving intensity-dependent processes in an EC. Section 2.3 summarizes basic principles of HHG.

### 2.1 Passive enhancement in optical cavities

ECs are the technological and methodological backbone of this thesis<sup>1</sup>. In the resonator, the light can be confined which leads to well-defined modes in the transverse and the longitudinal dimension. Due to finite round-trip losses, these modes have a finite width and are called resonances. In the following two sections, the spatial and spectral filtering properties of a cavity and the field and phase enhancement associated with the resonances are discussed.

#### 2.1.1 Frequency filtering

##### General aspects

We consider a passive resonator to which light from a coherent source emitting at frequency  $\omega$  is continuously coupled via a partially transmissive mirror (input coupler) characterized by a power transmission  $T_{\text{ic}}(\omega)$  and reflectivity  $R_{\text{ic}}(\omega)$ . A round-trip through the resonator can be parameterized by a power attenuation factor  $R_{\text{cav}}(\omega)$  and a spectral phase<sup>2</sup>  $\phi(\omega)$ . The latter incorporates all accumulated phase shifts upon a single round-trip, including those upon reflections from mirrors, transmission through dispersive material and geometric phase shifts due to focusing. Following the sketch in Fig. 2.1(a), the field transmitted through the input coupler  $\sqrt{T_{\text{ic}}(\omega)}\tilde{\mathcal{E}}_{\text{in}}(\omega)$  and the intracavity field after one additional round-trip reflected at the input coupler  $\sqrt{R_{\text{ic}}(\omega)R_{\text{cav}}(\omega)}e^{i\phi(\omega)}\tilde{\mathcal{E}}_{\text{cav}}(\omega)$  add up to the (new) intracavity field  $\tilde{\mathcal{E}}_{\text{cav}}(\omega)$ . In the steady state, this equation can be solved for  $\tilde{\mathcal{E}}_{\text{cav}}$ , and rearranged to define the frequency-resolved power enhancement as:

$$\mathbb{E}(\omega) := \left| \frac{\tilde{\mathcal{E}}_{\text{cav}}(\omega)}{\tilde{\mathcal{E}}_{\text{in}}(\omega)} \right|^2 = \left| \frac{\sqrt{T_{\text{ic}}(\omega)}}{1 - \sqrt{R_{\text{cav}}(\omega)R_{\text{ic}}(\omega)} \exp i\phi(\omega)} \right|^2. \quad (2.1)$$

<sup>1</sup>A textbook providing an excellent introduction to many aspects of ECs is [76].

<sup>2</sup>Note, that  $\phi$  includes the phase shift acquired upon reflection off the input coupler, but  $R_{\text{cav}}(\omega)$  does not include the power attenuation at reflection off the input coupler.

## 2 Theoretical background

Using two convenient definitions, this equation can be rewritten to highlight the resonant character of the power enhancement:

$$\mathbb{E}(\omega) = \mathbb{E}_R(\omega) \times \frac{1}{1 + (2\mathcal{F}(\omega)/\pi)^2 \sin^2(\phi(\omega)/2)}, \quad (2.2)$$

$$\text{with } \mathbb{E}_R := \frac{T_{ic}}{(1 - \sqrt{R_{cav}R_{ic}})^2} \quad \text{and} \quad \mathcal{F} := \frac{\pi(R_{cav}R_{ic})^{1/4}}{1 - \sqrt{R_{cav}R_{ic}}}. \quad (2.3)$$

On resonance, that is, when  $\phi$  equals a multiple of  $2\pi$ , the power enhancement reaches a local maximum ( $\mathbb{E} = \mathbb{E}_R$ ). A good approximation of the linewidth (full-width at half-maximum)  $\Gamma_{\text{FWHM}}$  of the resonance is  $\Gamma_{\text{FWHM}} = \mathcal{F}/2\pi$ . This approximation is valid in the low-loss limit ( $1 - R_{cav}R_{ic} \ll 1$ ), which is always obeyed in this thesis. Typically, this equation is used to define the finesse  $\mathcal{F}$ , as the ratio between the free spectral range (distance between two resonances) and the linewidth.

Note, that the finesse is only a function of the total cavity losses, but  $\mathbb{E}_R$  also depends on the input coupler transmission. Thus, at given finesse the highest  $\mathbb{E}_R$  is reached, when the cavity losses are only due to the input coupler transmission. In most situations, working in this overcoupled condition is highly desirable. For a given value of  $R_{cav} < 1$ , the impedance-matched configuration ( $T_{ic} = 1 - R_{cav}$ ) yields the highest possible  $\mathbb{E}_R$ . Typical values for the power-enhancement factors reached in this thesis are in the range of 100 to 1000.

In Fig. 2.1(b) the power enhancement and the total phase shift of the intracavity light relative to the input light are plotted. In the vicinity of the resonance, the phase of the intracavity light increases strongly and linearly with respect to the single-round-trip phase. This sensitivity enhancement is on the order of  $\mathcal{F}/\pi$  and makes EC ideal tools to measure small intracavity phase shifts that can subsequently be read out interferometrically. The ‘‘phase enhancement’’ is directly linked to the photon lifetime in the resonator, or in other words, to the many round-trips the light takes in the resonator.

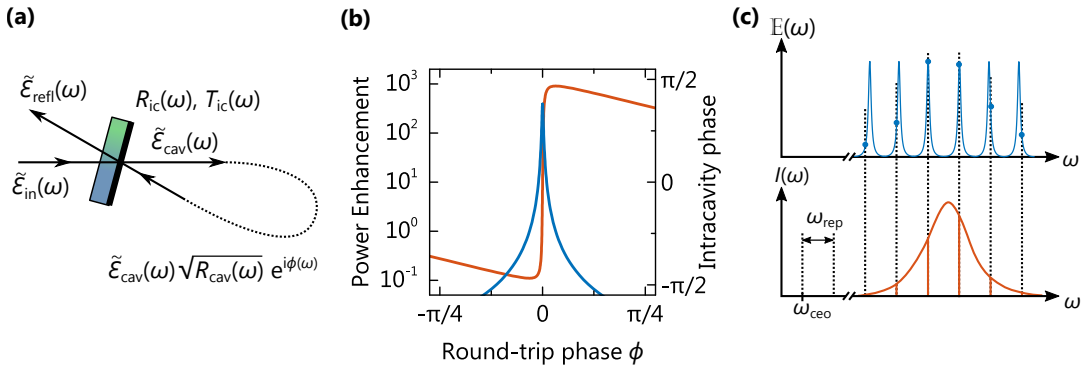


**Figure 2.1:** (a) Sketch of the electric fields at the input coupler used for deriving the steady-state relation of Eq. (2.1). (b) Power enhancement and intracavity phase as a function of the round-trip phase.  $T_{ic} = 1\%$ ,  $R_{cav} = 1$ . (c) Frequency comb with equidistant comb lines (lower panel) coupled to an EC with a round-trip phase that is nonlinear in frequency, limiting the enhanced spectral bandwidth.

### Particularities of fs-enhancement cavities

ECs can be efficiently seeded with pulse trains delivered by (amplified) mode-locked oscillators that guarantee sufficient pulse-to-pulse stability. Prerequisites for the enhancement are that both the losses and higher order dispersion<sup>3</sup> in the resonator are kept low over the spectral bandwidth of the pulses, such that the pulse shape and energy is well preserved. In that case, given the specific seeding spectrum, the EC dictates the pulse-to-pulse time delay  $\tau$  and the pulse-to-pulse CEP slip  $\Delta\phi_{\text{cep}}$ . Optimal power enhancement is achieved if the seeding pulse train matches both these parameters. In the frequency domain, the pulse train corresponds to a comb of equidistant spectral lines spaced by the pulse repetition frequency  $\omega_{\text{rep}}/2\pi = 1/\tau$  and offset from zero by the carrier-envelope offset frequency  $\omega_{\text{ceo}} = -(\Delta\phi_{\text{cep}}/2\pi) \omega_{\text{rep}}$  [77, 78]. The regular comb needs to be matched to the cavity resonances, which are slightly non-equidistant due to residual higher order dispersion in the cavity (see Fig. 2.1(c)). If the round-trip phase is sufficiently linear over the given input spectrum, then there is an optimal pair of comb parameters, in particular an optimal offset frequency of the seeding comb (see Chapter 6 for details).

To ensure power-enhancement factors that are larger than  $\mathbb{E}_R/2$ , deviations in  $\phi(\omega)$  from linearity in  $\omega$  need to be smaller than  $\pi/2\mathcal{F}$  (see Eq. (2.2)). With typical cavity mirrors, the higher order phase terms ultimately limit the enhanced spectral bandwidth and not their decrease in reflectivity. This means, that there is a trade-off between the cavity finesse (determining the linewidth of the resonances) and the spectral bandwidth of the pulses that can be (significantly) enhanced. Therefore, operating the cavity in the overcoupled limit is beneficial for the enhancement of broadband pulses, because it provides broader resonances at the same power enhancement.

The cavity optics are subject to intense and high average power laser radiation, requiring low absorption ( $\lesssim 10$  ppm) and high damage thresholds ( $\sim 10^{11}$  W/cm<sup>2</sup>). This can only be achieved by using dielectric multilayer coatings. Empirically, coating designs based on alternating layers of two materials with almost quarter wave thicknesses have proven to best fulfill the partially conflicting demands of damage threshold, low loss, and low group delay dispersion (GDD) in reflection, all at a manageable design complexity. For a perfect quarter-wave stack it can be shown, that the supported spectral bandwidth scales with the contrast of the real part of the refractive indices of the two materials [79]. At the same time, a high refractive index implies a small band gap and thus a lower damage threshold [80, 81]. Therefore, the high-index material typically sets the damage threshold of the coating, and optics supporting a broader spectrum usually suffer from a lower damage threshold. To maintain the same peak intensity on the cavity optics with shorter intracavity pulses (or higher pulse energy), the spot sizes on the optics must be increased. To this end, a number of concepts for ECs with large mode sizes were proposed [82–84].

#### 2.1.2 Spatial filtering

In a stable resonator, the confinement of the electric field in the transverse dimensions to a region close to the optical axis leads to the emergence of well-defined transverse modes. These field distributions reproduce themselves after one round-trip in the cavity. In the

<sup>3</sup>Higher order dispersion refers to terms in  $\phi(\omega)$  with a dependency in  $\omega$  that is at least quadratic.

paraxial approximation, and for a planar ring-resonator comprising only spherical optics, the set of orthogonal eigenmodes is given by the Gauss-Hermite (GH) modes. For a wave vector  $k = 2\pi/\lambda$  the field distributions of order  $m$  and  $n$  in the tangential (along  $x$ ) and sagittal plane (along  $y$ ), respectively, are given by [85]:

$$\text{GH}_{n,m}(x,y,z) = u_n(x,z) \times u_m(y,z) \times e^{-ikz}, \quad \text{with} \quad (2.4)$$

$$u_n(x,z) = \left(\frac{2}{\pi}\right)^{1/4} \left(\frac{1}{2^n n! w(z)}\right)^{1/2} H_n\left(\frac{\sqrt{2}x}{w(z)}\right) e^{i(n+\frac{1}{2})\psi(z) - i\frac{kx^2}{2q(z)}}. \quad (2.5)$$

Here,  $w$  is the beam waist and the term  $(n + \frac{1}{2})\psi(z)$  the Gouy phase, both retrievable from the complex beam parameter  $q$ :

$$\frac{1}{q(z)} = \frac{1}{R(z)} - i\frac{\lambda}{\pi w(z)^2},$$

$$\psi(z) = \arctan \frac{z}{z_R}, \quad \text{with} \quad z_R = \frac{\pi w(0)^2}{\lambda}. \quad (2.6)$$

Therefore, the field distribution as given in Eq. (2.5) is fully characterized by the complex beam parameter  $q(z)$ , the wave vector  $k$ , and the two integers  $n$  and  $m$ . The complex beam parameter must reproduce itself after one round-trip. It is retrieved by solving  $q = (Aq + B)/(Cq + D)$ , with the resonator described by its  $ABCD$ -matrix  $M = [[A,B],[C,D]]$ , which is in general different in the two planes. If a solution for  $q$  exists, the resonator is said to be stable.

Following Eq. (2.4) and Gaussian beam propagation, the phase shift that a GH mode of order  $(n, m)$  acquires in one cavity round-trip is given by:

$$\phi_{n,m} = -kL + (m + 1/2)\Psi_{\text{tan}} + (n + 1/2)\Psi_{\text{sag}}. \quad (2.7)$$

with the Gouy parameters  $\Psi_{\text{tan,sag}}$  again derived by from the resonator matrix  $M$  in the corresponding planes via  $\Psi = \text{sgn}(B) \arccos[(A + D)/2]$ . Therefore, transverse modes of different order typically have different resonance frequencies and the cavity acts as a spatial filter. As a consequence, the input laser beam needs to be adjusted to maximize the spatial overlap with the desired transverse mode of the resonator, typically the fundamental one.

In such a non-degenerate resonator a small distortion of the field<sup>4</sup>, for example, resulting from a small absorbing obstacle in the beam path, will introduce two kinds of losses. If the power transmission through the plane with the obstacle is given by  $T$  (corresponding to a factor of  $1 - T$  that is absorbed), then it can be shown that a factor of  $1 - T$  of the remaining power is coherently coupled into higher order modes [86]. If these modes are non-degenerate with the fundamental mode or efficiently suppressed, then a factor of  $T^2$  of the incident power remains in the fundamental mode and the total losses (absorption + diffraction) amount to  $1 - T^2$ . For a circular obstacle of radius  $r$  blocking the central part of a Gaussian beam ( $1/e^2$ -intensity radius  $w$ ), we calculate:

$$T = e^{-2(r/w)^2} \quad \text{and total losses} \quad L = 1 - T^2 = 1 - e^{-4(r/w)^2}. \quad (2.8)$$

---

<sup>4</sup>Small in the sense that the reduced finesse does not lead to degeneracy of the modes.

The situation is different, if the resonator is tuned such that a subset of modes is degenerate, for example, in the center of the stability range of a bowtie resonator where  $\Psi = -\frac{\pi}{2}$  holds<sup>5</sup>. According to Eq. (2.7), all modes that differ in their order by  $\Delta n = 4$  acquire the same round-trip phase shift. In an unperturbed resonator all of the modes of the degenerate subset can be simultaneously excited and their phases and amplitudes would be determined by the seeding laser. If an obstacle is introduced in the beam path, the phase relationship is fixed due to coherent coupling of the modes, and there is one mode combination that experiences the lowest losses, which is the fundamental eigenmode of the perturbed resonator. As the relative phases of the involved GH modes change upon propagation (see Gouy-phase term in Eq. (2.5)), the composite mode changes its shape within the resonator, but reproduces itself after one round-trip. For this reason, this resonator is called to be in the *quasi-imaging condition* and the mode is called to be the quasi-imaging mode. In particular, it can be shown that  $M^{\Delta n} = \mathbb{I}_2$ , which means that the resonator acts as an imaging resonator after  $\Delta n$  round-trips (i.e., any  $q$  parameter is reproduced after  $\Delta n$  round-trips).

Calculation of the losses induced by the obstacle can in principle be done similarly to the non-degenerate case. Typically, the losses are much smaller than for the non-degenerate case, because the new eigenmode tries to avoid the obstacle. For precise calculations of the losses, knowledge of the field distribution in the obstacle plane is necessary. This can be done using the coherent mode coupling model presented in [86]. The calculated losses strongly depend on the exact cavity geometry (determining the complex beam parameter), because even tiny changes in the mode shape can lead to significantly lower losses at the obstacle.

An EC offers valuable flexibility by operating it in mode degeneracy or in non-degeneracy. Depending on the experimental demands one or the other situation is preferable. The presented approach to treating spatial aberrations in resonators can be applied to a multitude of effects, including spatial phase shifts resulting from an intracavity plasma or to thermal deformations of mirrors.

## 2.2 Intracavity nonlinearities

It has been pointed out in Section 2.1.1 that the average power in an EC can be orders of magnitude higher than the power of the seeding source. This renders ECs an attractive means to driving nonlinear frequency conversion processes, where the intensity of the converted light and also the conversion efficiency depend in a nonlinear way on the driving field intensity. This argument, however, only holds if losses and phase distortions of the fundamental light can be kept low, such that the constructive interference with the seeding pulse is not impaired<sup>6</sup>. In the following we will first outline some general phenomena, which can occur in the presence of intracavity nonlinearities. Then, the case of intracavity ionization and its influence on the cavity behavior is discussed.

<sup>5</sup>The discussion presented closely follows [86] and is kept in a single plane.

<sup>6</sup>Furthermore, the phase-matching conditions and the efficiency of separating the generated light from the fundamental light need to be of similar order of magnitude as achievable in single-pass geometries.

### 2.2.1 General aspects

The intended frequency conversion introduces energy losses to the fundamental light. With the sensitivity of the EC to losses for the fundamental light, this ultimately limits the applicability of this scheme. The nonlinear light-matter interaction can, however, also change the phase of the intracavity pulse. This phase shift is typically intensity dependent and thus best described in the time domain. A time-dependent phase shift changes the oscillations of the electric field under the slowly varying envelope. If this temporal shift has a linear time dependence, it can be compensated by a change of the resonator length. Any nonlinear time dependence will manifest itself in the frequency domain as a change in the pulse spectral intensity and phase. In other words, energy is transferred from one spectral part to another. In the case of a regular pulse train, which has a comb-like structure in the frequency domain, this energy transfer happens only between the comb lines but not in-between comb lines, provided that the perturbation is identical for every pulse. The additional spectral phase alters the resonance conditions. The input comb can only be adapted to this spectral phase, if the latter shows a linear frequency dependency. Otherwise a spectral filtering will occur.

Owing to the intensity dependence of the phase shift, a beam of Gaussian shape in the transverse direction will acquire a spatially dependent phase shift. This perturbation can be treated as a coherent coupling mechanism, that transfers energy among the transverse modes of the resonator. It can either result in losses (in case of coupling to non-resonant modes) or in a change of the eigenmode (in case of a degenerate resonator), see Section 2.1.2.

In many cases, the perturbations in amplitude and phase arise not from the desired frequency conversion process itself, but from parasitic processes, for example, from ionization without recombination, in the case of HHG. Another example would be a parasitic  $\chi^{(3)}$ -nonlinearity in a medium, in the case of difference-frequency generation governed by the  $\chi^{(2)}$ -coefficient. Conversely, the resonator sensitivity to perturbations in amplitude and phase can be exploited to characterize a (non-)linear light-matter interaction with increased sensitivity [12, 14, 15, 87]. Note, that there are some fundamental differences between multi-pass approaches (that simply increase the interaction length) and an EC. For example, the resonance condition couples phase changes to amplitude changes. Or, when the EC is in the steady state, the (non-)linear interaction is effectively split up into many passages through the (non-)linear medium but always driven with the same initial field.

So far, the perturbative effects of the nonlinearity on the intracavity light were discussed with regards to the altered steady-state performance of the cavity. Due to the nonlinear nature of the interaction, the dynamic response of a nonlinear cavity can fundamentally differ from its linear behavior. Most notably, the intensity build-up in the cavity is changed, as the resonance condition is intensity dependent and, thus, changes with time. This can render the comb-to-cavity stabilization challenging or, it can lead to self-locking, where comb fluctuations and resulting intensity drops are counteracted by the self-adapting (nonlinear) resonance condition [62, 88].

### 2.2.2 Intracavity ionization

In the following paragraphs, we will specialize to the case of an intracavity gas target ionized by the intracavity pulse. To this end, we provide some theoretical background on the

modeling of the ionization process and then describe its influence on the propagation of the light. The section ends with a qualitative discussion of the cavity response in the presence of ionization.

### Ionization

Although the process of multi-photon-induced single ionization of a neutral atom is conceptually easy to understand, it requires very sophisticated modeling to describe even the most basic experimentally accessible quantities, such as ionization rates. To one part, this is due to the large field strengths that the atom is subject to. If they become comparable to the intra-atomic field strengths experienced by the electron(s), then, methods treating the laser field as a perturbation break down. Another part of the complexity is due to the (fast) oscillating nature of the laser field, with an amplitude, that is typically varying on the time scale of 10 fs. For the ionization of multi-electron atoms, which is the experimentally most relevant situation, a precise modeling still exceeds the available capabilities of computers.

Here, we will summarize ionization rates obtained with models using the single active electron approximation, a monochromatic laser field, in a short-range potential. These rates have shown reasonable agreement regarding their intensity dependency within the limits of applicability [89]. For a more detailed review on the subject of ionization, see [90, 91].

When an atom characterized by an ionization potential  $I_p$  is subject to a strong monochromatic laser field of frequency  $\omega_c \ll I_p/\hbar$ , one can distinguish two different limits of multi-photon-induced ionization: namely, the “multi-photon” limit ( $\gamma \gg 1$ ) and the “tunneling” limit ( $\gamma \ll 1$ ). Here,  $\gamma$  is the Keldysh parameter, that is defined as the ratio of the tunneling time (in a semiclassical picture) to the field oscillation period. It can be conveniently expressed using the ponderomotive potential  $U_p$  of the laser field as:

$$\gamma = \sqrt{\frac{I_p}{2U_p}}, \quad \text{with} \quad U_p = \frac{e^2 E^2}{4\omega_c^2 m}. \quad (2.9)$$

In the tunneling limit, that is, for low oscillation frequencies, or high intensities, multi-photon ionization is most conveniently described in an adiabatic picture. Here the ionization rates are calculated in a quasi-static approximation. The electric field of the laser is added to the Coulomb force between the electron and the atom and a potential barrier of finite width emerges. For a linearly polarized laser field of amplitude  $E$  the cycle-averaged tunneling or ionization rate through this barrier was derived by Ammosov-Delone-Krainov (ADK). In atomic units it reads:

$$\Gamma_{\text{ADK}} = |C_{n^*l^*}|^2 f_{lm} I_p \left[ \frac{2(2I_p)^{3/2}}{E} \right]^{2n^* - |m| - 3/2} \exp \left[ -\frac{2(2I_p)^{3/2}}{3E} \right]. \quad (2.10)$$

It shows the expected exponential dependence on the barrier energy (for the prefactors  $|C_{n^*l^*}|^2$  and  $f_{lm}$  see [89, 92]).

For  $\gamma > 1$  (high frequencies, low intensities), Eq. (2.10) predicts a much stronger suppression of tunneling than observed in experiments [89]. Here, the quasi-static approximation breaks down, and the processes is better described using standard time-dependent perturbation theory with the electric dipole approximation. The resulting ionization rate [91] has

a structure similar to Fermi's golden rule and scales as  $I^n$ , with  $I$  being the driving field intensity and  $n = \lfloor I_p / \hbar\omega_c \rfloor$  being the minimum number of photons required for ionization. In this approximation the ionization rate does not show any sub-cycle dynamics.

The intermediate range ( $\gamma \sim 1$ ) is most difficult to describe. An analytic model, that agrees reasonably well with experimental data presented in [89] is the one developed by Perelomov-Popov-Terent'ev (PPT) [93]. It is based on earlier work by Keldysh [94] and considers the case of a single electron in a short-range potential subject to an intense oscillating field. They find for the cycle-averaged ionization (in atomic units):

$$\begin{aligned} \Gamma_{\text{PPT}} &= |C_{n^*l^*}|^2 f_{lm} I_p \sqrt{\frac{6}{\pi}} \left[ \frac{2(2I_p)^{3/2}}{E} \right]^{2n^* - |m| - 3/2} (1 + \gamma^2)^{|m|/2 + 3/4} \\ &\quad \times A_m(\omega_c, \gamma) \exp \left[ -\frac{2(2I_p)^{3/2}}{3E} g(\gamma) \right], \\ g(\gamma) &= \frac{3}{2\gamma} \left[ \left( 1 + \frac{1}{2\gamma^2} \right) \sinh^{-1}(\gamma) - \frac{\sqrt{1 + \gamma^2}}{2\gamma} \right]. \end{aligned} \quad (2.11)$$

The prefactors  $|C_{n^*l^*}|^2$  and  $f_{lm}$  are the same as in Eq. (2.10), the prefactor  $A_m(\omega_c, \gamma)$  has only a weak dependence on its arguments and is given in Eq. (55) and (56) in [93]. To account for sub-cycle ionization dynamics beyond a simple quasi-static approximation (i.e., replacing  $E$  by  $E(t)$ ), an extension of the PPT model was given in [95].

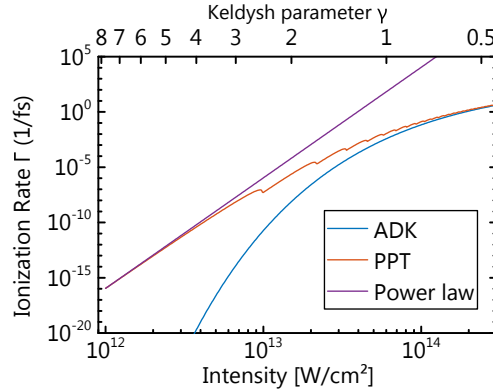


**Figure 2.2:** Ionization rates according to the ADK and the PPT model for a xenon atom ( $l=1$ ,  $m=0$ ,  $I_p = 12.13$  eV) for a carrier wavelength of  $1.04 \mu\text{m}$ . We also plot the result of a simple power law  $\Gamma \propto I^n$  with  $n = 10$  corresponding to  $I_p / \hbar\omega_c$ .

Note, that the above mentioned theories all presuppose a finite height of the Coulomb barrier and an unvarying ground state energy (neglecting the AC-Stark effect). For field strengths above a critical value the regime of barrier suppression is entered. A classically calculated estimate of the intensity required to suppress the barrier amounts to:

$$I_{\text{B.S.}} \approx 4 \times 10^{13} \text{ W/cm}^2 \times I_{\text{p,eV}}^4.$$

For laser intensities greater than  $I_{\text{B.S.}}$ , correction factors to the quasi-static ionization rates were calculated for simple atomic systems [96, 97]. As the barrier suppression is independent of the laser frequency, but the Keldysh parameter depends both on the laser frequency

and its intensity, it is possible that the tunneling limit is never reached, for example, in the case of xenon, where  $I_{\text{B.S.}} \approx 8.7 \times 10^{13} \text{ W/cm}^2$  at which  $\gamma \approx 0.8$  for a driving wavelength of  $1 \mu\text{m}$ .

### Nonlinear polarization and pulse propagation

In the following paragraphs, we will provide details on the modeling of self-phase and self-amplitude modulation effects occurring in the propagation of an ionizing pulse through a gas target. Starting from Maxwell's equations, Geissler *et al.* approximated the wave equation by a first order propagation equation, that describes a forward propagating wave (complex electric field  $\mathcal{E}$ ) in the presence of the nonlinear polarization response  $P_{\text{NL}}$  of the medium [98]. In a comoving reference frame, it reads:

$$\frac{d}{dz}\mathcal{E}(\tau, \mathbf{r}) = \frac{c}{2}\nabla_{\perp}^2 \int_{-\infty}^{\tau} \mathcal{E}(\tau', \mathbf{r})d\tau' - \frac{1}{2\epsilon_0 c} \frac{d}{d\tau} P_{\text{NL}}(\tau, \mathbf{r}). \quad (2.12)$$

Here,  $c$  denotes the speed of light,  $\epsilon_0$  the vacuum permittivity and  $\nabla_{\perp}^2$  is the transversal Laplace operator acting on  $x$  and  $y$ .

In an ionized gas, the response of the medium to the electric field is dominated by the free electron gas. A simple analytic expression for  $\frac{d}{d\tau} P_{\text{NL}}$  can be derived by considering the oscillating dipole formed by an electron and its parent ion after quasi-static tunneling through the Coulomb barrier and subsequent acceleration in the laser field [98]:

$$\frac{d}{d\tau} P_{\text{NL}}(\mathbf{r}, \tau) = n_{\text{gas}} \left[ I_{\text{p}} \frac{\partial_{\tau} \eta(\mathbf{r}, \tau)}{\mathcal{E}(\mathbf{r}, \tau)} + \frac{e^2}{m} \int_{-\infty}^{\tau} \eta(\mathbf{r}, \tau) \mathcal{E}(\mathbf{r}, \tau') d\tau' \right]. \quad (2.13)$$

Here,  $I_{\text{p}}$  denotes the ionization potential,  $n_{\text{gas}}$  the gas number density,  $\eta$  the ionized fraction.

Assuming transverse homogeneity  $\mathcal{E} = \mathcal{E}(\tau, z)$  and assuming highly multi-cycle pulses and not too high intensities, this expression can be further approximated to [88]:

$$\frac{d}{d\tau} P_{\text{NL}}(z, \tau) \approx \mathcal{E}(z, \tau) n_{\text{gas}} \left[ I_{\text{p}} \frac{1 - \eta(z, \tau)}{|\mathcal{A}(z, \tau)|^2} \Gamma_{\text{peak}}(z, \tau) - i2\epsilon_0 c r_e \lambda_c \eta(z, \tau) \right]. \quad (2.14)$$

Here,  $r_e$  is the classical electron radius, and  $\lambda_c$  is the carrier wavelength. Furthermore we have decomposed the (complex) electric field into a fast oscillating carrier and a slowly varying complex envelope  $\mathcal{A}$  (see Appendix A for details on the sign convention). With  $\Gamma_{\text{peak}}(\tau)$  we denote the value of the maximum of the non-cycle averaged ionization rate, given the current value of the pulse envelope. The main benefit of Eq. (2.14) is, that the propagation equation (2.12) can now be applied to the slowly varying envelope of a pulse. Thus, the numerical discretization can be much coarser.

To take into account the chromatic dispersion of a pre-existing plasma, the Drude model of a free electron gas in an oscillating field can be employed [91]. The frequency dependence of the refractive index is found to be:

$$n_{\text{p}}(\omega) = \sqrt{1 - \frac{\omega_{\text{p}}^2}{\omega^2}} \stackrel{\omega_{\text{p}} \ll \omega}{\approx} 1 - \frac{\omega_{\text{p}}^2}{2\omega^2}, \quad \text{with} \quad \omega_{\text{p}}^2 = \frac{e^2 n_{\text{gas}} \eta}{\epsilon_0 m}. \quad (2.15)$$

In fact, the Drude model provides an intuitive approach for the effects of the plasma on the pulse propagation. Although the derivation of Eq. (2.15) assumes a time independent plasma density, this density can later be adiabatically changed according to the field induced ionization. Following these lines, an increasing plasma density leads to a monotonically decreasing refractive index, and, thus, to a temporal phase shift of the pulse. Interestingly, this phase shift is identical to the one calculated via Eq. (2.14).

The monotonically increasing phase shift of the pulse has important consequences. First, the electric field is temporally compressed, as the oscillations get squashed under the envelope. This points to the fact that the center of mass of the spectrum in the Fourier domain shifts to higher frequencies. In fact, the propagation of a pulse through an ionizing medium is accompanied by a strongly asymmetric spectral broadening towards the blue (“blue-shifting”) [99]. The associated spectral phase is constant over most of the spectrum with distinct phase jumps (see Fig. 2.3(b)).

Second, in an EC the intensity-dependent spectral broadening towards the blue changes the transient behavior of the cavity. This can, for instance, be seen in an adiabatic sweep of the comb over the cavity resonances by varying the repetition rate of the input pulses. Here, the integrated power enhancement traces out an asymmetric curve in the case of intracavity ionization [100]. Third, temporal phase shift partially impairs the cavity buildup and we will later show, that it ultimately limits the intracavity intensity (see Section 4.3.4 and Section 5.3.2).

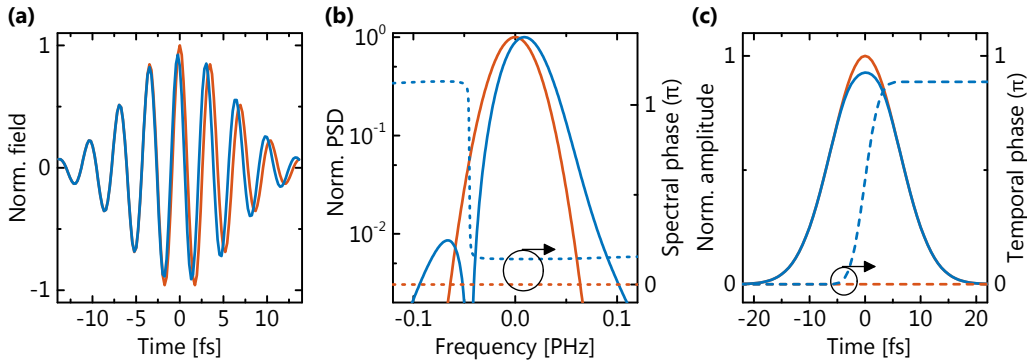


**Figure 2.3:** Self-amplitude and self-phase modulation of a pulse upon ionization. Input pulse, red; post-interaction pulse, blue. **(a)** Electric fields in the time domain. **(b)** Power spectral density (PSD) and spectral phase. **(c)** Amplitude (or envelope) and phase in the time domain.

### Steady-state plasma

Another particularity of the laser-induced ionization arises from the high repetition rates ( $\sim 100$  MHz) of the pulse train. If the time between two successive pulses is shorter than needed for complete recombination (or replenishment of the focal volume with neutral atoms), then a steady-state population of plasma emerges.

An obvious consequence of the steady-state plasma is, that the density of neutral atoms is reduced. In the case of HHG, less atoms contribute to the generation process, and the higher ionization fraction may alter the phase-matching conditions (see Section 2.3.2). Furthermore, it causes dispersion. For the cavity performance, also the zero order (constant

phase shift) and first order dispersion (group delay) play an important role. From Eq. (2.15) we deduce that the phase velocity in a plasma equals  $c/n_p(\omega)$ , and exceeds the vacuum speed of light  $c$  for frequencies above the plasma frequency (for our parameters  $\omega_p/2\pi$  is on the order of a few THz). The group velocity, however, is reduced due to  $n_p(\omega)c$ . Thus, the resonances of a cavity housing a plasma shift to higher frequencies and the round-trip time for the pulse is increased, requiring a different seeding comb for optimal enhancement (lower repetition rate, higher carrier-envelope offset (CEO) frequency). Neglecting higher-order dispersion (which is a good approximation for narrowband pulses), the optimal offset frequency due to a plasma of length  $L$  and plasma frequency  $\omega_p$  changes by:

$$\Delta f_{\text{ceo}} = \frac{\omega_c}{2\pi} \tau f_{\text{rep}} \left( 1 + \frac{1}{1 + \tau f_{\text{rep}}} \right), \quad \text{with} \quad \tau \approx \frac{L}{c} \frac{\omega_p^2}{2\omega_c^2}. \quad (2.16)$$

The repetition rate is decreased by:

$$\Delta f_{\text{rep}} = f_{\text{rep}} \left( 1 - \frac{1}{1 + \tau f_{\text{rep}}} \right). \quad (2.17)$$

In an adiabatic sweep of the input comb over the cavity resonances, the varying intracavity power changes the steady-state plasma density which again couples back to modify the resonance condition. If the comb parameters are gradually adjusted (in the right direction), the effective resonance width increases. For the other sweeping direction, the effective width of the resonance is much smaller [62].

The intensity-dependent resonance condition has three consequences for the comb-cavity stabilization servo loop. First, it causes optical bistability, that is, for the same effective round-trip time there are two possible states of the intracavity pulse: one with low intensity (no ionization) and one with high-intensity (ionization). Second, the comb parameters required for reliable lock are slightly detuned from the maximum of the nonlinear resonance. Here, self-locking occurs, that is, the effective cavity length adjusts itself (via the plasma) to fluctuations in the comb repetition rate [62]. Third, in the experiment, it is much harder to initially catch the lock of the servo loop.

In the remainder of this section, the mechanisms and the time scales of the recombination process and the rate of gas exchange are reviewed. We assume that the gas is supplied by a pressurized end-fire nozzle and that it expands freely into vacuum. At the nozzle orifice, the gas velocity along the nozzle axis is slightly below the speed of sound<sup>7</sup> and then accelerates to velocities that are about a factor of two higher (see Appendix E, or [101, 102]). Assuming xenon ( $c_{\text{sound}} \approx 169 \text{ m/s}$ ) and a typical focal spot radius of about  $25 \mu\text{m}$  this leads to a timescale on the order of 200 ns, which is much slower than the time between two pulses ( $\sim 10 \text{ ns}$ ).

There are two mechanisms that can contribute to the recombination of a plasma: photorecombination (electron capture and emittance of a photon) and recombination via three-body collisions (electron capture with an energy transfer to another electron) [103]. The recombination rate can change by orders of magnitude depending on the electron density  $n_e$  and on the temperature  $T$  of the electrons [104]. At high electron densities, the dominant mechanism of recombination is via three-body collisions. An estimate for the crossover is given

<sup>7</sup>In the calculation of the speed of sound, the temperature of the gas in the pressurized reservoir is taken.

by  $n_e \approx 3.1 \times 10^{13}/\text{cm}^3 \times T_{\text{eV}}^{3.75}$ , with  $T_{\text{eV}}$  being the electron temperature in electronvolt. A more detailed analysis carried out in Section 5.1.3 reveals that the intracavity produced plasma falls into the category, where three-body recombination dominates.

The electronic state of the atom after its recombination depends on the temperature of the electron gas. Slow electrons tend to recombine into high lying states. Typical time scales for the radiative lifetimes of states in xenon range from a few tens to several hundreds of nanoseconds [105, 106]. These lifetimes are, however, considerably shortened by collisional deactivation (quenching), provided that the gas density is high enough.

## 2.3 High-order harmonic generation

Building a laser oscillator requires highly reflecting optics for feedback, an adequate gain material and sufficient pumping to achieve inversion. In the XUV spectral region none of these prerequisites is easy to fulfill<sup>8</sup>. Most notably, the absence of high reflectivity cavity mirrors has so far precluded the construction of a laser oscillator in this spectral region [107], leaving only a few examples of laboratory scale amplifiers for XUV light (e.g., [108, 109])

Nonlinear optics provides a convenient means to transfer coherent radiation from one spectral region to another [110]. In our case the nonlinear process is termed high-order harmonic generation (HHG). Besides the exceptional coherence of the radiation provided by HHG sources [31], the emitted XUV pulses can be significantly shorter than the driving pulses, reaching pulse durations in the attosecond range [33, 36, 72].

In the following, we will first discuss theoretical approaches to modeling the harmonic emission of a single atom and then discuss macroscopic effects emerging from the coherent emission of an ensemble of atoms<sup>9</sup>.

### 2.3.1 Single-atom dipole response

The emission of radiation from an atom under the influence of an oscillating electric field (frequency  $\omega$ ) is due to the induced oscillating dipole moment (or response of the atomic polarization). For strong fields, the radiated light can contain frequencies that are harmonics of the driving frequency, and thus, it is natural to expand the induced polarization in a power series of the driving field [110]:

$$P(t) = \epsilon_0 [\chi^{(1)}E(t) + \chi^{(2)}E^2(t) + \dots]. \quad (2.18)$$

This ansatz is meaningful as long as the series converges. In HHG, the field strengths of the driving field approach the intra-atomic field strengths ( $E_a \approx 5 \times 10^{11} \text{ V/m}$ ), and the power series fails to converge. In other words, the intuitive picture of an oscillating electron cloud (in an anharmonic potential) is inappropriate. Experimentally, this can be seen in the plateau-like region of the harmonic spectrum. Here, the generated intensity  $I_q$  is largely

---

<sup>8</sup>The power required for pumping is about four orders of magnitude higher than in the visible: for a transition frequency  $\omega$ , the rate of spontaneous emission scales as  $\omega^3$  [76] and the energy gap is proportional to  $\omega$ , leading to a total power required for population inversion that scales as  $\omega^4$ .

<sup>9</sup>A textbook providing a thorough introduction to the subject is [91].

independent of the order  $q$  of the emitted harmonic. This is in contrast to the expected  $I_q \propto I_1^q$  dependency using the power series ansatz (with  $I_1$  being the intensity of the fundamental).

An accurate modeling of the HHG process can be achieved by numerically solving the time-dependent Schrödinger equation (TDSE) (in the single-active electron approximation), and by subsequently calculating the expectation value of the dipole operator [111, 112]. This is computationally demanding and hides the physics governing this process. Considerable insight can already be gained from a semi-classical picture [113]. Here, HHG is modeled as a three step process, comprising field-induced ionization of the electron from the ground state to the continuum, classical acceleration of the electron in the external field neglecting the Coulomb potential, and recombination to the ground state by emittance of a single photon.

Assuming a linearly polarized monochromatic laser field and zero initial velocity of the electron at the time it appears in the continuum (“birth time”  $t_b$ , position  $x_b$ ), one can easily calculate the classical trajectory  $x(t, t_b)$  by integrating the classical equation of motion. In this picture, recombination can only occur if the electron returns to the parent ion, that is, if the equation  $x(t, t_b) = x_b$  can be solved. For these trajectories Fig. 2.4(a) shows the time that the electron spends in the continuum as a function of the birth time. Figure 2.4(b) depicts the corresponding kinetic energy at the time of return.

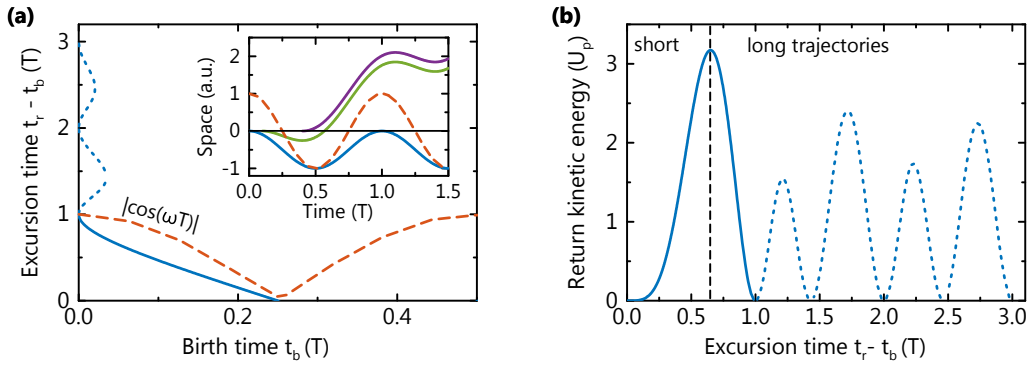


**Figure 2.4:** Classical electron trajectories. **(a)** Time in the continuum as a function of birth (ionization) time in the driving field (dashed line). Multiple return events are possible. Inset: three trajectories for different ionization times. The dashed line indicates the driving field. **(b)** Return kinetic energy as a function of the excursion time. Short, long and very long (dotted line) trajectories can be distinguished.

From this simple analysis, several conclusions can be drawn. First, for some ionization times, multiple re-collision events are possible, while for others (for positive slope of the absolute value of the field) the electron never returns to the parent ion. Typically, recollision events occurring more than one cycle later are very unlikely (due to a spreading of the electron wave-packet) and, thus, are neglected. Second, from the plot of the kinetic energy, we can deduce a clear maximum. The maximum energy of the emitted photons is given by  $\hbar\omega \approx I_p + 3.17U_p$ . Third, for all energies less than the cutoff energy, two kinds of electron trajectories exist. They are classified according to their excursion time as *long* and *short* trajectories. Therefore, interference effects between these two pathways are expected.

The semi-classical model was first justified by Lewenstein *et al.* in his seminal paper [114], where the authors developed a quantum-mechanical description of the HHG process. It is based on an approximate solution of the TDSE (within the single-active electron approxi-

mation) using perturbative techniques, however, not the standard lowest-order perturbation theory (a good text book providing a detailed understanding is [91]). The starting point is the TDSE of an electron in the potential of the atom subject to the oscillating field. With the electric dipole approximation (spatially homogeneous fields, no magnetic field) and in the length gauge (vanishing vector potential), the equation reads:

$$i\hbar \frac{\partial}{\partial t} |\psi(t)\rangle = H(t) |\psi(t)\rangle, \quad \text{with} \quad H(t) = \frac{\mathbf{p}^2}{2m} + V(\mathbf{r}) + e\mathbf{r}\mathbf{E}(t). \quad (2.19)$$

The Hamiltonian can be partitioned in two convenient ways:

$$H(t) = H_0 + e\mathbf{r}\mathbf{E}(t) = H_0 + H_{\text{int}}(t), \quad \text{or} \quad (2.20)$$

$$H(t) = H_{\text{GV}}(t) + V(\mathbf{r}). \quad (2.21)$$

Here,  $H_0$  is the Hamiltonian of the atom and  $H_{\text{GV}}$  is the so-called Gordon-Volkov Hamiltonian of a free electron in the laser field. For both of these operators, analytic expressions of the eigenfunction exist. The initial state of the system  $|\phi_0(t_0)\rangle$  is an eigenstate of  $H_0$  (atom in the ground state). The system state vector at the time  $t$  can be expressed using the evolution operator  $U(t, t_0)$ :

$$|\psi(t)\rangle = U(t, t_0) |\psi(t_0)\rangle = U(t, t_0) |\phi_0(t_0)\rangle. \quad (2.22)$$

The evolution operator is given by an integral equation. Using Eq. (2.20) as a possible partition of the Hamiltonian, it can be decomposed in a part that accounts for  $H_0$  and a part arising from the interaction Hamiltonian  $H_{\text{int}}$  [91]:

$$U(t, t_0) = U_0(t, t_0) - \frac{i}{\hbar} \int_{t_0}^t dt' U(t, t') H_{\text{int}}(t') U_0(t', t_0). \quad (2.23)$$

Thus the state vector can be formally written as:

$$|\psi(t)\rangle = |\phi_0(t)\rangle - \frac{i}{\hbar} \int_{t_0}^t dt' U(t, t') H_{\text{int}}(t') |\phi_0(t')\rangle. \quad (2.24)$$

It is still dependent on the (unknown) evolution operator  $U$ . Using the other decomposition of the Hamiltonian (i.e., Eq. (2.21)), the evolution operator can be expressed as:

$$U(t, t_0) = U_{\text{GV}}(t, t_0) - \frac{i}{\hbar} \int_{t_0}^t dt' U(t, t') V(\mathbf{r}) U_{\text{GV}}(t', t_0) \approx U_{\text{GV}}(t, t_0). \quad (2.25)$$

In the last step, we have only used the first element of the Dyson series, which is the explicit solution of this integral equation. As we essentially neglect the atomic potential in the evolution of the system, this approximation is named strong-field approximation. The convergence properties of the Dyson series with the atomic potential as the perturbation are difficult to determine. It is typically applicable in the low-frequency, high-intensity regime

( $\hbar\omega \ll I_p$ ,  $\gamma \lesssim 1$ ), because here, the ionization occurs predominantly at the peaks of the electric field (“tunneling regime”) and the electron wave packet is driven far away from the core (the classically calculated excursion is much greater than the Bohr radius  $a_0$ ).

When inserting Eq. (2.25) in the formal solution given by Eq. (2.24) of the TDSE, we can calculate the time-dependent dipole moment of the system via  $\mathbf{d}(t) = -e \langle \psi(t) | \mathbf{r} | \psi(t) \rangle$ . Assuming a centro-symmetric atomic ground state, and neglecting continuum-continuum transitions, the induced time-dependent dipole moment reads:

$$\begin{aligned} \mathbf{d}(t) &\approx \frac{2ie}{\hbar} \text{Im} \int_{t_0}^t dt' \langle \phi_0(t) | \mathbf{r} U_{\text{GV}}(t, t') H_{\text{int}}(t') | \phi_0(t') \rangle; \\ &= \frac{2ie^2}{\hbar} \text{Im} \int_{t_0}^t dt' E(t') \int d^3k \int d^3k' \langle \phi_0(t) | \mathbf{r} | \chi_{\text{GV}}(\mathbf{k}, t) \rangle \times \dots \\ &\quad \langle \chi_{\text{GV}}(\mathbf{k}, t) | U_{\text{GV}}(t, t') | \chi_{\text{GV}}(\mathbf{k}', t') \rangle \langle \chi_{\text{GV}}(\mathbf{k}', t') | \mathbf{r} \epsilon | \phi_0(t') \rangle. \end{aligned} \quad (2.26)$$

$$(2.27)$$

In the last step, we have inserted twice the unity-operator expanded in the basis formed by the Gordon-Volkov states and we have inserted the expression of the interaction Hamiltonian assuming a linearly polarized laser field (axis  $\epsilon$ ). This form allows a direct physical interpretation equivalent to the semi-classical three-step model: the induced dipole is proportional to the ionization (transition from the ground state to a Gordon-Volkov state via the dipole interaction), subsequent evolution in the laser-field, and the recombination (via the dipole interaction) to the ground-state. The standard representation of the evolution operator in Eq. (2.27), and making use of the orthogonality of different eigenstates of  $H_{\text{GV}}$  leads to:

$$\mathbf{d}(t) = \frac{2ie^2}{\hbar} \text{Im} \int_{t_0}^t dt' E(t') \int d^3k \langle \phi_0(t) | \mathbf{r} | \chi_{\text{GV}}(\mathbf{k}, t) \rangle \langle \chi_{\text{GV}}(\mathbf{k}, t') | \mathbf{r} \epsilon | \phi_0(t') \rangle.$$

These integrals can be solved numerically, for example, by using the saddle-point approximation for the fast oscillating phase term that appears when inserting the explicit form of the Gordon-Volkov states. The Fourier spectrum of the dipole moment is the key ingredient to the nonlinear polarization  $\tilde{P}_{\text{NL}}(\omega) = n_{\text{gas}} \tilde{d}(\omega)$  that enters the propagation equation<sup>10</sup>.

The success of the Lewenstein model relies on the fact, that it reproduces many of the results obtained from the numerical solution of the (full) TDSE, with much less computational effort. Most notably, the numerically calculated spectra of the dipole-response reproduce the plateau and the cutoff region that are measured in the experiment. Furthermore, the (intensity-dependent) phases of the long and short trajectories can be calculated. Since the Lewenstein model neglects electron dynamics in bound states and the Coulomb interaction between a free electron and its parent ion, it is not applicable to harmonics below the ionization threshold [120], and its accuracy increases with the harmonic order.

With the model, the scaling of the dipole moment  $d_q$  of the plateau harmonic  $q$  with the driving field intensity  $I$  can be derived. It roughly scales as  $I^{p/2}$  with  $p \approx 6 - 12$  depending

<sup>10</sup>In contrast, the emission of radiation of a single atom is proportional to  $\frac{d^2 \mathbf{d}(t)}{dt^2}$ .

on the gas species [115, 116]. Thus, the intensity of harmonic  $q$  scales as  $I^p$ . Given a driving field distribution of Gaussian shape with radius  $w_0$  (and divergence  $\Theta$ ), one can estimate<sup>11</sup> the radius  $w_q$  and the divergence  $\Theta_q$  of the harmonic  $q$  to scale as  $w_q = \frac{w_0}{\sqrt[p]{p}}$  and  $\Theta_q = \frac{\lambda_q}{\pi w_q} = \frac{\sqrt[p]{p}}{q} \Theta$ . This means that harmonics of high order are much less divergent than the fundamental beam (for experimental data see [117–119]).

### 2.3.2 Macroscopic response

To calculate the harmonic yield generated in a macroscopic target, the single atom dipole response is only the very first step. In principle, one needs to co-propagate the driving field and the harmonic field, for example, via two equations similar to Eq. (2.12) including the corresponding nonlinear polarization response. Here, we aim for a qualitative understanding of these macroscopic effects, that determine the harmonic beam profile and also partly the harmonic spectrum. We can expect significant harmonic yield, if the generation is phase-matched, that is, both fields (indexed according to the harmonic order) share the same phase velocity  $\omega_q/k_q$  with  $\omega_q = q\omega_1$ , and, thus:

$$\Delta k = k_q - qk_1 \stackrel{!}{=} 0 \quad \text{with} \quad k_q = \frac{d\phi_q}{dz}. \quad (2.28)$$

The phase mismatch typically depends on the position  $(z, r)$  and on time, and, thus phase matching can in general only be achieved transiently within a certain volume. We will keep the discussion to a region around the optical axis.

For the phase of the fundamental field, we have to take into account the refractive index of the gas ( $1 + \delta n_g$ ) and of the plasma (Eq. (2.15)), and the Gouy phase shift (Eq. (2.6)). For the harmonic field, there is also the dipole phase that linearly depends on the intensity of the fundamental field [114, 121]. Therefore, we find for the on axis phase evolution:

$$\begin{aligned} \phi_1(z) &= -[1 + \delta n_g(\omega_1) + \delta n_p(\omega_1)]k_1 z + \arctan \frac{z}{z_{R,1}}, \\ \phi_q(z) &= -[1 + \delta n_g(\omega_q) + \delta n_p(\omega_q)]k_q z + \arctan \frac{z}{z_{R,q}} - \frac{|\alpha_q|I_0}{1 + (z/z_{R,1})^2}. \end{aligned}$$

The Rayleigh range of the harmonic  $q$  can be estimated using the above mentioned scaling argument of the dipole moment to be on the same order of magnitude (though slightly larger) than the fundamental Rayleigh range. Considering that  $q$  is typically on the order of at least 10 (or even up to 100), we can safely neglect several terms, when computing the phase difference:

$$\Delta\phi(z) = \phi_q - q\phi_1 \approx [\delta n_g(\omega_1) + \delta n_p(\omega_1)]qk_1 z - q \arctan \frac{z}{z_{R,1}} - \frac{|\alpha_q|I_0}{1 + (z/z_{R,1})^2}. \quad (2.29)$$

The phase-matching condition stated in Eq. (2.28) requires a vanishing derivative of this quantity and therefore, the individual contributions to  $\Delta\phi(z)$  need to be balanced. As  $\alpha_q$

---

<sup>11</sup>Note, that this reasoning assumes that the harmonics are generated with a flat (radial) phase front. This is, however, not the case due to the intensity dependent phase factor of the dipole moment [31]. The (approximately parabolic) radial phase increases the divergence of the harmonic beam.

differs for the long and short trajectories [31, 114, 122, 123], typically only one of the two trajectories can be phase matched. At the focus ( $z = 0$ ), the derivative of Eq. (2.29) with respect to  $z$  yields:

$$\left. \frac{\partial \Delta\phi}{\partial z} \right|_{z=0} = [\delta n_g(\omega_1) + \delta n_p(\omega_1)]qk_1 - \frac{q}{z_{R,1}}. \quad (2.30)$$

Requiring this derivative to vanish, and introducing the expressions of the plasma frequency (see Eq. (2.15)), the Rayleigh range (Eq. (2.6)) and the parameter  $\xi$  defined as  $\delta n_g = \xi n_{\text{gas}}$ , we find:

$$n_{\text{gas}} = \frac{2c^2}{\omega_1^2 w_0^2 \xi \left(1 - \frac{e^2}{\epsilon_0 m \xi \omega_1^2} \eta\right)}. \quad (2.31)$$

Therefore, phase matched generation at the focus can be achieved if the gas density is adjusted according to Eq. (2.31). This is only possible if the ionized fraction is kept below the critical value  $n_{\text{crit}} = \frac{e^2}{\epsilon_0 m \xi \omega_1^2}$ . For xenon and a wavelength on the order of  $1 \mu\text{m}$  this is about 4%. From Eq. (2.31) it is also obvious that tighter focusing geometries require higher gas densities [124, 125].

If the generation is phase matched, the harmonic yield is expected to increase quadratically<sup>12</sup> with the length of the gas target, or more generally with the number of emitters. When increasing the gas target length beyond the coherence length defined as  $\pi/\Delta k$ , the finite phase mismatch causes destructive interference and the harmonic yield decreases again [115]. This leads to oscillations in the harmonic yield, called Maker fringes [125–128]. In the experiment, re-absorption of the harmonic radiation within the gas target will set a second boundary condition to the length and the density of the gas target [115, 125].

<sup>12</sup>The harmonic field strength increases linearly.



## 3 Experimental apparatus

This chapter provides an overview of the experimental apparatus used in the experiments presented in Chapters 4 to 6. Key components of the experimental infrastructure had been set up in the framework of the thesis described in [129]. Therefore, emphasis is put on the undertaken improvements compared to the status in the original publications [57, 130]. Technical details and diagnostic tools, that are only relevant for a specific experiment are presented in the corresponding chapters.

The laser system is required to produce pulses with a pulse duration of a few tens of femtoseconds, with as much pulse energy as possible at a repetition rate of several tens of MHz. Furthermore, the pulses must be sufficiently stable that subsequent passive enhancement is possible. We opted for the implementation of a Yb-based master-oscillator power amplification system relying on the combination of a fiber-chirped pulse amplification (CPA) system and subsequent nonlinear spectral broadening and temporal compression. Up to date, this kind of laser architecture provides the highest average power at the stated repetition rates [131, 132]. Figure 3.1 depicts the setup comprising the oscillator generating the initial pulses, the fiber-CPA system, the nonlinear broadening stage, the EC and various electronics for stabilization and for diagnostics. The following two sections are dedicated to the laser system. Section 3.3 provides insight to the passive enhancement of the broadband pulses. Section 3.4 discusses the stability of the comb offset frequency and Section 3.5 is dedicated to the cavity and the comb-cavity stabilization.

### 3.1 Oscillator and CPA

The laser system is based on a home-built setup constructed by the fiber laser group of the IAP in Jena in 2008 [130]. An Yb:KGW oscillator setup delivers pulses of 130 fs, carried at a wavelength of about  $1.04\ \mu\text{m}$  with a repetition rate of 78 MHz. One of the end mirrors has a transmission of 4% and serves as output coupler, the other one is a semiconductor saturable absorber mirror (SESAM) (SAM-1040-3-10ps-2.0b-0, BATOP) that ensures mode-locking. It is glued to a  $2 \times 2 \times 2\ \text{mm}^3$  multilayer piezo electric transducer (PZT) (PL022.30, Physik Instrumente) used for stabilization of the repetition rate. The oscillator comprises to fused-silica wedges that allow for a coarse adjustment of the comb offset frequency.

The laser pulses are amplified in a double stage Yb-doped fiber CPA-system, employing transmission gratings with 1250 lines/mm for stretching to 150 ps and for re-compression. Both amplifiers use double-clad fibers (DC-170-40-Yb, NKT Photonics) with a mode-field diameter of  $31\ \mu\text{m}$ . At the output of the CPA system, 180-fs pulses of  $\sim 0.8\ \mu\text{J}$  are reached on a daily basis, corresponding to 60 W of average power in near-diffraction limited beam quality.

Several technical improvements have been incorporated in the setup to ensure reliable and long-term operation. First of all, pumping the Yb:KGW crystal in the oscillator at a

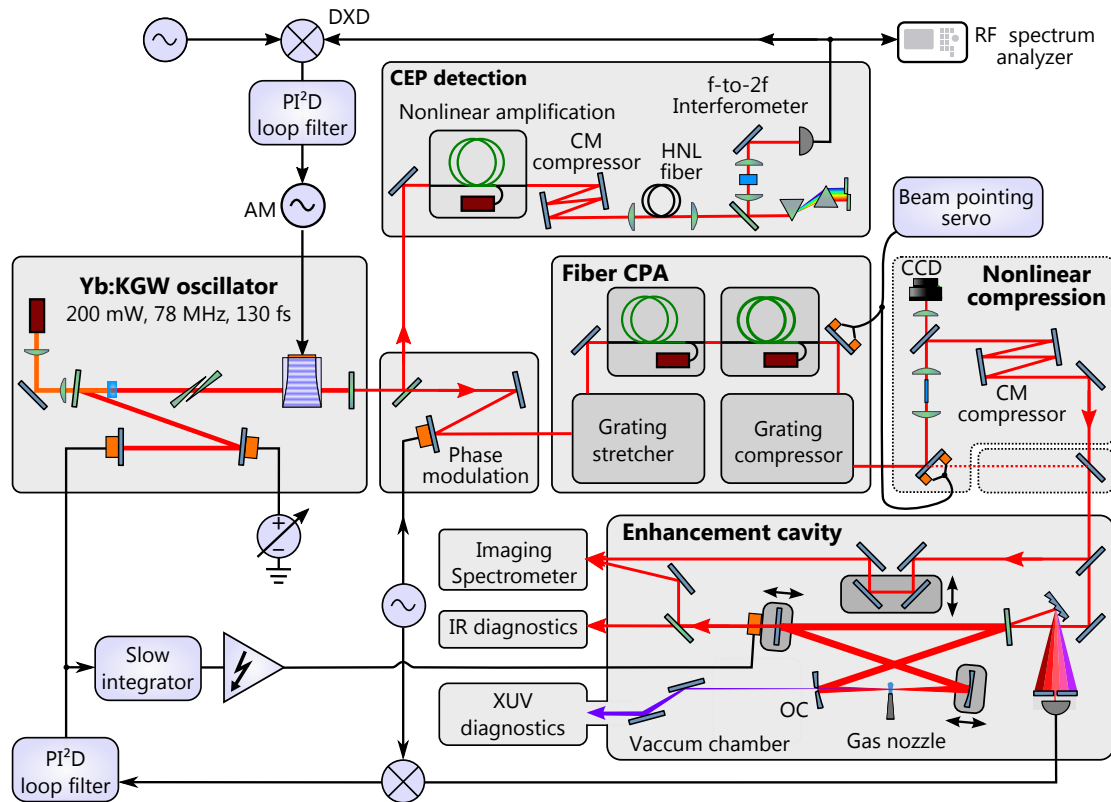


**Figure 3.1:** Schematic of the experimental setup. HNL, highly nonlinear fiber; CM, chirped mirrors; AM, amplitude modulation; DXD, digital phase detector.

wavelength, where the absorption-cross section has a smaller dependency on the wavelength (around 975 nm compared to 979 nm), dramatically reduces the oscillator phase noise. For active stabilization of the CEO frequency, the intracavity power can be controlled with an acousto-optical modulator (AOM) (see Section 3.4). Another important improvement of the oscillator concerns the mount of the PZT used for repetition rate stabilization (see Section 3.5 for details).

In the compressor and stretcher unit, the laser beam is prone to local density variations and turbulences of the ambient air. Housing the laser beam in these components, benefits the pulse-to-pulse stability at the CPA-output and even more at the output of the nonlinear fiber compression stage. Passive stabilization, for example, via water cooling of most optics and apertures, proofed an easy and effective measure to improve the overall system stability. To counteract fluctuations in the coupling of the beam to the fiber broadening stage, a beam-pointing stabilization was implemented. The fiber facets of the main amplification stage have been sealed with end caps to increase the spot size at the air-glass interface.

### 3.2 Nonlinear spectral broadening and compression

When pulse durations shorter than 180 fs are desired, nonlinear spectral broadening and subsequent temporal compression using chirped mirrors is employed. Here, for pulse en-

ergies in the range of  $1\ \mu\text{J}$  and peak powers below  $4\ \text{MW}$ , the state-of-the-art method is broadening in a solid core photonic crystal fibre (PCF) [130, 131, 133]. Typical signal core diameters range from  $20\ \mu\text{m}$  to  $60\ \mu\text{m}$ . Compared to broadening in bulk materials [133, 134], the guiding of the fiber provides much better output beam quality, especially in terms of homogeneity. The spectral broadening is a complex interplay of the nonlinear and the linear propagation in the fiber. In our case the nonlinearity is dominated by the Kerr-effect, but other nonlinear effects such as self-steepening and stimulated Raman scattering play a role [135, 136]. Soliton launching or fission is avoided by the overall normal dispersion of the fiber [135].

Compression ratios of about one order of magnitude can typically be achieved within a single broadening stage, limited by the chromatic dispersion of the fiber [136]. Inherent to the nonlinear spectral broadening is a modulated temporal pulse shape, resulting from the strongly modulated spectrum. The spectral phase induced in the broadening process can largely be compensated by reflection off chirped mirrors. For compression down to a few tens of femtoseconds, compensation of second-order dispersion (GDD), is mostly sufficient, resulting in pulse durations that are typically within 10% of the expected Fourier limit. In the experiment, compressed pulse durations ranging from 23 fs to 70 fs at average powers up to  $40\ \text{W}$  were targeted and reached on a daily basis. In contrast to the values in the original publication [130], output power was traded in for increased long-term stability and improved transverse beam quality.

Permanently imaging the beam at the output facet of the broadening fiber on a charge-coupled device (CCD) camera eases the coupling of the light to the fiber, especially in cases when optimal spatial homogeneity is required with short-pieces of PCFs. The fiber (with stripped off coating) lies in a V-shaped groove of two fused silica prisms, avoiding stress-induced polarization-rotation and mode changes. Furthermore, this type of mount guarantees negligible absorption of light not coupled to the fiber and, thus, avoids unnecessary thermal load in the vicinity of the fiber. To avoid long-term thermal drifts, the fused silica prism are placed on a water-cooled copper mount. Still, during high-power operation, the fiber end-facets considerably heat up and are most prone to damage.

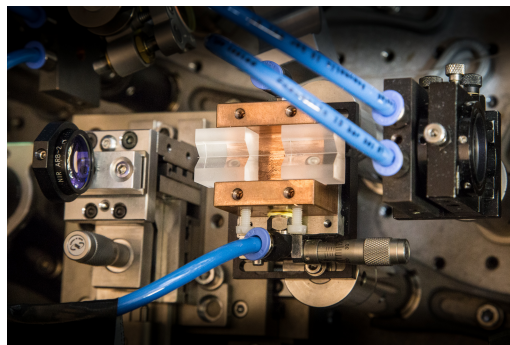


**Figure 3.2:** Photograph of the nonlinear compression stage, showing from left to right: the lens for input coupling, the fiber in a water-cooled mount, a water-cooled aperture and the lens for collimation.

The general limitation of broadening in solid core fibers is set by the self-focusing limit, reached at a peak power of about  $4\ \text{MW}$  in fused silica [136, 137]. In the experiment, the

onset of this regime is characterized by a fluctuating output mode. Furthermore, intensity-related damage, due to small defects resulting from imperfect fiber preparation or due to adsorbed dust particles can occur below the peak power limitation. Some of these limitations can be substantially mitigated by using hollow-core gas-filled PCFs, with a Kagome-type lattice design, that became available recently [138, 139].

The remainder of this section discusses the challenges that arise in the enhancement of nonlinearly compressed pulses. The beam quality at the output of the fiber is typically diminished compared to the beam quality from the fiber-CPA system. This is particularly the case, when relatively short pieces of fiber with large mode-field diameters are used (here, length down to 20 mm; mode-field diameter up to 59  $\mu\text{m}$ ). In such configurations, co-propagating higher-order spatial modes are not well suppressed and it is challenging to prepare the fiber end-facets in a plane manner to avoid phase front aberrations. Both effects reduce the spatial overlap with the cavity mode, typically by about 20 % compared to the pulses from the CPA system.

Besides this loss in power, stability issues on time scales ranging from microseconds to hours arise. Power fluctuations in the output signal result from fluctuating coupling conditions of the input beam to the fiber mode. This is partially compensated by an active stabilization of the input beam. Even more harmful than power fluctuations is the resulting phase noise (or even spectral changes), that is inevitable, because amplitude modulation (AM) to phase modulation (PM) coupling is at the heart of the nonlinear broadening process. For a Kerr-type nonlinearity the refractive index  $n$  depends on the intensity  $I$  according to  $n = n_0 + n_2 I(t)$ . A continuous wave laser of frequency  $\omega_c$  with a sinusoidal intensity-modulation  $I(t) = I_0 + \delta I \sin(\Omega t)$  acquires a phase  $\frac{\omega_c}{c} n_2 \delta I \sin(\Omega t) L$  after propagation of length  $L$  through the Kerr-nonlinearity [110]. In the spectral domain, this phase modulation manifests itself as sidebands separated by  $\Omega$  from the carrier, similar to the case of the error-signal generation in the Pound-Drever-Hall comb-cavity stabilization scheme [140]. For large values of  $\Omega$ , this light cannot be coupled to the cavity. For a pulsed laser, one can also think of the AM to PM conversion in terms of resulting CEP fluctuations [141]. For a single pulse, the induced CEP shift due to the nonlinearity can be calculated according to:

$$\delta\phi_{\text{cep}} = \frac{\omega_c L}{c} [n_g(\omega_c) - n(\omega_c)] \quad \text{with} \quad n_g(\omega) = n + \omega \frac{dn}{d\omega}.$$

being the group refractive index. Thus, after the Kerr nonlinearity, pulses initially differing in intensity by  $\delta I$  will show a difference in terms of their CEP that reads:

$$\delta\phi_{\text{cep}} = \omega_c^2 \frac{L}{c} \delta I \left. \frac{dn_2}{d\omega} \right|_{\omega_c}.$$

Assuming again a sinusoidal modulation of the intensity, that is,  $I(t) = I_0 + \delta I \sin(\Omega t)$  and an initial pulse train of identical pulses ( $\omega_{\text{ceo}} = 0$ ), the output pulse train shows a varying pulse-to-pulse phase slip. For a very low frequency modulation (much lower than the video and resolution bandwidth of the monitoring spectrum analyzer) this leads to a time varying offset frequency of the comb, according to:

$$\delta\omega_{\text{ceo}}(t) = \omega_c^2 \frac{L}{c} \frac{dI}{dt} \left. \frac{dn_2}{d\omega} \right|_{\omega_c}.$$

While broadening in solid-core PCFs was an established concept at the time of the start of this thesis, the question regarding the stability, the induced phase noise when operated behind a power amplifier and, thus, of the suitability of the output pulses for passive enhancement was still unclear. The experiments presented in the following chapters clearly reveal, that this is a viable route towards high-power short pulse ECs. It should be kept in mind, that the above discussed effect of AM to CEP-modulation can also occur in the spectral broadening required for the CEP detection.

### 3.3 Dynamics of broadband pulse enhancement

In this section, we will investigate the impact of the aforementioned phase and amplitude fluctuations on the intracavity pulse. It is straight-forward to show that the cavity acts as a first order low-pass filter for both amplitude and phase fluctuations of the input signal without cross-coupling terms, provided that the cavity is exactly on resonance and the excursions are small [142]. The filter cutoff frequency is given by the cavity resonance linewidth  $\Gamma_{\text{FWHM}} = f_{\text{rep}}/\mathcal{F}$ , which is on the order of 100 kHz for most of our experiments. Thus, fluctuations happening on shorter time scales than  $\Gamma_{\text{FWHM}}^{-1}$  are damped. If, however, a slight detuning between the comb line and the cavity resonance is present, PM-to-AM coupling terms (and vice versa) are present (see Appendix B for the derivation). These cross-coupling terms show a combined high-pass and low-pass characteristic with a maximum around  $\Gamma_{\text{FWHM}}$ . When driving a highly nonlinear process in the cavity such as HHG, amplitude fluctuations are detrimental to the stability of the generated XUV radiation. This is yet another reason, why input phase fluctuations need to be kept at a minimum.

Low frequency components of the phase noise ( $\lesssim 20$  kHz) can partially be compensated by adjusting the oscillator cavity length (and thus its repetition rate). For a small spectral bandwidth of the seeding laser ( $\frac{\delta\nu}{\nu_c} \ll 1$ ) or a low-finesse cavity, this is even feasible if the fluctuations originate from the other comb parameter, as it is the case in the AM-to-PM coupling in the nonlinear fiber. This is because acting on the repetition rate or on the offset frequency changes the comb in a very similar way at frequencies around the central frequency. For a seeding spectrum of Gaussian shape, we find an analytic formula for the change in integrated power enhancement  $\mathbb{E}_{\text{int}}$ , given a change  $\Delta f_{\text{ceo}}$  of the offset frequency, that is compensated as good as possible by a change in the repetition rate (see Appendix C for the derivation). With  $\text{Erfc}$  being the complex error function, the ratio of integrated power enhancement to its value for optimal comb parameters reads:

$$\frac{\mathbb{E}_{\text{int}}(\Delta f_{\text{ceo}}, \mathcal{F}, \Delta\nu)}{\mathbb{E}_{\text{int, opt}}} = \sqrt{\pi} x e^{x^2} \text{Erfc}(x), \quad (3.1)$$

$$\text{with } x = \left( \frac{1}{\sqrt{\log 2}} \frac{\Delta\nu}{\nu_c} \frac{\Delta f_{\text{ceo}}}{\Gamma_{\text{FWHM}}} \right)^{-1}.$$

The reduced integrated power enhancement results from the spectral filtering of the cavity. In Fig. 3.3 both effects are visualized.

With the increased sensitivity of the cavity to the comb offset frequency, the crosstalk of the oscillator length servo to the comb offset frequency becomes a critical issue. It can lead to a situation, where the central portion of the intracavity comb shows much lower amplitude

noise than the outer wings or the integrated power. We managed to considerably reduce this effect by monitoring the length-to-offset-frequency crosstalk in the final step of the oscillator alignment. To completely eliminate crosstalk in the oscillator, the length servo could be set up to work on the EC length.

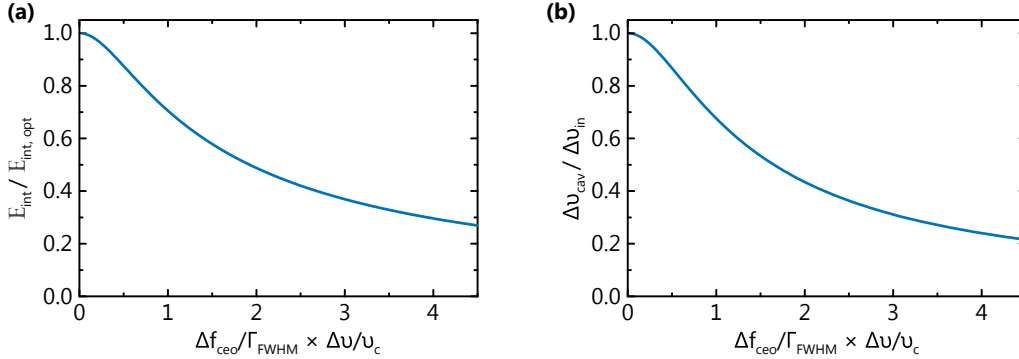


**Figure 3.3:** Partial compensation of changes in the comb offset frequency  $\Delta f_{\text{ceo}}$  by adaption of the repetition rate. **(a)** Resulting integrated power enhancement and **(b)** spectral bandwidth of the intracavity light.

## 3.4 CEO detection and stabilization

With increasing spectral bandwidth, it becomes essential to monitor and eventually control both degrees of freedom of the seeding frequency comb. To this end, an f-2f interferometer was integrated in the setup, and ways of acting on the CEP of the pulse train were evaluated. We will first briefly discuss the options for phase detection and phase stabilization in our system, and then present the experimental results<sup>1</sup>.

Ideally the additional stabilization scheme should provide a fully phase stabilized, zero-phase-slip ( $f_{\text{ceo}} = 0$ ) pulse train without conflicting with the repetition rate servo (crosstalk, sideband modulation), or constricting the flexibility offered by the optional nonlinear compression stage. It is obvious that fulfilling all of the requirements is impossible. Provided that CEP fluctuations are vastly dominated by the oscillator, a system comprising a detection at the output of the oscillator and a cavity-external stabilization scheme [143, 144] before the fiber amplifier is most promising. The pulse parameters of the oscillator are, however, not sufficient, to simultaneously generate a coherent supercontinuum [135, 145] as needed for the CEO frequency beat detection, and to seed the CPA system. Therefore, the output of the oscillator was split up before the stretcher, and approximately one third of the power was used to seed an additional fiber amplifier<sup>2</sup>, dedicated to simultaneously increase the pulse energy and the spectral width via self-phase modulation (SPM). After recompression to about 80 fs with chirped mirrors<sup>3</sup> providing a total GDD of  $-6000 \text{ fs}^2$ , an octave-spanning spectrum was generated in a highly-nonlinear PCF (SC-3.7-975, NKT Photonics) and the

<sup>1</sup>The considerations and measurements outlined in this section arose from a collaboration with F. Lücking.

<sup>2</sup>The fiber amplifier was designed and supplied by the Limpert group from the IAP in Jena.

<sup>3</sup>The chirped mirrors were produced by O. Razskazovskaya.

CEO frequency beatnote was detected in a standard common-path f-2f interferometer (see Fig. 3.1).

For a number of reasons the cavity-external stabilization scheme based on an acousto-optical frequency shifter failed to reach the envisaged phase stability and reliable operation. Most notably, this was due to the high requirements of the scheme on the stability of the free-running beat note which eventually resulted in spontaneous system failure and subsequent damage of the broadening fiber at the CPA output. Furthermore, out-of-loop CEP measurements of the high power compressed output pulses revealed considerable residual noise on a radian level (bandwidth: 1 Hz to 1 MHz).

Therefore, a feed-back system acting on the oscillator power via an intracavity AOM was installed [133]. We opted for beat signal detection after the nonlinear fiber amplifier, trading in uncompensated phase noise entering the CPA for the possibility to permanently monitor the offset-frequency also in case of non-broadened pulses. In Fig. 3.4 the measured CEP noise power spectral density (PSD) and the integrated phase noise are plotted, revealing an in-loop integrated phase noise on the radian level. In contrast, when detecting the beat note without the nonlinear fiber amplifier by pre-compressing the full oscillator output power in a step-index fiber, a noise level of 431 mrad was reached.

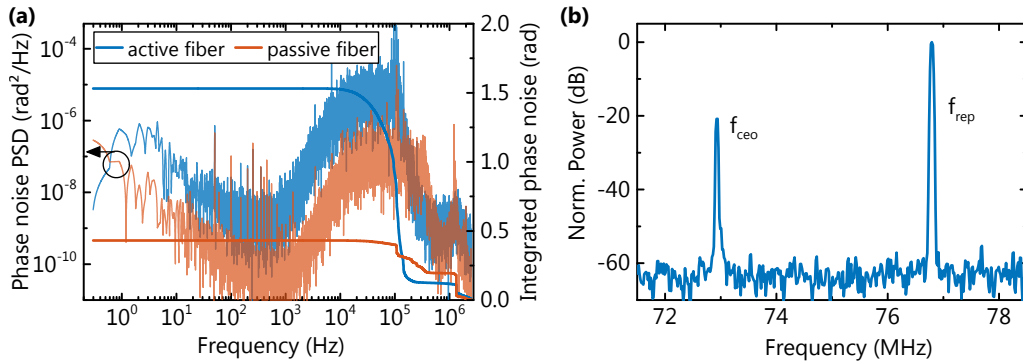


**Figure 3.4:** (a) CEP noise PSD and integrated CEP noise PSD when the oscillator is stabilized using the nonlinear fiber amplifier or with pre-broadening in a passive single-mode fiber. (b) Free-running CEO frequency beat note showing a linewidth of less than 100 kHz and a signal-to-noise ratio of more than 40 dB recorded with optimized oscillator.

In light of the reported performance achieved in similar systems [146–148], the measured noise levels are surprisingly high. Concerning the oscillator itself, most of the residual noise is located between 100 kHz to 400 kHz and, therefore, in a range where the gain of the servo loop is small or negligible. The origin could be AM-to-PM coupling in the oscillator, induced by fluctuations of the absorbed pump power, for example, by mode-competition in the pump diode that is simultaneously emitting at different wavelengths. A measurement of the oscillator intensity noise revealed considerable content (above the shot-noise limit) for frequencies up to 300 kHz. Note that the rate of increase of the inversion in the crystal is not limited by the rather long upper state lifetime of the gain material (on the order of a millisecond). Ideally a wavelength-stabilized, single-mode pump diode should be used for pumping the crystal. In experiments with a single-mode pump diode (AC1401-0750-0980-PM 25C, Gooch & Housego) employing a fiber-bragg-grating for wavelength stabilization,

much better short-term performance was achieved. The available pump power was, however, not high enough to ensure longterm reliable mode-locking. Further measures towards improving the free-running phase noise performance of the oscillator are currently carried out in the laboratory. With the nonlinear fiber amplifier in place, additional noise enters via several mechanisms. These include AM-to-PM coupling in the nonlinear amplifier and in the highly nonlinear fiber as discussed in Section 3.2, amplified spontaneous emission and amplified spontaneous raman scattering in the fiber amplifier, and modulational instability (unseeded four-wave-mixing [135, 136, 139]). Most of the additional noise is at frequencies below 150 kHz, that is, within the servo-loop bandwidth. This suggests a stochastic origin of the noise that is even increased by the servo loop when attempting to correct for random fluctuations. This is further corroborated by the fact that the additional noise is largely frequency independent in this range (constant offset of the two phase noise curves), hinting to amplified spontaneous emission as the origin of the noise added by the fiber amplifier.

The positive effect of the CEP-servo on the intracavity power is shown in Fig. 3.5. As expected from the discussion in Section 3.3, the stability of the intracavity power is significantly increased with the CEP servo engaged. Despite the availability of an improved cavity performance, most of the cavity-related experiments in this thesis were done without stabilizing the CEP of the oscillator. Instead, we opted for optimizing the free running CEP performance through various measures, most notably by pumping the laser crystal in a spectral region where the absorption cross-section is wavelength-independent and by optimizing the mode-locking state. In the CPA-system, the above mentioned active (beam pointing) and passive means (housing of the stretcher and compressor unit) to stabilize the coupling to the nonlinear fiber stage where undertaken. Provided that the oscillator was well-aligned (at the help of the  $f$ - $2f$ -interferometer) and in an optimal mode-locking state, the intrinsic phase stability of the free running oscillator was sufficient for all cavity based experiments (free-running  $f_{\text{ceo}}$  beat-note linewidth of 50 kHz compared to a linewidth on the MHz level in the non-optimized case).

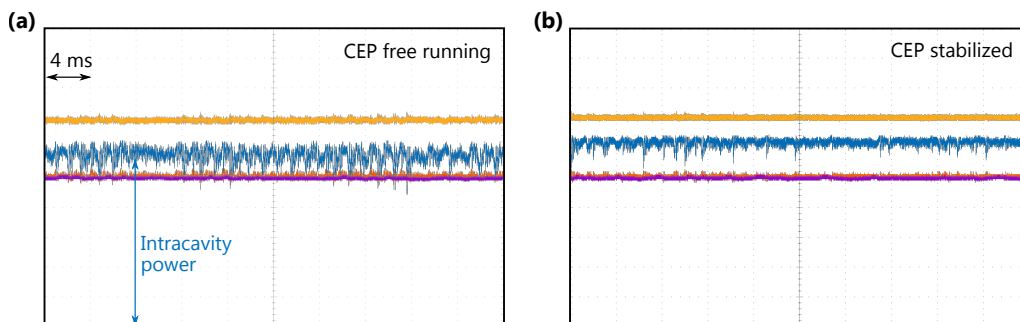


**Figure 3.5:** Oscilloscope screenshots showing, inter alia, the intracavity power when the CEP stabilization is (a) disengaged or (b) engaged. The cavity finesse exceeds 1000. Input pulse duration: 33 fs. Intracavity pulse duration is reduced from 41 fs in (a) to 39 fs in (b).

### 3.5 Enhancement cavity and comb-cavity stabilization

The EC<sup>4</sup> is set up in a standard planar bow-tie ring configuration placed in a vacuum chamber with a footprint of 0.5 m by 1 m. It is evacuated by a turbo-molecular drag pump with a pumping speed of 1000 l/s (TMP1000H, Pfeiffer Vacuum Technology), which is backed by a oil-free pre-pump (SCROLLVAC SC 30D, Oerlikon Leybold Vacuum), reaching a base pressure below  $1 \times 10^{-4}$  mbar. Standard opto-mechanics are used without precautions for potential outgasing. A spectrometer for analysis of the XUV radiation can readily be attached to the system.

In view of the cavity design considerations deduced in our group [84], the EC is typically set up to operate close to the inner edge of the stability range. This ensures large and similar spot sizes on all cavity optics at manageable robustness against mirror tilts. The length of the cavity can be adjusted by moving one of the plane folding mirrors via stepper motors. Moving one of the curved mirrors offers the additional flexibility to precisely position the resonator within its stability range, as it is required, for example, for the experiments presented in Section 4.4. In all experiments requiring the ionization of a gas target, the focus sizes of the resonator ranged from 12  $\mu\text{m}$  to 35  $\mu\text{m}$  to ensure sufficient peak intensity. In turn, this required focusing optics with radii of curvature below 300 mm. In view of supported spectral bandwidth and of minimal cavity losses, a four mirror cavity would be ideal. Due to practical constraints of the vacuum chamber, the experiments had to be performed with additional plane folding mirrors. The multilayer coatings used are based on quarter-wave-stack-like designs of either  $\text{Ta}_2\text{O}_5/\text{SiO}_2$  for experiments requiring only a narrow spectral bandwidth or  $\text{Nb}_2\text{O}_5/\text{SiO}_2$  in experiments requiring broader bandwidth.

Standard diagnostics of the cavity signal comprise monitoring of the (calibrated) leakage through one of the cavity mirrors in terms of power, spectrum, pulse duration and beam profile (see Fig. 3.1 for schematic of the setup). The light reflected at the input coupler is sent onto two photodiodes for monitoring the amount of light coupled to the cavity and for retrieving the error signal of the comb-cavity stabilization. In contrast to the experiments in [129] the comb-cavity servo is now based on a Pound-Drever-Hall scheme [140, 149, 150] providing superior capture range for locking [76]. Sidebands at 750 kHz are modulated on the signal prior to the stretcher by reflecting the light off the oscillating PZT-mounted mirror. Furthermore, the servo-loop filter now provides a  $\text{PI}^2\text{D}$  characteristic<sup>5</sup>. Compared to the original PI-filter, the additional double integrator stage allows for higher gain at low frequencies and the differential part introduces a phase lead at high frequencies (Fig. 3.6(a)).

The filtered error signal is fed back to two PZT-mounted mirrors. The small PZT glued to a home-built mount similar to the one in [151] provides flat frequency response up to 150 kHz and moves the SESAM end-mirror in the oscillator. Figure 3.7 shows the comparison of the response of the PZT-mirror when attached to the improved mount compared to the same system on the original brass mount from [129]. The second PZT in the oscillator is manually adjusted to ease catching of lock of the servo system. As this moves one of the folding mirrors in the oscillator, any adjustment of it also shifts the comb offset frequency. Thus, by turning this knob, the comb offset frequency can be adjusted during engaged cavity lock.

<sup>4</sup>The hardware for the EC-part had been mostly set up by I. Pupeza for the experiments described in [15, 57, 129].

<sup>5</sup>P, proportional; I, integral; D, differential.

### 3 Experimental apparatus

The servo control signal is additionally passed through another integration stage set to very low frequencies ( $\lesssim 1$  Hz), that feeds back on the EC length via a long-travel-range PZT. Besides improving the long-term stability of the system this scheme renders a high-voltage high-current amplifier for the fast PZT obsolete. Despite these improvements, the servo bandwidth is limited to about 30 kHz by the PZT resonance peak, as can be read from the Bode-plot in Fig. 3.6(b) showing the idealized open-loop system gain.

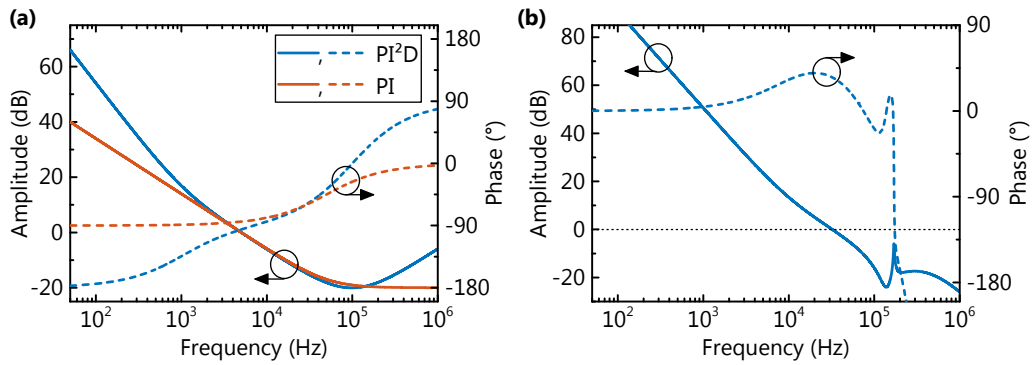


**Figure 3.6:** (a) Bode plot of the transfer function of a PI<sup>2</sup>D and a standard PI loop filter with typical corner frequencies. (b) Modeling the overall open-loop gain of the comb-cavity stabilization system, including a realistic PZT and the low-pass characteristics when deriving the error signal. Due to the overshoot of the PZT response at its resonance frequency ( $\sim 160$  kHz), it is difficult to achieve a servo-loop bandwidth exceeding  $\sim 30$  kHz.

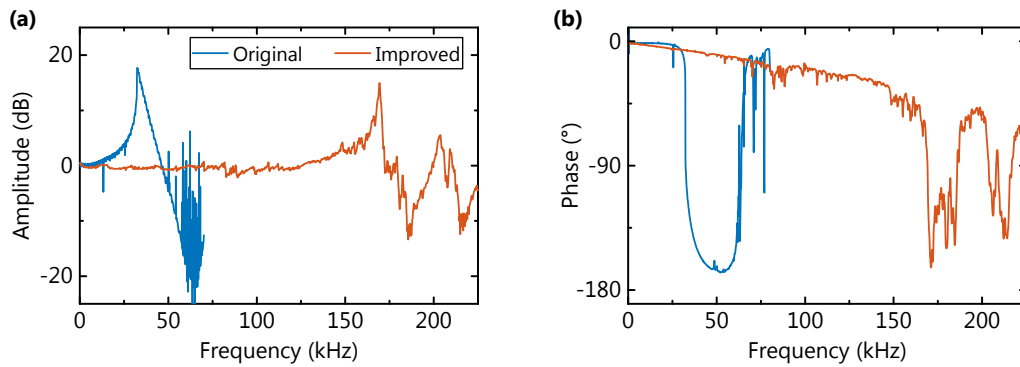


**Figure 3.7:** Interferometrically measured transfer functions of the PZT-actuated mirror mounts. Original, brass mount; Improved, copper-lead mount. The amplitude was normalized to its value at DC.

## 4 Cavity-enhanced HHG with geometrical output coupling

One of the main aims of this thesis was the improvement of cavity-based HHG towards an XUV light source for advancing the field of attosecond physics. This requires sufficient XUV photon flux and photon energies well above 20 eV. Ideally, the EC should support driving pulses short enough, that the XUV emission process can be restricted to one half cycle of the driving field. Therefore an XUV-IR beamsplitter is needed that allows for efficient XUV output coupling (OC) while not conflicting with any other requirements for the fundamental or the XUV radiation.

In this chapter we present several proof-of-principle type experiments, each of them representing milestones towards such a high-repetition rate XUV source. This includes, in particular, the demonstration of geometrical OC, the enhancement of nonlinearly broadened and compressed pulses and the use of a transverse field distribution other than a Gaussian, which introduces additional degrees of freedom for shaping the XUV emission.

The chapter is structured as follows. First, we introduce two principles of geometrical OC via openings in the cavity mirror following the cavity focus. Next, details about the experimental setup are provided. Two further sections are dedicated to the experimental results. Here, the first set of HHG experiments was performed with a Gaussian transverse beam profile and a pierced mirror was used for OC. In the second set of experiments, a mirror with a slit was employed for OC and a tailored driving mode was excited in the resonator. The chapter ends with a brief summary and a conclusion. The main findings presented in this chapter have been published in [66] and in [67].

### 4.1 Geometrical output coupling of XUV radiation

The term “geometrical output coupling” summarizes methods of spatially separating the generated XUV radiation from the driving field by geometrical means. They all exploit that the XUV emission can be spatially different from the propagation of the fundamental field. Thus, in geometrical OC, the output coupled XUV radiation does not interact with any material on its way out of the EC. In contrast, other established OC methods are based on spatially separating the XUV beam by reflection or diffraction at optical elements.

#### 4.1.1 Motivation

The main motivation for geometrical OC is that it renders additional optical elements serving as IR-XUV beam splitters unnecessary. Such beam splitters need to be placed between the focus and the following cavity mirror. Thus, the beam size on such an element is much smaller than on the other cavity optics, making it prone to damage and introducing strong thermal gradients. To increase the OC efficiency for the XUV, the angles of incidence are

typically large ( $\gtrsim 45$  deg), which makes the cavity response dependent on the polarization state of the fundamental light.

Diffraction output couplers typically suffer from a moderate XUV diffraction efficiency (less than 20% even if optimized) in a limited bandwidth [58, 152]. While the angular dispersion is beneficial for spectroscopic applications in the frequency domain [61], it is detrimental for time-domain application that exploit the extremely short durations of the XUV pulses. Although the angular dispersion can in principle be reversed, collinear OC methods are preferable in the latter case.

The simplest collinear XUV-IR beamsplitters exploit the chromatic dispersion of the refractive index of a dielectric material [29, 153]. Here, a thin plate transparent for the IR is placed under Brewster's angle in the cavity beam path. It partially reflects the generated XUV radiation (typically below 10%). To some extent the efficiency can be improved by increasing the angle of incidence (AOI) in combination with an anti-reflection coating for the IR radiation [59]. However, such plates might introduce GDD for the fundamental radiation, nonlinear effects at high intensities [65], and thermal lensing in the case of high average power.

Almost all of the above mentioned difficulties and shortcomings are avoided by geometrical OC methods [154, 155]. Here, a trade-off needs to be found between the amount of separation introduced during the harmonic emission process—potentially reducing the efficiency of the generation process—and the ratio of the OC efficiency to the loss for the fundamental beam occurring at the mirror following the emission process. The simplest way of introducing a geometrical separation of the harmonic radiation from the driving field, is the use of a Gaussian driving beam in combination with a small on-axis opening in the mirror subsequent to the cavity focus. As stated in Section 2.3, the divergence angle of the harmonic radiation can be much smaller than the divergence angle of the fundamental field, in particular for high-order harmonics. This offers the prospect of OC the XUV radiation through a small opening in a cavity mirror.

Another way of HHG with the XUV emission spatially separated from the fundamental beam is the case of non-collinear HHG [155–157]. Here, two pulses with a common focal spot intersect at a small angle, generating XUV radiation between the two beams. This approach is promising for the use in ECs, because it does not require any adaption of the mirror following the cavity focus. We implemented a modified version of non-collinear HHG in the limit of extremely small angles and that is intrinsically synchronized. In the experiment, this regime is readily accessible by using a Gauss-Hermite transverse field distribution of higher order, or, a combination of these modes (see Eq. (2.4)). Such field distributions can be tailored, to have zero intensity on axis on the curved mirror following the cavity focus and an on-axis intensity maximum within the focal region [86, 158]. Therefore the losses for the fundamental radiation at an on-axis opening in the mirror succeeding the cavity focus can be greatly reduced.

In summary, geometrical OC methods offer the prospect of broadband, highly efficient, collinear OC without transmissive or diffractive elements that are hit at a large AOI and at a small spot size. No additional GDD, nonlinearity or sensitivity to the polarization is introduced and thermal effects are avoided. The geometrical methods are particularly suited for high photon energies. The technological challenge is the production of the required small opening in the mirror, the size of which is determined by considering both the OC efficiency

of the XUV and the losses for the fundamental beam.

### 4.1.2 Fabrication of output coupling mirrors

The mirrors used for OC were fabricated in collaboration with partners experienced in the field of laser drilling. Most of the mirrors were micro-machined in a collaboration of our institute with the Fraunhofer Institute for Laser Technology ILT in Aachen<sup>1</sup>. A few other samples were manufactured by Micreon GmbH. The experimental results achieved within the collaboration with the ILT are published in [159]. Here, we provide a brief summary on the pursued approaches in both collaborations and the conclusions.

All openings were laser drilled in fused silica substrates with a thickness of 6.35 mm prior to the coating process. Figure 4.1 shows close-up photographs of two laser-machined samples. The in-house fabrication used the patented process of laser drilling in an *inverse* geometry (Fig. 4.2(a)) [160]. Here, the laser beam is focused through the transparent substrate to its bottom. Thus, dust and debris resulting from the ablation can be removed without perturbing the laser beam or any optics. Drilling is done layer-by-layer in a cone-type shape rejuvenating towards the (polished) front surface of the substrate. Pulses with an energy of 90  $\mu\text{J}$  and a duration of about 1 ns were used.

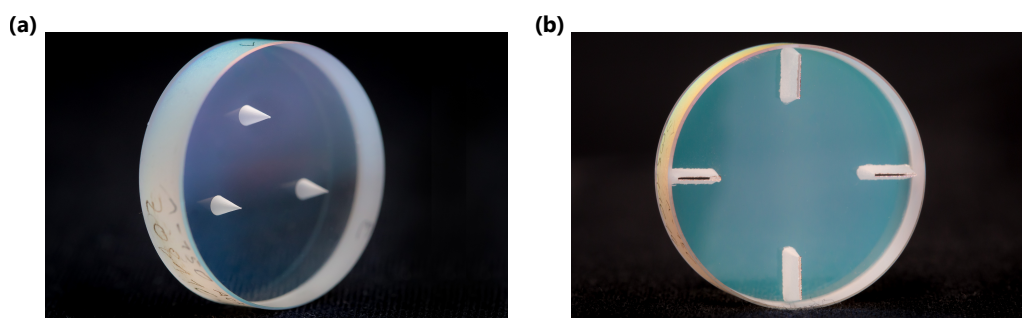


**Figure 4.1:** Close-up photograph of (a) a pierced mirror and (b) a slit mirror showing 3 (4) laser-drilled openings, of which one is used in the experiment.

In the external fabrication, a slightly different approach was used (Fig. 4.2(b)). After having removed most of the material using a *direct* approach (i.e., laser focused on surface facing the beam and substrate moving towards the laser beam), the substrate was turned around, and the opening created was enlarged by removing material from the edges, again in a direct approach. This procedure, however, limits the achievable aspect ratio of the opening due to the finite divergence of the laser beam. Therefore, no undercut is possible and the drilled shaped is slightly rejuvenating towards the back surface. While details on the process parameters were not disclosed by the manufacturer, it was confirmed that 10-ps-pulses of less than 10  $\mu\text{J}$  were used towards the end of the ablation process. This prevents excessive heat deposition in the substrate.

Microscope images of the front surface of various samples are presented in Fig. 4.3 and in Fig. 4.4. For all samples machined at ILT, substantial shell breaks (“chipping”) are visible in the proximity of the opening up to a distance of about 25  $\mu\text{m}$ , largely independent of the

<sup>1</sup>In the framework of the KORONA project, D. Esser laser-machined the mirrors at the ILT in Aachen.

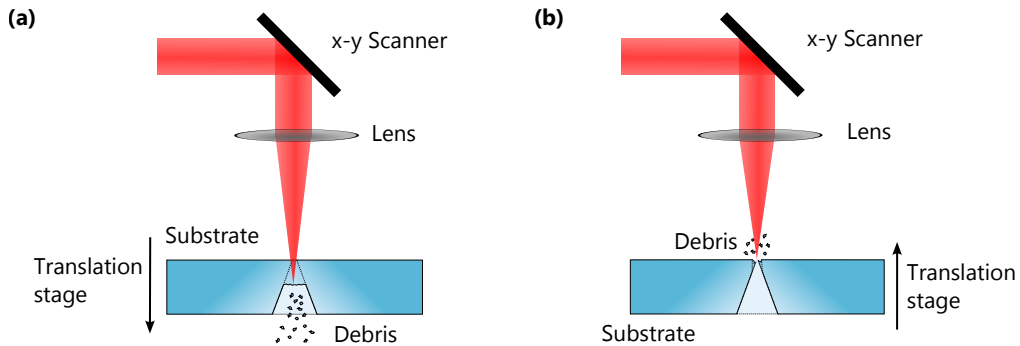


**Figure 4.2:** Schematic micro-structuring of transparent substrates. **(a)** Inverse geometry. **(b)** Final step of the ablation process in external fabrication: after break-through has been achieved the small opening is enlarged drilling in the conventional geometry.

opening size. In contrast, the samples manufactured by Micreon GmbH hardly show any chipping. We hypothesize that this can be rather attributed to the shorter pulse duration, the lower pulse energy or a smaller spot size than to the direction of the drilling process. In the direct-drilling approach, process-related contaminations are locally spoiling the polished front surface. Furthermore, a closer inspection with the focus in slightly increased depth, reveals the rejuvenation towards the back. Regarding the ratio of clear aperture (for the XUV light) to the diameter of the overall affected area, both approaches yield comparable results.

To analyze possible bulging of the surface, the processed samples were analyzed in a white light interferometer<sup>2</sup>. In all cases the surrounding surface is bend upwards. While for the pierced mirrors the detected bulging seems to be tolerable in terms of induced aberrations in the resonator, it is more severe for the slit mirrors. We found that polishing the substrates results in downward bend edges to roughly the same extend (not shown). Instead, by tempering the substrates, bulging can be considerably reduced and drilling induced stress, as apparent from a cross-polarizer analysis, can be relieved. Care needs to be taken that no dust particles are burned into the surface.

In conclusion, openings on the order of 100  $\mu\text{m}$  have been machined into standard cavity mirror substrates, allowing for the operation of a high-finesse cavity. Both approaches still need to be improved to provide fully satisfactory results. We believe, however, that a future thorough exploration of the (large) parameter space especially with regards to the pulse energy, the focal spot size and the pulse duration will considerably reduce the amount of chipping while avoiding an initial narrowing of the machined opening.

## 4.2 Experimental setup

A schematic of the experimental setup is depicted in Fig. 4.5. The pulses emitted by the CPA laser system can optionally be nonlinearly broadened and temporally compressed using a pair of chirped mirrors. For the experiments described in Section 4.3, a PCF with a mode-field diameter of 59  $\mu\text{m}$  and a length of only 26 mm was used to limit the spectral broadening

<sup>2</sup>The white light interferometer was operated by J. Weitenberg, ILT Aachen.

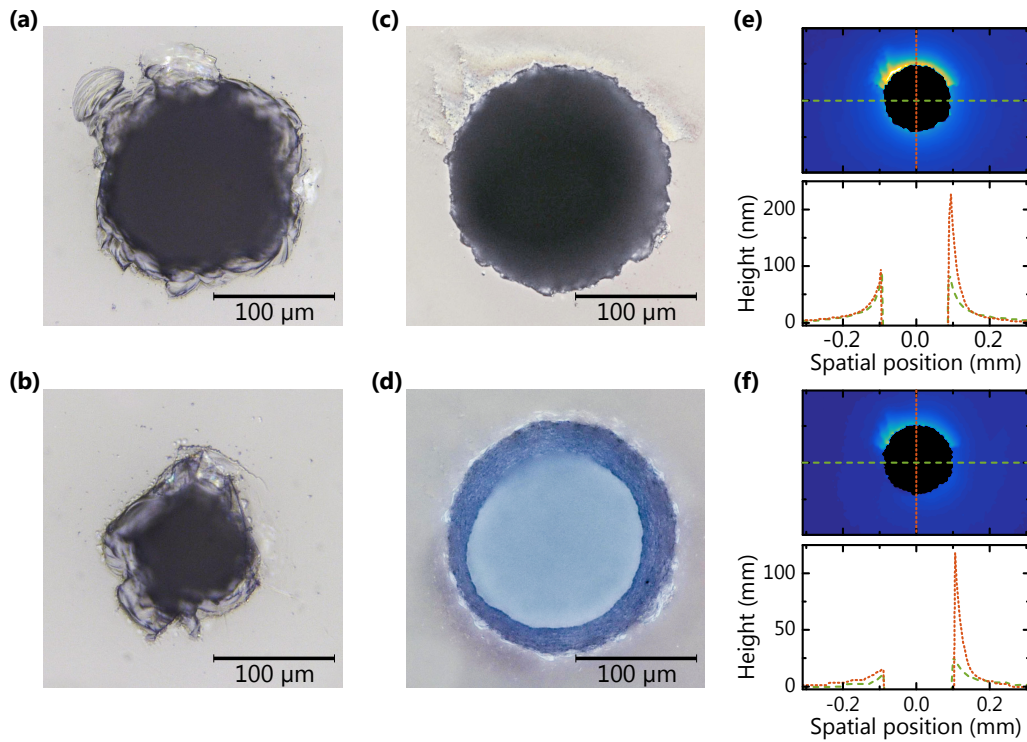


**Figure 4.3:** Pierced mirrors laser machined in (a,b) inverse geometry. (c,d) Externally fabricated samples using shorter pulses and a conventional geometry results in less chipping but in rejuvenation. Analysis of the same sample with a white light interferometer prior (e) and subsequent (f) to tempering reveals the relief of drilling induced bulging. Artifacts in the images are due to surface contaminations.

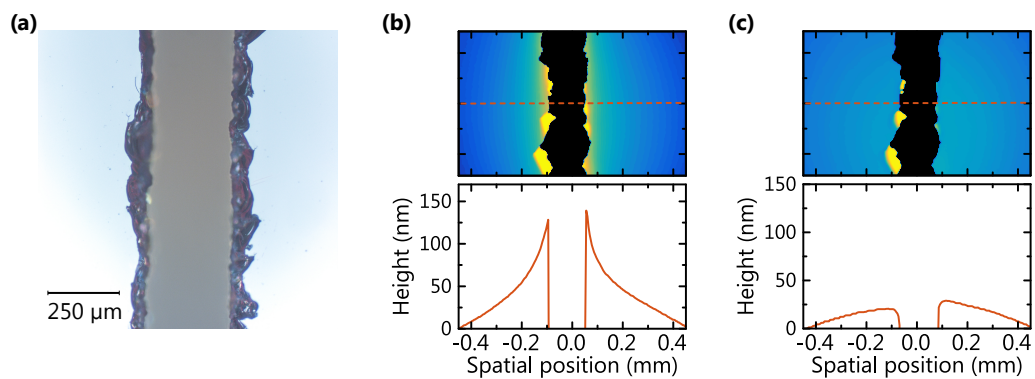


**Figure 4.4:** Slit mirrors laser machined in inverse geometry. (a) Microscope image. Image and lineout obtained via white-light interferometry (b) prior and (c) subsequent to tempering.

to about 60 nm spectral width (at  $-10$  dB), in the case of maximum input power. This largely prevents spectral filtering in the EC. To avoid damage by self-focusing in the fiber, circular polarization is used for spectral broadening, reducing the peak field strength by a factor of  $\sqrt{2}$ . The total acquired GDD in the chirped mirror compressor amounted to about  $-2600$  fs<sup>2</sup>. The close-to-fourier-limited pulse duration was measured to be 56 fs (assuming Gaussian pulse shapes). For the experiments described in Section 4.4 that employ a cavity with a higher finesse, a slightly shorter piece of fiber was used, resulting in pulses of slightly reduced spectral width with a pulse duration of about 71 fs. With compressed pulses, 45 W of output power were available.

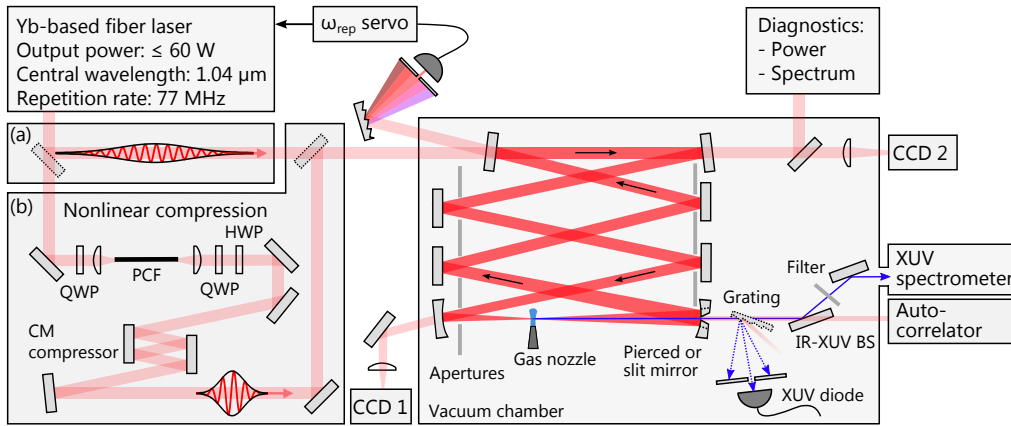


**Figure 4.5:** Experimental setup. The nonlinear compression stage and the grating for dispersing the output coupled XUV radiation are optional. PCF, photonic crystal fiber; HWP, half-wave plate; QWP, quarter-wave plate; BS, beam splitter.

The EC is set up using six plane and two curved mirrors. Three kinds of asymmetric focusing geometries are used, enabling desired focal spot sizes with appropriate beam sizes on the mirror. Table 4.1 summarizes details about the focusing geometry and the openings in the OC mirrors. Only output couplers fabricated by the Fraunhofer ILT are used in the experiments (see Section 4.1.2). The input coupler transmission amounts to 0.5%. The multilayer coating on three of the cavity mirrors with the smallest spot sizes was based on a quarter-wave-stack of SiO<sub>2</sub> and Ta<sub>2</sub>O<sub>5</sub> to ensure higher damage threshold. This, however, considerably limits the spectral bandwidth of the cavity.

**Table 4.1:** Details on mirrors for focusing and for OC.  $d_{in}$ , inner diameter (or width in case of slit) of the opening;  $d_{out}$ , outer diameter (or width in case of slit) of the opening.

Mirror 1 ROC (mm)	Mirror 2 ROC (mm)	Beam radius in focus ( $\mu\text{m}$ )	Beam radius on OC (mm)	Type of OC	$d_{out}$ ( $\mu\text{m}$ )	$d_{in}$ ( $\mu\text{m}$ )
-38	-150	12	2.7	hole	155	55
-100	-300	20	2.5	hole	155	75
-100	-150	19	1.4	slit	280	200

Gas is injected close to the cavity focus through an end-fire glass nozzle with an inner diameter of 100  $\mu\text{m}$ . It can be adjusted in all three dimensions using stepper motors providing a resolution of about 30 nm. Typically it is positioned to be as close to the optical axis as possible, without significantly reducing the intracavity power enhancement. To optimize the OC efficiency, fine tuning of the optical axis with respect to the opening in the OC mirror is possible by adjusting one of the cavity mirrors remotely. In a first-order approximation such a small tilt of a cavity mirror affects only the optical axis (lateral offset and angle) but not the eigenmode [84]. The alignment is facilitated by imaging the cavity beam profile at the OC mirror onto a CCD camera. Another CCD camera is used for monitoring the cavity beam at the mirror prior to the cavity focus allowing for the investigation of the beam profile that generates the harmonics.

Various apertures of appropriate size are placed in the cavity beam path. They efficiently suppress higher-order transverse modes from being populated and prevent stray light from the finite width of the rim of the opening from heating the mirror mounts. This allows for high power cavity operation without thermal drifts of the position of the optical axis.

The output coupled XUV light can be spectrally analyzed in two different ways. The first option is used for measuring the absolute power in a low-order harmonic (here below 27). To this end, the output coupled XUV light is dispersed using a grating with a period of 510 nm of known diffraction efficiency [152] onto a fluorescent screen coated with sodium salicylate. The lateral position of the screen can be adjusted, such that a particular harmonic fits through an opening in the screen onto a photodiode (AXUV100Al3, IRD). The diode is coated with a 100-nm-thick layer of aluminum to attenuate any residual IR light from adulterating the measurement. The responsivity at a wavelength of 50 nm amounts to 0.16 A/W. The photo current is measured by a low-noise transimpedance amplifier with a gain of either  $1 \times 10^8$  V/A or  $1 \times 10^5$  V/A. The power in the other harmonics can be inferred from the absolute power measurement of one harmonic, by taking a photograph of the screen and by accounting for the quantum efficiency of the sodium salicylate.

The second option for XUV analysis is provided by a commercially available grazing incidence spectrometer (248/310G, McPherson). It can be equipped with various curved diffraction gratings (e.g., with 133.6 lines/mm or 600 lines/mm) that disperse and focus the XUV light on the so-called Rowland circle. The harmonics are detected by an uncoated back-illuminated CCD camera (DO-series, Andor; 1024x256 pixel). The spectrometer provides spectral resolution in the tangential direction and spatial resolution in the sagittal direction, enabling the analysis of the beam profile of individual harmonics. Prior to entering the spectrometer, the co-propagating IR beam needs to be sufficiently attenuated. To this end, a fused-silica plate with an anti-reflection coating for the IR radiation is employed for steering the beam to the spectrometer. Further attenuation is reached by introducing thin metallic filters (aluminum or zirconium) into the beam path. When accounting for the quantum efficiency of the CCD, the conversion ratio of the AD-converter, the grating efficiency, the reflectivities of the steering mirrors and the transmission of the metallic filters, the output coupled harmonic power can in principle be estimated from the image acquired by the detector. Furthermore, the relative width of the spectrometer entrance slit to the harmonic beam profile and the re-absorption along the propagation to the spectrometer need to be considered. In practice, the so-obtained power value only represents a lower boundary of the output coupled harmonic power, as any misalignment of the beam in the spectrometer

will significantly reduce the detected photon flux. Furthermore, any contamination of the optics will lower their reflectivity or transmission. Therefore, this procedure is mainly used for relative power calibration of the recorded spectrum.

## 4.3 HHG with the fundamental mode and pierced mirror OC

### 4.3.1 Performance considerations

The purpose of this section is twofold. First, we will discuss the expected performance of a cavity comprising a pierced mirror OC in terms of losses and OC efficiency for the XUV. Second, we will provide some practical advice for adjusting the cavity for optimal operation.

According to the reasoning in Section 2.1.2 the effective losses for the fundamental mode in an EC comprising a small on-axis opening result from the truncation of the field at the opening and from the coupling to higher-order transverse modes. When  $w_F$  denotes the  $1/e^2$ -intensity radius of the beam at the mirror and  $d_{\text{out}}$  the diameter of the non-reflective area, the effective losses amount to  $1 - \exp[-(d_{\text{out}}/w_F)^2]$  (see Eq. (2.8)). In Fig. 4.6(a) the expected losses are plotted in the experimentally relevant parameter range. Even for openings of 150- $\mu\text{m}$  diameter and a spot size of 2 mm, the effective losses are about 0.5% allowing for a maximal power enhancement of 200.

To estimate the OC efficiency achievable in such a configuration, the divergence angle of the harmonic emission can be calculated in the strong-field-approximation (see Section 2.3). In this approximation, the ratio of the harmonic spot size to the fundamental one in the far field amounts to  $\sqrt{p}/q$ , with  $p \approx 6$  and  $q$  being the harmonic order. The transmission of a Gaussian beam of radius  $w_q$  through an opening with a *clear* aperture of diameter  $d_{\text{in}}$  amounts to  $1 - \exp[-(d_{\text{in}}/w_q)^2/2]$ . This is illustrated in Fig. 4.6(b). For the used pierced mirror with a ratio of  $d_{\text{in}}/w_F \approx 0.05$  the expected OC efficiency exceeds 10% for wavelengths below 45 nm and rises above 40% for wavelengths below 20 nm.

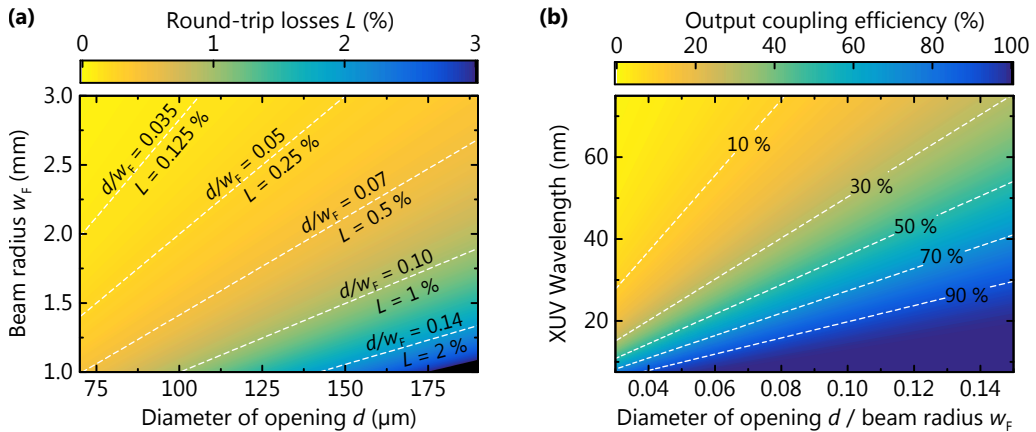


**Figure 4.6:** (a) Effective round-trip losses for an EC with fundamental mode operation comprising a pierced mirror. (b) Calculated OC efficiency.

In the experiment it is essential to adjust the relative position of the opening to the center of the beam. This affects the operation of the cavity as well as the OC efficiency. To precisely

position the optical axis relative to the opening a simple recipe can be followed: first, the cavity is adjusted for optimal performance without the pierced mirror. In a second step, the mirror following the cavity focus is replaced by the pierced mirror. By adjusting only the pierced mirror, optimal cavity performance can be recovered. To this end, a five-axis-platform is helpful. Furthermore, imaging the field distribution at the surface of the pierced mirror (in reflectance) onto a CCD camera is advantageous. Both the magnification and the numerical aperture of the lens (including limiting apertures in the beam path) need to be large enough to resolve the opening. In focus, no diffraction rings should be visible. The relative positioning of the cavity optical axis to the center of the opening is finely tuned by the orientation of the pierced mirror. Finally, if necessary, the input beam can be readjusted to maximize the overlap with the fundamental mode.

### 4.3.2 Cavity performance

In the empty cavity, and with 180-fs pulses, we measured a power enhancement of about 250. A transverse overlap of 85 % to 90 % was typically reached. This is in good agreement with the expected power enhancement of 290 calculated assuming an input coupler transmission of 0.5 % and an outer diameter of the opening of  $155\ \mu\text{m}$  at a beam radius of 2.7 mm. The beam profile in the cavity is as expected, that is, it is of Gaussian shape without noticeable higher-order mode content prior to the focus but exhibits the truncation in the center when imaged at the surface of the OC mirror (see Fig. 4.7).

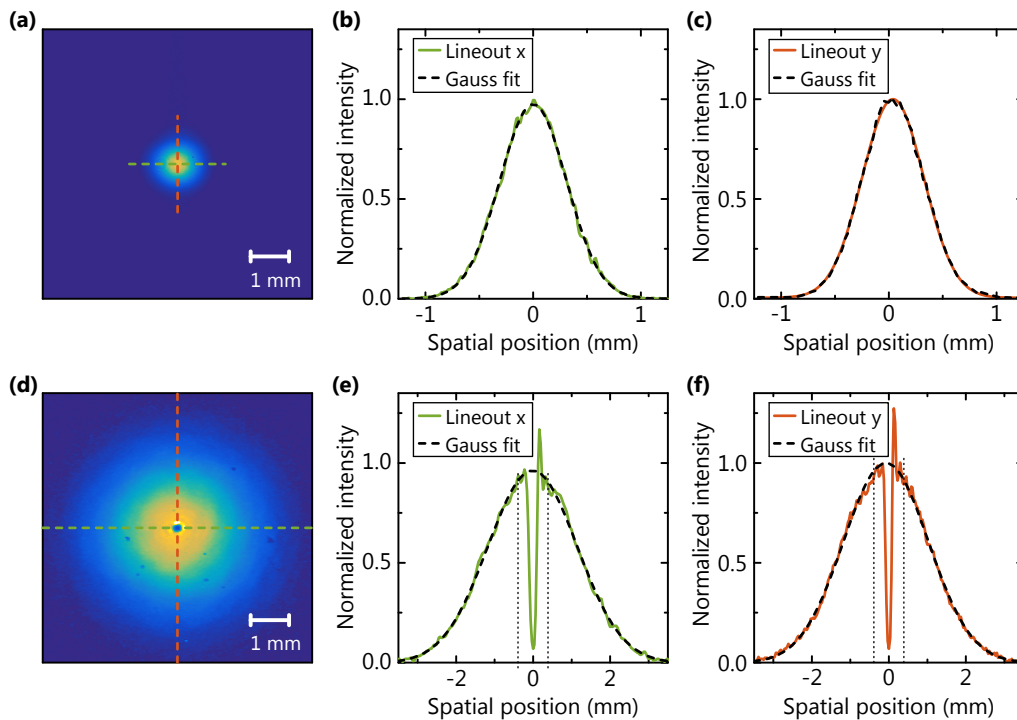


**Figure 4.7:** (a) Beam profile at the first curved mirror with a radius of curvature (ROC) of  $-38$  mm. (b,c) corresponding lineouts. (d) Beam profile at the pierced mirror used for OC (ROC =  $150$  mm) and (e,f) corresponding lineouts with Gaussian fits. The dotted lines indicate the region excluded in the fitting procedure.

With compressed pulses, the power enhancement is typically reduced by about 30% to 40%. To one part this can be attributed to an inferior spatial overlap due to inferior beam quality after the fiber broadening stage. Furthermore, spectral filtering occurs in the outer wings of the spectrum by the EC. The intracavity pulse durations were measured to be 187 fs in the case of uncompressed input pulses<sup>3</sup>, and 62 fs in the case of compressed pulses, which is slightly longer than the input pulse duration. The intensity autocorrelation traces are shown in Fig. 4.8. Stable locking was achieved with both uncompressed and compressed pulses, with a relative root-mean square of the intracavity intensity fluctuations lower than 0.5% in the range between 250 Hz and 1 MHz.

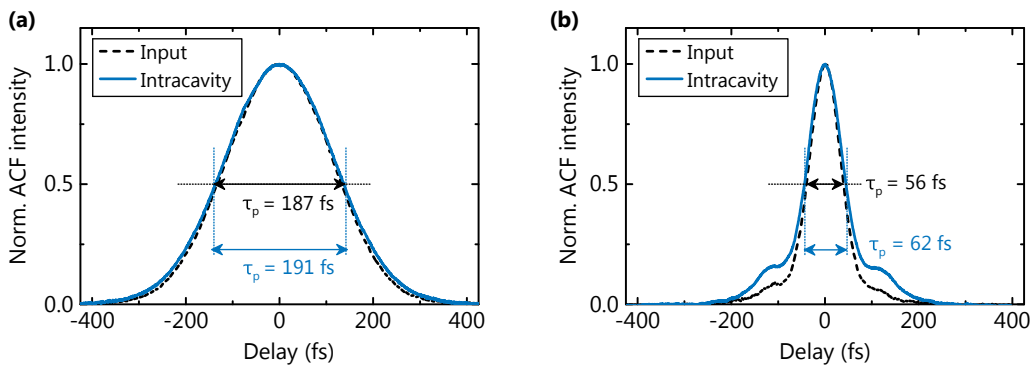


**Figure 4.8:** Recorded intensity autocorrelation of input and intracavity pulses when (a) directly emitted from CPA-system or (b) when nonlinearly broadened and compressed. Deconvolution factor for pulse duration, 1.41.

With uncompressed input pulses and in the tight focusing configuration, the circulating power in the empty cavity is limited to 8 kW by nonlinear effects in the mirrors. The loose focusing geometry allowed for about 30% higher intracavity average powers. In contrast to the experiments described in [57], where these effects occurred at an average power of 18 kW, the asymmetric focusing geometry leads to a much smaller spot size on the curved mirror prior to the focus. With compressed pulses, intracavity average powers of about 4.5 kW were reached, corresponding to similar intensities on the mirrors as in the aforementioned cases.

### 4.3.3 XUV output

The gas target position and backing pressure were chosen empirically to maximize the output coupled power of the high harmonics in the plateau (here 27-31). Typically the optimum was located within a quarter of a Rayleigh length behind the cavity focus (see Fig. 4.9(a)). In the case of argon as nonlinear medium an optimum backing pressure of 2.5 bar was found. Below this optimum pressure, the XUV yield increased quadratically with the nozzle backing pressure and thus with the number of atoms in the focal region. This corroborates a phase-matched generation process. Above the optimum pressure a steady decrease is noticeable. Several effects contribute to this decrease. First, the generation process is not anymore phase matched with the driving field. Second, re-absorption of the harmonics in the medium and

<sup>3</sup>Gaussian pulse shapes are assumed in the deconvolution of the autocorrelation trace.

on the way to the detector increases with the higher gas pressure. Third, the intracavity power (and intensity) decreases with increasing pressure due to the nonlinear phase shift that the driving pulse acquires (see Section 5.4.1). In the course of these experiments, the last effect could only be partially be compensated by increasing the input power.

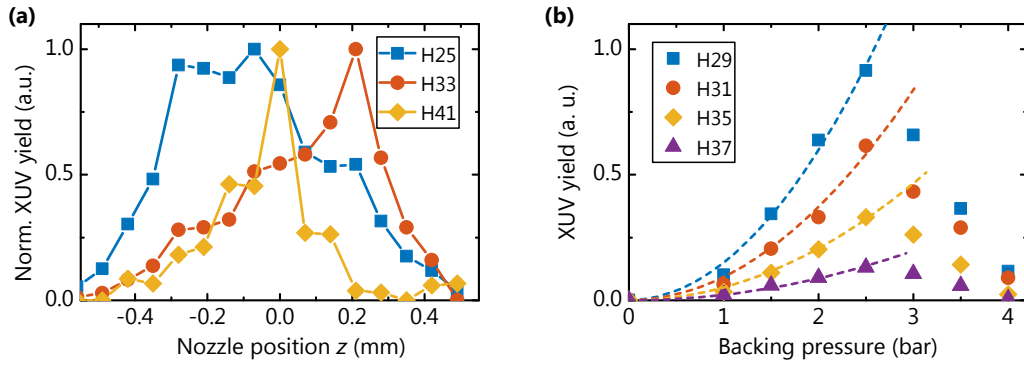


**Figure 4.9:** Empirical optimization of (a) the nozzle position relative to the beam waist and (b) of the argon backing pressure. The dashed lines indicate the initially quadratic increase of the detected XUV yield with the backing pressure.

In Fig. 4.10 the output coupled PSD of the harmonic radiation generated under optimal conditions is depicted. Using the procedure described in Section 4.2, the recorded counts of the AD-converter can be converted into a relative PSD that is output coupled through the pierced mirror. Using the calibrated XUV photodiode placed in the spectrally dispersed XUV beam, absolute calibration of the PSD is realized. We detected micro-watt-level harmonics down to wavelengths below 30 nm. This power level approaches the values demonstrated with the at the time of publishing [66] brightest state-of-the-art low-repetition-rate sources (see [63] and references therein). The use of nonlinearly compressed pulses leads to a significant increase in the XUV average power and in the generated XUV photon energies, as it allows for higher intracavity intensities.

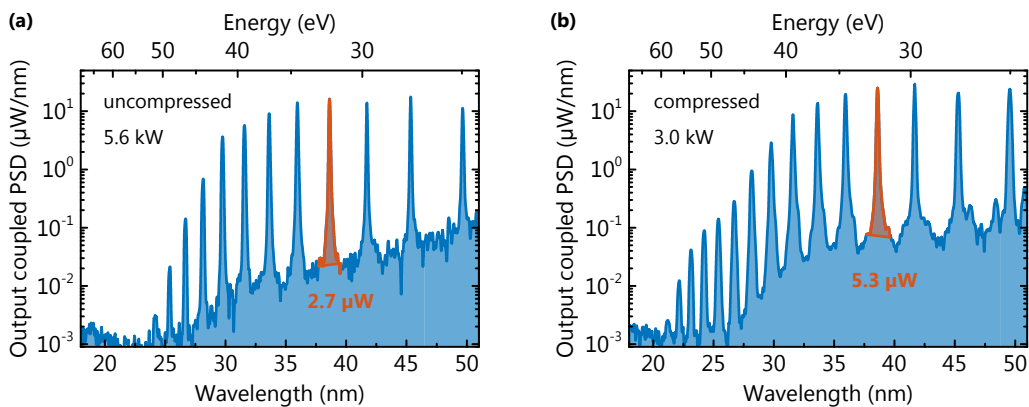


**Figure 4.10:** Output coupled XUV power spectral density (PSD) when using (a) uncompressed pulses directly emitted by the CPA-system and (b) when using nonlinearly broadened and compressed pulses.

To demonstrate the scalability of the concept of pierced mirror OC towards the soft X-ray region, we used tighter focusing and neon as a nonlinear medium because of its high ionization potential. Harmonics up to order 91, corresponding to 11.5 nm or 108 eV, were detected (Fig. 4.11(b)), surpassing the highest previously generated photon energies at similar repetition rates [61, 161–163] by a factor of almost 4. Here, the cutoff energy was most likely limited by the vanishing detection efficiency for higher XUV energies. The measured harmonic power steadily increased with the backing pressure in the gas nozzle; however, this pressure was limited to 1 bar by the capacity of our turbo-molecular vacuum pump. For the neon measurement, the gas target parameters were chosen to optimize phase matching for the cutoff region, resulting in powers too low for a measurement with the XUV photodiode in its sensitive spectral range. The retrieved output coupled power of about 8 pW per harmonic for radiation around 100 eV is therefore a rough estimate obtained from the spectrometer measurement and can be considered as a lower bound for the actual power. For completeness we also show the retrieved output coupled XUV spectrum in the case of xenon as nonlinear medium. Using the tight cavity focus and a relatively low nozzle backing pressure of 0.5 bar intensities of approximately  $6 \times 10^{13} \text{ W/cm}^2$  can be reached extending the harmonic cutoff to about 40 nm.

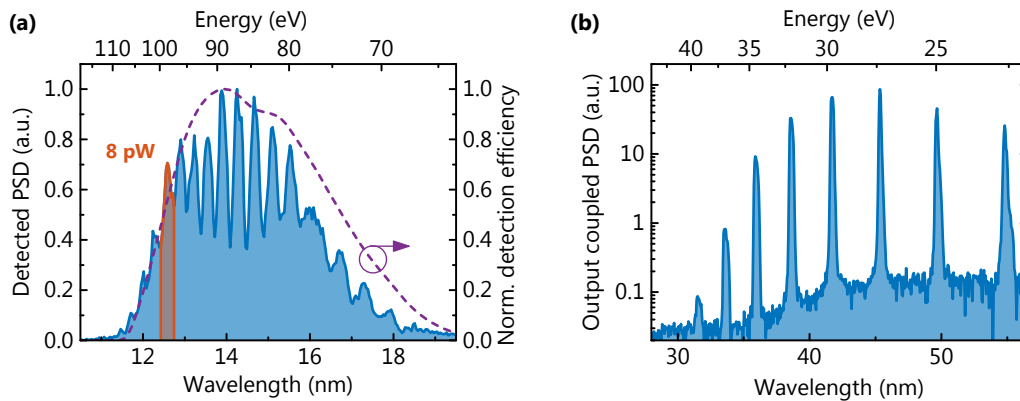


**Figure 4.11:** (a) Output coupled XUV power spectral density (PSD) when using xenon. Low order harmonics are not detected at the chosen spectrometer settings. (b) Detected XUV PSD with neon as nonlinear medium and corresponding detection efficiency. Harmonics up to order 91 are detected most likely limited by the drastically decreasing detection efficiency, in particular due to the IR-XUV beam splitter prior to the spectrometer.

We further analyzed the harmonic radiation by recording the spatial beam profiles using the grazing incidence spectrometer (Fig. 4.12). The pierced mirror output coupler intrinsically represents a spatial filter for the transverse profile of the XUV beam. For the 35th harmonic, the XUV beam inside the cavity is substantially larger than the clear aperture of the hole, leading to an Airy-type diffraction pattern in the far field as expected for the diffraction of a plane wave at a circular aperture [85]. The solid black line indicates the intensity distribution for the diffraction of a wave with homogeneous intensity within the opening and a parabolic curvature of the phase front as expected for a Gaussian beam. The radius of curvature is assumed to be equal to the distance from the cavity focus to the output coupling mirror (75 mm), which is a reasonable assumption for distances much greater that

the Rayleigh length. For higher orders (here 79th), the far-field distribution and its comparison to the model reveal that the phase front curvature plays a non-negligible role in the propagation to the detector.

Assuming a Gaussian intensity distribution for harmonic 79 right before the opening, one can deduce an upper limit of the output coupling efficiency. We find that in this case the calculated and the measured diffraction pattern agree well for beam radii larger than approximately 2.5 times the radius of the opening. This leads to an upper limit of the output coupling efficiency of harmonic 79 that is on the order of 30 %.

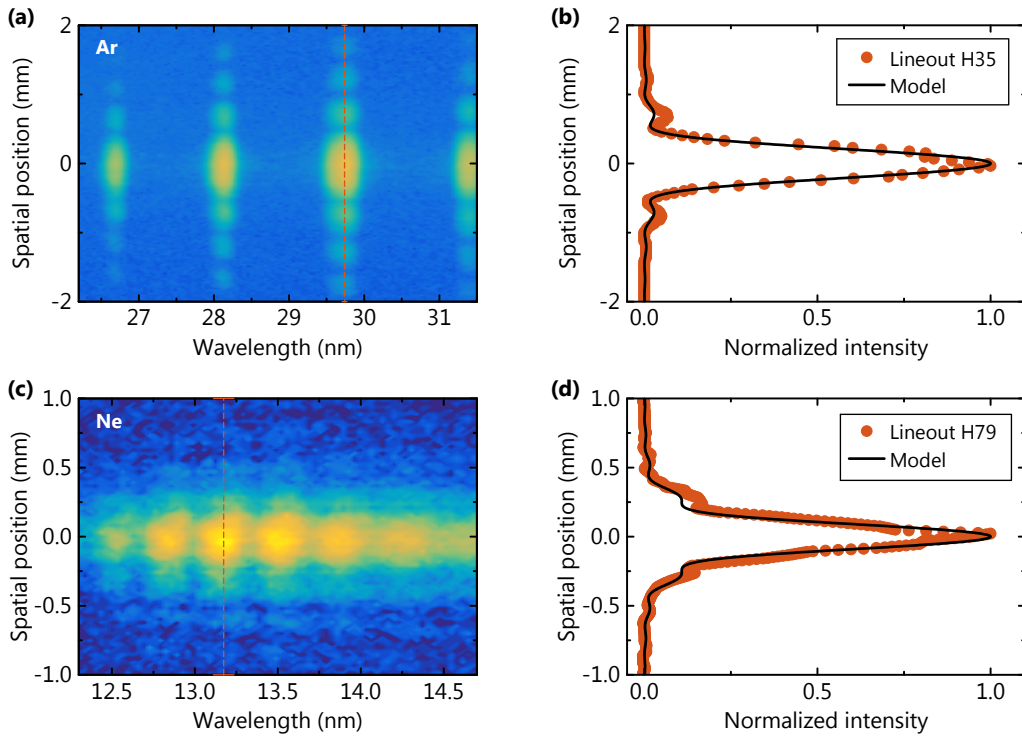


**Figure 4.12:** Recorded XUV beam profiles generated (a) in argon and (c) in neon. A logarithmic color-scale was chosen to visualize the airy-type diffraction pattern. Corresponding lineouts of (b) the 35th and (d) the 79th harmonic along with the results of a model described in the text.

#### 4.3.4 Limitations

In the course of the proof-of-principle type HHG experiments described in the previous section, limitations regarding the scaling of the photon flux and regarding the long-term operation of the source were observed.

It is well known that the efficiency of the HHG process increases with the driving field strength and with the number of emitters, as long as the generation process can be phase matched. In our experiments we observed that the intracavity intensity is limited when the nonlinear medium is present. This effect has been previously reported on [62, 100] and is attributed to the rapid ionization of the gas target on the time scale of the pulse, leading to a temporal phase shift (see qualitative discussion in Section 2.2.2).

While a systematic study of the intracavity ionization is subject of Chapter 5, the experimental setup present at the time of the HHG experiments offered the possibility to acquire first experimental evidence of mitigating this effect by using shorter driving pulses. In Fig. 4.13 we plot the retrieved intracavity peak intensity with respect to the input peak power when using the pulses directly emitted by the CPA system, or, when nonlinearly broadened and compressed. When accounting correctly for the slightly different transverse overlap, both measurements show the same linear dependence without a gas target. When argon is injected at the cavity focus, the intracavity intensity shows a distinct saturation behavior. This clamping intensity is higher with the shorter input and intracavity pulses. This finding is also corroborated by the higher cutoff energy and the higher photon flux observed in the HHG experiments when using shorter driving pulses (see Fig. 4.10).

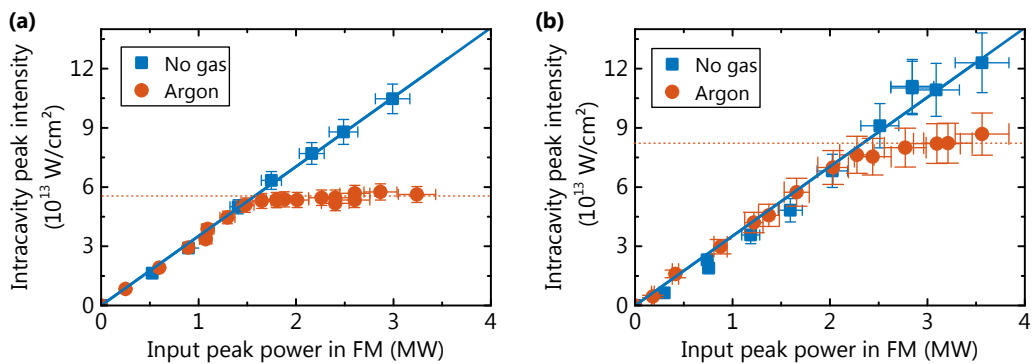


**Figure 4.13:** Clamping of the intracavity peak intensity when (a) using uncompressed pulses and (b) when using nonlinearly broadened and compressed pulses with argon as nonlinear medium.

While from today's point of view this finding seems fairly obvious, it was not at the time of the experiments. First, it was not clear whether or not the much steeper increase in the ionized fraction resulting from the shorter IR pulses will be even more harmful to the build-up process. Second, at the same peak intensity longer driving pulses offer the advantage of more cycles that generate harmonics, however, only if phase matched generation is still guaranteed. Our findings experimentally answered this question and our efforts of enhancing shorter driving pulses to ultimately restrict the emission process of harmonics to a single event per pulse tie in with our goal of increasing the conversion efficiency to the XUV and to extend the XUV cutoff energy.

The second limitation observed is of technical nature and affects the longterm operation of our XUV source. In Fig. 4.14 microscope images of the output coupler before and after long-term use (on the order of a few weeks) in the cavity are presented. Around the opening some wear is visible. Bubble-type modifications of the coating appeared, especially at sharp edges of the original opening. This increases the amount of dead area, that is, area which is non-reflective for the IR and non-transmissive for the XUV. We have, however, no indication that this is a runaway process. The fact that this effect appears only locally suggests that pierced mirrors with better machined openings might not suffer from this degradation.

Another type of degradation is apparent in a larger field of view around the opening of the pierced mirror output coupler. We observed the deposition of a thin layer of material.

We find this modification of the surface to be considerably smaller than the spot size on the mirror and to be strongest at the mirror subsequent to the cavity focus but also—significantly less though—on the two subsequent cavity mirrors. Furthermore, as it is apparent from the microscope image, the deposited material can be partially removed by intensive wiping and scrubbing with acetone-soaked cleaning tissue. Other cleaning procedures in oxygen plasma seem to be much more efficient and to completely reverse the process. Thus, we believe that this degradation originates from the UV and XUV induced cracking of organic molecules resulting in the deposition of mainly carbon on the mirror surface. With the cavity-based HHG systems delivering more and more XUV power, this effect has been observed in all these systems in the meantime [63, 164, 165]. While this has been known for XUV optics (see [166] and references therein), it is much more harmful for the cavity-based systems as it lowers the reflectivity of the cavity optics and thus diminishes the power enhancement.

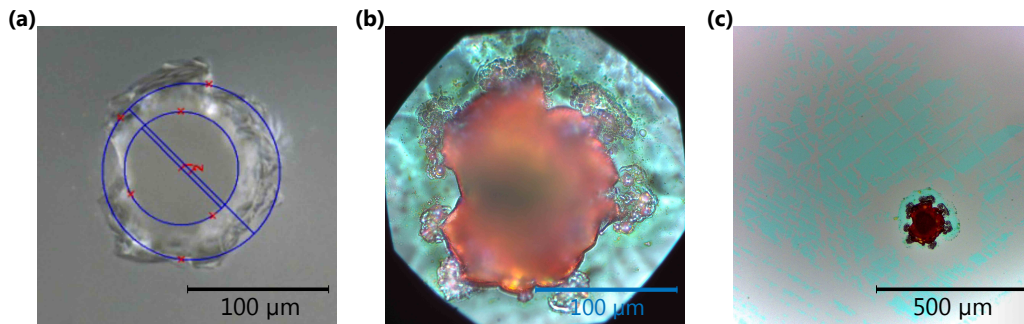


**Figure 4.14:** Microscope images of a pierced mirror (a) before and (b),(c) after longterm employment in the EC. Damages and contaminations are visible.

It is difficult to give a meaningful timescale under which the degradation is observed, because it strongly depends on the amount of harmonic radiation being generated. Furthermore, we find in accordance with a similar but much more severe degradation observed in a cavity seeded by visible light [167], that the degradation can be circumvented by continuously flushing the relevant cavity optics with ozone. Although this solution imposes further technical constraints, it prevents the degradation at our power levels.

#### 4.4 HHG with tailored driving field in a degenerate resonator

Our proof-of-principle type HHG experiments described in the previous sections demonstrated the huge potential of geometrical OC using a pierced mirror in combination with the  $\text{GH}_{00}$  transverse mode. We are convinced that this is the method of choice for OC of high-order harmonics in many cases, especially for pump-probe experiments with the fundamental light and the cutoff harmonics. For lower-order harmonics, however, the presented method suffers from a relatively low OC efficiency (see Fig. 4.6(b)). Furthermore, it is obvious, that the pierced mirror will constitute the bottleneck in a high-power EC with equal spot sizes on all mirrors as discussed in [84] simply due to the high intensity in the vicinity of the opening, where the density of coating defects will most likely be increased. Furthermore, it would be very attractive to conceptually extend geometrical OC in a way that allows for similar—or even superior—OC efficiencies with lower losses for the fundamental mode.

The key to achieving considerable progress in this direction is, to use a transverse field distribution other than the  $\text{GH}_{00}$  mode. Using a tailored transverse field distribution that avoids an on-axis obstacle, offers the prospect of dramatically reducing the round-trip losses. This was previously demonstrated by stable operation of a high finesse ( $\gtrsim 3000$ ) cavity that contained a 100- $\mu\text{m}$  thick wire placed across the optical axis, in the so-called quasi-imaging condition [158].

A more general motivation for the use of non-Gaussian transverse modes is, to exploit additional degrees of freedom in order to influence the harmonic emission in a desired way, for example, for improving the OC efficiency or potentially even for exploiting intracavity lighthouse effects [157, 168]. The question of whether these transverse field distributions are suitable for HHG in terms of phase matching and harmonic beam profile, however, remain open. In the following sections, we address these questions using both numerical simulations and our EC-setup<sup>4</sup>. The main results have been published in [67].

#### 4.4.1 Properties of the tailored driving field and expected XUV output

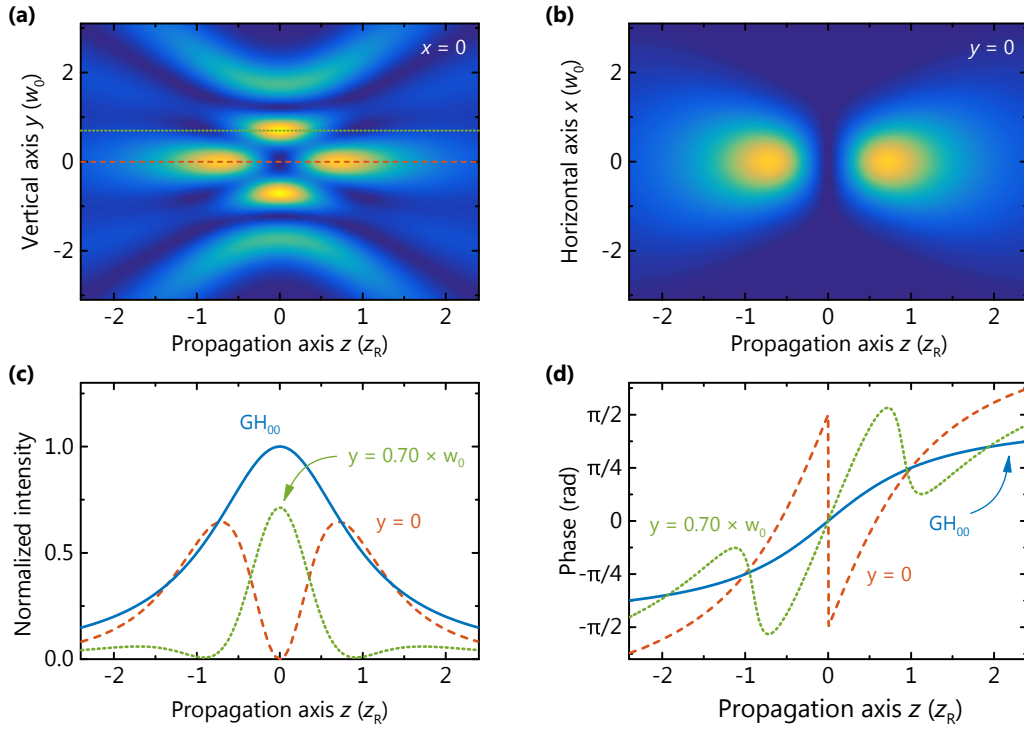
In our experiment, the transverse driving field is tailored by means of the quasi-imaging technique described in detail in [86, 158] (see also Section 2.1.2). In short, a subset of degenerate eigenmodes of the unperturbed resonator can be coupled by introducing an obstacle in the beam path, to construct a field distribution which avoids the obstacle. Here, coupling is achieved by the macroscopic slit through the mirror following the focus, that serves the purpose of XUV OC. The slit is arranged horizontally (along the  $x$  axis) and the distance between the curved mirrors is tuned to achieve degeneracy of the  $\text{GH}_{00}$  and  $\text{GH}_{04}$  modes in the sagittal plane (parallel to the  $y$  axis). The  $z$  axis coincides with the optical axis. The resulting complex field amplitude is described by  $\sqrt{3/11}\text{GH}_{00} - \sqrt{8/11}\text{GH}_{04}$ . This is the mode combination in a quasi-imaging bow-tie resonator with on-axis intensity maxima close to the focus, which has the fewest lobes [86]. We refer to this transverse mode as “simple slit mode” SSM, because no further higher-order degenerate transverse modes are involved.

Figure 4.15 illustrates the simple-slit-mode (SSM) in the focal region. The field distribution is symmetric with respect to the  $x$ - $z$  and the  $y$ - $z$  plane and the maximum intensity in the  $x$ - $y$ -plane at  $z = 0$  (the focus) is 0.71 times that the  $\text{GH}_{00}$  would reach under the same focusing conditions, that is, the same Rayleigh length and with the same average power. Due to the different Gouy phases of the two GH modes contributing to the SSM, its shape changes upon propagation. Approximately one Rayleigh length ( $z_R$ ) from  $z = 0$  the SSM exhibits on-axis intensity lobes. The maximum intensity of these lobes is 0.64 times that the  $\text{GH}_{00}$  mode would reach at  $z = 0$ . As the Gouy phase changes as  $(n + m + 1) \arctan \frac{z}{z_R}$ , the difference in acquired Gouy phase approaches  $2\pi$  for  $z \gg z_R$ , that is, far away from the focus. Thus, the shape of the SSM at the output coupler is similar to that at the focus and exhibits vanishing intensity in a region close to  $y = 0$ .

From the above considerations, it is clear that significant HHG yield can be expected, when the nozzle is either positioned exactly at the focus (generation in the two off-axis lobes) or

---

<sup>4</sup>The numerical simulations were mainly carried out by M. Högnér while the measurements were conducted by a team comprising J. Weitenberg, I. Pupeza and myself.



**Figure 4.15:** SSM in the focal region. (a) and (b) Intensity distribution in the  $y$ - $z$ -plane and the  $x$ - $z$ -plane, respectively. (c) Intensity and (d) phase along the lineouts shown in (a).

when the nozzle is positioned about one Rayleigh length away from the focus (on-axis generation). The second prerequisite for significant HHG yield is that the generation is phase matched with the driving field. From Fig. 4.15(d) one can infer that the on-axis phase evolution of the driving field (red curve) is smooth and only about a factor of two steeper than the phase evolution of  $\text{GH}_{00}$  in the region of maximum on-axis intensity. To quantify the effect of a possibly shorter coherence length of the harmonic emission, the  $x$ - $y$ -integrated signals generated in different interaction volumes (slices) along the  $z$  axis can be compared. To this end, we calculate the harmonic emission by evaluating the single-atom dipole response  $d(\mathbf{r}, t)$  using the standard version of Lewenstein's model with hydrogen-like bound-continuum matrix elements [169] at each position in the interaction region. From the polarization response of the medium  $P(\mathbf{r}, t) = n_{\text{at}} d(\mathbf{r}, t)$ , we calculate the macroscopic harmonic field at the exit plane of the slice taking phase matching and absorption into account<sup>5</sup>.

The results of this procedure are depicted in Fig. 4.16 exemplary for harmonics 15 and 19. Phase mismatch is negligible for the 1- $\mu\text{m}$ -slice, which explains the symmetry of the signal with respect to  $z = 0$  (blue curves). With increasing interaction volume, the harmonic signal increases, until phase mismatch leads to destructive interference of the harmonic radiation generated at different  $z$  positions. This explains the fact that the signal from the 200- $\mu\text{m}$  slice is in general weaker than that from the 100- $\mu\text{m}$  slice<sup>6</sup>. Also, due to the opposite phase front

<sup>5</sup>For further details on the theoretical model see Section 2.3 and for the numerical implementations see [170].

<sup>6</sup>For all simulations in this section a fundamental wavelength of 1.042  $\mu\text{m}$  and a Rayleigh length of 1.045 mm is assumed, corresponding to a Gaussian focal spot size of  $w_0 = 18.6 \mu\text{m}$ .

curvatures before and after the focus, the signals emitted from the two macroscopic volumes are asymmetric with respect to  $z = 0$ . The signal from the 100- $\mu\text{m}$  slice is only  $\sim 1/4$  of the signal from the 1- $\mu\text{m}$  slice scaled up by the squared ratio of the two volumes. This is about half the XUV yield which we calculate assuming a  $\text{GH}_{00}$  transverse field distribution of otherwise identical parameters (in particular, with the same peak intensity as in the on-axis maxima of the SSM).

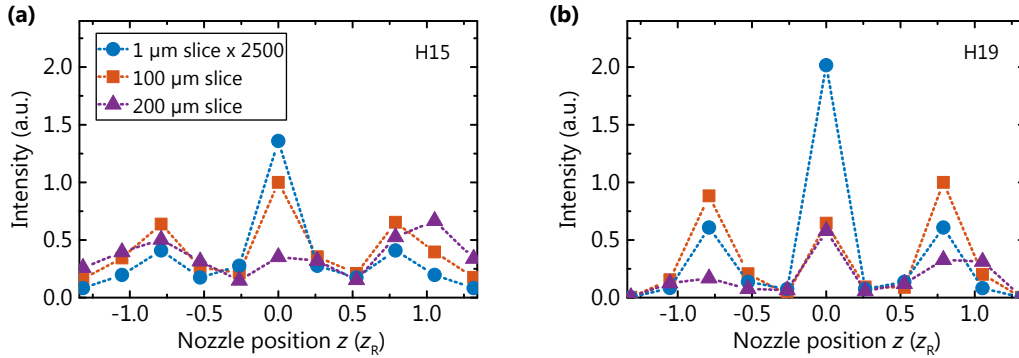


**Figure 4.16:** Total harmonic yield generated in a 1- $\mu\text{m}$ , a 100- $\mu\text{m}$  and a 200- $\mu\text{m}$ -long slice for harmonic 15 in (a) and harmonic 19 in (b), as a function of the nozzle position relative to the focus. Carrier wavelength 1.04  $\mu\text{m}$ , Rayleigh length  $z_R = 1.045$  mm.

A further investigation of the beam quality of the harmonic radiation and the quantification of the OC efficiency require the knowledge of the generated field at the position of the OC mirror. To this end, we decompose the near-field complex amplitudes of the harmonic beam into plane waves and reassembled them after appropriate propagation. Figure 4.17 shows the beam profiles of the harmonics 15 and 19 at the OC mirror, calculated for the three different nozzle positions. As the driving field has fundamentally different shapes at the three considered  $z$ -positions, the profiles of the generated harmonic beams also strongly differ. This is a fundamental difference to HHG with a Gaussian driving beam, illustrating the influence of additional degrees of freedom of spatial tailoring on the harmonic emission. Nearly-collimated beams are generated when positioning the nozzle close to either one of the two on-axis maxima. A fringe-patterned far-field intensity distribution results from HHG in the two lobes at nozzle position  $z = 0$ . Most notably, the symmetry of the SSM implies the on-axis constructive interference of radiation contributions from the two main lobes.

In Fig. 4.18(a) the calculated OC efficiency is plotted for several harmonics, assuming the generation in a 100- $\mu\text{m}$  thin slice centered at  $z \approx 0.8z_R$ . At parameters similar to the ones in the experiment, that is, a slit width (clear aperture) of  $d_{\text{in}} \approx 200 \mu\text{m}$  and a fundamental beam radius of 1.4 mm, the expected OC efficiency exceeds 50 % already for wavelengths as long as 55 nm (see dotted line in Fig. 4.18).

Finally, we estimate the effective losses that the SSM experiences upon a single round-trip through a cavity comprising a slit mirror. This can be done using a coherent mode coupling model (see Section 2.1.2 or Section 6 in [86] for details). Determination of the exact losses would require the calculation of the transverse mode that experiences the lowest losses and that can still be resonantly enhanced in cavity. Although for large ratios of slit widths to mode diameters the retrieved field distributions only slightly differ from the SSM, the round-trip

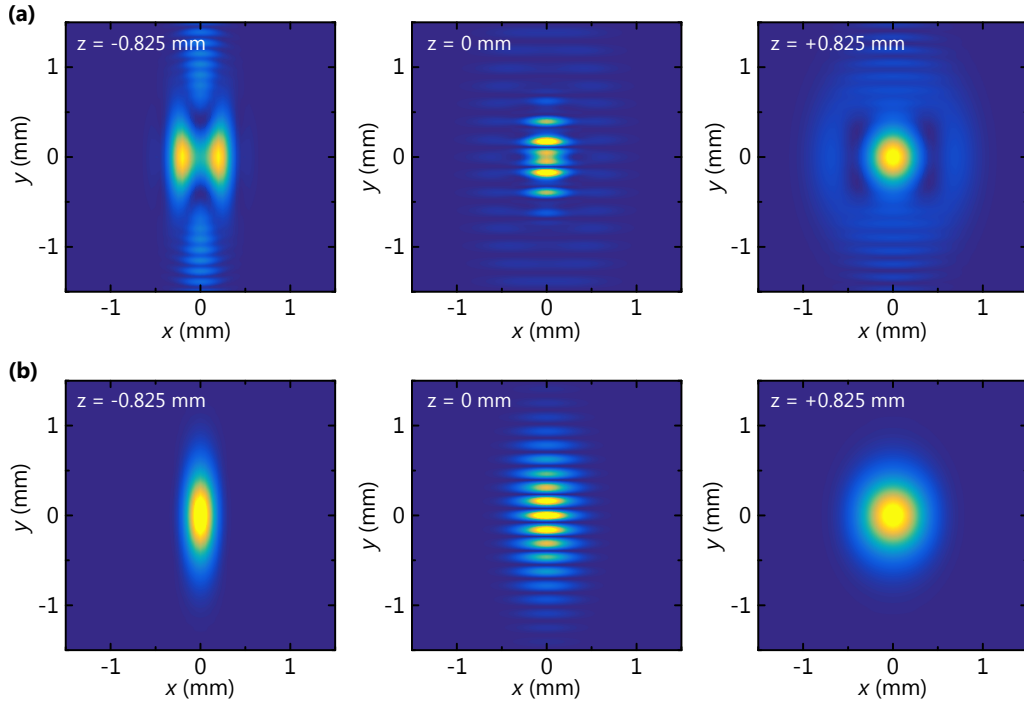


**Figure 4.17:** Calculated beam profiles at the position of the OC mirror for **(a)** harmonic 15 and **(b)** harmonic 19, assuming three different nozzle positions relative to the focus. Pulse parameters corresponding to a peak intensity of  $4.5 \times 10^{13} \text{ W/cm}^2$  for the  $\text{GH}_{00}$  mode were assumed.

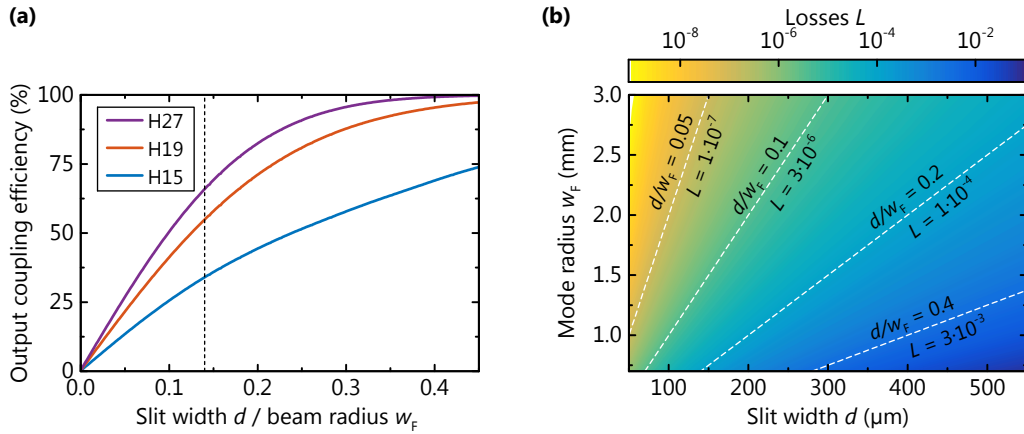


**Figure 4.18:** **(a)** OC efficiency through the slit, when generating the harmonics with the SSM and positioning the nozzle at  $z \approx 0.8z_R$  behind the focus and assuming a target length of  $100 \mu\text{m}$ . For the cut-off harmonics, the results are largely independent of other parameters, such as the peak intensity (here, corresponding to  $4.5 \times 10^{13} \text{ W/cm}^2$  for the  $\text{GH}_{00}$  mode). **(b)** Effective round-trip losses for an EC comprising a mirror with a slit when excited by the SSM.

losses can be considerably smaller than for the SSM. For very small ratios of slit width to beam size, other coupling mechanisms, for example, due to spherical aberrations induced by the focusing mirrors, completely dominate the transfer of energy to other modes.

Therefore, we rely on a much simpler loss model, that has proven to provide reliable results in the experimentally relevant parameter range (see Fig. 10 in [86]). It assumes that the cavity is excited by the SSM (e.g., by suppression of modes of higher order) and only calculates the amount of light transmitted through the slit. In Fig. 4.18(b) the expected effective losses are plotted for a range of slit widths and a range of mode radii. Due to the vanishing on-axis intensity of the driving mode, much larger apertures can be tolerated compared to the situation described in Section 4.3.1. When employing a slit mirror with an outer diameter of the opening of about  $280\ \mu\text{m}$ , as done in the experiments, the induced round-trip losses for the SSM are smaller than 100 ppm.

### 4.4.2 Cavity performance

Considering the aforementioned losses due to the slit, the reflectivities of the cavity mirrors and an input coupler reflectivity of 99.5 %, a power enhancement of  $\sim 600$  is expected. In the experiment, the incoming laser beam is transversally matched to the  $\text{GH}_{00}$  cavity mode, leading to a theoretical maximum spatial overlap of  $3/11 \approx 27\%$ . Using cylindrical optics, this value can readily be improved to 44 % [86]. In practice, the overlap is somewhat smaller. Moreover, spectral filtering by the cavity is observed. It is stronger than for the experiments performed with the fundamental mode in Section 4.3 due to the higher cavity finesse. Therefore, an intracavity pulse duration of 100 fs was measured. This pulse duration was a trade-off between the compression fiber length of 20 mm (a shorter fiber is unpractical), the bandwidth supported by the cavity mirrors and the available input power (here 45 W). The measured effective power enhancement was 50, which is in good agreement with the theoretically expected value, taking into account the spatial and spectral overlap. At the full laser input power, an average power of 2.2 kW was reached in the cavity. This corresponds to a peak intensity of  $4.5 \times 10^{13}\ \text{W}/\text{cm}^2$  (calculated for the  $\text{GH}_{00}$  mode on axis at  $z = 0$ ), multiplied by the  $z$ -dependent relative intensity of the SSM (e.g., by 0.64 in the on-axis lobe after the focus, see Fig. 4.15(c)). This power regime was just below the intensity clamping limit observed in the previous HHG experiments due to ionization of the gas target. In Fig. 4.19 the imaged cavity mode (at the slit mirror) and a photograph of the focal region is shown.

### 4.4.3 XUV Output

To verify the numerical simulations, we injected Xe through the nozzle at different  $z$ -positions in the vicinity of the cavity focus and recorded the far-field intensity distributions of the output coupled and spatially dispersed harmonics (see Fig. 4.5 for the schematic setup). The backing pressure (3 bar) and the nozzle diameter ( $100\ \mu\text{m}$ ) were empirically optimized to maximize the harmonic yield. The estimated cross-sectional particle density using the tools described in Appendix E is in good agreement with the optimum parameters predicted by the simulations.

Figure 4.20(a) shows a linecut through the intensity distribution of the output-coupled

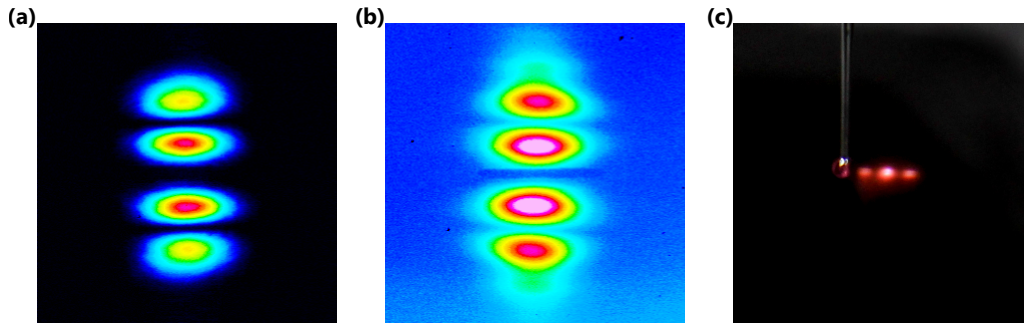


**Figure 4.19:** (a), (b) Cavity beam profile imaged at the position of the output coupler using two different exposure values. In the case of overexposure the horizontal slit is clearly visible. (c) Photograph of the focal region, when filling the chamber with 3 mbar of xenon in an intermediate power regime illustrating the three distinct regions of high intensity and the end-fire nozzle.

harmonics 15-19 spatially dispersed by a grating on the fluorescent screen along the  $x$  axis at  $y = 0$ , together with the simulation results obtained by accounting for the setup geometry. In this plot, the intensity level of each individual simulated harmonic is fitted to the corresponding peak of the measured harmonic, while the shapes of the curves are the result of the simulation. The relative intensity levels for this fit correspond to the product of the grating efficiency with the screen quantum efficiency within  $\sim 10\%$  accuracy, indicating a good agreement of the simulations with the measurement. The harmonics 17 and 19 are close to the cutoff region of the generated XUV spectrum and exhibit a single-lobe structure for all  $z$ -positions of the nozzle. For these harmonics, the full-width at half-maximum (FWHM) of the measured far-field intensity distributions is compared with the simulation results, while scanning the nozzle along the  $z$  axis (Fig. 4.20), and an excellent agreement is found. With a calibrated XUV photodiode we measured the power of the 17<sup>th</sup> harmonic, and from the screen photographs we calculated the output coupled power for other harmonics by considering the grating efficiency and the screen quantum efficiency. For harmonic 13-19 we find the output coupled power in a single harmonic to be on the order of  $10 \mu\text{W}$ . These power levels are comparable to the record values (at the time of the measurements) achieved with systems employing the fundamental mode [61, 163].

## 4.5 Conclusions

In conclusion, we have overcome previous limitations of cavity-enhanced HHG by introducing three major improvements. First, we enhanced nonlinearly compressed pulses generated by an Yb-based laser. This provides a unique combination of short pulse durations and high average powers, mitigating ionization-related effects and, thus, allowing for a scaling of the generated photon energies. Second, we coupled out the generated radiation using geometric techniques, experimentally applying these methods for high harmonics for the first time. Our experiments with the fundamental mode and the pierced mirror demonstrate the potential of this technique towards the generation of soft x-rays at repetition rates of several tens of MHz and identify a straightforward strategy for scaling cavity-enhanced HHG towards both

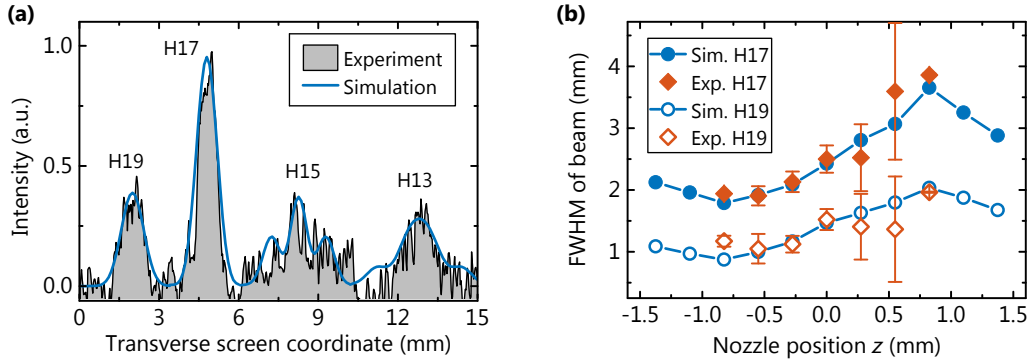


**Figure 4.20:** Measured and simulated harmonic far-field intensity distribution. **(a)** Linecut through the beam profile on the screen (after the diffraction grating) along the  $x$  axis at  $y = 0$  for the nozzle position  $z = -0.55$  mm. **(b)** FWHM of the beam profiles (in  $x$ -direction) of harmonic 17 and 19 at the screen for the entire range of investigated nozzle positions. Data for harmonic 17 was offset by 1 mm for clarity. The error bars indicate the standard deviation for several measurements and the larger error bars are caused by poor signal-to-noise ratio at  $z$ -positions with low driving intensity.

higher XUV photon energies and photon flux. Third, we generated high-order harmonics in a kW-level EC with a spatially tailored field distribution for the first time. We found that the conversion efficiency is comparable to that achieved with the fundamental  $\text{GH}_{00}$  mode for parameters relevant to cavity-enhanced HHG. The large region of low intensity around the on-axis opening in the OC mirror creates unparalleled power scaling premises. Furthermore, the OC efficiency can be significantly improved compared to any alternative technique demonstrated so far. Most notably, the efficiency of geometric OC can be improved by an order of magnitude for lower-order harmonics compared to using the fundamental cavity mode with an on-axis hole.

The unparalleled versatility of geometric OC and the fact that it is suitable for broadband driving pulses of arbitrary polarization state, promises the applicability of gating techniques for confining HHG to a single cycle of the intracavity field. This can be envisaged by either shaping the polarization of the driving field [171, 172], or by controlling the direction of harmonics emitted from individual half-cycles of the fundamental pulse by spatially tailoring the driving field [157, 168].

To reveal the full potential of our source, workpackages in four different directions need to be addressed. First, higher input powers delivered by state-of-the-art lasers need to be coupled to ECs with thermally robust designs enabling larger spot sizes on the mirrors. Second, the bandwidth of the EC needs to be further enlarged to allow even shorter driving pulses. Third, the laser machined openings in the output couplers need to be improved. And last, the ionization-induced intensity limitations needs to be thoroughly understood and further strategies for its mitigation need to be found.

## 5 Quantitative description of enhancement cavities in the nonlinear regime

A driving motivation for the development of femtosecond-ECs has been the prospect of a high photon-flux XUV source based on HHG. Starting with the pioneering work by Gohle *et al.* and Jones *et al.* [28, 29], it has been argued that the low single-pass conversion efficiency of HHG and the high power enhancement factor of the cavity are a perfect technological match. Although it had been foreseen that intensity dependent effects in the cavity mirrors and the transmissive output coupler could limit the coherent build-up [28, 29, 65, 173], the standard reasoning neglected the process of “pure” ionization of the gas target. This parasitic effect can not be avoided, is orders of magnitude more likely than HHG, and the rapidly increasing electron density is detrimental for the phase of the pulse (see Section 2.2.2). In the cavity this leads to intensity limitations as observed in the experiments presented in Section 4.3 and to a dramatically changed dynamic response of the cavity. A first understanding of these effects and the underlying physics was given in [88, 100]. These models, however, rely on free scaling parameters validated in only a narrow parameter range. To explore the full potential of cavity-enhanced frequency conversion processes in a gas target, a quantitative understanding of the nonlinear cavity response is required. Furthermore, optimizing the cavity design with respect to the nonlinear conversion remains an open challenge.

In this chapter, these research gaps are addressed. By using the phase sensitivity of a high-finesse EC—the very effect responsible for the intensity clamping—we precisely study the nonlinear interaction of a laser pulse with a gas target. A complete pulse characterization allows for the formulation of a quantitative, ab-initio nonlinear propagation model, experimentally validated in a wide range of the critical parameters.

The chapter is structured as follows: in Section 5.1 the theoretical modeling of the nonlinear cavity build-up is presented and its range of validity is discussed. Section 5.2 focuses on the details of the experimental setup and on the phase retrieval algorithm. In Section 5.3 the model is validated by comparing the experimental results to the calculations. Section 5.4 discusses several implications and predictions of the model: First, we deduce an empirical scaling law quantitatively describing the intensity-clamping behavior in ECs employing mirrors according to the *standard approach* used in all setups reported so far. Second, we discuss effects when changing the driving wavelength and the repetition rate of the laser system. Third, we address the question whether nonlinear ECs can be operated beyond the intensity limitations exhibited by the standard approach. The model predicts that the ionization-induced spectral broadening could be used to dramatically compress the intracavity pulse in time, while maintaining a high power enhancement factor, revealing a viable route towards significantly surpassing the intensity limitations of state-of-the-art nonlinear ECs. The main findings presented in this chapter have been published in [68].

## 5.1 Modeling the cavity response

We aim for deriving a model for the response of a passive EC containing a gas target, valid in the typical parameter range for cavity-assisted HHG. In particular, a driving wavelength of about  $1\ \mu\text{m}$  is considered and the peak intensities at the gas target are assumed to be low enough such that the critical electron density (Eq. (2.31)) is not surpassed within a single pass through the target. In Section 5.1.1, a 1D pulse propagation model is derived. To validate the 1D approximation, the model is compared to simulations in 3+1 dimension (space and time) in Section 5.1.2. As the pulse repetition rate used with ECs is typically in the range of 100 MHz, the time interval between two successive pulses is shorter than the time needed for replenishing the focal volume with new atoms (assuming end-fire nozzles and typical focus sizes). Therefore, Section 5.1.3 is dedicated to the plasma dynamics relevant for the cavity build-up.

### 5.1.1 Nonlinear pulse propagation in cavities

In the following two subsections we will introduce the propagation model. In two further subsections, we address the necessary adaption of the ionization rate and investigate the validity of the envelope description.

#### Single pass through the gas target

Our model describing the pulse propagation through the ionized medium in the cavity focus is based on the first-order propagation equation derived by Geissler *et al.* (see Eq. (2.12)). In the experiments, the transverse beam profile is typically of Gaussian shape. For computational simplicity, we will assume a homogeneous transverse beam profile with similar on-axis peak intensity. This reduces the model to one spatial dimension. For normalization purposes of the pulse energy, the beam profile formally extends over an area of  $\pi w_0^2/2$ . Furthermore, we use the approximation of a complex envelope description for the nonlinear polarization response as given in [88]. Thus, at the position  $z = z_0$ , the time evolution of the (complex) pulse envelope is given in a co-moving reference frame by  $\mathcal{A}(z_0, \tau)$  with  $\tau = t - c/z_0$ . The nonlinear laser-gas interaction is governed by a differential equation for the complex pulse envelope  $\mathcal{A}(z, \tau)$  that reads in the co-moving reference frame<sup>1</sup>:

$$\begin{aligned} \frac{d\mathcal{A}(z, \tau)}{dz} &= \mathcal{A}(z, \tau) \left[ -\frac{I_p n_{\text{gas}}}{2\epsilon_0 c} (1 - \eta(z, \tau)) \Gamma_{\text{peak}}(\tau) \frac{1}{|\mathcal{A}(z, \tau)|^2} + i r_e \lambda_c n_{\text{gas}} \eta(z, \tau) \right]; \quad (5.1) \\ &:= \mathcal{A}(z, \tau) \Delta(z, \tau). \end{aligned}$$

Here,  $I_p$  is the ionization potential,  $n_{\text{gas}}$  the gas number density,  $\eta$  the ionized fraction,  $r_e$  the classical electron radius,  $\lambda_c$  carrier wavelength,  $c$  the speed of light and  $\epsilon_0$  the vacuum permittivity. With  $\Gamma_{\text{peak}}(\tau)$  we denote the value of the maximum of the non-cycle averaged ionization rate, given the current value of the pulse envelope  $\mathcal{A}(\tau)$ . The first term on the right-hand side of Eq. (5.1) accounts for the energy loss upon ionization (absorption) and the second term describes a temporal phase shift due to the rapidly changing electron density

---

<sup>1</sup>See Appendix A for details on the sign convention of the Fourier transform.

$n_e(t) = n_{\text{gas}}\eta(t)$ . We take into account the depletion of the gas target upon ionization by calculating the electron density according to:

$$\begin{aligned}\frac{dn_e(t)}{dt} &= \Gamma(n_{\text{gas}} - n_e(t)); \\ n_e(t) &= (n_{\text{gas}} - n_{e,\text{ini}}) \exp\left(-\int_{-\infty}^{\infty} \Gamma(I(t))dt\right).\end{aligned}$$

We solve the differential equation Eq. (5.1) by recursively applying the Euler method:

$$\begin{aligned}\mathcal{A}(z_0 + \Delta z, \tau) &\approx \mathcal{A}(z_0, \tau)[1 + \Delta(z_0, \tau)\Delta z]; \\ \Rightarrow \mathcal{A}(z_0 + L, \tau) &\approx \mathcal{A}(z_0, \tau) \lim_{N \rightarrow \infty} \prod_{n=1}^N \left[1 + \Delta\left(z_0 + n\frac{L}{N}, \tau\right)\frac{L}{N}\right].\end{aligned}$$

Assuming that the changes to the pulse are small enough that the nonlinear polarization response does not change on the length  $L$  of the gas target, the pulse envelope at the end of the gas target reads:

$$\mathcal{A}(z_0 + L, \tau) \approx \mathcal{A}(z_0, \tau) \lim_{N \rightarrow \infty} \left(1 + \frac{L\Delta(z_0, \tau)}{N}\right)^N = \mathcal{A}(z_0, \tau)e^{L\Delta(z_0, \tau)}. \quad (5.2)$$

When operating a high finesse EC ( $\mathcal{F} \gtrsim 100$ ), equipped with a gas target much shorter than the Rayleigh length, this approximation seems reasonable as the high cavity finesse requires the pulse to remain essentially identical even after a many round-trips. The approach taken in Eq. (5.2) reduces the nonlinear pulse propagation model to a single dimension (time), and the propagation through the gas target is done in a single step. The approximation leads to a slight overestimation of the losses and the phase shift in the trailing part of the pulse, as the pulse actually loses energy upon propagation through the medium.

### Cavity build-up

The build-up process of the intracavity pulse is described in the frequency-domain. At the input coupler (reflectivity  $R_{\text{ic}}$ ), the input field (“in”) and the field exciting the plasma (“post”) must add up to the field, that will enter the plasma (“prior”):

$$\tilde{\mathcal{A}}_{\text{cav,prior}}(\omega) = \sqrt{1 - R_{\text{ic}}(\omega)}\tilde{\mathcal{A}}_{\text{in}}(\omega) + \sqrt{R_{\text{ic}}(\omega)R_{\text{cav}}(\omega)}e^{i\phi(\omega)}\tilde{\mathcal{A}}_{\text{cav,post}}(\omega). \quad (5.3)$$

Here,  $R_{\text{cav}}$  is the product of the reflectivities of all other cavity mirrors and  $\tilde{\mathcal{A}}$  denotes the Fourier components of the field envelope. To simulate a full cavity build-up, a split-step Fourier algorithm is used to solve the coupled equations (5.2) and (5.3).

The spectral phase  $\phi(\omega)$  is acquired upon one cavity round-trip. It also includes the contribution from a potential steady-state plasma, that is, from electrons in the focal region, that neither leave the focal region by replenishment, nor recombine with ions within one cavity round-trip time. For a free-electron gas of number density  $n_e$  the spectral phase is calculated according to the Drude model (see Eq. (2.15)):

$$\phi_e = \frac{\omega}{c} (n(\omega) - 1)L \approx \frac{\omega_p^2}{2c\omega}L = \frac{2\pi}{\omega}r_e c L n_e. \quad (5.4)$$

As long as the dispersive effects of the plasma are small ( $|\text{GDD}| < 0.04 \text{ fs}^2$  for  $L = 200 \mu\text{m}$ , at  $n_e = 1 \times 10^{17} / \text{cm}^3$ ), one pass through the gas target can be modeled in a single split-step propagation: first, the effects in the time domain are calculated according to Eq. (5.2), then dispersive effects are accounted for in the Fourier domain via Eq. (5.4), assuming an average electronic density of the values right before and after the pulse.

### Effective ionization rates

The approximation of the transverse intensity distribution by a homogeneous beam profile with similar peak intensity requires an adaption of the ionization rate. Since the density of freed electrons determines the phase shift and the losses of the pulse (Eq. (5.1)), it is essential to mimic this quantity in the 1D model. In other words, we need to find a meaningful spatial average of the generated electron density. Here, we set two boundary conditions. First, the overall number of generated electrons per cycle and for a given intensity should be the same in both models. Second, we require consistency with previous approximations: the homogeneous beam profile formally extends up to a radius of  $w_0/\sqrt{2}$ . Thus, for a peak intensity  $I_0$  we can define an effective ionization rate<sup>2</sup> by requiring:

$$\begin{aligned} \Gamma_{\text{eff}}(I_0) \cdot \frac{2\pi}{\omega_c} \cdot n_{\text{gas}} \cdot L \cdot \frac{\pi w_0^2}{2} &\stackrel{!}{=} \int_{-\infty}^{\infty} dx \int_{-\infty}^{\infty} dy \Gamma(I(x,y)) \cdot \frac{2\pi}{\omega_c} \cdot n_{\text{gas}} \cdot L ; \\ \Rightarrow \Gamma_{\text{eff}}(I_0) &:= \frac{\int_{-\infty}^{\infty} \int_{-\infty}^{\infty} \Gamma(I(x,y)) dx dy}{\pi w_0^2 / 2} \quad \text{with} \quad I(x,y) = I_0 e^{-2(x^2+y^2)/w_0^2}. \end{aligned} \quad (5.5)$$

In contrast to earlier works [88, 100], we find the PPT model [93] for the cycle-averaged ionization rates to be better suited for the intensity range under investigation, that is, for Keldysh parameters around or greater than 1 (see also Section 2.2.2). Whenever sub-cycle dynamics need to be considered, for example, for the peak-rates in Eq. (5.1), we use the extension of the PPT model as given in [95].

### Range of validity of the envelope approximation

As pointed out in Section 2.2.2, the envelope approximation of the nonlinear polarization (i.e., the right-hand side of Eq. (5.1)) renders the neglect of a third term in the nonlinear polarization necessary. This approach was originally intended for pulses consisting of many cycles ( $\frac{\omega_c}{2\pi} \tau_p \gg 1$ ;  $\omega_c$ , carrier frequency;  $\tau_p$ , pulse duration) in a regime of moderate intensity, that is, at low ionization levels. To justify the use of Eq. (5.1) in a broader parameter range, we solve this propagation equation and its original counterpart (Eqs. (2.12) to (2.13)) using a fourth-order Runge-Kutta solver with initial parameters that greatly exceed currently reachable values in enhancement cavities. In particular, we use a 10-fs pulse (comprising only a few cycles) with a peak intensity of  $8 \times 10^{13} \text{ W/cm}^2$ , propagated through a xenon gas

---

<sup>2</sup>Interestingly, the retrieved effective ionization rate can be approximated by a scaled ionization rate, that is,  $\Gamma_{\text{eff}}(I_0) \approx \beta \Gamma(\alpha I_0)$ . In the case of xenon and for the PPT model, we find  $\alpha = 0.93$  and  $\beta = 0.39$ . Although we do not use this formula, it provides some physical insight, namely, that the ionization can be approximated using a slightly lower peak intensity and a radius of the interaction zone of  $w_0 \sqrt{\beta}$ .

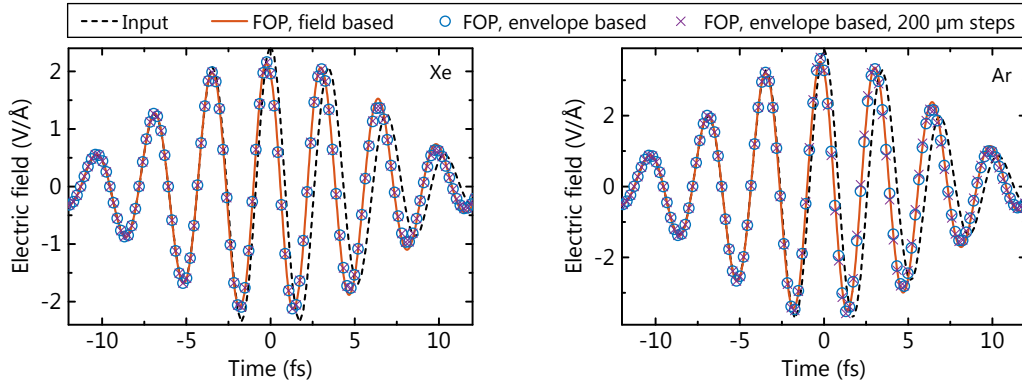


**Figure 5.1:** Nonlinear pulse propagation of a 10-fs pulse via the 1D first-order propagation equations (FOP) as given in Eq. (2.12) (field based) and in Eq. (5.1) (envelope based). We also show the solution of the latter, when solved in step sizes of  $200\ \mu\text{m}$  via Eq. (5.2). Total propagation distance: 1 cm. Particle density:  $4 \times 10^{18}/\text{cm}^3$ . Left panel: xenon gas target, input peak intensity:  $8 \times 10^{13}\ \text{W}/\text{cm}^2$ . Right panel: argon gas target, input peak intensity:  $2 \times 10^{14}\ \text{W}/\text{cm}^2$ . For neon (not shown) we obtain similar results at a peak intensity of  $5.5 \times 10^{14}\ \text{W}/\text{cm}^2$ .

target of a particle density of  $4 \times 10^{18}/\text{cm}^3$ . The propagation length is 1 cm which corresponds to 50 passes through a  $200\text{-}\mu\text{m}$  long gas target. In the case of argon and neon the peak intensity is set to  $2 \times 10^{14}\ \text{W}/\text{cm}^2$  and  $5.5 \times 10^{14}\ \text{W}/\text{cm}^2$ , respectively. Furthermore, Eq. (5.1) is solved using the scheme of Eq. (5.2), that is, in step sizes of the actual gas target length ( $200\ \mu\text{m}$ ). To get the full oscillatory fields in the envelope-based models, we interpolate the obtained complex envelope on a finer time grid and multiply it by the phase from the carrier ( $e^{i\omega_c t}$ ). The results of the three approaches are shown in Fig. 5.1. The overall agreement is excellent. In the trailing part of the pulse, a small deviation of the envelope-based models can be seen, where the envelope approximation overestimates the losses.

### 5.1.2 Comparison to simulations in 4D

Due to the strongly nonlinear dependence of the ionization rate on the intensity, the induced phase shifts and losses show a pronounced spatial dependence in the transverse coordinates after a single pass through the gas target. The 1D model employed neglects this spatial dependence and, therefore, the coupling of energy to higher-order transverse modes. When the cavity is operated such that only the fundamental mode is resonant, transverse effects of the plasma result in additional losses and the cavity beam profile remains spatially homogeneous. In the experiment this can be verified by imaging the cavity mode on a CCD (check for Gaussian intensity distribution) and by the imaging 2D spectrometer (check for homogeneous spectrum in one spatial dimension). From a theoretical point of view, the situation can be treated analogously to the case of the pierced mirror output coupler (see Section 2.1.2).

In the following, we investigate the parameter range in which the 1D approximation can be applied. To this end, we simulate one pass through the gas target, by employing the 1D model and by solving the first-order propagation equation in 3+1 dimensions (3 space coordinates and the time coordinate), and compare the resulting field distributions. Both

simulations use the same peak intensity, pulse energy and time dependence of the incident pulse<sup>3</sup>.

For the 4D simulation, we rely on the first-order propagation equation as given in Eq. (2.12) with the envelope approximation for the nonlinear polarization response as validated in the previous section. We take a split-step approach that calculates the propagation  $z \rightarrow z + dz$  in the Fourier space  $(k_x, k_y, z, \omega)$  and the nonlinear polarization response in real space and time  $(x, y, z, t)$ . The numerical algorithm is based on a Predictor-Corrector method in combination with a Crank-Nicolson scheme [174]. This permits to propagate in step sizes of  $10 \mu\text{m}$  through an initially homogeneous gas target of neutral xenon atoms at a particle density of  $4 \times 10^{18}/\text{cm}^3$  and a total length of  $200 \mu\text{m}$ .

To compare the results of the two models, we use the fact that the cavity acts as a spatial filter. Due to the Gouy phase, the resonator can be tuned such that only the fundamental transverse mode  $\text{GH}_{00}$  is resonant in the cavity. Subsequent to the nonlinear propagation (index “n”) through the gas target, we decompose the field distribution  $\tilde{\mathcal{A}}^{(n)}(x, y, \omega)$  at  $z = z_0$  into the normalized transverse modes of the resonator without the gas target ( $\text{GH}_{i,j}(x, y, \omega)$ ). We proceed in the same manner for the case of linear propagation (index “l”), that is, without a gas target, yielding the field  $\tilde{\mathcal{A}}^{(l)}(x, y, \omega)$  at the same  $z$ -position. In the decomposition, we are mainly interested in the coefficient  $c_{0,0}$  describing the field content in the fundamental transverse mode, that is calculated<sup>4</sup> as:

$$c_{0,0}^{(n,\ell)}(\omega) = \int_{-\infty}^{\infty} \int_{-\infty}^{\infty} \tilde{\mathcal{A}}^{(n,\ell)}(x, y, \omega) \text{GH}_{0,0}^*(x, y, \omega) dx dy.$$

The fundamental-mode-filtered version  $\tilde{\mathcal{A}}_{0,0}^{(n,\ell)}$  of the fields  $\tilde{\mathcal{A}}^{(n,\ell)}$  is then given by:

$$\tilde{\mathcal{A}}_{0,0}^{(n,\ell)}(x, y, \omega) = c_{0,0}^{(n,\ell)}(\omega) \text{GH}_{0,0}(x, y, \omega).$$

Next, the corresponding fields in the time domain  $\mathcal{A}_{0,0}^{(n,\ell)}(x, y, t)$  are retrieved via inverse Fourier transformation. From these fields we can compute the temporal losses and the acquired temporal phase shift according to:

$$\text{Loss}(t) = 1 - \frac{\int_{-\infty}^{\infty} \int_{-\infty}^{\infty} \left| \mathcal{A}_{0,0}^{(n)}(x, y, t) \right|^2 dx dy}{\int_{-\infty}^{\infty} \int_{-\infty}^{\infty} \left| \mathcal{A}_{0,0}^{(\ell)}(x, y, t) \right|^2 dx dy}; \quad (5.6)$$

$$\varphi(t) = \arg \frac{\mathcal{A}_{0,0}^{(n)}(x, y, t)}{\mathcal{A}_{0,0}^{(\ell)}(x, y, t)} \Big|_{x=0, y=0}. \quad (5.7)$$

Note, that the  $x$ - $y$ -dependency of the phase of the fields (i.e.,  $\arg[\mathcal{A}_{0,0}^{(n,\ell)}]$ ) is an intrinsic attribute of Gaussian beams and is not linked to the plasma effects accounted for by  $c_{0,0}^{(n)}(\omega)$ . Therefore, the relative phase shift has a negligible variation with respect to the transverse

<sup>3</sup>The numerical implementation for solving the nonlinear propagation in 4D was done by M. Högner.

<sup>4</sup>For the linear case this is trivial because  $c_{0,0}^{(\ell)}(\omega) = 1$ .

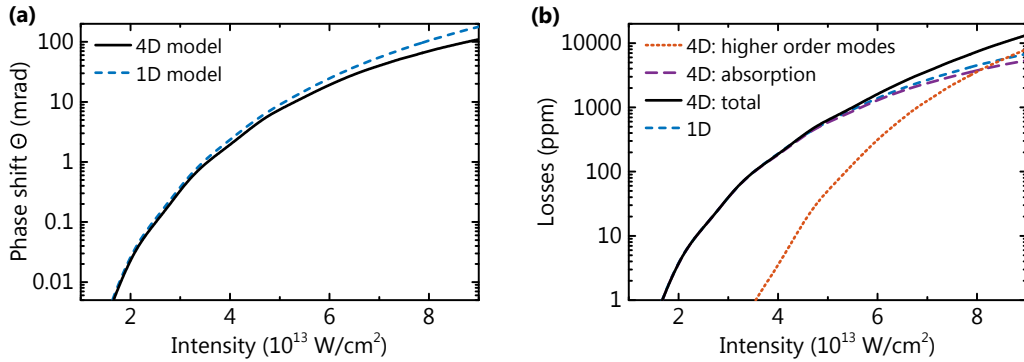


**Figure 5.2:** Comparison of a single pass through a xenon gas target in the 1D approach to the model in 3+1 dimensions for a range of intensities. Pulse duration: 30 fs. **(a)** acquired temporal phase shift  $\varphi$  at the trailing edge of the pulse. **(b)** Losses due to energy transfer to higher-order modes during the ionization, due to absorption and resulting total losses. In addition, we plot the losses in the 1D model.

coordinates in the parameter range discussed here, and we evaluate the phase shift on the optical axis.

In Fig. 5.2 we compare the overall losses and the total acquired phase shift calculated from Eq. (5.6) and (5.7) to the corresponding values of the 1D model. It can be seen that the intensity at which a given phase shift is reached is quite similar. The 1D model, however, slightly overestimates the total phase shift. In the cavity model, this is partially counterbalanced by the fact that the 1D model underestimates the losses, as it only accounts for energy absorption due to the ionization. For intensities up to  $7 \times 10^{13}$  W/cm $^2$  the losses are dominated by absorption with a crossover at  $8 \times 10^{13}$  W/cm $^2$ . Therefore, the 1D model is a useful approximation for intensities up to approximately  $8 \times 10^{13}$  W/cm $^2$  (when using xenon).

The transverse effects of a (pre-existing) steady-state plasma can in principle be treated similarly. A rigorous treatment would require detailed calculations about the spatially-resolved plasma dynamics considering also the continuous flow of gas from the nozzle orifice. As an estimate of the order of magnitude of this effect, we calculate the losses for a non-ionizing pulse directly following the ionizing pulse. It turns out that the transfer of energy in higher-order modes of this non-ionizing pulse is about a factor of 2 higher than the losses for the ionizing pulse due to the coupling. This reasoning provides an upper limit for this loss mechanism, as the steady-state plasma density is lower than the one assumed for the non-ionizing pulse.

It is interesting to further analyze the transfer of energy to higher order modes by calculating the exact decomposition of the field  $\tilde{\mathcal{A}}^{(n)}(x, y, \omega)$  into the GH modes. In Fig. 5.3 this is illustrated for an exemplary peak intensity of  $7 \times 10^{13}$  W/cm $^2$  and the above mentioned parameters for the propagation. Due to the rotational symmetry, only modes of even order need to be considered in the expansion. Most of the energy is transferred to the lowest order mode, that is, GH $_{2,0}$  and the GH $_{0,2}$ . Owing to the small spatial extent of the perturbation (or the high degree of nonlinearity of photoionization), also modes of very high order are populated. While the amount of energy in the individual modes decrease with its order, the amount of energy coupled to a set of modes characterized by  $m + n = M$  decreases only

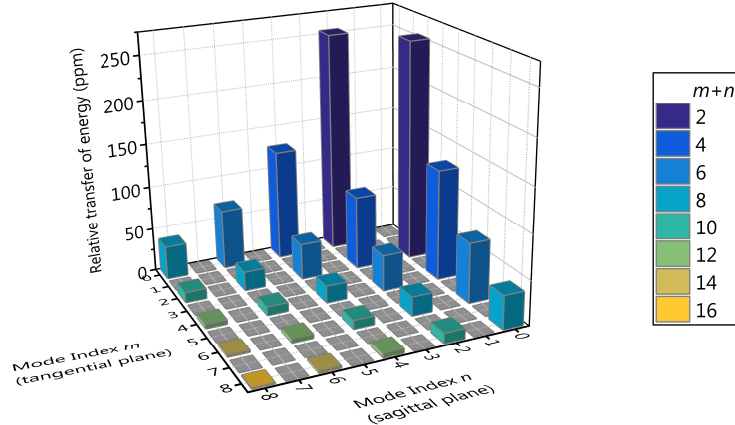


Figure 5.3: Transfer of energy to higher order modes.

slowly with  $M$ . In an anastigmatic resonator, all modes of a set  $M$  acquire the same Gouy-phase shift upon a round-trip. If a transfer of energy was resonant, it would be resonant for the whole set.

On a personal computer, the calculation of a single pass through the gas target takes about 15 s using the 4D code. This is fast when doing a few calculations, but for investigating a wide parameter sweep requiring hundreds of complete cavity build-ups, a faster computational model is desirable. A single calculation with the 1D model takes a few ms. For typical gas-density-length products that are below  $2 \times 10^{17}/\text{cm}^2$  and for the intensity range studied here, the 1D model is a good approximation. Additionally the 1D model could be readily extended by including a precomputed intensity-dependent loss factor.

One of the key assumptions is the non-resonant character of the coupling, especially with the revealed energy transfer to modes of very high order. In practice, it is inevitable that some of those are degenerate<sup>5</sup> with the fundamental mode. Still, this typically does not harm the fundamental mode operation as these modes can be efficiently suppressed at the finite apertures of the mirrors or apertures specifically placed in the beam path. When operating the cavity close to the inner edge of the stability range, all modes of even  $M$  converge to the fundamental mode, with the (0,2)-mode having the smallest separation. Ultimately, the degeneracy of the latter with the fundamental mode will limit the applicability of the 1D model in this regime.

### 5.1.3 Plasma recombination

In Appendix E, fluid flow simulations of noble gases through end-fired nozzles are presented. They indicate that the velocity of the xenon atoms along the nozzle axis (and perpendicular to the optical axis) is about 220 m/s. Given the strong intensity dependence of the ionization rate, the region where ionization mostly occurs is significantly smaller than the  $1/e^2$ -intensity radius  $w_0$  of the focus. For xenon, we argued in Section 5.1.1 that  $r_{\text{ionization}} \sim 0.4w_0$ . Assuming a focus size of  $w_0 = 35 \mu\text{m}$ , only a fraction of about 10% of the plasma leaves the

<sup>5</sup>Degenerate in the sense that coherent coupling between the modes is possible.

region of ionization ( $2r_{\text{ionization}}$ ) within one cavity round-trip time of 13 ns and is replaced by neutral atoms. Therefore the recombination of electrons with ions needs to be considered.

For electron densities exceeding  $10^{14}/\text{cm}^3$  and electron temperatures on the order of  $k_{\text{B}}T \sim 1 \text{ eV}$ , the dominant mechanism of electron-ion recombination is via three-body collisions (see Section 2.2.2 and [103]). Here, we assume a homogeneous plasma, that is characterized by a uniform electron temperature and density. Furthermore, it is assumed that the temperature changes only due to ionization. In particular, the plasma expansion and, thus, cooling [175], and the plasma heating due to the recombination are neglected. In such a situation the evolution of the electron density is governed by:

$$\frac{dn_e(t)}{dt} = -bn_e^3, \quad \text{with} \quad b = \hat{b} \frac{10^{-27} \text{ cm}^6 \text{ eV}^{9/2}}{(k_{\text{B}}T)^{9/2} \text{ s}}. \quad (5.8)$$

Literature values for  $\hat{b}$  vary from  $\sim 1$  to  $9$  [103, 104, 176]. We assume an intermediate value of  $\hat{b} = 2$ . We will later see, that this uncertainty plays a minor role for the steady state plasma and a negligible role for describing the intensity clamping. A parameter entering Eq. (5.8) with a much stronger dependence is the temperature of the plasma. Assuming thermodynamic equilibrium it is related to the mean kinetic energy of an electron by  $\langle \varepsilon_{\text{kin}} \rangle = \frac{3}{2}k_{\text{B}}T$ . We calculate the kinetic energy classically, by integrating the equation of motion of an electron in the field  $E(t)$  assuming that the electron was born in the field at  $t_b$  with vanishing velocity. Thus, we find

$$\varepsilon_{\text{kin,e-}}(t, t_b) = \frac{e^2}{2m} (\mathcal{A}(t) - \mathcal{A}(t_b))^2,$$

with  $\mathcal{A}(t)$  being the vector potential, which is related to the electric field via  $\mathcal{E} = -\frac{d\mathcal{A}}{dt}$ . The total kinetic energy deposited in the electron gas at the time  $t$  reads:

$$\varepsilon_{\text{kin,tot}}(t) = \frac{e^2}{2m} \int_{-\infty}^t (\mathcal{A}(t) - \mathcal{A}(t'))^2 \frac{dn_e}{dt'} dt'.$$

At the end of the pulse, where  $\mathcal{A}(t = \infty) = 0$  and with  $\Delta n_e$  being the newly generated electron density this becomes:

$$\langle \varepsilon_{\text{kin,e}}(t = \infty) \rangle = \frac{1}{\Delta n_e} \frac{e^2}{2m} \int_{-\infty}^{\infty} \mathcal{A}(t)^2 \frac{dn_e}{dt} dt. \quad (5.9)$$

From the point of numerics, the calculation of this quantity is the bottleneck in the 1D model, as it requires interpolation and integration on a much finer time grid than for beam propagation. An approximation to Eq. (5.9), for example, via Taylor expansion of the integrand, is hard to find: while ionization predominantly occurs at the maxima of the electric field – where the vector potential vanishes and is linear in time, but where  $\frac{dn_e}{dt} = \max$  and  $\frac{d^2 n_e}{dt^2} \approx \text{const}$  – the maxima of the vector potential occur at the zero crossings of the electric field and, thus, where  $\frac{dn_e}{dt} \approx 0$  and  $\frac{d^2 n_e}{dt^2} \approx \text{const}$ . We empirically find that the following

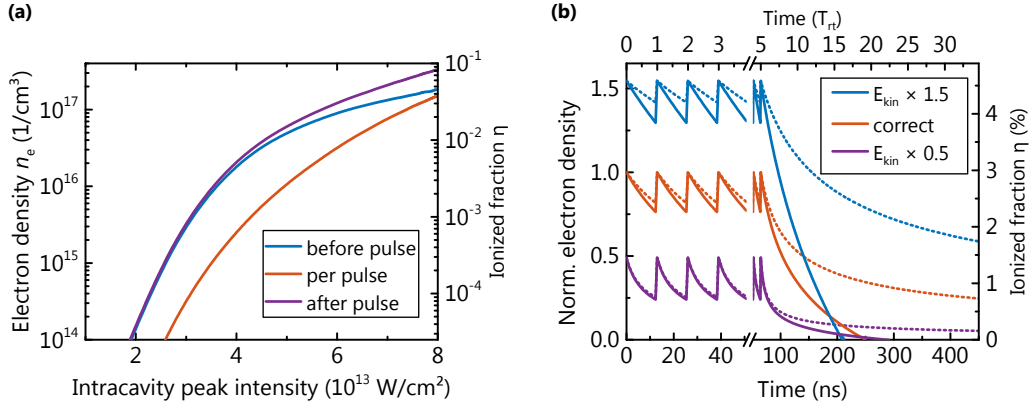


**Figure 5.4:** (a) Electron density as a function of the pulse peak intensity for a 30-fs pulse in a cavity with a pulse repetition rate of 77 MHz. (b) Time resolved plot of the electron density for a peak intensity of  $6 \times 10^{13} \text{ W/cm}^2$  and otherwise identical parameters. Furthermore, the effect of a higher or lower kinetic energy is illustrated. The data was normalized to the maximum of the density in the model with the correct kinetic energy. The dotted lines indicate the ionized fraction without the continuous flow from the nozzle. After about 55 ns ionization was turned off. Further parameters used in both simulations: xenon particle density,  $4 \times 10^{18}/\text{cm}^3$ ; target length,  $200 \mu\text{m}$ ; focus radius,  $40 \mu\text{m}$ .

approximation requiring only the pulse envelope describes the kinetic energy well in our parameter regime, that is, for intensities below  $7 \times 10^{13} \text{ W/cm}^2$  and for not extremely chirped pulses:

$$\langle \varepsilon_{\text{kin},e} \rangle \approx 0.31 \frac{1}{\Delta n_e} \frac{e^2}{4m\omega_c^2} \int_{-\infty}^{\infty} dt \frac{dn_e}{dt} |\mathcal{A}(t)|^2. \quad (5.10)$$

It can be used when computation speed is more important than accuracy.

At intensities of up to  $\sim 6 \times 10^{13} \text{ W/cm}^2$  and at our repetition rate (77 MHz), the model predicts the steady-state plasma density to be below  $1 \times 10^{17}/\text{cm}^3$  (see Fig. 5.4(a)). Thus, the higher-order dispersion plays a negligible role ( $|\text{GDD}| < 0.04 \text{ fs}^2$  for  $200 \mu\text{m}$ , at  $n_e = 1 \times 10^{17}/\text{cm}^3$ ). The dominant effect of the steady-state plasma is a global shift of the cavity resonances and a change in the effective cavity length (see Eqs. (2.16) to (2.17)). As the depletion of the neutral gas is only a few percent, the influence on the clamping intensity is negligible. In our parameter range (density, temperature), we find with Eq. (5.8) that a fraction of about 10% to 30% of the electrons recombines within the first cavity round-trip time. The temporal evolution of the electron density is illustrated in Fig. 5.4(b), exemplary for a peak intensity of  $6 \times 10^{13} \text{ W/cm}^2$ .

Despite the strong temperature dependence of the recombination coefficient  $b \propto T^{-9/2}$ , the emerging steady-state electron density is rather robust against variations in  $T$  (only linear dependence, see Fig. 5.4(b)). Underestimating the electron temperature  $T$  in the model leads to a much faster recombination time and thus an even lower steady-state ionized fraction (purple dashed line in the plot). An overestimation of the electron temperature would mean a much slower recombination rate, however, the  $n_e^3$  dependence of the recombination counteracts the resulting increase in electron density (blue dashed line in the plot). Fur-

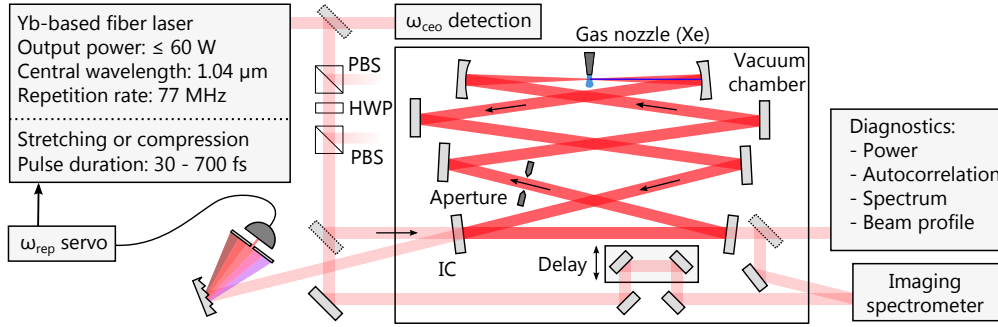


**Figure 5.5:** Experimental setup: laser system with optional fiber broadening and compression, comb offset frequency ( $\omega_{\text{ceo}}$ ) detection unit, enhancement cavity, active stabilization of the center frequency to the cavity resonance, and imaging spectrometer. Attenuation unit consisting of half-wave plate (HWP) and polarizing beam splitter (PBS).

thermore, the error is bound by the timescale set by the replenishment of the plasma in the interaction region with neutral atoms. Therefore, more accurate calculations of the electron temperature, as, for example, known from the interpretation of electron energy spectra in above threshold ionization [177–180], will not significantly affect the results. For the same reasons, uncertainties in  $\hat{b}$  have a minor influence on the steady-state ionized fraction and a negligible influence on the clamping intensity.

In summary, the cavity response is mainly affected by the temporal phase shift and not by the dispersive effects of a pre-existing plasma. This holds when the induced GDD is small (for the finesse and bandwidth considered) and when the depletion of the neutral gas is small ( $\lesssim 15\%$ ). At the gas parameters used in the experiments, both criteria are fulfilled, rendering more detailed modeling of the plasma recombination unnecessary.

## 5.2 Experimental methodology

In the following two sections, particularities of the experimental setup are emphasized and details about the phase retrieval algorithm are given.

### 5.2.1 Experimental apparatus

A sketch of the experimental setup is depicted in Fig. 5.5. The CPA-based laser system provides valuable flexibility in terms of output pulse duration. Fourier-limited pulses with a duration of about 180-fs are available directly from the CPA system. By varying the separation between the compressor gratings, a linear chirp (i.e., a quadratic spectral phase) in both directions can be applied. We will refer to upchirped pulses as pulses with increasing instantaneous frequency with time. In the experimental campaign a chirp up to  $400 \text{ fs}^2$  was introduced leading to pulse durations as long as 640 fs. Using the nonlinear compression stage, close-to-Fourier-limited pulses of 30 fs are obtained.

Here, spectral broadening was achieved in a 5-cm long large-mode area fiber with a mode-field diameter of  $26 \mu\text{m}$  (LMA-35, NKT Photonics). In contrast to the double-clad fibers used in the HHG experiments presented in Chapter 4, these fibers provide superior beam quality.

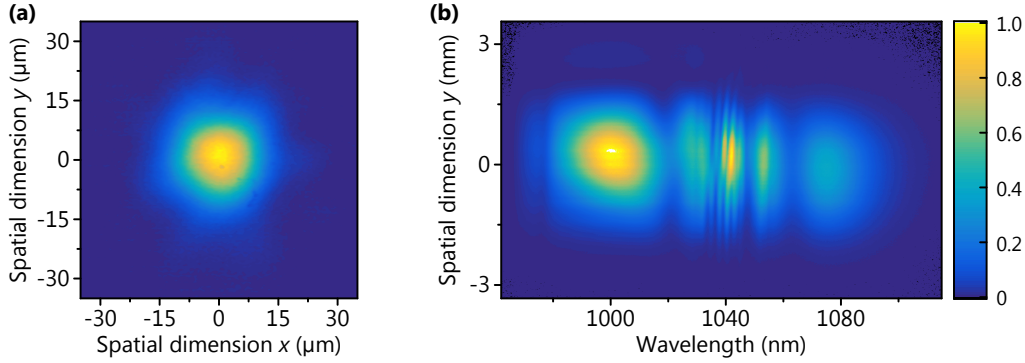


**Figure 5.6:** (a) Beam profile imaged at the output facet of the fiber used for spectral broadening (LMA-35). (b) Measured spectrum sent to the cavity spatially resolved in the vertical direction. Around the central wavelength, interference with non-broadened light leads to spatial inhomogeneity (see text for details). Both plots share the same color axis.

This can be partially attributed to the smaller core diameter, easing the preparation process of the fiber facets. Additionally, the pump core of the double-clad fiber provides another means to guiding light not coupled into the signal core. While the intensity in the signal channel is high enough for nonlinear effects such as SPM, this is typically not the case for the radiation propagating in the pump core. When both channels finally interfere, a spatially inhomogeneous beam profile is recorded, that is, a position dependent spectral content and spectral phase. In single-clad fibers, such as the LMA-35, this effect is strongly suppressed but still visible due to unintended guiding of the light in the fused silica cladding material via total internal reflection (see Fig. 5.6).

The setup comprises an attenuator stage consisting of a polarizing beam splitter, an achromatic half-wave plate and a pair of thin film polarizers. The first polarizing beam splitter cleans the polarization. It is necessary because nonlinear effects in the fiber transfer light, that is initially well polarized along a certain axis, into the other polarization component. The overall throughput of the nonlinear broadening, the compression and the attenuation stage amounts to about 60% leading to an available average power of 23 W in the case of compressed pulses.

The pulses are coherently enhanced in a standard-approach, symmetric bow-tie cavity comprising eight mirrors. The radius of curvature of the two curved mirrors is  $-300$  mm. The cavity is operated close to the inner edge of the stability range ensuring nearly identical spot sizes on all mirrors and focus sizes ( $1/e^2$ -radius of the intensity) in the range of  $22 \mu\text{m}$  to  $35 \mu\text{m}$  depending on the exact configuration. Two types of multilayer coatings are used. For the experiments using pulses of  $\sim 7$  nm of bandwidth,  $\text{Ta}_2\text{O}_5$  and  $\text{SiO}_2$  were used as coating materials. For the broadband pulses  $\text{Nb}_2\text{O}_5$  was used as high index material in the multilayer coating. An input coupler with 0.5% transmission was chosen. An aperture of variable diameter suppresses transverse modes of high order to which light might be coupled by the plasma.

The leakage through one of the cavity mirrors in the collimated arm of the cavity provides access to the intracavity pulse. It interferes with a delayed copy of the input pulse at a small vertical separation angle ( $< 4^\circ$ ) at the entrance slit of an imaging spectrometer (Shamrock

SR-303i, Andor). It is set-up in a Czerny-Turner configuration using a grating of either 1200 or 300 lines per mm and images the entrance slit onto a 2D-array. Thus, images acquired with the CCD provide spatial resolution in the vertical direction and spectral resolution along the horizontal direction.

The error signal for the stabilization of the oscillator cavity length to the length of the EC is derived in a narrow spectral region close the carrier wavelength of the input pulses. The offset frequency is sufficiently stable on the timescale of data acquisition, so that active stabilization is not compelling. The linewidth of the beat-note was typically  $\sim 200$  kHz, measured with a resolution bandwidth of 100 kHz.

### 5.2.2 Phase measurement and phase retrieval

To enable a quantitative comparison of the experimental results to the predictions of the model, both pulses need to be characterized precisely. Both the input and the cavity spectra are recorded. To assess the spectral phase of the temporally compressed input pulses, frequency-resolved optical gating was used. For pulses of reduced bandwidth, the spectral phase was inferred from the pulse duration measured via intensity autocorrelation (assuming a quadratic dependence of the phase).

We employ spatial-spectral interferometry (SSI) to measure the spectral phase difference between the intracavity and the input pulses [15, 181]. Replicas of each of these beams intersect noncollinearly at an angle  $\alpha$  and the resulting interference pattern in the spatial and spectral plane  $(y, \omega)$  is given by:

$$I_{\text{if}}(y, \omega) = I_{\text{in}}(y, \omega) + I_{\text{cav}}(y, \omega) + 2\sqrt{I_{\text{in}}(y, \omega)I_{\text{cav}}(y, \omega)} \cos\left(\theta(\omega) + \frac{y\omega}{c} \sin \alpha\right). \quad (5.11)$$

Here,  $\theta(\omega)$  is the relative spectral phase of the two pulses, and  $I$  denotes the intensity. From Eq. (5.11)  $\theta(\omega)$  can be retrieved, without individual phase measurements of both pulses. This offers the advantage that one directly characterizes the system under investigation (here, cavity-enhanced ionization). The recorded spectral information eases the phase retrieval, because the cosine term in Eq. (5.11) can be isolated. Yet, slight variations as typical within a measurements series have only a minor influence on the retrieved phase.

Further data processing consists of several steps. First, only these parts of the data are considered, that show sufficient signal to noise ratio and good spatial homogeneity. To this end the outer spatial parts of the pre-processed interferogram (i.e.,  $(I_{\text{if}} - I_{\text{in}} - I_{\text{cav}})/(2\sqrt{I_{\text{in}}I_{\text{cav}}})$ ) are excluded. Although the phase retrieval problem is in principle largely overdetermined (unknowns  $\theta(\omega)$  and  $\alpha$ ), the huge amount of data (on the order of  $10^5$  points) requires an efficient algorithm<sup>6</sup>. The key idea is that  $\theta(\omega)$  can be determined from a linear system of algebraic equations, if the angle  $\alpha$  was known. Therefore, the fitting routine reduces to a single parameter optimization problem. A detailed description of the algorithm is given in Appendix D.

In the retrieved phase  $\theta(\omega)$ , only quadratic and higher-order terms in  $\omega$  are considered, as there are multiple uncontrolled sources of group delays in the experiment. Thus, a linear function must be added when comparing the retrieved phases to simulations. When using

<sup>6</sup>The robust numerical implementation of the phase retrieval was done by M. Trubetskov.

fiber-broadened pulses the spatial inhomogeneity is the main source of experimental uncertainty in the retrieved phase, limiting the sensitivity to about 60 mrad. It can be as low as 10 mrad, when the pulses directly emitted by the CPA system are used.

Without nonlinearity in the cavity, one can deduce the single-round-trip phase  $\phi$  from  $\theta$  via Eq. (2.1). In a high finesse cavity, the phase enhancement factor relating  $\theta$  to  $\phi$  amounts to about  $\sim F/\pi$  and can be several orders of magnitude, rendering cavity-enhanced SSI a highly sensitive phase measurement technique. With nonlinearities present in the EC, a definition of the frequency-resolved power enhancement via  $\tilde{\mathcal{E}}_{\text{cav}}(\omega)/\tilde{\mathcal{E}}_{\text{in}}(\omega)$  is not possible, as in general new frequency components are generated. For the same reason, a single round-trip through the cavity can not be described by an attenuation and a phase shift via  $\sqrt{R_{\text{cav}}(\omega)}e^{i\phi(\omega)}$ . Still, tiny phase shifts (may it be spectral or temporal) are significantly enhanced by the many round-trips the pulse takes in the resonator. This is why we apply this technique to investigate the phase modulation induced in a nonlinear interaction driven in the steady-state regime of an EC.

### 5.3 Experimental results and comparison with the model

In the following, we present the recorded experimental data and compare them to results obtained with the cavity model. In a first step, we restrict the discussion to the case of linear power enhancement in order to validate the acquisition and the phase retrieval and to check the consistency of the cavity model.

#### 5.3.1 Linear cavity in the steady state

We validate the phase retrieval in a series of measurements for which the vacuum chamber is flooded with argon gas. The input power is kept sufficiently low such that only the linear dispersion of the gas plays a role. In all measurements, the central part of the comb is kept on resonance and the offset frequency of the comb is adjusted to maximize the overall power enhancement. In Fig. 5.7(a) the measured spectral phases and the results of the *ab-initio* simulations are presented. The spectral properties of the mirrors were taken from the design curves provided by the manufacturer. The phase acquired in a single round-trip can in principle be retrieved by inverting Eq. (2.1). This is, however, hampered by the fact that the measured phase is only known up to a linear function. For optimal comb offset frequency, and when the error signal for locking the comb to the cavity is generated in a known narrow spectral region, the acquired phase must vanish in the vicinity of this wavelength. This fixes the unknown slope in the measured phase and the single round-trip phase can be unambiguously calculated. By applying a parabolic fit to the difference of the single round-trip phase with and without argon gas, we find the group velocity dispersion (GVD) of the gas (see Fig. 5.7(b) and (c)). The results excellently agree with the expected pressure-dependent GVDs.

In a second set of experiments, we validate that the cavity model and the phase measurements provide consistent data in the case of detuned offset frequency. Furthermore, it is instructive to see how the acquired intracavity phase evolves with a detuning of the offset frequency. To this end, we take SSI data for a range of fixed offset frequencies of the seeding laser while keeping the central part of the comb on resonance. The results are depicted in

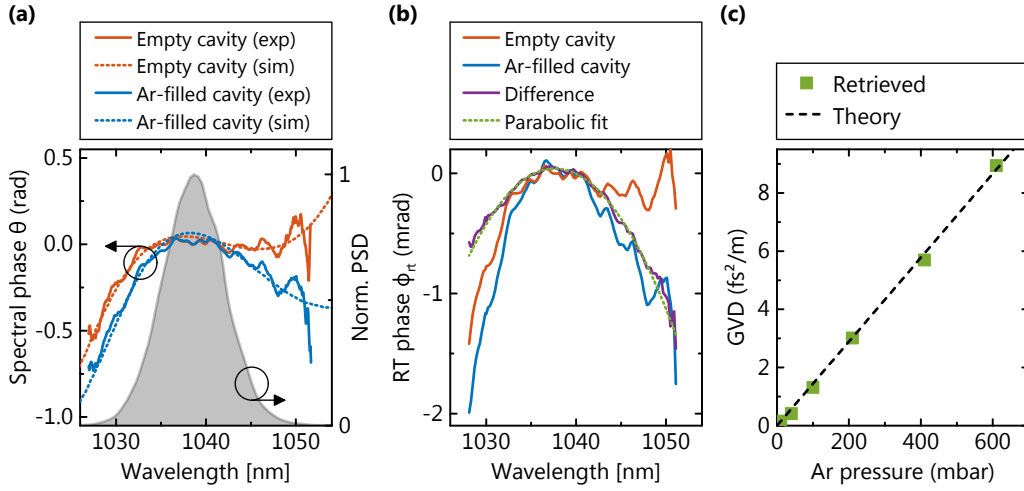


**Figure 5.7:** (a) Measured spectral phase in the empty cavity and when flooded with 100 mbar of argon along with the results of simulations. (b) Retrieved single round-trip phases and their difference, isolating the spectral phase induced by the argon gas. (c) GVD as a function of argon gas pressure retrieved via parabolic fits of the data presented in (b). The theoretical data is taken from [182].

Fig. 5.8. Again, the simulations excellently agree with the experimental data. While the phase is almost flat for optimal offset frequency, it shows a pronounced wavelength dependency for a detuning. For a dispersion free cavity, the single round-trip phase would linearly increase (with frequency) in case of detuned offset frequency. At the same time, the power enhancement diminishes for the outer spectral regions leading to a saturation behavior of the overall acquired intracavity phase. In the vicinity of the central wavelength, the power enhancement factor is almost constant and, thus, the single round-trip phase and overall cavity phase can be related to each other by a constant phase enhancement factor. This is highlighted by the linear dependence of the phase on the wavelength around the central wavelength.

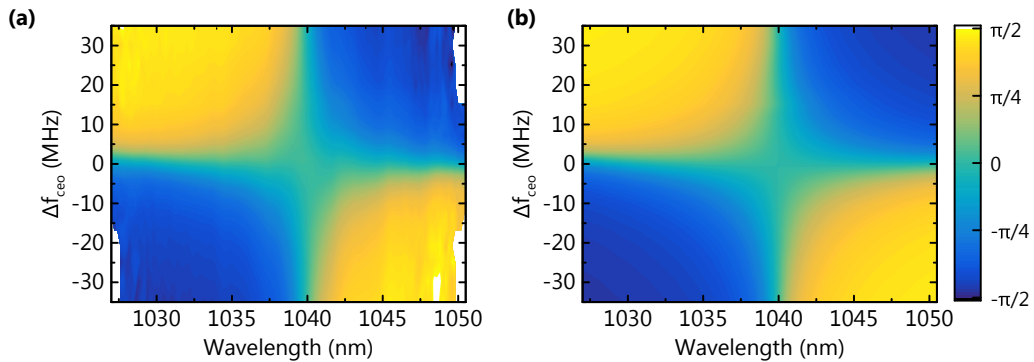


**Figure 5.8:** (a) Measured spectral phase of the cavity pulse relative to the input pulse for different offset frequencies and (b) corresponding results from the simulations. Both plots share the same color axis.

### 5.3.2 Nonlinear cavity in the steady state

To validate the nonlinear cavity model we compare the intracavity spectra, the acquired spectral phase and the intracavity intensity to the results of the corresponding simulations. This is done for a range of input powers and for several pulse durations. In the left and center panels of Fig. 5.9, we show four examples of recorded spectra and spectral phase shifts. The input pulse durations from (a) to (d) were 640 fs up-chirped and down-chirped, and close-to-Fourier limit (FL) pulses of 180 fs and 30 fs duration. With 30-fs input pulses, an intracavity pulse duration of 35 fs at a power enhancement factor of 250 was reached, leading to an average power of 3.3 kW without a gas target.

All inputs to the model are taken as measured or as calculated by other independent simulations so that fit parameters are not necessary. For the simulations, the mirror reflectivities and phases are again taken from multilayer design calculations and the gas parameters are extracted from fluid flow simulations (see Appendix E). The input pulse parameters are set as measured. For the broadband pulses, the deviation of the comb offset frequency from the value required by the cavity for optimum enhancement is particularly critical, because even deviations as small as 2 MHz from the optimum value lead to a drop in intracavity power by 50 % and to a spectral filtering. A small detuning of the locked central comb line from the empty cavity resonance is introduced, avoiding the regime of optical bistability [62, 88] and keeping intracavity power fluctuations below 1 % root mean square (RMS) (band: 2.5 Hz to 5 MHz). It also ensures operation close to the nonlinear resonance maximum.

Using chirped pulses provides a more accurate means for the phase measurements. This is partly due to more accurate knowledge of the spectral phase of the input pulses. Even more important is the susceptibility of the chirped pulses to temporal phase distortions owing to their linear time-frequency dependence [183]. This results in pronounced jumps in the spectral phase.

In the right panels of Fig. 5.9(a)-(d) the dependence of the intracavity peak intensity on the input peak power is depicted. All curves reveal the intensity clamping behavior reported previously [62, 66]. The simulated intensities agree well with the experimentally determined ones, validating the nonlinear cavity model in the range of parameters relevant to intracavity HHG. From the simulations we deduce an upper limit for the intracavity intensity (blue line in the right panels). This is found by optimizing the input frequency comb ( $\omega_r, \omega_{\text{ceo}}$ ) while keeping all other parameters fixed. It has been shown that this optimum is located at nonzero detuning of the comb from the linear cavity resonances and coincides with a local bifurcation of the intracavity power at which stable operation of the cavity is impossible [88].

When calculating the ionization rates according to ADK theory [92] instead of PPT theory, the nonlinearity is considerably underestimated and, thus, the reachable intracavity peak intensity is overestimated by about  $\sim 25\%$  compared to the experiments. The simulations yield the ionized population before the pulse and the ionization per pulse to be both on the order of  $2 \times 10^{16}/\text{cm}^3$ . Despite the highly sensitive dispersion measurement, this electron density is too low to be detectable via its higher-order dispersion. In complementary measurements of the offset frequency for which the comb is optimally enhanced, we did not find a measurable difference for the linear and the nonlinear case ( $\lesssim 1$  MHz), setting an upper boundary for the steady-state plasma density, that is in accordance with the simulations (see discussion in Section 2.2.2).

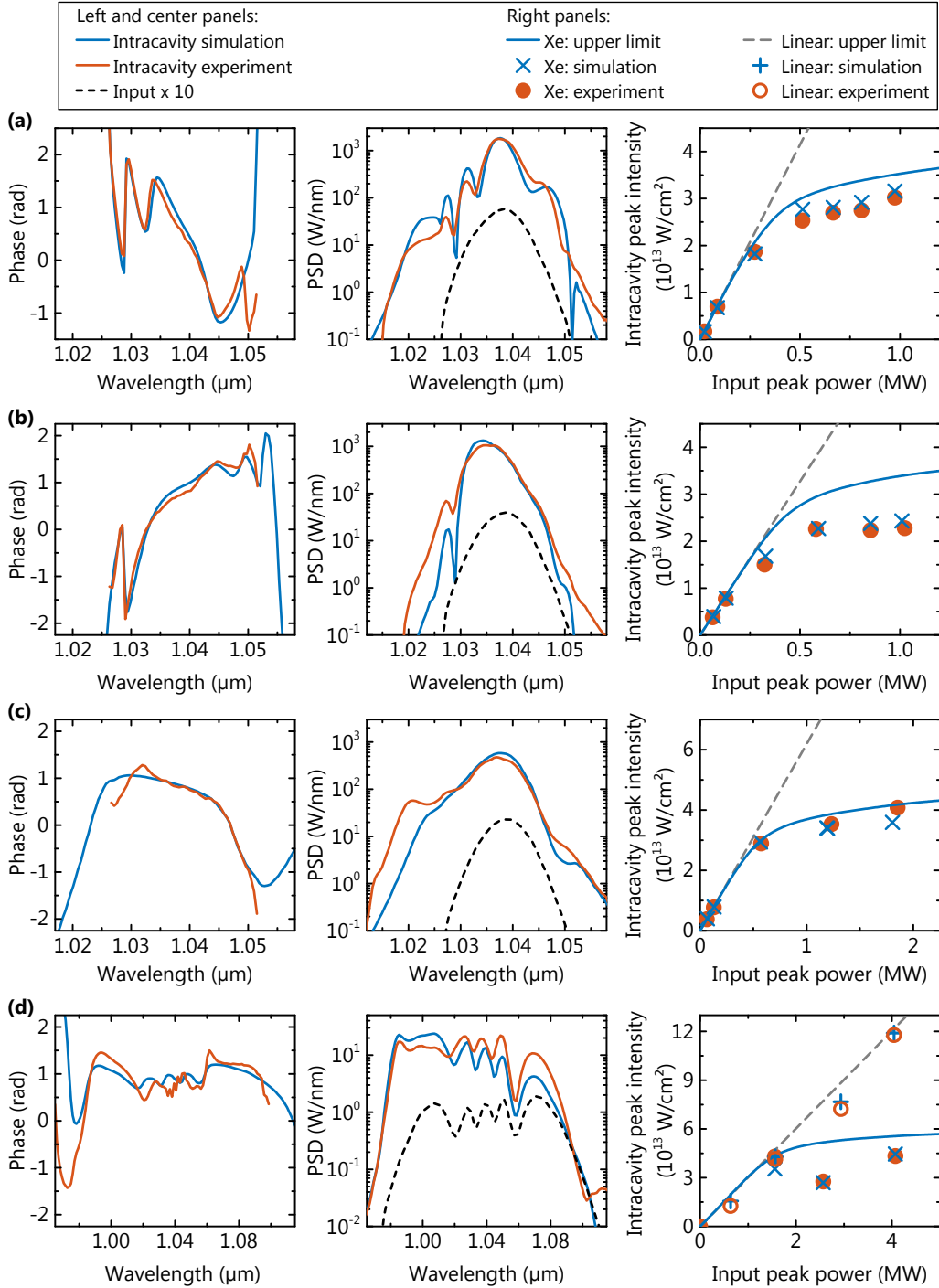


**Figure 5.9:** Validation of the nonlinear cavity model in a standard-approach cavity. Acquired spectral phases (left panels) and measured power spectral densities (PSD, center panels) of the intracavity pulse along with simulation results. Input pulse durations from (a)-(d): 640 fs (up-chirped), 640 fs (down-chirped) 180 fs (Fourier limited), 30 fs (fiber-broadened). Without ionization, the spectrum is symmetrically enhanced around the central wavelength. Right panels: Intracavity peak intensity as function of input peak power for. The outlier in the case of the broadband pulses is due to an incorrectly-set offset frequency of the comb. Gas density:  $9 \times 10^{18}/\text{cm}^3$ , interaction length: 180  $\mu\text{m}$ , finesse: 1190 (narrowband case) and 950 (broadband case).

## 5.4 Implications

With the ab-initio model being well validated in the relevant parameter range, one can numerically investigate the nonlinear cavity performance in an even wider parameter range, or, in non-standard-approach ECs. For the layout of an experiment, it is important to predict the reachable intracavity intensity. Here, a simple analytic expression would be convenient. This is addressed in Section 5.4.1. Sections 5.4.2 and 5.4.3 are dedicated to adapting the model to different driving wavelengths and pulse repetition rates, respectively. Section 5.4.4 focuses on the question, whether an EC can be driven beyond the intensity-clamping limit.

### 5.4.1 Empirical scaling law for standard-approach cavities

To optimize the nonlinear laser-gas interaction, for example, for maximizing the conversion efficiency to the XUV via HHG [184], a simple expression relating the achievable intracavity intensity to the given cavity, gas and input pulse parameters is desirable. To this end, we calculate the clamping behavior for a broad range of hundreds of different combinations of values for the gas parameters (density-length product<sup>7</sup>:  $n_{\text{gas}}L = 4 \times 10^{16}/\text{cm}^2 - 20 \times 10^{16}/\text{cm}^2$ ), the finesse ( $\mathcal{F} = 250 - 2500$ ) and the pulse duration ( $\tau = 12 \text{ fs} - 600 \text{ fs}$ ). Standard-approach cavities are considered: we assume a uniform mirror reflectivity, symmetric to the central wavelength and zero GDD over sufficient bandwidth to limit intracavity pulse lengthening to 1% in the absence of gas and at an input coupler transmission of 1%. The temporal profile of the pulses is considered to be of Gaussian type.

Although the intracavity intensity seems to be unbound, the distinct saturation behavior of the intracavity intensity with respect to the input peak power motivates the definition of a clamping intensity. We find that for given gas and pulse parameters and for a targeted intensity there is an optimum cavity finesse that minimizes the required input peak power. Conversely, each finesse is optimal for a desired intensity. This intensity is reached when the peak power enhancement has dropped to about 60% to 70% of its value without a gas target. Therefore, we define the clamping intensity  $I_{\text{CL}}$  as the intracavity intensity, at which the peak power enhancement equals 65% of its linear value (see dotted crosses in the right panels of Fig. 5.9). We find that the following empirical law with the parameters  $\alpha$ ,  $\beta$ ,  $\gamma$  and  $\delta$  describes the entire range of simulations within 7% of accuracy:

$$I_{\text{CL}}(\tau, \mathcal{F}, nL) = I_0 \times \left( \frac{\tau_0 - \alpha}{\tau - \alpha} \frac{\mathcal{F}_0 - \beta}{\mathcal{F} - \beta} \frac{n_{\text{gas},0}L_0 - \gamma}{n_{\text{gas}}L - \gamma} \right)^\delta. \quad (5.12)$$

All coefficients are given in Table 5.1. It is not surprising that the three input parameters pulse duration, finesse, and the gas-density-length product scale with the same exponent  $\delta$ : in terms of accumulated temporal phase shift, increasing the finesse is very similar to having a longer or denser gas jet or to increasing the pulse duration. The small value of  $\delta$  is a direct consequence of the high degree of nonlinearity of the ionization process. It reveals that the ionization constitutes a rather severe limit for scaling the intensity in the presence of an

---

<sup>7</sup>We only consider the product of the gas density and its length as only the product enters the formulas. The only exception to this is the recombination of the plasma, which is, however, not critical for the clamping intensity.

**Table 5.1:** Parameters for the empirical scaling law of Eq. (5.12) describing the intensity clamping.  $\tau_0 = 100$  fs,  $\mathcal{F}_0 = 416$  and  $n_{\text{gas},0}L_0 = 8 \times 10^{16}/\text{cm}^2$ . Simulations were performed with a repetition rate of 100 MHz and with a gas target length of 200  $\mu\text{m}$ . The bandwidth of the ECs corresponded to the input pulse durations at 1.04  $\mu\text{m}$  central wavelength.

Parameter	Xenon	Argon	Neon
$\alpha$ (fs)	0.8	3.3	5.3
$\beta$	61	69	72
$\gamma$ ( $10^{16}/\text{cm}^2$ )	0.96	0.97	1.0
$\delta$	0.159	0.153	0.148
$I_0$ ( $10^{14}$ W/cm <sup>2</sup> )	0.461	1.24	3.72

intracavity gas target. For instance, in the clamping regime doubling the intensity requires a decrease in any of the other parameters by roughly a factor of 90.

#### 5.4.2 Wavelength scaling

It is straight forward to adapt the simulations to other driving wavelengths in the visible or near IR, as long as no other physical processes are involved (e.g., resonant excitation or absorption). Knowing that in our intensity range, the phase-modulation term in Eq. (5.1) is the predominant limitation, one can derive a rule of thumb for the totally acquired phase shift. For a single pass through the gas target the phase shift takes the approximate form  $\varphi_{\text{sp}}(t) = r_e \lambda_c \eta(t) n_{\text{gas}} L$ .

At the clamping limit intensity we find the single-pass phase shift at the end of the pulse to take a value of about  $\varphi_{\text{sp,max}} = 6.3/\mathcal{F}$  with a minor dependence on other parameters<sup>8</sup>. This is about a factor of two higher than the previously reported rule of thumb of  $\pi/\mathcal{F}$  [65, 100]. The expression for  $\varphi_{\text{sp}}$  and the tolerable single-pass phase shift  $\varphi_{\text{sp,max}}$  are a good starting point for transferring our findings to other driving wavelengths, for example, when considering a means to extending the XUV cutoff wavelength.

In Fig. 5.10, we plot the total acquired single-pass phase shift  $\varphi_{\text{sp}} = r_e \lambda_c \eta(t = \infty) n_{\text{gas}} L$  for three different carrier wavelengths  $\lambda_c$  as a function of the peak intensity. To keep the number of field oscillations constant, we scale the pulse durations accordingly. While  $\varphi_{\text{sp}}$  has an explicit linear dependence on  $\lambda_c$ , the ionized fraction  $\eta$  also strongly depends on  $\lambda_c$ . In terms of scaling the cutoff wavelength a 2- $\mu\text{m}$  based system would outperform the 1- $\mu\text{m}$  system up to intensities of about  $5 \times 10^{13}$  W/cm<sup>2</sup>, because it acquires less phase shift and allows for quadratically higher cut-off energies ( $E_{\text{cut-off}} = I_p + 3.17U_p(\lambda)$ ). In an EC seeded with frequency-doubled IR light (i.e. in the green spectral range), the intensity clamping should be much more pronounced. This is corroborated by the reported peak intensity of about  $1.2 \times 10^{13}$  W/cm<sup>2</sup> in [167]. In turn, at the clamping limit, that is, for a given single-pass phase shift, a short-wavelength-seeded enhancement cavity works at much higher ionization levels, which might be beneficial for some applications. Although in single-

<sup>8</sup>This value can be interpreted as a total phase shift of  $\pi$  reached at approximately  $\mathcal{F}$  number of round-trip for both the leading and the trailing edge of the pulse, while the central part of the pulse always interferes constructively.

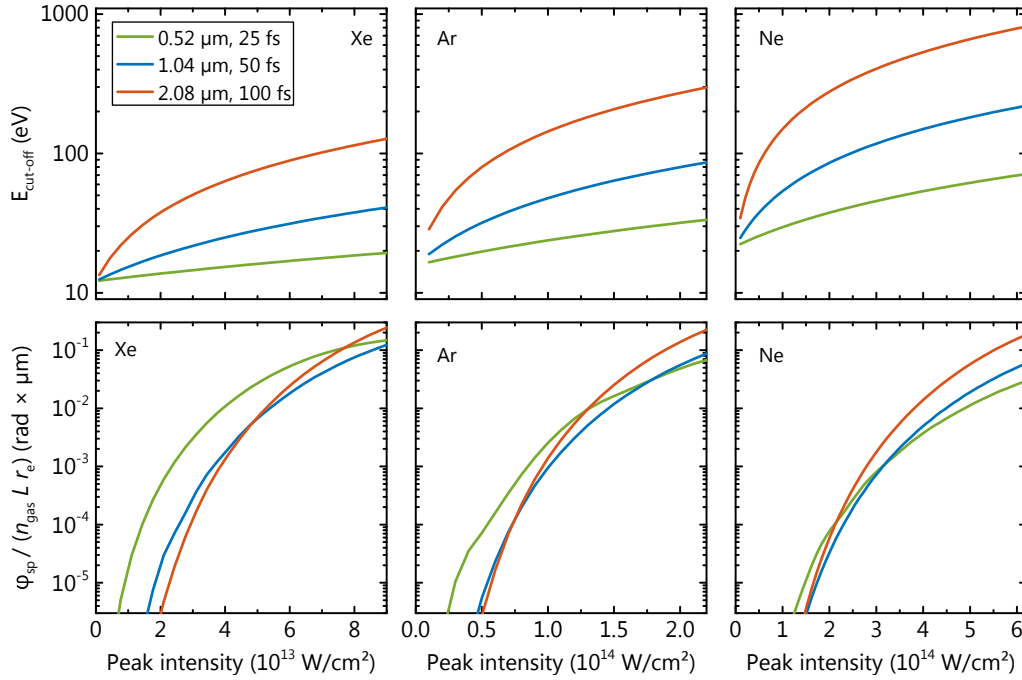


**Figure 5.10:** Lower panels: Single-pass phase shift  $\varphi_{\text{sp}}$  acquired as a function of the intensity for three different carrier wavelengths and pulse durations (but equal number of field oscillations) in a xenon, argon and neon gas target (from left to right). With identical gas parameters and for most intensities shorter driving wavelengths are disadvantageous for reaching higher intensities. Upper panels: corresponding cut-off energies for HHG with the three laser systems in the corresponding gas targets.

pass HHG experiments the conversion efficiency strongly increases for shorter driving wavelengths ( $\propto \lambda^{-5 \dots -6}$ ), in a cavity based experiment this will most likely be outweighed by the lower attainable peak-intensity and the higher ionization levels, that can impair the phase matching conditions (see Section 2.3.2).

### 5.4.3 Repetition rate scaling

When changing the pulse repetition rate in the model, care needs to be taken, that all (implicit) assumptions about the plasma recombination are still reasonable. With the model being well validated for a repetition rate of  $\sim 80$  MHz, lower repetition rates should also be well described. Although to date there has only been one report on a HHG system working with a repetition rate above 100 MHz [61], increasing the repetition rate is interesting because such a laser system opens a way of increasing the XUV flux which is not restricted by the intensity clamping. This is, however, only viable as long as the steady-state plasma and neutral atoms in excited states have a tolerable influence on both the phase matching of the conversion process and the robustness of the stabilization system.

Our model of the recombination process assumes that the electron capture directly populates the ground state of the atoms, a simplification which is only valid for sufficiently long cavity round-trip times, and high electron temperatures [105, 106]. Hence, at very high repetition rates and in cavities with large focii, a population of neutral but excited atoms might

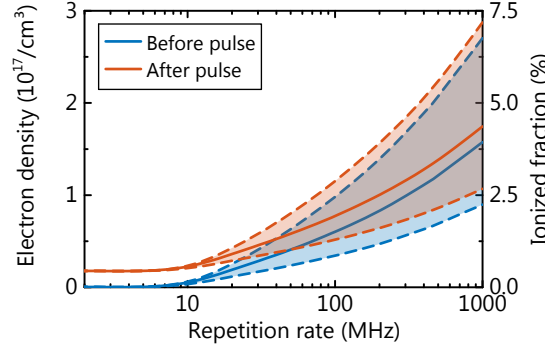


**Figure 5.11:** Electronic density before and after the pulse (solid lines) as a function of the repetition rate, keeping other parameters constant (in particular, pulse energy and peak intensity). Xe density:  $4 \times 10^{18}/\text{cm}^3$ , target length  $200 \mu\text{m}$ , intensity:  $4.3 \times 10^{13} \text{ W}/\text{cm}^2$ , focus radius:  $30 \mu\text{m}$ . The dashed lines bounding the shaded areas were calculated assuming a five times higher or lower value of  $\hat{b}$  in the recombination rate (see Eq. (5.8)). This again underlines the minor influence of  $\hat{b}$  on the steady-state ionization, because the latter changes only by  $\sim 50\%$ .

evolve. The effectively lower ionization energy would lead to a more pronounced clamping behavior. Moreover, the critical electron density for phase matching the HHG process might be at least temporally exceeded. This, however, could to some extent be relieved by a slightly higher gas pressure leading to a lower ionized fraction due to the clamped electron density. Although the finite recombination time and thus the increasing steady-state electronic density seem to set a fundamental barrier to increasing the pulse repetition rate, this is not the case as long as one can increase the rate of gas exchange. This can for instance be accomplished by use of a lighter gas (mass  $m$ ), or, by heating the gas prior to the expansion, because the gas velocity scales as  $\sqrt{k_B T/m}$  [101].

#### 5.4.4 Beyond standard-approach ECs

The tradeoff between intracavity intensity and cavity finesse (see Eq. (5.12)) raises the question whether parameters leading to record XUV conversion efficiencies in single-pass HHG experiments operating in the tight focusing regime [125, 185] can ever be reached in ECs at a reasonable power enhancement. With our experimentally validated model this question can be addressed, and strategies which for instance involve a EC in a non-steady-state regime can be simulated. Here, we will focus on optics customized to optimize an EC for a nonlinear interaction as an example for illustrating the potential of the model.

Contrary to the usual strategy, our idea towards an optimized nonlinear EC is based on accounting for the nonlinearity right from the beginning, instead of optimizing the EC for its linear response first. Our approach can be subdivided into three steps. First, for given gas parameters and a given cavity configuration, we will presuppose the intracavity field prior to the nonlinear interaction,  $\tilde{\mathcal{A}}_{\text{cav,prior}}(\omega)$ . From this field, the pulse after the nonlinear interaction and the cavity round-trip immediately follows. Next, we compute the input pulse  $\tilde{\mathcal{A}}_{\text{in}}(\omega)$  by requiring the initial intracavity pulse to be a steady-state solution. In other words,

the fields must fulfill Eq. (5.3) that can be rearranged into:

$$\tilde{\mathcal{A}}_{\text{in}}(\omega) = \frac{1}{\sqrt{1 - R_{\text{ic}}(\omega)}} \left( \tilde{\mathcal{A}}_{\text{cav,prior}}(\omega) - \sqrt{R_{\text{ic}}(\omega)R_{\text{cav}}(\omega)} e^{i\phi(\omega)} \tilde{\mathcal{A}}_{\text{cav,post}}(\omega) \right). \quad (5.13)$$

In a second step, we will exploit a degree of freedom hidden in Eq. (5.13). One can adjust the input coupler reflectivity  $R_{\text{ic}}(\omega)$  in order to minimize the input pulse energy, which is proportional to  $\int |\tilde{\mathcal{A}}_{\text{in}}(\omega)|^2 d\omega$ . This minimization routine can conveniently be done independently for every value of  $\omega$  and, in principle, even analytically. Completing steps one and two, one has found an optimal input pulse for a given intracavity spectrum using a tailored input coupler reflectivity.

In a third step, the presupposed initial intracavity field is varied, and steps one and two are repeated. This variation can, for example, be aimed at maximizing the peak power enhancement or, it can be aimed at finding an optimal input spectrum that is close to the one is available in the experiment.

In a first example, we only carry out steps one and two by presupposing an intracavity pulse of Gaussian shape centered at a wavelength of  $1.04 \mu\text{m}$  and with a pulse duration of 16 fs. Cavity mirror designs based on complementary phase characteristics are used (see Fig. 7.1(b)). With these mirrors power enhancement factors exceeding 200 are possible (at least in theory) without nonlinearity with 16-fs input and intracavity pulses. With the intracavity nonlinearity (here, xenon) it is sufficient to pump the cavity in the long-wavelength region, in a comparatively narrow bandwidth, since the nonlinearity constantly transfers energy from the red part of the spectrum to the blue end. Therefore, the input pulse duration can be as long as 28 fs, while still maintaining 16-fs intracavity pulses at an intracavity peak intensity of  $8 \times 10^{13} \text{ W/cm}^2$  (Fig. 5.12(a)). In the case of a standard-approach input coupler of similar bandwidth and a laser with the same input pulse duration, a three times higher input peak power is required to reach the same intracavity peak intensity at significantly longer intracavity pulse durations (Fig. 5.12(b)).

In another example, we will demonstrate the above mentioned third step by manually varying the intracavity spectrum in order to maximize the peak power enhancement. The intracavity peak intensity is kept at  $8 \times 10^{13} \text{ W/cm}^2$ . At the same time, we require the input spectrum to be centered at a wavelength of  $1.05 \mu\text{m}$ , where laser systems are commonly available. Hence cavity mirrors with designs centered at around  $0.95 \mu\text{m}$  are used. Again, mirror designs with complementary phase characteristics are employed. As a starting point for the optimization we take a Gaussian intracavity spectrum as used in the last example.

With the optimized spectra shown in Fig. 5.13(a), a peak power enhancement surpassing 450 is possible at intracavity pulse durations of 10 fs and with incident pulses as long as 52 fs. In contrast, enhancing the same seeding laser spectrum to the same peak intensity in a standard-approach cavity, requires 10 times the incident power and results in considerably longer intracavity pulses (see Fig. 5.13(b)).

Comparing the optimized solution to a system with external pulse compression to  $\sim 10$  fs pulse durations seeding a standard-approach cavity of similar (broad) bandwidth, the (peak) power enhancement is around 50. Furthermore, the additional external pulse compression to the few cycle regime will be accompanied by losses and is far from being trivial at the envisaged average power levels.

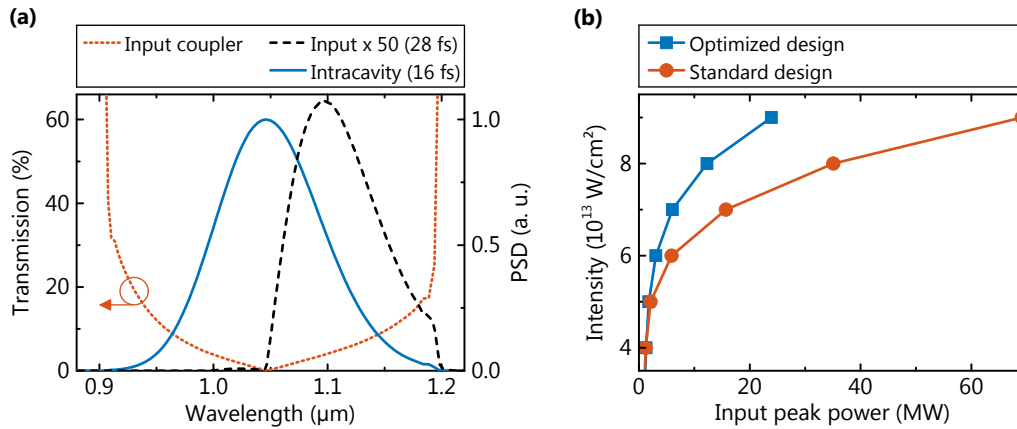


**Figure 5.12:** (a) Tailored input coupler transmission for best peak power enhancement at  $8 \times 10^{13} \text{ W/cm}^2$  peak intensity and corresponding intracavity and input spectrum (right y-axis). Note the reduced width of the input spectrum. (b) Comparison of the intensity in the focus of a cavity supporting 16-fs pulses with an optimized input coupler transmission to the same cavity with a standard-approach input coupler. For an targeted intensity an increase in peak power enhancement by a factor of three is possible. Focus radius:  $50 \mu\text{m}$ , Xe gas target length:  $400 \mu\text{m}$ , particle density:  $2.5 \times 10^{18}/\text{cm}^3$ .

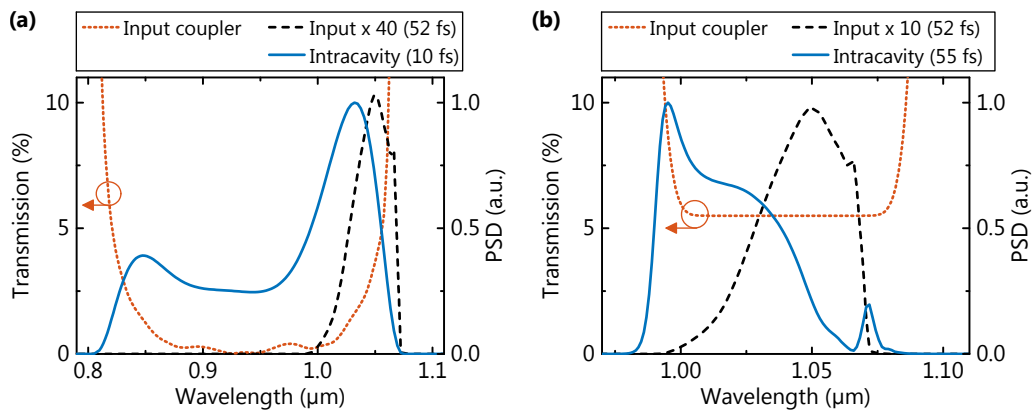


**Figure 5.13:** (a) Example of a tailored input coupler transmission for best peak power enhancement at  $8 \times 10^{13} \text{ W/cm}^2$  peak intensity and corresponding intracavity and input spectrum (right y-axis). Note the reduced width of the input spectrum. (b) The same input spectrum enhanced in a standard cavity requires a 10 times more powerful laser to reach the same peak intensity at 5 times longer intracavity pulses. Xe gas target length:  $400 \mu\text{m}$ , particle density:  $2.5 \times 10^{18}/\text{cm}^3$ .

The results outlined in this section are encouraging in the sense that phase-matched cavity-enhanced HHG can be done at similar intensities as in single-pass HHG experiments. Still, the realization of ECs with tailored optics for a specific intracavity nonlinearity is challenging. First of all, there is the challenge of manufacturing input couplers with the optimized transmission. Second, the required input spectrum that is calculated by the optimization routine should match the laser spectrum available in the laboratory as close as possible. Third, the obtained solutions must be stable with respect to fluctuations in the pulse parameters. This includes imperfect stabilization of the frequency comb to the cavity as well as power fluctuations or changes in the input spectrum. We verified in the example presented in Fig. 5.13 that the solution is stable against fluctuations of up to 8% of the input power and of the pulse duration, and against a shift of the carrier wavelength of several nanometers.

Another issue might arise from the build-up process, a challenge well-known from starting mode-locked oscillators. For pulse-compression ratios of two, as depicted in Fig. 5.12, this can be handled by setting the input comb parameters to specific values. Larger compression ratios as presented in Fig. 5.13 might require more sophisticated means. This could for instance be accomplished by a supplementary gas jet providing a gas with a lower ionization potential which increases the nonlinearity during the build-up process and which can later be turned off.

Despite the remaining challenges, the suggested strategy offers the prospect of a dramatically increased peak power enhancement accompanied with an intracavity pulse compression. In the above mentioned example this would boost the conversion efficiency by more than three orders of magnitude compared to a single-pass HHG experiment using the same driving laser. In the same sense, the optimized cavity would by far outperform the standard-approach cavity due to the much shorter intracavity pulses and the one order of magnitude higher power enhancement.

## 5.5 Conclusions

In this chapter, we have studied experimentally and theoretically the nonlinear interaction of laser pulses with a gas target in a high-finesse EC. This represents the first quantitative study of the nonlinear phase associated with the propagation of an ultrashort laser pulse through a nonlinear medium exploiting the sensitivity enhancement of more than two orders of magnitude provided by the resonator<sup>9</sup>. The improved measurement sensitivity allowed for the quantitative validation of a refined interaction model in a large parameter range.

The significance of this work is threefold: first, it establishes the combination of ECs with SSI as a highly sensitive measurement technique for nonlinear light-matter interactions in general. For instance, the methodology presented here can readily be applied to  $\chi^{(3)}$  nonlinearities in bulk dielectrics. In comparison to single-pass propagation, the dramatically improved sensitivity of the measurement to phase shifts enables a deeper insight in the underlying physical mechanisms of the nonlinear interaction. Furthermore, replacing the gas jet by a gas cell<sup>10</sup>, our setup could be used as a sensitive probe for ionization rates measured indirectly via the nonlinear phase shift.

---

<sup>9</sup>A complementary approach to studying the plasma dynamics in an EC has recently been reported on in [186].

<sup>10</sup>In a gas cell, the density distribution is homogeneous and can be much better controlled.

Second, we use the model derived here to formulate the first quantitative description of nonlinearity-induced enhancement limitations in fs-ECs. As all fs-EC-HHG systems reported to date employ cavity mirrors with a uniform spectral reflectivity, symmetric with respect to the input spectrum, a quantitative description of this limitation for these standard-approach ECs is of high practical importance. When used in conjunction with models for phase matching in HHG [184], it is possible to globally optimize the conversion efficiency to the XUV. The improved accuracy of our model will benefit numerous other experiments involving nonlinear conversion processes in gas targets such as THz generation in photoinduced plasmas and, thus, will pave the way to new coherent sources delivering ultrabroadband frequency combs ranging from the mid-IR to the far-IR [187].

Third, we address the question whether fs-EC can be operated beyond the intensity limitations exhibited by the standard approach. We show that tailoring the spectral reflectivities of EC mirrors and exploiting the spectral broadening induced by the intracavity nonlinearity is a viable route towards a dramatic increase in the peak power enhancement over standard-approach ECs. To the best of our knowledge, this finding represents the first viable route towards significantly surpassing the intensity limitations of state-of-the-art fs-EC and, therefore, reveals an enormous new potential of the fs-EC for high-power coherent XUV sources. In particular, a temporal compression of the intracavity pulse down to the few-cycle regime can be reached for parameters typical for phase-matched HHG. This will enable intracavity HHG experiments at similar laser pulse and gas parameters as state-of-the-art single-pass setups [185] but at significantly higher repetition rates and, thus, increased XUV output powers.



## 6 Cavities for zero phase slip pulse trains

In an EC, the round-trip phase  $\phi(\omega)$  defines the frequencies at which resonant enhancement occurs (see Eq. (2.2)). For maximum (integrated) power enhancement, both parameters of the frequency comb,  $\omega_{\text{rep}}$  and  $\omega_{\text{ceo}}$ , are matched to the values required by the cavity, in particular, to an optimal offset frequency (OOF). In HHG the generation of XUV bursts is triggered by the electric field of the driving pulse train. Thus, for the shot-to-shot stability of the generated XUV spectrum and for the precise synchronization of the XUV pulses to the of the driving field, it is a prerequisite to have driving pulses with identical electrical fields, that is, the pulse-to-pulse changes of the CEP must be 0 or  $\pi/2$ .

To efficiently enhance a comb with predefined offset frequency, it is not sufficient anymore, that the round-trip phase is linear in frequency over a broad bandwidth. The phase must also be offset from zero by a specific value. Although the concept of an OOF for the enhancement of a frequency comb in a external resonator is well known from experiments [12, 13, 63, 78], control of this parameter has not been reported so far. In the following chapter the concept of the OOF is introduced. We will demonstrate that setting the OOF of a broadband, high power cavity to zero can be achieved without sacrificing other prerequisites of intracavity as-pulse generation. For the experimental validation, a train of sub-30 fs pulses is enhanced to more than 3 kW intracavity average power, limited by the input power of the seed source. The most important findings of this chapter are presented in [69].

### 6.1 Optimal offset frequency

We have argued in Section 2.1.1 that for a given seeding spectrum, an EC dictates the pulse-to-pulse time delay  $\tau$  and the pulse-to-pulse CEP slip  $\Delta\phi_{\text{cep}}$ . An optimum of the enhancement (for example, for maximizing the intracavity power) is achieved, if the seeding pulse train matches both these parameters. Thus a frequency comb with  $\omega_{\text{rep}}/2\pi = 1/\tau$  and carrier-envelope offset frequency  $\omega_{\text{ceo}} = -(\Delta\phi_{\text{cep}}/2\pi) \omega_{\text{rep}}$  is required [78, 188].

This simple reasoning, however, implicitly assumes that the shape of the intracavity pulse remains unchanged after one round-trip. Otherwise, the pulse-to-pulse delay cannot be unambiguously defined. Preserving the pulse shape is ensured if the spectral power attenuation is constant and the group-delay dispersion in the resonator is identical to zero, leading to equidistantly spaced resonances. Here, the determination of the OOF is trivial. Although such an EC is highly desirable, it currently seems to be out of reach. Yet, it is empirically known that cavities have a well-defined OOF, as long as the input spectrum can be uniformly enhanced across most of its bandwidth. For this case, that is, for a sufficiently flat round-trip phase, we will show an elegant way to deduce the round-trip phase slip  $\Delta\phi_{\text{cep}}$  given a round-trip phase  $\phi(\omega)$  and a laser spectrum  $I(\omega)$ .

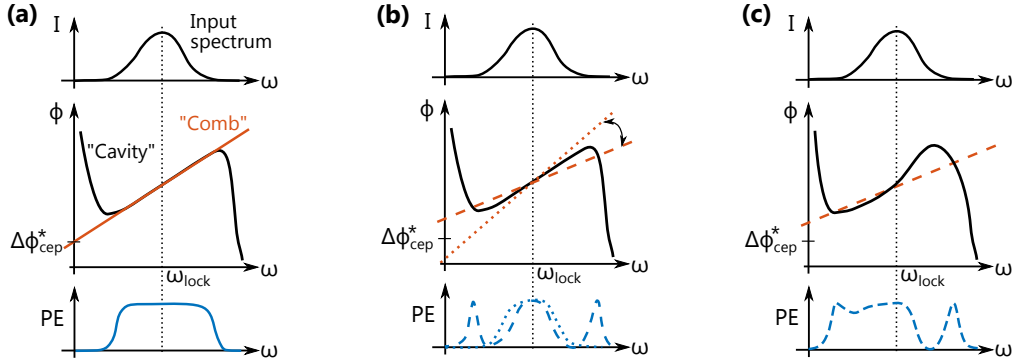


**Figure 6.1:** Graphical phase analysis in case of (a) optimal comb parameters, (b) too high or too low offset frequency and (c) in case of too high offset frequency and residual GDD in the resonator. Upper panels: input power spectrum. Center panels: sketch of the cavity round-trip phase and of the frequency comb. Lower panels: spectrally resolved power enhancement (PE).

### 6.1.1 Determination of the OOF

Given the (complex) electric field of a pulse  $\mathcal{E}(t)$  and its Fourier transform  $\tilde{\mathcal{E}}(\omega) \bullet \dashv \mathcal{E}(t)$ , one can investigate, how certain spectral phases acquired by the pulse, manifest themselves in the time domain. From Fourier theory, it is known that:

$$\tilde{\mathcal{E}}(\omega)e^{i\phi_0} \bullet \dashv \mathcal{E}(t)e^{i\phi_0} \quad \text{and} \quad \tilde{\mathcal{E}}(\omega)e^{-i\omega t_0} \bullet \dashv \mathcal{E}(t - t_0). \quad (6.1)$$

Thus, terms in the round-trip phase  $\phi(\omega)$  that are proportional to  $\omega$  merely delay the pulse and can be ignored. A constant term in  $\phi(\omega)$  changes the CEP. This suggests to Taylor-expand  $\phi(\omega)$  around a central frequency  $\omega_0$ . The resulting terms would, however, strongly depend on the choice of  $\omega_0$ . Instead, the  $\phi$ -intercept of a linear fit in  $\omega$  to  $\phi(\omega)$  with weights according to the reflected pulse spectrum constitutes the induced phase slip  $\Delta\phi_{\text{cep}}$ , while the slope represents the group delay  $\tau$ . Optimal enhancement in this resonator requires a seeding comb with parameters given by:

$$\omega_{\text{rep}}^* = 2\pi/\tau, \quad (6.2)$$

$$\omega_{\text{ceo}}^* = -(\Delta\phi_{\text{cep}}/2\pi)\omega_{\text{rep}}^*. \quad (6.3)$$

Hence, in Fig. 6.1 we identify the fitted straight line given by  $\phi_{\text{comb}}(\omega) = 2\pi(\omega - \omega_{\text{ceo}}^*)/\omega_{\text{rep}}^*$  with the optimal frequency comb. Note, that the round-trip phase is always only sampled at the comb lines  $\omega_n = n\omega_{\text{rep}} + \omega_{\text{ceo}}$ . At these frequencies, the straight line  $\phi_{\text{comb}}(\omega_n)$  always equals a multiple of  $2\pi$ . Thus, when evaluating the frequency-resolved power enhancement via equation Eq. (2.1),  $\phi(\omega_n)$  is equivalent to  $\phi(\omega_n) - \phi_{\text{comb}}(\omega_n)$ , which is the deviation from the fit. In this sense, one can graphically identify those spectral regions in which good power enhancement is ensured by the distance of the phase curve from the straight line.

The graphical phase analysis can also serve to explain the characteristic shapes of the spectral power enhancement in the case of too high or too low offset frequency of the seeding comb (see Fig. 6.1(b)). Keeping the central region of the input spectrum on resonance, for example, by deriving the error signal for the locking electronics in that spectral part, any

detuning of the offset frequency will significantly narrow the intracavity bandwidth. In the case of a too high offset frequency, additional side peaks appear in the spectrally resolved power enhancement at positions where the straight line representing the comb intersects with the round-trip phase curve<sup>1</sup>. Residual curvature of the phase in the central region would show up as a tilt in the spectral power enhancement (see Fig. 6.1(c)). In summary, if the round-trip phase is sufficiently linear over the bandwidth of the input pulse, then the integrated power enhancement traces out a curve with a clear maximum when sweeping the offset frequency of the seeding comb while keeping the central frequency of the comb on resonance [13, 63].

In fact, the approach presented above is just an approximation to maximizing the integrated power enhancement. It is valid in the case of small deviations of the round-trip phase from linearity (in  $\omega$ ) and also assumes a frequency independent power transmission of the input coupler. In this case, maximizing the integrated power enhancement (Eq. (2.1)) is equivalent to finding:

$$\min \left[ \sum_{\omega_n} I(\omega_n) \left| 1 - \sqrt{R_{\text{cav}}(\omega_n) R_{\text{ic}}(\omega_n)} e^{i\phi(\omega_n)} \right|^2 \right].$$

Here,  $I(\omega_n)$  is the input spectrum and serves as a weight function for the minimization. Using again constant input coupler reflectivity, this can be simplified to:

$$\max \left[ \sum_{\omega_n} I(\omega_n) \sqrt{R_{\text{cav}}(\omega_n)} \cos \phi(\omega_n) \right].$$

Using the fact that  $\phi_{\text{comb}}(\omega_n) = 2\pi n$  and assuming small deviations of the phase from linearity, we can omit higher order terms in the power series representation of the cosine term, leading to:

$$\min \left[ \sum_{\omega_n} I(\omega_n) \sqrt{R_{\text{cav}}(\omega_n)} [\phi(\omega_n) - \phi_{\text{comb}}(\omega_n)]^2 \right].$$

This equation mathematically describes the procedure of fitting a straight line to the phase curve with appropriate weights.

### 6.1.2 Tuning the optimal offset frequency

Tuning the cavity phase curve to achieve a desired value of  $\Delta\phi_{\text{cep}}$  is possible by manipulating three different contributions to  $\phi(\omega)$ . First, varying the focusing geometry of the resonator, directly changes the round-trip Gouy phase  $\phi_{m,n} = (m + 1/2)\Psi_{\text{tan}} + (n + 1/2)\Psi_{\text{sag}}$  which a transverse Gauss-Hermite mode of order  $m, n$  acquires per round-trip. Here,  $\Psi$  are the Gouy parameters, that can be derived from the resonator geometry (see Section 2.1.2). Despite the advantage of being continuously adjustable over a large range, the Gouy phase is of limited variability in most experiments, as it is directly linked to the cavity mode size. Note, that the Gouy phase is independent of the wavelength.

<sup>1</sup>This reasoning assumes quarter-wave stack like mirrors resulting in a characteristic shape of the round-trip phase as sketched in Fig. 6.1

Second, inserting a transparent material with a refractive index  $n(\omega)$  in the resonator, adds  $\omega\tau[n(\omega) - 1]$  to the phase curve. In principle, this can even be done without adding higher-order dispersion, for example, if a material with an index of refraction according to  $n(\omega) = c_1 + c_2/\omega$  with two constants  $c_1, c_2$  is employed. For such a refractive index,  $dn/d\omega \neq 0$  holds, and thus, the phase velocity differs from the group velocity, leading to a phase slipping underneath the envelope. The group velocity, however, is independent of frequency and, therefore, the pulse envelope remains unchanged upon propagation. In the vicinity of a material's zero-dispersion wavelength, the frequency dependence of the refractive index fulfills the above mentioned relations. In practice, this is difficult to achieve in a broad bandwidth and is likely to be in conflict with other experimental requirements, such as high vacuum, high damage threshold, polarization insensitivity, or low losses. Hence, usability of this handle is limited.

Third, and for the case of intracavity HHG most importantly, the phase upon reflection off the cavity mirrors can be tailored. This needs to be done without altering higher-order dispersion terms<sup>2</sup> or significantly lowering the damage threshold of the coating. To date, active control over this degree of freedom has not been demonstrated. In most applications, the group delay and phase shift induced by reflection off a multilayer coating can be readily compensated for by other elements. Thus, only the GDD and the reflectivity of the coating are specified as target functions for the design optimization algorithm and the group delay and the global phase offset remain as adjustable parameters in the optimization. Optimizing a multilayer structure to reach a predefined CEP shift requires major changes in the target function and in the design optimization algorithm. Details on the presumed approach are subject to a future publication.

The additional requirement for the target function can reduce the number of possible solutions in a given optimization problem. In the design of CEP-optimized mirrors for ECs, the additional constraint is partially relieved, because only the round-trip CEP shift is critical. This can be exploited in two ways. First, the distribution of the total round-trip phase shift on the input coupler and on the other cavity mirrors is irrelevant. Furthermore, assuming  $k$  identical cavity mirrors and a target value for their total CEP shift of  $\phi_\Sigma = k\phi_t$ , there are  $k$  different target values  $\phi_t$  for the coating, namely  $\phi_t = \phi_\Sigma/k + n2\pi/k$  with  $n$  being an integer value.

## 6.2 Experimental setup

In the following, particularities about the experimental setup and details on the customized CEP-controlled cavity mirrors are presented.

### 6.2.1 Overview of the experimental apparatus

A sketch of the experimental setup is depicted in Fig. 6.2. Either pulses with a duration of about 180 fs directly emitted by the CPA system or the nonlinearly broadened and compressed pulses were used. In the latter case, close-to-Fourier-limited pulses of 28 fs were available at a maximum output power of 20 W. Occasionally, stronger spectral broadening

---

<sup>2</sup>Second or higher order with respect to frequency.

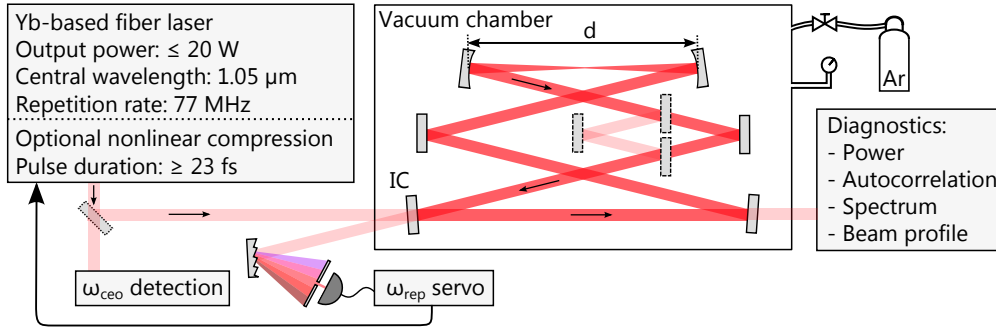


**Figure 6.2:** Experimental setup. The cavity configuration can be changed from a six mirrors to eight mirrors. The position in the stability range is varied by changing the separation  $d$  between the curved mirrors (radius of curvature: 600 mm).

was employed. Temporal compression down to 23 fs is achieved by decreasing the amount of negative GDD of the chirped mirror compressor either by reducing the number of bounces on the mirrors or by introducing fused silica plates with positive GDD.

The comb offset frequency of the oscillator was freely running with a typical linewidth of  $\sim 50$  kHz, rendering active stabilization unnecessary. In all experiments the RMS stability of the intracavity power was typically better than 0.25% in the range from 2.5 Hz to 5 MHz, limited by the free-running offset frequency of the laser. In this measurement campaign, input couplers with a transmission of 1% or 3% were used. In all cases the cavity is operated in the strongly overcoupled regime. Due to geometric constraints of the vacuum chamber, a minimum of six cavity mirrors is required in the experiment, although less cavity mirrors would increase the supported bandwidth. Two supplementary mirrors can be added without significantly changing the AOIs. This is needed when retrieving individual  $\Delta\phi_{\text{cep}}$  values of a mirror (at close to zero AOI). By changing the separation  $d$  between the curved mirrors while keeping the overall cavity length constant, the position of the cavity in the stability range can be varied. If not stated otherwise, the cavity is operated close to the inner edge of the stability range, ensuring nearly identical spot sizes on all mirrors.

### 6.2.2 Broadband coatings with controlled CEP-shift

For the broadband dielectric mirrors, coating designs based on quarter-wave stacks are employed. They provide low dispersion at a manageable design complexity and exhibit high damage thresholds. To maximize the bandwidth of the coatings,  $\text{Nb}_2\text{O}_5$  and  $\text{SiO}_2$  are chosen as coating materials due to their large contrast in the refractive indices [79]. The topmost layers of the coating deviate from quarter-wave thicknesses and serve as phase correctors. This leads to slight oscillations in their GDD (as apparent from the phase) and increases the spectral width, in which the phase deviates from linearity by less than 1 mrad, to 150 nm. Additionally, and even more important, this opens the possibility to vary the phase slip imprinted on the pulse upon reflection. For the experiment, we implemented two different designs named *A* and *B*, differing in  $\Delta\phi_{\text{cep}}$  by about 1 rad (with a slight dependency on the assumed laser spectrum). Figure 6.3 depicts the multilayer structure and the resulting spectrally resolved reflectivity and phase, including the calculated values of  $\Delta\phi_{\text{cep}}$ .

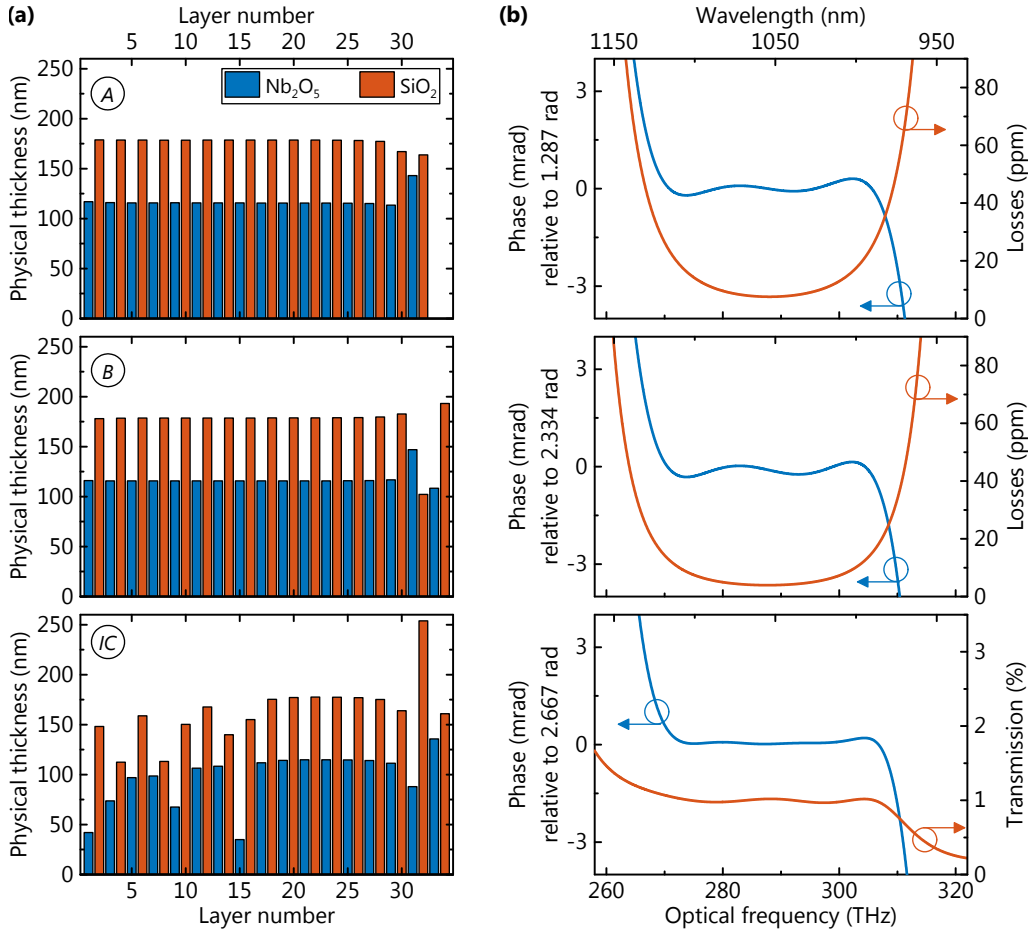


**Figure 6.3:** Specifications of multilayer coatings of the cavity mirrors *A*, *B* and one of the input couplers. (a) Thicknesses of oxide layers of the dielectric coatings. First layer refers to the first deposited layer on the fused silica substrate. (b) Calculated power transmission and phase shift upon reflection omitting the induced group delay for the designs shown in (a). Note that all panels in (b) share the frequency axis (bottom) and the corresponding wavelength axis (top).

For the input coupler, the multilayer coating design must significantly differ from a quarter-wave stack in order to assure a nearly constant transmission over the entire bandwidth. As it has been pointed out in Section 2.1.1 a close to wavelength independent reflectivity of a quarter-wave stack is only possible in the limit of zero transmission. On the one hand, the increased complexity of the multilayer design makes this coating more susceptible to systematic deposition errors in the coating production process. On the other hand, residual oscillations of the phase can be more efficiently suppressed.

All mirrors are designed for close-to-zero AOI. We verified with the designs and in the experiment, that a change in AOI of up to  $7^\circ$  does not alter the induced CEP shift. Furthermore, at small AOI the mirrors are not polarization discriminating. This is illustrated in Fig. 6.4, where the resonance peak separation between s and p polarization is plotted as a function of the AOI at five different wavelengths. Depending on the cavity finesse, this leads to a re-

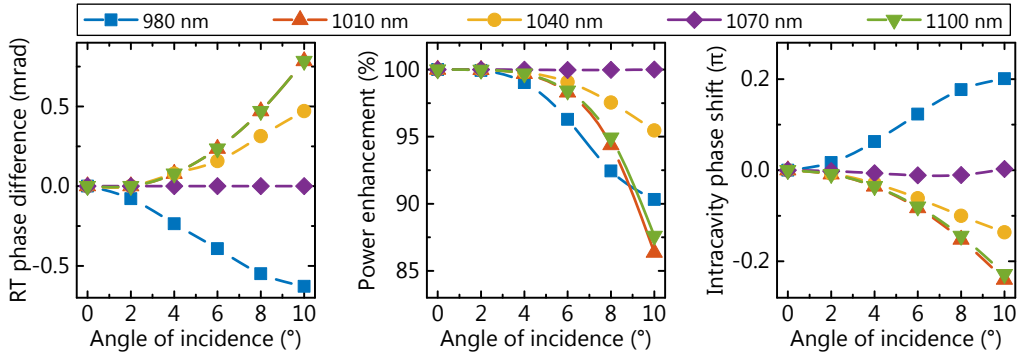


**Figure 6.4:** Polarization discrimination in a six mirror cavity using the mirror coatings of Fig. 6.3 as a function of the angle of incidence for five different wavelengths. Left panel: round-trip (RT) phase difference of s and p-polarized light. Center panel: effective power enhancement for circular polarized light relative to the nominal power enhancement of about 400 reached at zero AOI. Right panel: relative phase shift between the two orthogonal polarization components in case of identical power enhancement of the two components.

duced power enhancement and an overall phase shift between the orthogonal polarization components of the intracavity light. For AOI up to  $4^\circ$  and a six-mirror EC, the relative separation of the resonances is below 0.25 mrad. When equipped with a 1% transmission input coupler, the additional relative phase shift between the s and p light is well below  $\pi/20$  in a bandwidth of about 100 nm. The reduction in the power enhancement is negligible. Typically, ECs are operated with AOI on the mirrors below  $2^\circ$ . Hence, the enhancement of femtosecond pulses maintaining the (arbitrary) polarization state of the input pulses should be possible with the presented coating designs.

## 6.3 Experimental findings

In a first set of experiments, control over the OOF of a broadband cavity is demonstrated. In all experiments described in the next section, the input coupler with 1% transmission was employed. In Section 6.3.2 we present a second set of experiments dedicated to the intracavity average power scaling and the scaling of the intracavity bandwidth.

### 6.3.1 Controlling the optimal offset frequency

We determine the OOF of a cavity configuration by recording the steady-state power enhancement while locking the repetition rate of the input laser to the cavity for different comb offset frequencies. The error signal for the repetition rate lock is generated close to the carrier wavelength and, thus, the central part of the spectrum is always kept on resonance. Fig. 6.5(a) demonstrates the tunability of the OOF of a broadband EC by controlling the phase of the highly reflective cavity mirrors. To this end, we measured the OOF of the EC while stepwise replacing cavity mirrors of type A by mirrors of type B. A constant shift of the OOF is observed. In particular, an OOF of zero was measured, when only one mir-

ror of type *B* was employed. For all mirror combinations<sup>3</sup>, a power enhancement of more than 200 was reached with optimal comb parameters. Here, the full width at half the maximum (FWHM) of the intensity autocorrelation of the intracavity pulse was measured to be 43 fs, corresponding to a pulse duration of 30 fs assuming a deconvolution factor of 1.41 (see Fig. 6.5 (b)). Note that this optimal pulse duration was reached in all combinations of cavity mirrors.

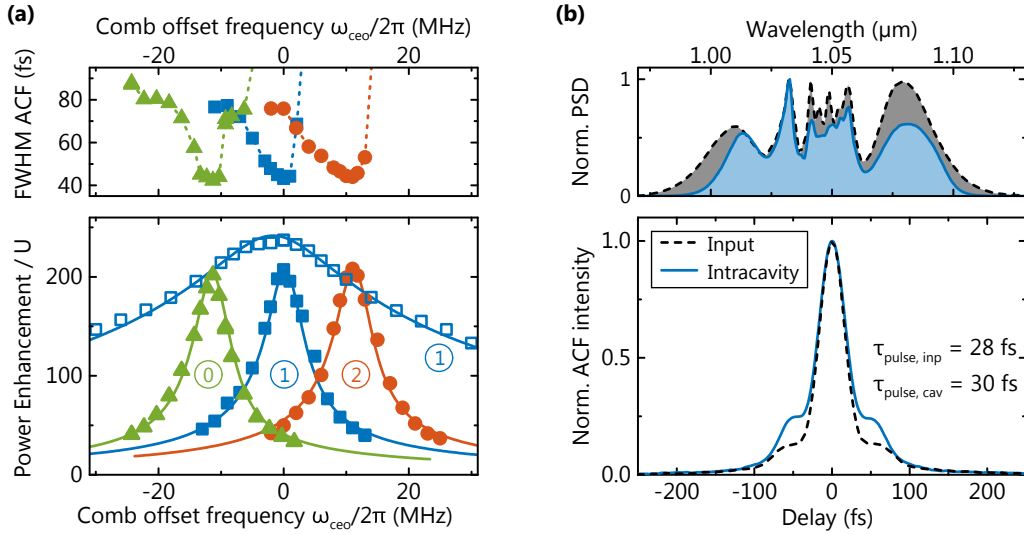


**Figure 6.5:** Controlling the OOF of the cavity by phase-tailored cavity mirrors. **(a)** Lower panel: power enhancement corrected for the spatial overlap ( $U$ ) vs. offset frequency of the seeding comb for a cavity employing 0, 1, or 2 mirrors of type *B* (indicated by the numbers). Solid symbols: broadband input pulses. Open symbols: input pulses of reduced bandwidth, illustrating the dependence of the OOF on the spectrum. Solid lines: corresponding model results. Upper panel: FWHM of the intensity autocorrelation recorded in the corresponding experiments. Dashed lines are a guide for the eye. **(b)** Intensity autocorrelation trace of the pulses in case of optimal comb parameters (lower panel) and corresponding normalized power spectral density (PSD) with 100 nm intracavity bandwidth at  $-10$  dB (upper panel).

Repeating the measurement of the OOF with pulses of a reduced spectral width of  $\sim 8$  nm confirms that the sensitivity of the cavity to the comb offset frequency strongly depends on the bandwidth of the pulses. The necessary precision in controlling the round-trip phase and the seeding laser phase noise scales with the bandwidth of the pulses and with the finesse. On closer inspection, the maxima of the two curves of identical cavity configuration probed with different input spectra, are slightly shifted. This highlights that the OOF is not a property of the resonator itself but also depends on the spectrum, whenever the round-trip phase slightly deviates from a perfectly linear dependence on  $\omega$ .

To quantify the CEP slip imprinted upon reflection off a single mirror, we inserted two supplementary mirrors and measured the change in OOF. When repeating this procedure for three combinations of the two additional mirrors, the resulting linear system of equations can be easily solved. The retrieved phase slip of a mirror of type *A* was 1.34 rad, and 2.25

<sup>3</sup>In the experiment, the broadest cavity bandwidth was reached by combining mirrors from two different coating runs. This effectively balanced small amounts of residual GDD by the mirrors.

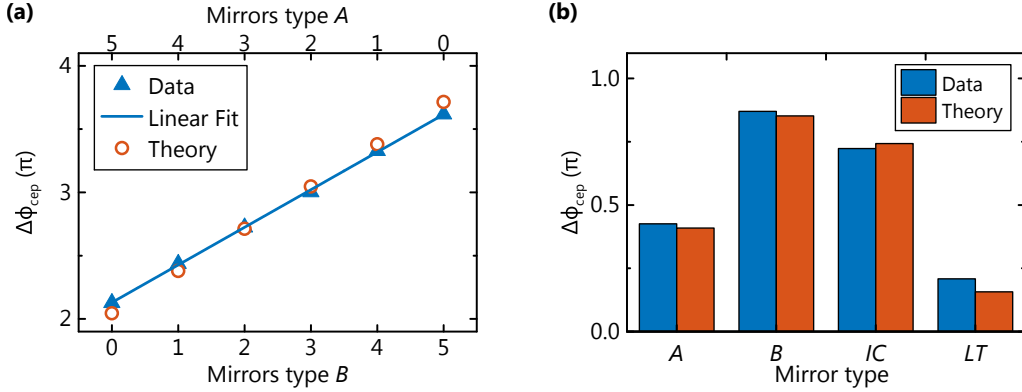


**Figure 6.6:** (a) Retrieved CEP-shift upon reflection off five cavity mirrors and calculated values from the coating design. (b) Comparison of CEP-shift upon reflection off a single mirror, of type A, B, the input coupler IC, and a commercially available broadband mirror labeled LT.

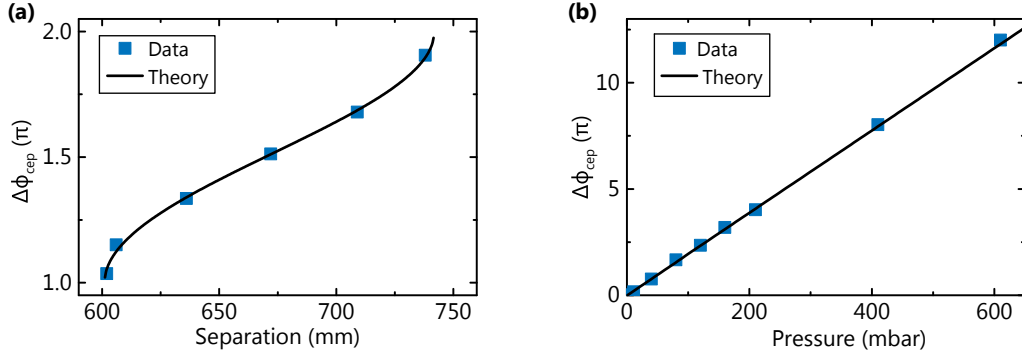


**Figure 6.7:** Dependence of the optimal pulse-to-pulse phase slip  $\Delta\phi_{\text{cep}}$  on (a) the resonator geometry by varying the separation between the curved mirrors and (b) on the argon pressure in the chamber. In (b), input pulses of  $\sim 8$  nm bandwidth were used to avoid spectral narrowing. In both cases a global offset was added to the data.

rad in case of type B. Both differ by less than 80 mrad from their design values. To proof that all mirrors from one coating run (A or B) are identical, we plot the measured phase differences and the expected ones in Fig. 6.6(a). The excellent linear fit to the data, which is also in good agreement with the calculated values, clearly validates the reproducibility. In Fig. 6.6(b) a comparison of the retrieved values of the CEP-shift from the expected values is given for several investigated mirrors.

In Fig. 6.7(a) the phase slip introduced by Gaussian beam propagation through free space is shown. By stepwise increasing the separation between the curved mirrors, we varied the position of the EC in the stability range and, thus, the Gouy parameter. For each cavity geometry we recorded the OOF. The experimental results excellently agree with theory. If the cavity mode size is not a critical parameter, the Gouy phase constitutes an option to fine-tune the OOF.

In Fig. 6.7(b) the dependence of the phase slip on the gas dispersion is plotted. By gradually introducing argon gas in the vacuum chamber one can widely tune the OOF. However,

the higher-order dispersion terms also lead to spectral narrowing of the intracavity spectrum. In the case of broadband, 30-fs pulses and for our finesse, about  $0.1 \text{ fs}^2$  of additional GDD is tolerable without sacrificing the intracavity pulse duration. Given the dispersion of argon this transfers to about 3 mbar of tolerable gas pressure and thus a maximal shift in  $\Delta\phi_{\text{cep}}$  of about  $0.06\pi$ . Similarly, the insertion of, for example, a pair of thin sapphire wedges ( $< 4 \mu\text{m}$ ) is tolerable and would allow for a phase tunability of  $0.15\pi$ . A robust implementation of such a thin wedge was demonstrated by optically contacting it to a mirror [129].

### 6.3.2 Power and bandwidth scaling

In a second set of experiments, we address the limits in terms of the intracavity power and the intracavity pulse duration. To this end, the compressed 28-fs pulses of the laser are attenuated, and subsequently enhanced in the cavity. In Fig. 6.8(a) the measured values of the intracavity power are plotted versus the input power showing the expected linear dependency. Using the full input power of the laser, the intracavity average power surpassed 3 kW with 30-fs intracavity pulses.

To investigate the limits of the supported spectral bandwidth of this cavity, we stepwise increase the power in the nonlinear fiber broadening stage and, thus, vary the spectrum sent to the cavity. The recorded input and intracavity spectra are shown in Fig. 6.8(b). Here, we are only interested in the enhanced spectral bandwidth and the overall power enhancement. Therefore, the input pulses were not temporally compressed, and the corresponding FL pulse duration is quoted instead. Spectral narrowing starts to become noticeable for intracavity spectra with a FL of about 35 fs and is pronounced at 30 fs. At this point, the power enhancement is diminished by 15% (see Fig. 6.8(c)). Even broader input spectra led to a slightly shorter FL of the spectrum in the cavity, however, at significantly reduced power enhancement.

Enhancing even broader spectra in a cavity given the same single round-trip phase is only possible by reducing the cavity finesse. To this end, we employed an input coupler with a three times higher transmission. Here, intracavity pulse durations below 25 fs were obtained at average powers exceeding 1 kW, limited by the power of the seed source. In Fig. 6.9 the autocorrelation trace and the recorded spectra are shown.

The damage threshold of the mirror coating was determined to be on the order of  $1 \times 10^{11} \text{ W/cm}^2$  using a spot size of  $200 \mu\text{m}$  at pulse durations of 30 fs. This is in good agreement with measurements performed in [81]. Owing to spatial inhomogeneities in the multilayer coating, it can be assumed, that the damage threshold will be reduced when using a larger spot size. In a cavity configuration with nearly identical spot sizes on the mirrors, this argument is even more important, due to the increased effectively irradiated area.

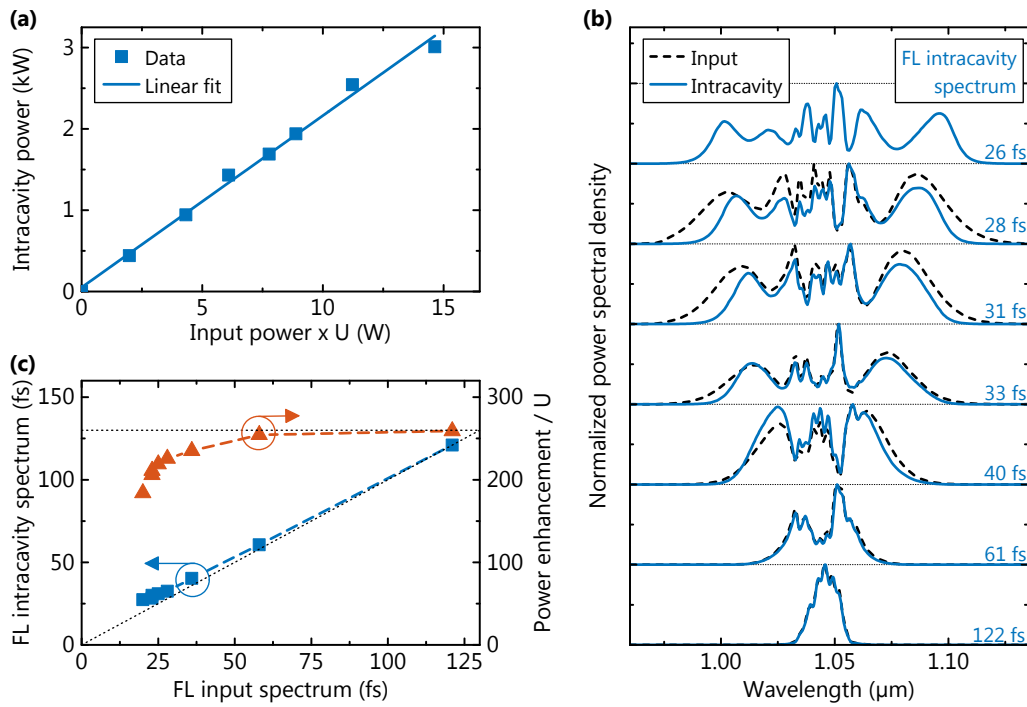


**Figure 6.8:** (a) Scaling of the intracavity power with respect to the incident power with 30-fs intracavity pulses and an input coupler transmission of 1%. (b) Evolution of the input and intracavity spectra for increasing power in the fiber-broadening stage. The FL of the intracavity spectrum is quoted. (c) Extracted from the data presented in (b): FL of the intracavity spectrum as a function of the FL of the input spectrum along with the recorded power enhancement. The dashed and dotted lines are guides for the eye, indicating that the limit in terms of bandwidth at this cavity finesse is reached with pulses of about 30 fs.

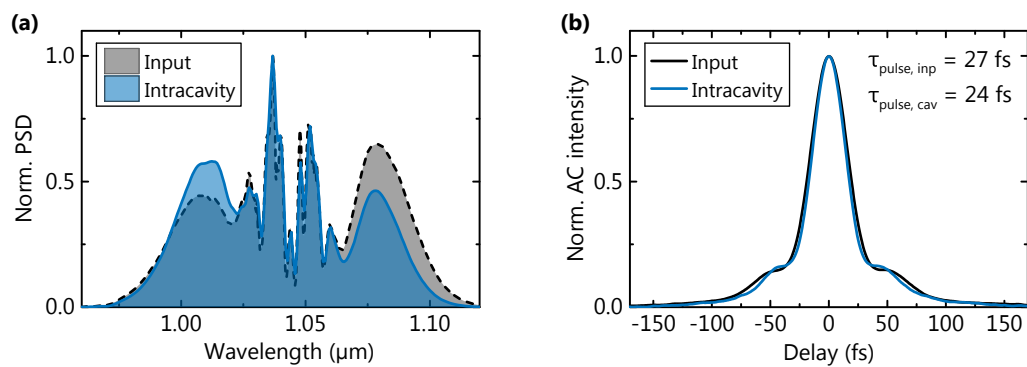


**Figure 6.9:** Increasing the intracavity bandwidth by using an input coupler with a transmission of 3%. (a) Input and intracavity spectrum and (b) measured autocorrelation signal revealing an intracavity pulse duration of 25 fs. Note that the input pulse was not fully compressed to its Fourier limit, resulting in a slightly longer input pulse duration despite the broader input spectrum.

## 6.4 Conclusions and outlook

Although the generation of as-pulses or attosecond pulse trains via HHG does not per se require a field stable driving pulse train, synchronization of the driving field envelope to the XUV bursts is only possible with a phase stable driving field pulse train. When single isolated as-pulses are required, for example, for pump-probe experiments aimed at probing atomic processes with sub-fs timing resolution [33, 34, 43, 189–191], the CEP phase must take a specific value in order to guarantee identical replica of the as-pulses [192]. Hence, a driving pulse train with zero pulse-to-pulse CEP slip is required. In the case of cavity-enhanced as-pulse generation, the cavity must support such a driving pulse train. Additionally, the cavity should support broadband pulses at a high damage threshold and it should not impose any further constraints that might conflict with the propagation of the harmonics or possible strategies for gating the harmonic emission.

In this chapter, we have succeeded in meeting these challenges, by designing, producing and characterizing low-loss, broadband mirrors, that shift the CEP of a pulse upon reflection in a controlled way. To the best of our knowledge, this is the first demonstration of the control over this degree of freedom of the mirror phase. Through careful design, neither the bandwidth nor the damage threshold of the mirrors is compromised by the additional “control knob”. Using these phase-controlled mirrors, we operated a high-finesse, non-polarization-discriminating EC that supports pulses of 30 fs at a power enhancement of 200, with vanishing pulse-to-pulse phase slip. The intracavity average power was measured to exceed 3 kW, limited by the available input power. These results underline the huge potential of nonlinearly broadened and compressed Yb-based laser systems as seed sources to obtain multi-kW level pulses of sub-30-fs duration in passive EC. In addition, for the first time, these pulse parameters and the polarization insensitivity fulfill the prerequisites for the generation of isolated attosecond pulses in ECs via gating mechanisms restricting the XUV emission process to a single event per driving pulse [171, 172].

When polarization insensitivity is not a prerequisite, including a cavity mirror under grazing incidence could enable the fine tunability of the resulting intracavity phase slip by varying the AOI. In Fig. 6.10 the phase upon reflection of such a mirror design is shown for two different AOI, highlighting that the bandwidth merely changes, but the induced CEP slip can be varied by approximately 0.3 rad.

The here demonstrated technological know-how will have significant impact well beyond intracavity HHG. One potential application also requiring a zero-OOF cavity is the enhancement of frequency combs generated via difference-frequency mixing of spectral components originating from the same comb, a process that intrinsically sets  $\omega_{\text{ceo}}$  to zero [193, 194]. Such a source is highly desirable and would greatly benefit high-repetition-rate spectroscopic schemes for mid-infrared vibrational spectroscopy [193, 195]. Furthermore, our results establish ECs as a simple yet powerful tool to determine the CEP shift imposed on the pulse upon propagation or reflection. This would otherwise require streaking measurements [36, 72].

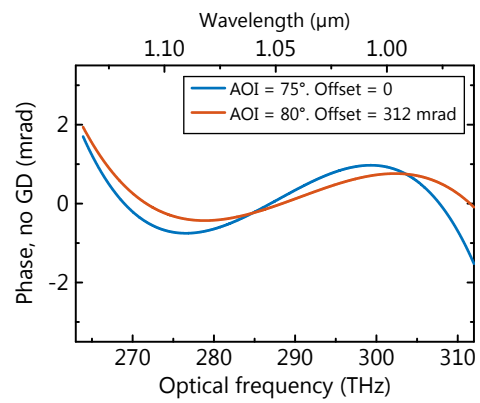


**Figure 6.10:** Phase upon reflection of a mirror similar to the ones used in this chapter, designed to operate under grazing incidence, though. By changing the AOI the phase curve essentially shifts in the vertical direction, that is, acts on the CEP but does not significantly affect the GDD.



## 7 Outlook

HHG driven by visible or near-infrared lasers has become the standard approach for obtaining XUV radiation with high spatial and temporal coherence from a table-top setup. By succeeding in restricting the emission process to a single event per driving pulse, the era of attosecond metrology was entered in 2001 [33], and since then has provided us with a magnifying glass and a steering wheel for fundamental processes in matter which unfolds on this ultrafast time scale [72–74].

Extending HHG to the regime of repetition rates of several tens of MHz opens the door to new classes of experiments and, thus, a tremendous impact on the fields of attosecond physics and frequency metrology is expected. For example, experiments revealing the dynamics of localized plasmonic fields ask for simultaneous spatial and temporal resolution. With space charge effects limiting the number of XUV photons per pulse, such experiments are impracticable with standard HHG sources<sup>1</sup> [46]. HHG with MHz-repetition rates also has the potential to advance the field of precision frequency metrology, for instance, via direct frequency comb spectroscopy in the XUV [61]. Currently, the most promising approach for the required XUV source is based on cavity-enhanced HHG, and first experiments in the wavelength region above 50 nm have recently been demonstrated [31, 61, 196–198].

The efforts to advancing the source presented in this thesis are under continuation at our institute. Three different EC setups are based on findings presented in this thesis.

The first experiment is aimed at an additional increase of the intracavity power (and thus the HHG flux) at similar pulse durations. Here, the laser system provides about an order of magnitude more average power [131] than that available in the presented work. The cavity is set up in a thermally robust geometry with even larger mode radii [84, 199], and the laser-machined output couplers have been tremendously improved (with regards to shell breaks).

The second experiment is dedicated to a further increase of the cavity bandwidth by using mirrors with complementary-phase characteristics [200, 201]. In this approach, the cavity comprises two types of mirrors, one with positive GDD and the other with negative GDD with a transmission below 0.1 % (see Fig. 7.1(a)). The round-trip phase of such an ultra-broadband complementary-phase six-mirror cavity is plotted in Fig. 7.1(b). It exhibits residual oscillations of about 2 mrad peak-to-peak, extending over a bandwidth of more than 270 nm. When equipped with an input coupler of 1 % transmission, this cavity supports pulses as short as 13 fs at a power-enhancement factor of 250. First tests of these mirrors in the EC-setup used in this thesis are ongoing during the writing of this work.

The third project combines the current developments to build a reliable cavity-based HHG source which generates enough photon flux to attempt the first time domain applications

---

<sup>1</sup>Here, it is implicitly assumed that data can be acquired with MHz repetition rates. This is, however, just a technical challenge that can, in principle, be met. Ultimately, the relaxation time of the sample and its damage threshold (in terms of average power) will set the limit for the repetition rate.

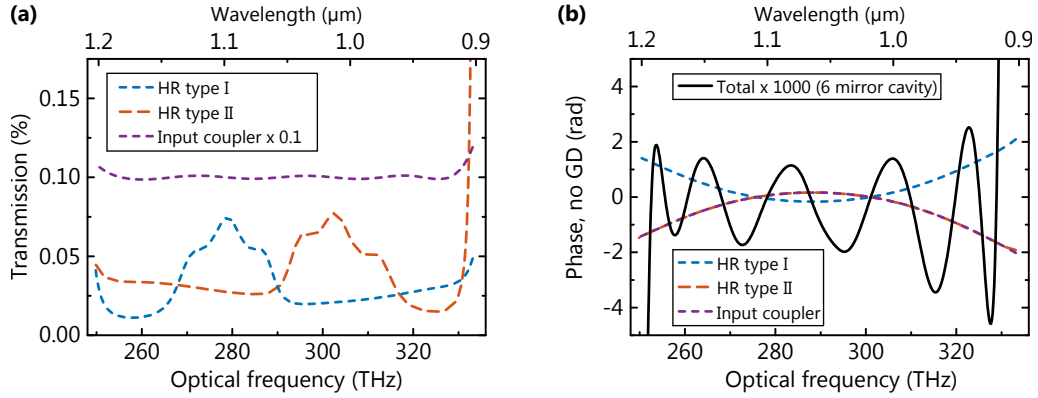


**Figure 7.1:** Ultra-broadband cavity mirror design with two types of highly reflecting (HR) mirrors that have a complementary phase characteristic. **(a)** Transmission and **(b)** phase characteristics. In **(b)** we also show the round-trip phase of a six-mirror cavity showing residual oscillations on the mrad level.

with fs or even sub-fs resolution at MHz repetition rates. Here, a state-of-the-art coherently-combined fiber laser system [119, 202] delivers CEP stable pulses that are nonlinearly compressed in Kagome-type fibers and subsequently enhanced in a 40-MHz EC. The geometrically output coupled XUV radiation will be used to investigate micro-to-nanoscale objects with a photoemission electron microscope [46, 190, 203]. We are confident that the pulse parameters demonstrated here in conjunction with the flexibility of our resonators will permit the generation of isolated attosecond pulses in ECs via mechanisms that restrict the XUV emission process to a single event per driving pulse [171, 172].

In addition to their relevance for high-photon-energy and high-repetition-rate HHG, the demonstrated parameters, the theoretical modeling and the measurement techniques introduced have implications for the field of nonlinear optics in a wider sense. One possible application would be intracavity-intrapulse difference frequency generation in a medium with a  $\chi^{(2)}$ -nonlinearity affording a broadband high-power source emitting in the mid-infrared. State-of-the-art coherent sources in this spectral region suffer either from a narrow bandwidth or low average power (see [193] and references therein). With cavity-enhanced difference frequency generation one could trade single pass conversion efficiency for increased bandwidth by using thinner nonlinear crystals [194], because nonconverted fundamental light is effectively reused. The feasibility of mirrors with controlled phase slip offers a convenient solution for the enhancement of seed sources with a predetermined offset frequency, for instance, due to difference-frequency generation [204], or due to external-cavity CEP-stabilization [143, 144]. The cavity-enhanced phase measurement technique is readily applicable to the investigation of nonlinearly acquired phase shifts in dielectrics. From such a measurement one can trace back the polarization response of the medium, which is directly linked to the free carriers generated in the material, as recently demonstrated with XUV transient absorption spectroscopy [205] and streaking measurements of the transmitted light field [206].

Apart from these prospects, there are of course many more paths into which the presented work can be directed. The unique parameter regime accessible in ECs can be exploited for colliding photons with electrons (inverse Compton scattering) to generate a beam of highly-

---

brilliant hard X-rays in a laboratory-scale setup [207, 208]. Additionally, there are schemes using ECs as temporal pulse combiners to effectively reduce the repetition rate and increase the pulse energy of a high-power laser source [209–211]. In conclusion, despite—or maybe because of its conceptional simplicity—a passive optical resonator excited by an (amplified) laser oscillator will continue to be a versatile tool and an indispensable component for many sources of coherent radiation to explore physics on almost any time and length scale.



## List of Acronyms

<b>ADK</b>	Ammosov-Delone-Krainov
<b>AM</b>	amplitude modulation
<b>AOI</b>	angle of incidence
<b>AOM</b>	acousto-optical modulator
<b>ASE</b>	amplified spontaneous emission
<b>CCD</b>	charge-coupled device
<b>CEO</b>	carrier-envelope offset
<b>CEP</b>	carrier-envelope phase
<b>CPA</b>	chirped pulse amplification
<b>EC</b>	enhancement cavity
<b>FFT</b>	fast Fourier transform
<b>FL</b>	Fourier limit
<b>FWHM</b>	full width at half the maximum
<b>GD</b>	group delay
<b>GDD</b>	group delay dispersion
<b>GH</b>	Gauss-Hermite
<b>GVD</b>	group velocity dispersion
<b>HHG</b>	high-order harmonic generation
<b>IR</b>	infrared
<b>KGW</b>	Potassium Gadolinium Tungstate
<b>OC</b>	output coupling
<b>OOF</b>	optimal offset frequency
<b>PCF</b>	photonic crystal fibre
<b>PM</b>	phase modulation

<b>PSD</b>	power spectral density
<b>PPT</b>	Perelomov-Popov-Terent'ev
<b>PZT</b>	piezo electric transducer
<b>RBW</b>	resolution bandwidth
<b>RMS</b>	root mean square
<b>ROC</b>	radius of curvature
<b>SESAM</b>	semiconductor saturable absorber mirror
<b>SSI</b>	spatial-spectral interferometry
<b>SPM</b>	self-phase modulation
<b>SSM</b>	simple-slit-mode
<b>TDSE</b>	time-dependent Schrödinger equation
<b>XUV</b>	extreme ultra-violet

## Bibliography

- [1] M. Planck, “Ueber irreversible Strahlungsvorgänge,” *Ann. Phys.* **306**, 69–122 (1900).
- [2] M. Planck, “Ueber das Gesetz der Energieverteilung im Normalspectrum,” *Ann. Phys.* **309**, 553–563 (1901).
- [3] D. Giulini and N. Straumann, “100 Jahre Quantenphysik: „...ich dachte mir nicht viel dabei...“: Plancks ungerader Weg zur Strahlungsformel,” *Physik Journal* **56**, 37–41 (2000).
- [4] R. Levy and S. B. Cohn, “A history of microwave filter research, design, and development,” *IEEE Trans. Microw. Theory Tech.* **32**, 1055–1067 (1984).
- [5] J. P. Gordon, H. J. Zeiger, and C. H. Townes, “The maser—new type of microwave amplifier, frequency standard, and spectrometer,” *Phys. Rev.* **99**, 1264–1274 (1955).
- [6] A. L. Schawlow and C. H. Townes, “Infrared and optical masers,” *Phys. Rev.* **112**, 1940–1949 (1958).
- [7] T. H. Maiman, “Stimulated optical radiation in ruby,” *Nature* **187**, 493–494 (1960).
- [8] M. T. Murphy, T. Udem, R. Holzwarth, A. Sizmman, L. Pasquini, C. Araujo-Hauck, H. Dekker, S. D’Odorico, M. Fischer, T. W. Hänsch, and A. Manescau, “High-precision wavelength calibration of astronomical spectrographs with laser frequency combs,” *M. Not. R. Astron. Soc.* **380**, 839–847 (2007).
- [9] T. Steinmetz, T. Wilken, C. Araujo-Hauck, R. Holzwarth, T. W. Hänsch, L. Pasquini, A. Manescau, S. D’Odorico, M. T. Murphy, T. Kentischer, W. Schmidt, and T. Udem, “Laser frequency combs for astronomical observations,” *Science* **321**, 1335–1337 (2008).
- [10] P. Zalicki and R. N. Zare, “Cavity ring-down spectroscopy for quantitative absorption measurements,” *J. Chem. Phys.* **102**, 2708 (1995).
- [11] G. Berden, R. Peeters, and G. Meijer, “Cavity ring-down spectroscopy: experimental schemes and applications,” *Int. Rev. Phys. Chem.* **19**, 565–607 (2010).
- [12] F. Adler, M. J. Thorpe, K. C. Cossel, and J. Ye, “Cavity-enhanced direct frequency comb spectroscopy: technology and applications,” *Annu. Rev. Anal. Chem.* **3**, 175–205 (2010).
- [13] A. Schliesser, C. Gohle, T. Udem, and T. W. Hänsch, “Complete characterization of a broadband high-finesse cavity using an optical frequency comb,” *Opt. Express* **14**, 5975 (2006).
- [14] T. J. Hammond, A. K. Mills, and D. J. Jones, “Simple method to determine dispersion of high-finesse optical cavities,” *Opt. Express* **17**, 8998–9005 (2009).

- [15] I. Pupeza, X. Gu, E. Fill, T. Eidam, J. Limpert, A. Tünnermann, F. Krausz, and T. Udem, “Highly sensitive dispersion measurement of a high-power passive optical resonator using spatial-spectral interferometry,” *Opt. Express* **18**, 26184–26195 (2010).
- [16] C. Gohle, B. Stein, A. Schliesser, T. Udem, and T. W. Hänsch, “Frequency comb vernier spectroscopy for broadband, high-resolution, high-sensitivity absorption and dispersion spectra,” *Phys. Rev. Lett.* **99**, 263902 (2007).
- [17] S. A. Diddams, L. Hollberg, and V. Mbele, “Molecular fingerprinting with the resolved modes of a femtosecond laser frequency comb,” *Nature* **445**, 627–630 (2007).
- [18] H. Walther, Varcoe, Benjamin T H, B.-G. Englert, and T. Becker, “Cavity quantum electrodynamics,” *Rep. Prog. Phys.* **69**, 1325–1382 (2006).
- [19] S. Gröblacher, K. Hammerer, M. R. Vanner, and M. Aspelmeyer, “Observation of strong coupling between a micromechanical resonator and an optical cavity field,” *Nature* **460**, 724–727 (2009).
- [20] M. Aspelmeyer, T. J. Kippenberg, and F. Marquardt, “Cavity optomechanics,” *Rev. Mod. Phys.* **86**, 1391–1452 (2014).
- [21] D. Vitali, S. Gigan, A. Ferreira, H. R. Böhm, P. Tombesi, A. Guerreiro, V. Vedral, A. Zeilinger, and M. Aspelmeyer, “Optomechanical entanglement between a movable mirror and a cavity field,” *Phys. Rev. Lett.* **98**, 030405 (2007).
- [22] A. Abramovici, W. E. Althouse, R. W. P. Drever, Y. Gursel, S. Kawamura, F. J. Raab, D. Shoemaker, L. Sievers, R. E. Spero, K. S. Thorne, R. E. Vogt, R. Weiss, S. E. Whitcomb, and M. E. Zucker, “LIGO: the laser interferometer gravitational-wave observatory,” *Science* **256**, 325–333 (1992).
- [23] B. Willke et al., “The GEO 600 gravitational wave detector,” *Class. Quantum Grav.* **19**, 1377–1387 (2002).
- [24] G. M. Harry, “Advanced LIGO: the next generation of gravitational wave detectors,” *Class. Quantum Grav.* **27**, 084006 (2010).
- [25] R. Paschotta, P. Kürz, R. Henking, S. Schiller, and J. Mlynek, “82% efficient continuous-wave frequency doubling of 10.6  $\mu\text{m}$  with a monolithic  $\text{MgO}:\text{LiNbO}_3$  resonator,” *Opt. Lett.* **19**, 1325 (1994).
- [26] R. J. Jones and J. Ye, “Femtosecond pulse amplification by coherent addition in a passive optical cavity,” *Opt. Lett.* **27**, 1848–1850 (2002).
- [27] E. L. Falcão-Filho, C.-J. Lai, K.-H. Hong, V.-M. Gkortsas, S.-W. Huang, L.-J. Chen, and F. X. Kärtner, “Scaling of high-order harmonic efficiencies with visible wavelength drivers: a route to efficient extreme ultraviolet sources,” *Appl. Phys. Lett.* **97**, 061107 (2010).
- [28] C. Gohle, T. Udem, M. Herrmann, J. Rauschenberger, R. Holzwarth, H. A. Schuessler, F. Krausz, and T. W. Hänsch, “A frequency comb in the extreme ultraviolet,” *Nature* **436**, 234–237 (2005).
- [29] R. J. Jones, K. D. Moll, M. J. Thorpe, and J. Ye, “Phase-coherent frequency combs in the vacuum ultraviolet via high-harmonic generation inside a femtosecond enhancement cavity,” *Phys. Rev. Lett.* **94**, 193201 (2005).

- 
- [30] M. Bellini, C. Lyngå, A. Tozzi, M. B. Gaarde, T. W. Hänsch, A. L’Huillier, and C.-G. Wahlström, “Temporal coherence of ultrashort high-order harmonic pulses,” *Phys. Rev. Lett.* **81**, 297–300 (1998).
- [31] C. Benko, T. K. Allison, A. Cingöz, L. Hua, F. Labaye, D. C. Yost, and J. Ye, “Extreme ultraviolet radiation with coherence time greater than 1 s,” *Nature Photon.* **8**, 530–536 (2014).
- [32] E. Goulielmakis, M. Schultze, M. Hofstetter, V. S. Yakovlev, J. Gagnon, M. Uiberacker, A. L. Aquila, E. M. Gullikson, D. T. Attwood, R. Kienberger, F. Krausz, and U. Kleineberg, “Single-cycle nonlinear optics,” *Science* **320**, 1614–1617 (2008).
- [33] M. Hentschel, R. Kienberger, C. Spielmann, G. A. Reider, N. Milosevic, T. Brabec, P. Corkum, U. Heinzmann, M. Drescher, and F. Krausz, “Attosecond metrology,” *Nature* **414**, 509–513 (2001).
- [34] R. Kienberger, M. Hentschel, M. Uiberacker, C. Spielmann, M. Kitzler, A. Scrinzi, M. Wieland, T. Westerwalbesloh, U. Kleineberg, U. Heinzmann, M. Drescher, and F. Krausz, “Steering attosecond electron wave packets with light,” *Science* **297**, 1144–1148 (2002).
- [35] A. Baltuška, T. Udem, M. Uiberacker, M. Hentschel, E. Goulielmakis, C. Gohle, R. Holzwarth, V. S. Yakovlev, A. Scrinzi, T. W. Hänsch, and F. Krausz, “Attosecond control of electronic processes by intense light fields,” *Nature* **421**, 611–615 (2003).
- [36] E. Goulielmakis, M. Uiberacker, R. Kienberger, A. Baltuška, V. S. Yakovlev, A. Scrinzi, T. Westerwalbesloh, U. Kleineberg, U. Heinzmann, M. Drescher, and F. Krausz, “Direct measurement of light waves,” *Science* **305**, 1267–1269 (2004).
- [37] M. Uiberacker, T. Uphues, M. Schultze, A. J. Verhoef, V. Yakovlev, M. F. Kling, J. Rauschenberger, N. M. Kabachnik, H. Schröder, M. Lezius, K. L. Kompa, H.-G. Müller, M. J. J. Vrakking, S. Hendel, U. Kleineberg, U. Heinzmann, M. Drescher, and F. Krausz, “Attosecond real-time observation of electron tunnelling in atoms,” *Nature* **446**, 627–632 (2007).
- [38] P. Eckle, A. N. Pfeiffer, C. Cirelli, A. Staudte, R. Dorner, H. G. Müller, M. Buttiker, and U. Keller, “Attosecond ionization and tunneling delay time measurements in helium,” *Science* **322**, 1525–1529 (2008).
- [39] M. Schultze, M. Fiess, N. Karpowicz, J. Gagnon, M. Korbman, M. Hofstetter, S. Neppl, A. L. Cavalieri, Y. Komninos, T. Mercouris, C. A. Nicolaides, R. Pazourek, S. Nagele, J. Feist, J. Burgdorfer, A. M. Azzeer, R. Ernstorfer, R. Kienberger, U. Kleineberg, E. Goulielmakis, F. Krausz, and V. S. Yakovlev, “Delay in photoemission,” *Science* **328**, 1658–1662 (2010).
- [40] S. Neppl, R. Ernstorfer, A. L. Cavalieri, C. Lemell, G. Wachter, E. Magerl, E. M. Bothschafter, M. Jobst, M. Hofstetter, U. Kleineberg, J. V. Barth, D. Menzel, J. Burgdorfer, P. Feulner, F. Krausz, and R. Kienberger, “Direct observation of electron propagation and dielectric screening on the atomic length scale,” *Nature* **517**, 342–346 (2015).
- [41] M. F. Kling, C. Siedschlag, A. J. Verhoef, J. I. Khan, M. Schultze, T. Uphues, Y. Ni, M. Uiberacker, M. Drescher, F. Krausz, and M. J. J. Vrakking, “Control of electron localization in molecular dissociation,” *Science* **312**, 246–248 (2006).

- [42] E. Goulielmakis, Z.-H. Loh, A. Wirth, R. Santra, N. Rohringer, V. S. Yakovlev, S. Zherebtsov, T. Pfeifer, A. M. Azzeer, M. F. Kling, S. R. Leone, and F. Krausz, “Real-time observation of valence electron motion,” *Nature* **466**, 739–743 (2010).
- [43] F. Calegari, D. Ayuso, A. Trabattoni, L. Belshaw, S. d. Camillis, S. Anumula, F. Frassetto, L. Poletto, A. Palacios, P. Decleva, J. B. Greenwood, F. Martin, and M. Nisoli, “Ultrafast electron dynamics in phenylalanine initiated by attosecond pulses,” *Science* **346**, 336–339 (2014).
- [44] T. T. Luu, M. Garg, S. Y. Kruchinin, A. Moulet, M. T. Hassan, and E. Goulielmakis, “Extreme ultraviolet high-harmonic spectroscopy of solids,” *Nature* **521**, 498–502 (2015).
- [45] G. Vampa, T. J. Hammond, N. Thiré, B. E. Schmidt, F. Légaré, C. R. McDonald, T. Brabec, and P. B. Corkum, “Linking high harmonics from gases and solids,” *Nature* **522**, 462–464 (2015).
- [46] S. H. Chew, F. Süßmann, C. Späth, A. Wirth, J. Schmidt, S. Zherebtsov, A. Guggenmos, A. Oelsner, N. Weber, J. Kapaldo, A. Gliserin, M. I. Stockman, M. F. Kling, and U. Kleineberg, “Time-of-flight-photoelectron emission microscopy on plasmonic structures using attosecond extreme ultraviolet pulses,” *Appl. Phys. Lett.* **100**, 051904 (2012).
- [47] A. L. Cavalieri, N. Müller, T. Uphues, V. S. Yakovlev, A. Baltuška, B. Horvath, B. Schmidt, L. Blumel, R. Holzwarth, S. Hendel, M. Drescher, U. Kleineberg, P. M. Echenique, R. Kienberger, F. Krausz, and U. Heinzmann, “Attosecond spectroscopy in condensed matter,” *Nature* **449**, 1029–1032 (2007).
- [48] P. Wernet, J. Gaudin, K. Godehusen, O. Schwarzkopf, and W. Eberhardt, “Femtosecond time-resolved photoelectron spectroscopy with a vacuum-ultraviolet photon source based on laser high-order harmonic generation,” *Rev. Sci. Inst.* **82**, 063114 (2011).
- [49] G. Sansone, F. Kelkensberg, J. F. Perez-Torres, F. Morales, M. F. Kling, W. Siu, O. Ghafur, P. Johnsson, M. Swoboda, E. Benedetti, F. Ferrari, F. Lépine, J. L. Sanz-Vicario, S. Zherebtsov, I. Znakovskaya, A. L’Huillier, M. Y. Ivanov, M. Nisoli, F. Martín, and M. J. J. Vrakking, “Electron localization following attosecond molecular photoionization,” *Nature* **465**, 763–766 (2010).
- [50] B. Bergues, M. Kübel, N. G. Johnson, B. Fischer, N. Camus, K. J. Betsch, O. Herrwerth, A. Senftleben, A. M. Saylor, T. Rathje, T. Pfeifer, I. Ben-Itzhak, R. R. Jones, G. G. Paulus, F. Krausz, R. Moshhammer, J. Ullrich, and M. F. Kling, “Attosecond tracing of correlated electron-emission in non-sequential double ionization,” *Nat. Commun.* **3**, 813 (2012).
- [51] E. E. Eyler, D. E. Chieda, M. C. Stowe, M. J. Thorpe, T. R. Schibli, and J. Ye, “Prospects for precision measurements of atomic helium using direct frequency comb spectroscopy,” *Eur. Phys. J. D* **48**, 43–55 (2008).
- [52] M. Herrmann, M. Haas, U. D. Jentschura, F. Kottmann, D. Leibfried, G. Saathoff, C. Gohle, A. Ozawa, V. Batteiger, S. Knünz, N. Kolachevsky, H. A. Schüssler, T. W. Hänsch, and T. Udem, “Feasibility of coherent XUV spectroscopy on the 1S–2S transition in singly ionized helium,” *Phys. Rev. A* **79** (2009).

- 
- [53] D. Z. Kandula, C. Gohle, T. J. Pinkert, W. Ubachs, and K. S. E. Eikema, “Extreme ultraviolet frequency comb metrology,” *Phys. Rev. Lett.* **105**, 063001 (2010).
- [54] C. J. Campbell, A. G. Radnaev, and A. Kuzmich, “Wigner crystals of Th229 for optical excitation of the nuclear isomer,” *Phys. Rev. Lett.* **106**, 223001 (2011).
- [55] C. J. Campbell, A. G. Radnaev, A. Kuzmich, V. A. Dzuba, V. V. Flambaum, and A. Derevianko, “Single-ion nuclear clock for metrology at the 19th decimal place,” *Phys. Rev. Lett.* **108**, 120802 (2012).
- [56] A. D. Panov, “Quantitative conversion spectroscopy of the ultrasoft isomeric transition of uranium-235 and the electronic structure of uranium oxides,” *J. Exp. Theor. Phys.* **85**, 313–324 (1997).
- [57] I. Pupeza, T. Eidam, J. Rauschenberger, B. Bernhardt, A. Ozawa, E. Fill, A. Apolonski, T. Udem, J. Limpert, Z. Alahmed, A. Azzeer, A. Tünnermann, T. W. Hänsch, and F. Krausz, “Power scaling of a high-repetition-rate enhancement cavity,” *Opt. Lett.* **35**, 2052–2054 (2010).
- [58] D. C. Yost, T. R. Schibli, and J. Ye, “Efficient output coupling of intracavity high-harmonic generation,” *Opt. Lett.* **33**, 1099–1101 (2008).
- [59] O. Pronin, V. Pervak, E. Fill, J. Rauschenberger, F. Krausz, and A. Apolonski, “Ultra-broadband efficient intracavity XUV output coupler,” *Opt. Express* **19**, 10232–10240 (2011).
- [60] I. Pupeza, E. Fill, and F. Krausz, “Low-loss VIS/IR-XUV beam splitter for high-power applications,” *Opt. Express* **19**, 12108 (2011).
- [61] A. Cingöz, D. C. Yost, T. K. Allison, A. Ruehl, M. E. Fermann, I. Hartl, and J. Ye, “Direct frequency comb spectroscopy in the extreme ultraviolet,” *Nature* **482**, 68–71 (2012).
- [62] D. C. Yost, A. Cingöz, T. K. Allison, A. Ruehl, M. E. Fermann, I. Hartl, and J. Ye, “Power optimization of XUV frequency combs for spectroscopy applications [invited],” *Opt. Express* **19**, 23483–23493 (2011).
- [63] A. K. Mills, T. J. Hammond, M. H. C. Lam, and D. J. Jones, “XUV frequency combs via femtosecond enhancement cavities,” *J. Phys. B* **45**, 142001 (2012).
- [64] A. Ozawa, J. Rauschenberger, C. Gohle, M. Herrmann, D. R. Walker, V. Pervak, A. Fernandez, R. Graf, A. Apolonski, R. Holzwarth, F. Krausz, T. W. Hänsch, and T. Udem, “High harmonic frequency combs for high resolution spectroscopy,” *Phys. Rev. Lett.* **100**, 253901 (2008).
- [65] K. D. Moll, R. J. Jones, and J. Ye, “Nonlinear dynamics inside femtosecond enhancement cavities,” *Opt. Express* **13**, 1672–1678 (2005).
- [66] I. Pupeza, S. Holzberger, T. Eidam, H. Carstens, D. Esser, J. Weitenberg, P. Rußbüldt, J. Rauschenberger, J. Limpert, T. Udem, A. Tünnermann, T. W. Hänsch, A. Apolonski, F. Krausz, and E. Fill, “Compact high-repetition-rate source of coherent 100 eV radiation,” *Nature Photon.* **7**, 608–612 (2013).
- [67] I. Pupeza, M. Högner, J. Weitenberg, S. Holzberger, D. Esser, T. Eidam, J. Limpert, A. Tünnermann, E. Fill, and V. S. Yakovlev, “Cavity-enhanced high-harmonic generation with spatially tailored driving fields,” *Phys. Rev. Lett.* **112**, 103902 (2014).

- [68] S. Holzberger, N. Lilienfein, H. Carstens, T. Saule, M. Högner, F. Lücking, M. Trubetskov, V. Pervak, T. Eidam, J. Limpert, A. Tünnermann, E. Fill, F. Krausz, and I. Pupeza, “Femtosecond enhancement cavities in the nonlinear regime,” *Phys. Rev. Lett.* **115**, 023902 (2015).
- [69] S. Holzberger, N. Lilienfein, M. K. Trubetskov, H. Carstens, F. Lücking, V. Pervak, F. Krausz, and I. Pupeza, “Enhancement cavities for zero-offset-frequency pulse trains,” *Opt. Lett.* **40**, 2165 (2015).
- [70] H. N. Chapman and K. A. Nugent, “Coherent lensless X-ray imaging,” *Nature Photon.* **4**, 833–839 (2010).
- [71] M. Zürch, J. Rothhardt, S. Hädrich, S. Demmler, M. Krebs, J. Limpert, A. Tünnermann, A. Guggenmos, U. Kleineberg, and C. Spielmann, “Real-time and sub-wavelength ultrafast coherent diffraction imaging in the extreme ultraviolet,” *Sci. Rep.* **4**, 7356 (2014).
- [72] F. Krausz and M. Y. Ivanov, “Attosecond physics,” *Rev. Mod. Phys.* **81**, 163–234 (2009).
- [73] L. Gallmann, C. Cirelli, and U. Keller, “Attosecond science: recent highlights and future trends,” *Annu. Rev. Phys. Chem.* **63**, 447–469 (2012).
- [74] F. Krausz and M. I. Stockman, “Attosecond metrology: from electron capture to future signal processing,” *Nature Photon.* **8**, 205–213 (2014).
- [75] M. Theuer, D. Molter, K. Maki, C. Otani, J. A. L’huillier, and R. Beigang, “Terahertz generation in an actively controlled femtosecond enhancement cavity,” *Appl. Phys. Lett.* **93**, 041119 (2008).
- [76] W. Nagourney, *Quantum electronics for atomic physics* (Oxford University Press, 2010).
- [77] S. T. Cundiff, “Phase stabilization of ultrashort optical pulses,” *J. Phys. D* **35**, R43–R59 (2002).
- [78] L. Arissian and J.-C. Diels, “Investigation of carrier to envelope phase and repetition rate: fingerprints of mode-locked laser cavities,” *J. Phys. B* **42**, 183001 (2009).
- [79] S. A. Furman and A. V. Tikhonravov, *Basics of optics of multilayer systems* (Ed. Frontières, Gif-sur-Yvette, 1992).
- [80] M. Mero, J. Liu, W. Rudolph, D. Ristau, and K. Starke, “Scaling laws of femtosecond laser pulse induced breakdown in oxide films,” *Phys. Rev. B* **71** (2005).
- [81] I. B. Angelov, M. v. Pechmann, M. K. Trubetskov, F. Krausz, and V. Pervak, “Optical breakdown of multilayer thin-films induced by ultrashort pulses at MHz repetition rates,” *Opt. Express* **21**, 31453 (2013).
- [82] J. M. Kaster, I. Pupeza, T. Eidam, C. Jocher, E. Fill, J. Limpert, R. Holzwarth, B. Bernhardt, T. Udem, T. W. Hänsch, A. Tünnermann, and F. Krausz, “Towards MW average powers in ultrafast high-repetition-rate enhancement cavities,” in *Advances in Optical Materials* (2011), HFB4.
- [83] W. P. Putnam, D. N. Schimpf, G. Abram, and F. X. Kärtner, “Bessel-Gauß beam enhancement cavities for high-intensity applications,” *Opt. Express* **20**, 24429–24443 (2012).

- 
- [84] H. Carstens, S. Holzberger, J. Kaster, J. Weitenberg, V. Pervak, A. Apolonski, E. Fill, F. Krausz, and I. Pupeza, “Large-mode enhancement cavities,” *Opt. Express* **21**, 11606 (2013).
- [85] A. E. Siegman, *Lasers* (University Science Books, Sausalito, 1986).
- [86] J. Weitenberg, P. Rußbüldt, I. Pupeza, T. Udem, H.-D. Hoffmann, and R. Poprawe, “Geometrical on-axis access to high-finesse resonators by quasi-imaging: a theoretical description,” *J. Opt.* **17**, 025609 (2015).
- [87] N. Lilienfein, H. Carstens, S. Holzberger, C. Jocher, T. Eidam, J. Limpert, A. Tünnermann, A. Apolonski, F. Krausz, and I. Pupeza, “Balancing of thermal lenses in enhancement cavities with transmissive elements,” *Opt. Lett.* **40**, 843–846 (2015).
- [88] T. K. Allison, A. Cingöz, D. C. Yost, and J. Ye, “Extreme nonlinear optics in a femtosecond enhancement cavity,” *Phys. Rev. Lett.* **107**, 183903 (2011).
- [89] Larochelle, S F J, A. Talebpour, and S. L. Chin, “Coulomb effect in multiphoton ionization of rare-gas atoms,” *J. Phys. B* **31**, 1215–1224 (1998).
- [90] V. S. Popov, “Tunnel and multiphoton ionization of atoms and ions in a strong laser field (Keldysh theory),” *Phys. Usp.* **47**, 855–885 (2004).
- [91] C. J. Joachain, N. J. Kylstra, and R. M. Potvliege, *Atoms in intense laser fields* (Cambridge University Press, Cambridge, 2012).
- [92] M. V. Ammosov, N. B. Delone, and V. P. Krainov, “Tunnel ionization of complex atoms and of atomic ions in an alternating electromagnetic field,” *Sov. Phys. JETP* **64**, 1191–1194 (1986).
- [93] A. M. Perelomov, V. S. Popov, and M. V. Terent’ev, “Ionization of atoms in an alternating electric field,” *Sov. Phys. JETP* **23**, 924–934 (1966).
- [94] L. V. Keldysh, “Ionization in the field of a strong electromagnetic wave,” *Sov. Phys. JETP* **20**, 1307–1314 (1965).
- [95] G. L. Yudin and M. Y. Ivanov, “Nonadiabatic tunnel ionization: looking inside a laser cycle,” *Phys. Rev. A* **64**, 013409 (2001).
- [96] A. Scrinzi, M. Geissler, and T. Brabec, “Ionization above the coulomb barrier,” *Phys. Rev. Lett.* **83**, 706–709 (1999).
- [97] X. M. Tong and C. D. Lin, “Empirical formula for static field ionization rates of atoms and molecules by lasers in the barrier-suppression regime,” *J. Phys. B* **38**, 2593–2600 (2005).
- [98] M. Geissler, G. Tempea, A. Scrinzi, M. Schnürer, F. Krausz, and T. Brabec, “Light propagation in field-ionizing media: extreme nonlinear optics,” *Phys. Rev. Lett.* **83**, 2930–2933 (1999).
- [99] W. M. Wood, C. W. Siders, and M. C. Downer, “Measurement of femtosecond ionization dynamics of atmospheric density gases by spectral blueshifting,” *Phys. Rev. Lett.* **67**, 3523–3526 (1991).
- [100] D. R. Carlson, J. Lee, J. Mongelli, E. M. Wright, and R. J. Jones, “Intracavity ionization and pulse formation in femtosecond enhancement cavities,” *Opt. Lett.* **36**, 2991–2993 (2011).

- [101] G. Scoles, ed., *Atomic and molecular beam methods* (Oxford University Press, New York, 1988).
- [102] H. Pauly, *Atom, molecule, and cluster beams I: basic theory, production, and detection of thermal energy beams* (Springer, Berlin, 2000).
- [103] Y. B. Zel'dovič, Y. P. Rajzer, and W. D. Hayes, *Physics of shock waves and high-temperature hydrodynamic phenomena* (Dover Publications, Mineola and New York, 2002).
- [104] E. Hinnov and J. Hirschberg, "Electron-ion recombination in dense plasmas," *Phys. Rev.* **125**, 795–801 (1962).
- [105] L. Allen, D. G. C. Jones, and D. G. Schofield, "Radiative lifetimes and collisional cross sections for Xe I and II," *J. Opt. Soc. Am.* **59**, 842 (1969).
- [106] M. R. Bruce, W. B. Layne, C. A. Whitehead, and J. W. Keto, "Radiative lifetimes and collisional deactivation of two-photon excited xenon in argon and xenon," *J. Chem. Phys.* **92**, 2917 (1990).
- [107] P. Jaeglé, *Coherent sources of XUV radiation: soft X-ray lasers and high-order harmonic generation* (Springer Science+Business Media Inc, New York, 2006).
- [108] Y. Wang, E. Granados, M. A. Larotonda, M. Berrill, B. M. Luther, D. Patel, C. S. Menoni, and J. J. Rocca, "High-brightness injection-seeded soft-X-ray-laser amplifier using a solid target," *Phys. Rev. Lett.* **97**, 123901 (2006).
- [109] P. Zeitoun, G. Faivre, S. Sebban, T. Mocek, A. Hallou, M. Fajardo, D. Aubert, P. Balcou, F. Burgy, D. Douillet, S. Kazamias, G. d. Lachèze-Murel, T. Lefrou, S. Le Pape, P. Mercère, H. Merdji, A. S. Morlens, J. P. Rousseau, and C. Valentin, "A high-intensity highly coherent soft X-ray femtosecond laser seeded by a high harmonic beam," *Nature* **431**, 426–429 (2004).
- [110] R. W. Boyd, *Nonlinear optics*, 3rd ed. (Academic Press, Amsterdam, 2008).
- [111] K. C. Kulander and B. W. Shore, "Calculations of multiple-harmonic conversion of 1064-nm radiation in Xe," *Phys. Rev. Lett.* **62**, 524–526 (1989).
- [112] J. H. Eberly, Q. Su, and J. Javanainen, "Nonlinear light scattering accompanying multiphoton ionization," *Phys. Rev. Lett.* **62**, 881–884 (1989).
- [113] P. Corkum, "Plasma perspective on strong field multiphoton ionization," *Phys. Rev. Lett.* **71**, 1994–1997 (1993).
- [114] M. Lewenstein, P. Salières, and A. L'Huillier, "Phase of the atomic polarization in high-order harmonic generation," *Phys. Rev. A* **52**, 4747–4754 (1995).
- [115] E. Constant, D. Garzella, P. Breger, E. Mével, C. Dorrer, C. Le Blanc, F. Salin, and P. Agostini, "Optimizing high harmonic generation in absorbing gases: model and experiment," *Phys. Rev. Lett.* **82**, 1668 (1999).
- [116] S. Kazamias, D. Douillet, F. Weihe, C. Valentin, A. Rousse, S. Sebban, G. Grillon, F. Augé, D. Hulin, and P. Balcou, "Global optimization of high harmonic generation," *Phys. Rev. Lett.* **90**, 193901 (2003).
- [117] P. Salières, T. Ditmire, K. S. Budil, M. D. Perry, and A. L'Huillier, "Spatial profiles of high-order harmonics generated by a femtosecond Cr:LiSAF laser," *J. Phys. B* **27**, L217–L222 (1994).

- 
- [118] J. W. G. Tisch, R. A. Smith, J. E. Muffett, M. Ciarrocca, J. P. Marangos, and Hutchinson, M. H. R., “Angularly resolved high-order harmonic generation in helium,” *Phys. Rev. A* **49**, R28–R31 (1994).
- [119] S. Hädrich, M. Krebs, A. Hoffmann, A. Klenke, J. Rothhardt, J. Limpert, and A. Tünnermann, “Exploring new avenues in high repetition rate table-top coherent extreme ultraviolet sources,” *Light Sci. Appl.* **4**, e320 (2015).
- [120] L. Plaja and J. A. Pérez-Hernández, “A quantitative S-matrix approach to high-order harmonic generation from multiphoton to tunneling regimes,” *Opt. Express* **15**, 3629 (2007).
- [121] P. Balcou, P. Salières, A. L’Huillier, and M. Lewenstein, “Generalized phase-matching conditions for high harmonics: the role of field-gradient forces,” *Phys. Rev. A* **55**, 3204–3210 (1997).
- [122] P. Balcou, A. S. Dederichs, M. B. Gaarde, and A. L’Huillier, “Quantum-path analysis and phase matching of high-order harmonic generation and high-order frequency mixing processes in strong laser fields,” *J. Phys. B* **32**, 2973–2989 (1999).
- [123] D. C. Yost, T. R. Schibli, J. Ye, J. L. Tate, J. Hostetter, M. B. Gaarde, and K. J. Schafer, “Vacuum-ultraviolet frequency combs from below-threshold harmonics,” *Nature Phys.* **5**, 815–820 (2009).
- [124] C. M. Heyl, J. Gädde, A. L’Huillier, and U. Höfer, “High-order harmonic generation with  $\mu\text{J}$  laser pulses at high repetition rates,” *J. Phys. B* **45**, 074020 (2012).
- [125] J. Rothhardt, M. Krebs, S. Hädrich, S. Demmler, J. Limpert, and A. Tünnermann, “Absorption-limited and phase-matched high harmonic generation in the tight focusing regime,” *New J. Phys.* **16**, 033022 (2014).
- [126] P. D. Maker, R. W. Terhune, M. Nisenoff, and C. M. Savage, “Effects of dispersion and focusing on the production of optical harmonics,” *Phys. Rev. Lett.* **8**, 21–22 (1962).
- [127] S. Kazamias, D. Douillet, C. Valentin, F. Weihe, F. Augé, T. Lefrou, G. Grillon, S. Sebban, and P. Balcou, “Observation of high-contrast coherence fringes in high-order harmonic generation,” *Phys. Rev. A* **68**, 033819 (2003).
- [128] C. M. Heyl, J. Gädde, U. Höfer, and A. L’Huillier, “Spectrally resolved maker fringes in high-order harmonic generation,” *Phys. Rev. Lett.* **107**, 033903 (2011).
- [129] I. Pupeza, “Power scaling of enhancement cavities for nonlinear optics,” PhD thesis (Ludwig-Maximilians-Universität München, 2011).
- [130] T. Eidam, F. Röser, O. Schmidt, J. Limpert, and A. Tünnermann, “57 W, 27 fs pulses from a fiber laser system using nonlinear compression,” *Appl. Phys. B* **92**, 9–12 (2008).
- [131] C. Jocher, T. Eidam, S. Hädrich, J. Limpert, and A. Tünnermann, “Sub 25 fs pulses from solid-core nonlinear compression stage at 250 W of average power,” *Opt. Lett.* **37**, 4407–4409 (2012).
- [132] J. Brons, V. Pervak, E. Fedulova, D. Bauer, D. Sutter, V. L. Kalashnikov, A. Apolonski, O. Pronin, and F. Krausz, “Energy scaling of Kerr-lens mode-locked thin-disk oscillators,” *Opt. Lett.* **39**, 6442 (2014).

- [133] O. Pronin, M. Seidel, F. Lücking, J. Brons, E. Fedulova, M. K. Trubetskov, V. Per-  
vak, A. Apolonski, T. Udem, and F. Krausz, “High-power multi-megahertz source of  
waveform-stabilized few-cycle light,” *Nat. Commun.* **6**, 6988 (2015).
- [134] C. Rolland and P. B. Corkum, “Compression of high-power optical pulses,” *J. Opt.*  
*Soc. Am. B* **5**, 641 (1988).
- [135] J. M. Dudley, G. Genty, and S. Coen, “Supercontinuum generation in photonic crystal  
fiber,” *Rev. Mod. Phys.* **78**, 1135–1184 (2006).
- [136] G. P. Agrawal, *Nonlinear fiber optics*, 5th ed (Academic Press, Amsterdam, 2013).
- [137] G. Fibich and A. L. Gaeta, “Critical power for self-focusing in bulk media and in  
hollow waveguides,” *Opt. Lett.* **25**, 335 (2000).
- [138] F. Emaury, C. J. Saraceno, B. Debord, D. Ghosh, A. Diebold, F. Gèrôme, T. Südmeyer,  
F. Benabid, and U. Keller, “Efficient spectral broadening in the 100-W average power  
regime using gas-filled kagome HC-PCF and pulse compression,” *Opt. Lett.* **39**, 6843  
(2014).
- [139] P. S. J. Russell, P. Hölzer, W. Chang, A. Abdolvand, and J. C. Travers, “Hollow-core  
photonic crystal fibres for gas-based nonlinear optics,” *Nature Photon.* **8**, 278–286  
(2014).
- [140] E. D. Black, “An introduction to Pound–Drever–Hall laser frequency stabilization,”  
*Am. J. Phys.* **69**, 79 (2001).
- [141] T. M. Fortier, D. J. Jones, J. Ye, and S. T. Cundiff, “Highly phase stable mode-locked  
lasers,” *IEEE J. Sel. Top. Quantum Electron.* **9**, 1002–1010 (2003).
- [142] J. C. Bienfang, R. F. Teehan, and C. A. Denman, “Phase noise transfer in resonant  
optical cavities,” *Rev. Sci. Instr.* **72**, 3208 (2001).
- [143] S. Koke, C. Grebing, H. Frei, A. Anderson, A. Assion, and G. Steinmeyer, “Direct  
frequency comb synthesis with arbitrary offset and shot-noise-limited phase noise,”  
*Nature Photon.* **4**, 462–465 (2010).
- [144] F. Lücking, A. Assion, A. Apolonski, F. Krausz, and G. Steinmeyer, “Long-term carrier-  
envelope-phase-stable few-cycle pulses by use of the feed-forward method,” *Opt.*  
*Lett.* **37**, 2076 (2012).
- [145] J. M. Dudley and S. Coen, “Coherence properties of supercontinuum spectra gener-  
ated in photonic crystal and tapered optical fibers,” *Opt. Lett.* **27**, 1180 (2002).
- [146] S. A. Meyer, J. A. Squier, and S. A. Diddams, “Diode-pumped Yb:KYW femtosecond  
laser frequency comb with stabilized carrier-envelope offset frequency,” *Eur. Phys.*  
*J. D* **48**, 19–26 (2008).
- [147] T. Balčiunas, O. D. Mücke, P. Mišeikis, G. Andriukaitis, A. Pugžlys, L. Giniunas, R.  
Danielius, R. Holzwarth, and A. Baltuška, “Carrier envelope phase stabilization of a  
Yb:KGW laser amplifier,” *Opt. Lett.* **36**, 3242 (2011).
- [148] T. Balčiunas, T. Flöry, A. Baltuška, T. Stanislaukas, R. Antipenkov, A. Varanavičius,  
and G. Steinmeyer, “Direct carrier-envelope phase control of an amplified laser sys-  
tem,” *Opt. Lett.* **39**, 1669 (2014).

- 
- [149] R. V. Pound, "Electronic frequency stabilization of microwave oscillators," *Rev. Sci. Inst.* **17**, 490 (1946).
- [150] R. W. P. Drever, J. L. Hall, F. V. Kowalski, J. Hough, G. M. Ford, A. J. Munley, and H. Ward, "Laser phase and frequency stabilization using an optical resonator," *Appl. Phys. B* **31**, 97–105 (1983).
- [151] T. C. Briles, D. C. Yost, A. Cingöz, J. Ye, and T. R. Schibli, "Simple piezoelectric-actuated mirror with 180 kHz servo bandwidth," *Opt. Express* **18**, 9739–9746 (2010).
- [152] Y.-Y. Yang, F. Süßmann, S. Zherebtsov, I. Pupeza, J. Kaster, D. Lehr, H.-J. Fuchs, E.-B. Kley, E. Fill, X.-M. Duan, Z.-S. Zhao, F. Krausz, S. L. Stebbings, and M. F. Kling, "Optimization and characterization of a highly-efficient diffraction nanograting for MHz XUV pulses," *Opt. Express* **19**, 1954–1962 (2011).
- [153] C. Gohle, J. Rauschenberger, T. Fuji, T. Udem, A. Apolonski, F. Krausz, and T. W. Hänsch, "Carrier envelope phase noise in stabilized amplifier systems," *Opt. Lett.* **30**, 2487 (2005).
- [154] C. Gohle, "A coherent frequency comb in the extreme ultraviolet," PhD thesis (Ludwig-Maximilians-Universität München, 2006).
- [155] K. D. Moll, R. J. Jones, and J. Ye, "Output coupling methods for cavity-based high-harmonic generation," *Opt. Express* **14**, 8189–8197 (2006).
- [156] A. Ozawa, A. Vernaleken, W. Schneider, I. Gotlibovych, T. Udem, and T. W. Hänsch, "Non-collinear high harmonic generation: a promising outcoupling method for cavity-assisted XUV generation," *Opt. Express* **16**, 6233–6239 (2008).
- [157] C. M. Heyl, S. N. Bengtsson, S. Carlström, J. Mauritsson, C. L. Arnold, and A. L'Huillier, "Noncollinear optical gating," *New J. Phys.* **16**, 052001 (2014).
- [158] J. Weitenberg, P. Rußbüldt, T. Eidam, and I. Pupeza, "Transverse mode tailoring in a quasi-imaging high-finesse femtosecond enhancement cavity," *Opt. Express* **19**, 9551–9561 (2011).
- [159] D. Esser, J. Weitenberg, W. Bröring, I. Pupeza, S. Holzberger, and H.-D. Hoffmann, "Laser-manufactured mirrors for geometrical output coupling of intracavity-generated high harmonics," *Opt. Express* **21**, 26797 (2013).
- [160] K. Du, P. Loosen, and R. Poprawe, "Verfahren für die Materialbearbeitung und Verwendung desselben," DE 100 29 110.4 (2000).
- [161] I.-Y. Park, S. Kim, J. Choi, D.-H. Lee, Y.-J. Kim, M. F. Kling, M. I. Stockman, and S.-W. Kim, "Plasmonic generation of ultrashort extreme-ultraviolet light pulses," *Nature Photon.* **5**, 677–681 (2011).
- [162] A. Vernaleken, J. Weitenberg, T. Sartorius, P. Russbüeldt, W. Schneider, S. L. Stebbings, M. F. Kling, P. Hommelhoff, H.-D. Hoffmann, R. Poprawe, F. Krausz, T. W. Hänsch, and T. Udem, "Single-pass high-harmonic generation at 20.8 MHz repetition rate," *Opt. Lett.* **36**, 3428–3430 (2011).
- [163] J. Lee, D. R. Carlson, and R. J. Jones, "Optimizing intracavity high harmonic generation for XUV fs frequency combs," *Opt. Express* **19**, 23315–23326 (2011).

- [164] D. C. Yost, “Development of an extreme ultraviolet frequency comb for precision spectroscopy,” PhD thesis (University of Colorado, Boulder, 2011).
- [165] T. J. Hammond, “Intracavity generation of high order harmonics,” PhD thesis (University of British Columbia, 2011).
- [166] A. Pereira, E. Quesnel, and M. Reymermier, “Dynamic measurements of ultraviolet-enhanced silica contamination by photoluminescence-based diagnostic,” *J. Appl. Phys.* **105**, 013109 (2009).
- [167] B. Bernhardt, A. Ozawa, A. Vernaleken, I. Pupeza, J. Kaster, Y. Kobayashi, R. Holzwarth, E. Fill, F. Krausz, T. W. Hänsch, and T. Udem, “Vacuum ultraviolet frequency combs generated by a femtosecond enhancement cavity in the visible,” *Opt. Lett.* **37**, 503–505 (2012).
- [168] K. T. Kim, C. Zhang, T. Ruchon, J.-F. Hergott, T. Augustine, D. Villeneuve, P. Corkum, and F. Quéré, “Photonic streaking of attosecond pulse trains,” *Nature Photon.* **7**, 651–656 (2013).
- [169] M. Lewenstein, P. Balcou, M. Y. Ivanov, A. L’Huillier, and P. Corkum, “Theory of high-harmonic generation by low-frequency laser fields,” *Phys. Rev. A* **49**, 2117 (1994).
- [170] M. Högner, “Optical high-order harmonic generation in gas targets with spatially tailored driving fields: Erzeugung optischer Hoher Harmonischer in Gas-Targets mit räumlich maßgeschneiderten treibenden Feldern,” MA thesis (Ludwig-Maximilians-Universität München, 2013).
- [171] P. Tzallas, E. Skantzakis, C. Kalpouzos, E. P. Benis, G. D. Tsakiris, and D. Charalambidis, “Generation of intense continuum extreme-ultraviolet radiation by many-cycle laser fields,” *Nature Phys.* **3**, 846–850 (2007).
- [172] X. Feng, S. Gilbertson, H. Mashiko, H. Wang, S. D. Khan, M. Chini, Y. Wu, K. Zhao, and Z. Chang, “Generation of isolated attosecond pulses with 20 to 28 femtosecond lasers,” *Phys. Rev. Lett.* **103**, 183901 (2009).
- [173] V. L. Kalashnikov, “Femtosecond pulse enhancement in an external resonator: impact of dispersive and nonlinear effects,” *Appl. Phys. B* **92**, 19–23 (2008).
- [174] W. H. Press, *Numerical recipes: The art of scientific computing*, 3rd ed. (Cambridge University Press, Cambridge, 2007).
- [175] E. P. Kanter, R. Santra, C. Höhr, E. R. Peterson, J. Rudati, D. A. Arms, E. M. Dufresne, R. W. Dunford, D. L. Ederer, B. Krässig, E. C. Landahl, S. H. Southworth, and L. Young, “Characterization of the spatiotemporal evolution of laser-generated plasmas,” *J. Appl. Phys.* **104**, 073307 (2008).
- [176] M. v. d. Sanden, J. d. Regt, and D. Schram, “Recombination of argon in an expanding plasma jet,” *Phys. Rev. E* **47**, 2792–2797 (1993).
- [177] P. Agostini, F. Fabre, G. Mainfray, G. Petite, and N. K. Rahman, “Free-free transitions following six-photon ionization of xenon atoms,” *Phys. Rev. Lett.* **42**, 1127–1130 (1979).

- 
- [178] S. Augst, D. Strickland, D. D. Meyerhofer, S. L. Chin, and J. H. Eberly, “Tunneling ionization of noble gases in a high-intensity laser field,” *Phys. Rev. Lett.* **63**, 2212–2215 (1989).
- [179] E. Mevel, P. Breger, R. Trainham, G. Petite, P. Agostini, A. Migus, J.-P. Chambaret, and A. Antonetti, “Atoms in strong optical fields: evolution from multiphoton to tunnel ionization,” *Phys. Rev. Lett.* **70**, 406–409 (1993).
- [180] G. G. Paulus, W. Nicklich, H. Xu, P. Lambropoulos, and H. Walther, “Plateau in above threshold ionization spectra,” *Phys. Rev. Lett.* **72**, 2851–2854 (1994).
- [181] A. P. Kovács, K. Osvay, Z. Bor, and R. Szipöcs, “Group-delay measurement on laser mirrors by spectrally resolved white-light interferometry,” *Opt. Lett.* **20**, 788 (1995).
- [182] E. R. Peck and D. J. Fiissier, “Dispersion of argon,” *J. Opt. Soc. Am.* **54**, 1362 (1964).
- [183] C. Y. Chien, B. La Fontaine, A. Desparois, Z. Jiang, T. W. Johnston, J. C. Kieffer, H. Pépin, F. Vidal, and H. P. Mercure, “Single-shot chirped-pulse spectral interferometry used to measure the femtosecond ionization dynamics of air,” *Opt. Lett.* **25**, 578 (2000).
- [184] S. Kazamias, S. Daboussi, O. Guilbaud, K. Cassou, D. Ros, B. Cros, and G. Maynard, “Pressure-induced phase matching in high-order harmonic generation,” *Phys. Rev. A* **83**, 063405 (2011).
- [185] S. Hädrich, A. Klenke, J. Rothhardt, M. Krebs, A. Hoffmann, O. Pronin, V. Pervak, J. Limpert, and A. Tünnermann, “High photon flux table-top coherent extreme-ultraviolet source,” *Nature Photon.* **8**, 779–783 (2014).
- [186] D. R. Carlson, T.-H. Wu, and R. J. Jones, “Dual-comb femtosecond enhancement cavity for precision measurements of plasma dynamics and spectroscopy in the xuv,” in *Conference on lasers and electro-optics (Optical Society of America, 2015)*, SW3G.1.
- [187] E. Matsubara, M. Nagai, and M. Ashida, “Coherent infrared spectroscopy system from terahertz to near infrared using air plasma produced by 10-fs pulses,” *J. Opt. Soc. Am. B* **30**, 1627 (2013).
- [188] S. T. Cundiff and J. Ye, “Colloquium: femtosecond optical frequency combs,” *Rev. Mod. Phys.* **75**, 325 (2003).
- [189] A. Stolow, A. E. Bragg, and D. M. Neumark, “Femtosecond time-resolved photoelectron spectroscopy,” *Chem. Rev.* **104**, 1719–1758 (2004).
- [190] M. I. Stockman, M. F. Kling, U. Kleineberg, and F. Krausz, “Attosecond nanoplasmonic-field microscope,” *Nature Photon.* **1**, 539–544 (2007).
- [191] C.-H. Zhang and U. Thumm, “Attosecond photoelectron spectroscopy of metal surfaces,” *Phys. Rev. Lett.* **102**, 123601 (2009).
- [192] G. G. Paulus, F. Grasbon, H. Walther, P. Villoresi, M. Nisoli, S. Stagira, E. Priori, and S. d. Silvestri, “Absolute-phase phenomena in photoionization with few-cycle laser pulses,” *Nature* **414**, 182–184 (2001).
- [193] A. Schliesser, N. Picqué, and T. W. Hänsch, “Mid-infrared frequency combs,” *Nature Photon.* **6**, 440–449 (2012).

- [194] I. Pupeza, D. Sanchez, J. Zhang, N. Lilienfein, M. Seidel, N. Karpowicz, T. Paasch-Colberg, I. Znakovskaya, M. Pescher, W. Schweinberger, V. Pervak, E. Fill, O. Pronin, Z. Wei, F. Krausz, A. Apolonski, and J. Biegert, “High-power sub-two-cycle mid-infrared pulses at 100 MHz repetition rate,” *Nature Photon.*, Advance online publication, doi:10.1037/a0028240 (2015).
- [195] A. Foltynowicz, P. Masłowski, A. J. Fleisher, B. J. Bjork, and J. Ye, “Cavity-enhanced optical frequency comb spectroscopy in the mid-infrared application to trace detection of hydrogen peroxide,” *Appl. Phys. B* **110**, 163–175 (2013).
- [196] A. Ozawa and Y. Kobayashi, “Single comb mode excitation of ground state xenon in VUV,” in *Conference on lasers and electro-optics (Optical Society of America, 2012)*, CTh5D.9.
- [197] C. Benko, L. Hua, T. K. Allison, F. Labaye, and J. Ye, “Cavity-enhanced field-free molecular alignment at a high repetition rate,” *Phys. Rev. Lett.* **114**, 153001 (2015).
- [198] A. K. Mills, S. Zhdanovich, A. Sheyerman, G. Levy, A. Damascelli, and D. J. Jones, “An XUV source using a femtosecond enhancement cavity for photoemission spectroscopy,” in *Advances in X-ray Free-Electron Lasers Instrumentation III*, Vol. 9512, edited by S. G. Biedron, *Proc. SPIE* (2015), p. 95121I.
- [199] H. Carstens, N. Lilienfein, S. Holzberger, C. Jocher, T. Eidam, J. Limpert, A. Tünnermann, J. Weitenberg, D. C. Yost, A. Alghamdi, Z. Alahmed, A. Azzeer, A. Apolonski, E. Fill, F. Krausz, and I. Pupeza, “Megawatt-scale average-power ultrashort pulses in an enhancement cavity,” *Opt. Lett.* **39**, 2595–2598 (2014).
- [200] F. X. Kärtner, U. Morgner, R. Ell, T. R. Schibli, J. G. Fujimoto, E. P. Ippen, V. Scheuer, G. Angelow, and T. Tschudi, “Ultrabroadband double-chirped mirror pairs for generation of octave spectra,” *J. Opt. Soc. Am. B* **18**, 882 (2001).
- [201] V. Pervak, A. V. Tikhonravov, M. K. Trubetskov, S. Naumov, F. Krausz, and A. Apolonski, “1.5-octave chirped mirror for pulse compression down to sub-3 fs,” *Appl. Phys. B* **87**, 5–12 (2007).
- [202] J. Limpert, A. Klenke, M. Kienel, S. Breitkopf, T. Eidam, S. Hadrich, C. Jauregui, and A. Tünnermann, “Performance scaling of ultrafast laser systems by coherent addition of femtosecond pulses,” *IEEE J. Sel. Top. Quantum Electron.* **20**, 268–277 (2014).
- [203] M. F. Kling and P. Hommelhoff, eds., *Attosecond nanophysics: from basic science to applications* (Wiley-VCH, Weinheim, 2015).
- [204] M. Wunram, P. Storz, D. Brida, and A. Leitenstorfer, “Ultrastable fiber amplifier delivering 145-fs pulses with 6- $\mu$ J energy at 10-MHz repetition rate,” *Opt. Lett.* **40**, 823 (2015).
- [205] M. Schultze, E. M. Bothschafter, A. Sommer, S. Holzner, W. Schweinberger, M. Fiess, M. Hofstetter, R. Kienberger, V. Apalkov, V. S. Yakovlev, M. I. Stockman, and F. Krausz, “Controlling dielectrics with the electric field of light,” *Nature* **493**, 75–78 (2012).
- [206] A. Sommer, E. M. Bothschafter, N. Karpowicz, S. Sato, V. S. Yakovlev, K. Yabana, C. Jakubeit, O. Razskazovskaya, T. Latka, M. Schultze, and F. Krausz, “Attosecond spectroscopy of nonlinear polarization dynamics,” in *10th International Conference on Ultrafast Optics* (2015), UFO0067.

- [207] R. J. Loewen, “A compact light source: design and technical feasibility study of a laser-electron storage ring X-ray source,” PhD thesis (Stanford University, 2003).
- [208] E. Eggl, S. Schleede, M. Bech, K. Achterhold, R. Loewen, R. D. Ruth, and F. Pfeiffer, “X-ray phase-contrast tomography with a compact laser-driven synchrotron source,” *Proc. Natl. Acad. Sci. U.S.A.* **112**, 5567–5572 (2015).
- [209] Y. Vidne, M. Rosenbluh, and T. W. Hänsch, “Pulse picking by phase-coherent additive pulse generation in an external cavity,” *Opt. Lett.* **28**, 2396 (2003).
- [210] S. Breitkopf, T. Eidam, A. Klenke, L. v. Grafenstein, H. Carstens, S. Holzberger, E. Fill, T. Schreiber, F. Krausz, A. Tünnermann, I. Pupeza, and J. Limpert, “A concept for multiterawatt fibre lasers based on coherent pulse stacking in passive cavities,” *Light Sci. Appl.* **3**, e211 (2014).
- [211] T. Zhou, J. Ruppe, C. Zhu, I.-N. Hu, J. Nees, and A. Galvanauskas, “Coherent pulse stacking amplification using low-finesse gires-tournois interferometers,” *Opt. Express* **23**, 7442 (2015).



# Appendix A

## Definitions

This sections summarizes a few definitions and conventions used to describe electric fields in this thesis. Typically, the calculations use a complex description of the electric field, and a convenient decomposition of the field into fast oscillating carrier (frequency  $\omega_c$ ) and slowly varying (complex) envelope  $\mathcal{A}$ . The envelope can be further decomposed into its absolute value  $A$  and its phase relative to the carrier  $\theta$ :

$$E(t) = \text{Re}[\mathcal{E}(t)] = \text{Re}[\mathcal{A}(t)e^{i\omega_c t}], \quad (\text{A.1})$$

$$\mathcal{A}(t) = A(t)e^{i\theta(t)}. \quad (\text{A.2})$$

For the Fourier components of the complex field amplitudes, the following convention of the Fourier transform is used:

$$\tilde{\mathcal{A}}(\omega) = \int_{-\infty}^{\infty} dt \mathcal{A}(t) e^{-i\omega t} \quad \longleftrightarrow \quad \mathcal{A}(t) = \int_{-\infty}^{\infty} \frac{d\omega}{2\pi} \tilde{\mathcal{A}}(\omega) e^{i\omega t}. \quad (\text{A.3})$$

Functions defined in Fourier space are distinguishable from their counterparts in real space by a tilde sign.

With the definition of the Fourier transform, a forward (i.e., in  $+z$ -direction) propagating plane wave (wave vector  $k_c$ ) is given by  $\mathcal{E}(t, z) = \mathcal{E}_0 e^{i(\omega_c t - k_c z)}$ . The phase fronts of this wave are propagating with the phase velocity  $\frac{\omega_c}{k_c}$  in  $+z$ -direction as time increases. Therefore, at a given time  $t$  the phase at the distance  $z + L$  is shifted by  $-ik_c L$  relative to the phase at position  $z$ .



## Appendix B

### Dynamic response of enhancement cavities in the linear regime

In this chapter, we derive the filtering properties of a linear EC for amplitude and phase modulation of a continuous-wave input signal. To this end, the differential equation governing the cavity build-up is derived and its stationary solutions are given. Then, the dynamic response of the intracavity field around its stationary value is given, assuming a slow sinusoidal phase or amplitude modulation of the input field. The derivation follows the approach presented in [142].

#### Cavity build-up in time domain

At the input coupler (power transmission  $T_{\text{ic}}$ , reflectivity  $R_{\text{ic}}$ ), the transmitted portion of the input field  $\mathcal{E}_{\text{in}}$  and the reflected portion of the returning field  $\mathcal{E}_{\text{ret}}$  add up to the new intracavity field  $\mathcal{E}_{\text{cav}}$ :

$$\mathcal{E}_{\text{cav}}(t) = \sqrt{T_{\text{ic}}}\mathcal{E}_{\text{in}}(t) + \sqrt{R_{\text{ic}}}\mathcal{E}_{\text{ret}}(t) \quad \text{with} \quad \mathcal{E}_{\text{ret}}(t) = \sqrt{R_{\text{cav}}}\mathcal{E}_{\text{cav}}(t - \tau). \quad (\text{B.1})$$

The returning field itself is a delayed and attenuated copy of the (former) intracavity field<sup>1</sup> (delay,  $\tau$ ; power attenuation,  $R_{\text{cav}}$ ). Using the definition of the slowly varying envelope (Eq. (A.1)), the fast oscillating carrier wave is omitted, resulting in an equation with a much slower time dependence:

$$\mathcal{A}_{\text{cav}}(t) = \sqrt{T_{\text{ic}}}\mathcal{A}_{\text{in}}(t) + \sqrt{R_{\text{ic}}R_{\text{cav}}}e^{-i\omega_c\tau}\mathcal{A}_{\text{cav}}(t - \tau). \quad (i = 1, 2)$$

With a shift of the time axis by  $-\tau$  and with the definition of the phase  $\phi = -\omega_c\tau$ , this reads:

$$\mathcal{A}_{\text{cav}}(t + \tau) = \sqrt{T_{\text{ic}}}\mathcal{A}_{\text{in}}(t + \tau) + \sqrt{R_{\text{ic}}R_{\text{cav}}}e^{i\phi}\mathcal{A}_{\text{cav}}(t). \quad (\text{B.2})$$

As we are only interested in small variations of the intracavity field, we will Taylor-expand the  $\mathcal{A}_{\text{cav}}$  to first order. The incident field is expanded only to zero order:

$$\begin{aligned} \mathcal{A}_{\text{cav}}(t + \tau) &\approx \mathcal{A}_{\text{cav}}(t) + \tau \frac{d\mathcal{A}_{\text{cav}}(t)}{dt}; \\ \mathcal{A}_{\text{in}}(t + \tau) &\approx \mathcal{A}_{\text{in}}(t). \end{aligned}$$

---

<sup>1</sup>Equation (B.1) can also be obtained by starting from the Fourier domain as done in Section 2.1.1, with a cavity round-trip imposing a spectral phase of  $\phi(\omega) = -k(\omega)L = -\omega\tau$  in accordance with the sign conventions of the forward propagating plane wave decomposition as defined in Appendix A.

Insertion into Eq. (B.2) yields:

$$\begin{aligned} \Rightarrow \mathcal{A}_{\text{cav}}(t) + \frac{d\mathcal{A}_{\text{cav}}(t)}{dt} \tau &= \sqrt{T_{\text{ic}}}\mathcal{A}_{\text{in}}(t) + \sqrt{R_{\text{ic}}R_{\text{cav}}}e^{i\phi} \mathcal{A}_{\text{cav}}(t); \\ \Leftrightarrow \frac{d\mathcal{A}_{\text{cav}}(t)}{dt} &= -\underbrace{\frac{1 - \sqrt{R_{\text{ic}}R_{\text{cav}}}e^{i\phi}}{\tau}}_{\Gamma} \mathcal{A}_{\text{cav}}(t) + \underbrace{\frac{\sqrt{T_{\text{ic}}}}{\tau}}_{\gamma} \mathcal{A}_{\text{in}}(t); \\ \frac{d\mathcal{A}_{\text{cav}}(t)}{dt} &= -\Gamma \mathcal{A}_{\text{cav}}(t) + \gamma \mathcal{A}_{\text{in}}(t). \end{aligned} \quad (\text{B.3})$$

In the last step, we have introduced the rate of decay  $\Gamma$  and the rate of pumping  $\gamma$ . For convenience, we will use the index 1 for the for the input field (“in”) and the index 2 for the intracavity field (“cav”). Furthermore, we will decompose the complex envelope  $\mathcal{A}$  into its absolute value  $A$  and phase  $\theta$  as in Eq. (A.2). For the time derivative of the field, we find:

$$\frac{d\mathcal{A}_i(t)}{dt} = \left( \frac{dA_i}{dt} + i \frac{d\theta_i}{dt} A_i \right) e^{i\theta_i(t)}.$$

With the new notation Eq. (B.3) turns into:

$$\left( \frac{dA_2}{dt} + i \frac{d\theta_2}{dt} A_2 \right) e^{i\theta_2} = -\Gamma A_2 e^{i\theta_2} + \gamma A_1 e^{i\theta_1}. \quad (\text{B.4})$$

Next, we will separate this equation into its real part and imaginary part using the definitions  $\alpha = \text{Re } \Gamma$  and  $\beta = \text{Im } \Gamma$ :

$$\begin{aligned} \text{Re}[\text{Eq. (B.4)}] : \frac{dA_2}{dt} \cos \theta_2 - \frac{d\theta_2}{dt} A_2 \sin \theta_2 &= -\alpha A_2 \cos \theta_2 + \beta A_2 \sin \theta_2 + \gamma A_1 \cos \theta_1; \\ \text{Im}[\text{Eq. (B.4)}] : \frac{dA_2}{dt} \sin \theta_2 + \frac{d\theta_2}{dt} A_2 \cos \theta_2 &= -\beta A_2 \cos \theta_2 - \alpha A_2 \sin \theta_2 + \gamma A_1 \sin \theta_1; \end{aligned}$$

To simplify this system of linear differential equations, we apply the following operations:

$$\begin{aligned} \text{Re}[\text{Eq. (B.4)}] \times \cos \theta_2 + \text{Im}[\text{Eq. (B.4)}] \times \sin \theta_2; \\ \text{Re}[\text{Eq. (B.4)}] \times \sin \theta_2 - \text{Im}[\text{Eq. (B.4)}] \times \cos \theta_2; \end{aligned}$$

Using trigonometric identities, we find the first order differential equations for  $\theta_2$  and  $A_2$ :

$$\boxed{\frac{dA_2}{dt} = -\alpha A_2 + \gamma A_1 \cos(\theta_2 - \theta_1)} \quad (\text{B.5})$$

$$\boxed{\frac{d\theta_2}{dt} = -\gamma \frac{A_1}{A_2} \sin(\theta_2 - \theta_1) - \beta} \quad (\text{B.6})$$

## Stationary solution

As a first step, we will seek for the steady-state solution of Eqs. (B.5) to (B.6), i.e., we assume that the input and the intracavity field envelope is time independent, i.e.,  $\frac{dA_i}{dt} = 0$  and  $\frac{d\theta_i}{dt} = 0$ . Defining  $\Delta\theta = \theta_2 - \theta_1$ , we find:

$$\Rightarrow \alpha A_{2,\text{ss}} = \gamma A_{1,\text{ss}} \cos(\Delta\theta_{\text{ss}}); \quad (\text{B.7})$$

$$\beta A_{2,\text{ss}} = -\gamma A_{1,\text{ss}} \sin(\Delta\theta_{\text{ss}}); \quad (\text{B.8})$$

Using the squared sum of the two equations and the ratio of the two equations, one yields:

$$A_{2,ss}^2 = \frac{\gamma^2}{\beta^2 + \alpha^2} A_{1,ss}^2;$$

$$\Delta\theta_{ss} = \arctan\left(-\frac{\beta}{\alpha}\right);$$

Reminding that  $\alpha + i\beta = \Gamma$ , and the inserting the definitions of  $\Gamma$  and  $\gamma$  this transforms to:

$$A_{2,ss} = \left| \frac{\sqrt{T_{ic}}}{1 - \sqrt{R_{ic}R_{cav}}e^{i\phi}} \right| A_{1,ss}; \quad (\text{B.9})$$

$$\theta_{2,ss} = \theta_{1,ss} + \arctan\left(\frac{\sqrt{R_{ic}R_{cav}}\sin\phi}{1 - \sqrt{R_{ic}R_{cav}}\cos\phi}\right); \quad (\text{B.10})$$

$$\Rightarrow \mathcal{A}_{2,ss} = \frac{\sqrt{T_{ic}}}{1 - \sqrt{R_{ic}R_{cav}}e^{i\phi}} \mathcal{A}_{1,ss}; \quad (\text{B.11})$$

As expected, this is identical with the solution obtained in the Fourier domain (see (2.2)).

## Response of the cavity field to time-varying input fields

Now, we will turn to the dynamics of the intracavity field, in case of a varying input field. To this end, we consider small deviations of the input field (characterized by  $\delta$ ) from its steady-state value (index “ss”) and compute the resulting variations of the intracavity field around its steady-state value to first order in  $\delta$ . In formulas this ansatz reads:

$$A_i(t) = A_{i,ss} [1 + \delta\epsilon_i(t)]$$

$$\theta_i(t) = \theta_{i,ss} + \delta\vartheta_i(t)$$

$$\Rightarrow \Delta\theta(t) = \theta_2(t) - \theta_1(t) = \Delta\theta_{ss} + \delta(\vartheta_2(t) - \vartheta_1(t)) = \Delta\theta_{ss} + \delta\Delta\vartheta(t)$$

Inserting this ansatz into the differential equations Eqs. (B.5) to (B.6), we obtain:

$$\delta A_{2,ss} \frac{d\epsilon_2}{dt} = -\alpha A_{2,ss} (1 + \delta\epsilon_2) + \gamma A_{1,ss} (1 + \delta\epsilon_1) \cos(\Delta\theta) \quad (\text{B.12})$$

$$\delta \frac{d\vartheta_2}{dt} = -\beta - \gamma \frac{A_{1,ss} (1 + \delta\epsilon_1)}{A_{2,ss} (1 + \delta\epsilon_2)} \sin(\Delta\theta) \quad (\text{B.13})$$

We will Taylor-expand these equations to first order in  $\delta$ . With

$$\cos(\Delta\theta) = \cos[\Delta\theta_{ss} + \delta\Delta\vartheta] = \cos(\Delta\theta_{ss}) \cos(\delta\Delta\vartheta) - \sin(\Delta\theta_{ss}) \sin(\delta\Delta\vartheta)$$

$$\approx \cos(\Delta\theta_{ss}) - \sin(\Delta\theta_{ss}) \cdot \delta\Delta\vartheta$$

and

$$\sin(\Delta\theta) = \sin[\Delta\theta_{ss} + \delta\Delta\vartheta] = \sin(\Delta\theta_{ss}) \cos(\delta\Delta\vartheta) + \cos(\Delta\theta_{ss}) \sin(\delta\Delta\vartheta)$$

$$\approx \sin(\Delta\theta_{ss}) + \cos(\Delta\theta_{ss}) \cdot \delta\Delta\vartheta$$

we find for Eq. (B.12):

$$\begin{aligned}\delta A_{2,ss} \frac{d\epsilon_2}{dt} &= -\delta\gamma A_{1,ss} \sin(\Delta\theta_{ss})\Delta\vartheta - \delta\alpha A_{2,ss}\epsilon_2 + \delta\gamma A_{1,ss}\epsilon_1 \cos(\Delta\theta_{ss}) \\ \Leftrightarrow \frac{d\epsilon_2}{dt} &= -\gamma \frac{A_{1,ss}}{A_{2,ss}} \sin(\Delta\theta_{ss})\Delta\vartheta - \alpha\epsilon_2 + \gamma \frac{A_{1,ss}}{A_{2,ss}}\epsilon_1 \cos(\Delta\theta_{ss}) \\ \Leftrightarrow \frac{d\epsilon_2}{dt} &= \beta\Delta\vartheta - \alpha(\epsilon_2 - \epsilon_1)\end{aligned}$$

Here, the steady-state relations from Eqs. (B.7) to (B.8) were applied several times. With Eq. (B.13) we proceed in a similar manner:

$$\begin{aligned}\delta \frac{d\vartheta_2}{dt} &= -\beta - \gamma \frac{A_{1,ss}}{A_{2,ss}} [1 + \delta(\epsilon_1 - \epsilon_2)] \cdot [\sin(\Delta\theta_{ss}) + \cos(\Delta\theta_{ss}) \cdot \delta\Delta\vartheta] \\ \Leftrightarrow \frac{d\vartheta_2}{dt} &= -\gamma \frac{A_{1,ss}}{A_{2,ss}} (\epsilon_1 - \epsilon_2) \sin(\Delta\theta_{ss}) - \gamma \frac{A_{1,ss}}{A_{2,ss}} \cos(\Delta\theta_{ss})\Delta\vartheta \\ \Leftrightarrow \frac{d\vartheta_2}{dt} &= \beta(\epsilon_1 - \epsilon_2) - \alpha\Delta\vartheta\end{aligned}$$

In summary, we obtain for the time-dependent variation of the intracavity field:

$$\boxed{\frac{d\epsilon_2}{dt} = \beta(\vartheta_2 - \vartheta_1) - \alpha(\epsilon_2 - \epsilon_1)} \quad (\text{B.14})$$

$$\boxed{\frac{d\vartheta_2}{dt} = -\alpha(\vartheta_2 - \vartheta_1) - \beta(\epsilon_2 - \epsilon_1)} \quad (\text{B.15})$$

We solve this system of coupled differential equations applying a Fourier transformation (see Eq. (A.3)). Here, the operators for the time derivative are replaced by a multiplication with  $i\omega$ . Solving the resulting system of algebraic equations is straightforward. In Fourier space we find:

$$\boxed{\tilde{\epsilon}_2 = \frac{\alpha(\alpha + i\omega) + \beta^2}{(\alpha + i\omega)^2 + \beta^2} \tilde{\epsilon}_1 - \frac{i\omega\beta}{(\alpha + i\omega)^2 + \beta^2} \tilde{\vartheta}_1} \quad (\text{B.16})$$

$$\boxed{\tilde{\vartheta}_2 = \frac{\alpha(\alpha + i\omega) + \beta^2}{(\alpha + i\omega)^2 + \beta^2} \tilde{\vartheta}_1 + \frac{i\omega\beta}{(\alpha + i\omega)^2 + \beta^2} \tilde{\epsilon}_1} \quad (\text{B.17})$$

These equations describe, how a modulation of the input signal in amplitude or phase at a given frequency transfers to a modulation of the intracavity amplitude or phase (in a first order approximation), for arbitrary detuning from the resonance. Apparently, for  $\beta \neq 0$ , i.e. for a finite detuning from the resonance, there is phase-to-amplitude and amplitude-to-phase coupling.

It is illustrative to specialize to the case, where the stationary solution is slightly detuned from resonance, i.e., where both the single-round-trip phase  $\phi$  and the intracavity phase shift  $\Delta\theta_{ss}$  are much smaller than 1. With the notation of  $\Gamma_0 = \Gamma(\phi = 0)$  being the rate of energy decay when the cavity is on resonance, a Taylor expansion of the steady-state solutions from Eqs. (B.7) to (B.8) for small  $\Delta\theta_{ss}$  lead to:

$$\alpha = \Gamma_0 + O(\Delta\theta_{ss}^2) \quad \text{and} \quad \beta = \Gamma_0\Delta\theta_{ss} + O(\Delta\theta_{ss}^3)$$

---

Inserting this into the modulation transfer functions from Eqs. (B.16) to (B.17) and keeping only terms up to linear order in  $\Delta\theta_{ss}$ , we find:

$$\tilde{\epsilon}_2 = \frac{\Gamma_0}{\Gamma_0 + i\omega} \tilde{\epsilon}_1 - \frac{i\omega\Gamma_0\Delta\theta_{ss}}{(\Gamma_0 + i\omega)^2} \tilde{\vartheta}_1 \quad (\text{B.18})$$

$$\tilde{\vartheta}_2 = \frac{\Gamma_0}{\Gamma_0 + i\omega} \tilde{\vartheta}_1 + \frac{i\omega\Gamma_0\Delta\theta_{ss}}{(\Gamma_0 + i\omega)^2} \tilde{\epsilon}_1 \quad (\text{B.19})$$

Now, the frequency characteristic is much more obvious: The cavity is a low-pass filter with characteristic frequency  $\Gamma_0$  for AM-to-AM and PM-to-PM coupling. The cross terms, however, show a combined first-order high and low pass characteristics. For low frequency phase modulations (much slower than the lifetime) the cavity can adiabatically follow the phase of the input signal and, thus, there is negligible influence on the amplitude of the intracavity signal. For very high-frequency phase modulations, the cavity cannot respond at all (“too high inertia”), and again, there is negligible amplitude modulation. Around frequencies  $\omega \approx \Gamma_0$ , however, there is significant coupling. Thus, fluctuations of the input signal phase in this frequency range must be avoided in order to ensure constant intracavity power. The same is true for amplitude-to-phase coupling.



## Appendix C

### Cavity enhancement using a single degree of freedom

In this chapter we derive the analytic expression Eq. (3.1) of the integrated power enhancement for a comb coupled to an EC, when the offset frequency is detuned by  $\Delta f_{\text{ceo}}$  from its optimal value  $f_{\text{ceo}}^*$  and the repetition rate is used to best compensate for this deviation. The input comb is characterized by two parameters, the central frequency  $\nu_c$  (comb line number  $N_c$ ) and the repetition rate  $f_{\text{rep}}$ . Thus, all lines are given by  $\nu_n = \nu_c + n \cdot f_{\text{rep}}$ . The input power spectrum  $P_{\text{in}}(\nu)$  is of Gaussian shape with its width noted by  $\sigma$ :

$$P(\nu_n) = P_{\text{in}} \frac{f_{\text{rep}}}{\sqrt{2\pi}\sigma^2} e^{-\frac{(\nu_n - \nu_c)^2}{2\sigma^2}} \quad \text{and} \quad P_{\text{in}} = \sum_n P(\nu_n).$$

The cavity has vanishing round-trip dispersion over the bandwidth of the input spectrum and a frequency-independent finesse  $\mathcal{F}$ . For simplicity, but without loss of generality, we assume  $f_{\text{ceo}}^* = 0$ . Thus, in case of optimal comb parameters  $\nu_c = N_c \cdot f_{\text{rep}}^*$  holds, with  $f_{\text{rep}}^*$  being equal to the inverse of the (fixed) cavity round-trip time  $T_{\text{rt}}$ .

It is clear that best integrated power enhancement in case of a detuned offset frequency requires a small adaption of the repetition rate. The new repetition rate is calculated such that the central comb line  $N_c$  stays on resonance. Therefore, we can write for the round-trip phase at the central frequency:

$$\phi(\nu_c) = 2\pi \nu_c T_{\text{rt}} = 2\pi(N_c f_{\text{rep}} + \Delta f_{\text{ceo}}) T_{\text{rt}} \stackrel{!}{=} 2\pi N_c.$$

This expression relates a change in the offset frequency to the change in repetition rate. Explicitly, the new repetition rate is given by:

$$f_{\text{rep}} = f_{\text{rep}}^* - \frac{\Delta f_{\text{ceo}}}{N_c}.$$

The round-trip phase at an arbitrary comb line  $\nu_n$  is given by:

$$\begin{aligned} \phi(\nu_n) &= 2\pi \nu_n T_{\text{rt}} = 2\pi \underbrace{\nu_c}_{N_c} T_{\text{rt}} + 2\pi n \frac{f_{\text{rep}}}{f_{\text{rep}}^*}; \\ &\cong 2\pi n \left( 1 - \frac{\Delta f_{\text{ceo}}}{N_c f_{\text{rep}}^*} \right); \\ &\cong -2\pi n \frac{\Delta f_{\text{ceo}}}{\nu_c}; \end{aligned} \tag{C.1}$$

Here, the  $\cong$  symbol means equal up to a multiple of  $2\pi$ .

The intracavity power  $P_{\text{cav}}$  is given by the sum over all the input comb lines multiplied by the frequency resolved power enhancement factor PE as defined in Eq. (2.2), which is repeated here again for convenience:

$$P_{\text{cav}} = \sum_n \mathbb{E}(\nu_n) P_{\text{in}}(\nu_n) \quad \text{with} \quad \mathbb{E}(\nu_n) = \mathbb{E}_R \cdot \frac{1}{1 + \left[ \frac{2\mathcal{F}}{\pi} \sin \frac{\phi(\nu_n)}{2} \right]^2}. \quad (\text{C.2})$$

Here,  $\mathbb{E}_R$  is the power enhancement on resonance which equals the integrated power enhancement  $\mathbb{E}_{\text{int,opt}}$  in case of optimal comb parameters. For a very large number of dense comb lines, the sum in Eq. (C.2) can be replaced by an integration. Furthermore, we will use the continuous variable  $f$  describing the optical frequency  $\nu$ , that is offset from the central line by  $f = \nu - \nu_c$ . Using this notation, the expression for the round-trip phase at the frequency  $\nu_n$  from Eq. (C.1) transforms to:

$$\phi(\nu_n) = -2\pi n \cdot f_{\text{rep}} \frac{\Delta f_{\text{ceo}}}{f_{\text{rep}} \nu_c} \quad \rightarrow \quad \phi(f) = -2\pi f \cdot \frac{\Delta f_{\text{ceo}}}{f_{\text{rep}} \nu_c}. \quad (\text{C.3})$$

Putting all ingredients together, the intracavity power can be calculated as:

$$\begin{aligned} P_{\text{cav}} &= \mathbb{E}_R P_{\text{in}} \int df \frac{1}{1 + \left( \frac{2\mathcal{F}}{\pi} \right)^2 \sin^2 \left( \frac{\phi(f)}{2} \right)} \cdot \frac{1}{\sqrt{2\pi\sigma^2}} e^{-\frac{f^2}{2\sigma^2}}; \\ &\approx \mathbb{E}_R P_{\text{in}} \int df \frac{1}{1 + \left( \frac{2\mathcal{F}}{\pi} \right)^2 \frac{\phi^2(f)}{4}} \cdot \frac{1}{\sqrt{2\pi\sigma^2}} e^{-\frac{f^2}{2\sigma^2}}; \\ &= \mathbb{E}_R P_{\text{in}} \int df \frac{1}{1 + \left( \frac{2\mathcal{F}\Delta f_{\text{ceo}}}{f_{\text{rep}} \nu_c} \right)^2 f^2} \cdot \frac{1}{\sqrt{2\pi\sigma^2}} e^{-\frac{f^2}{2\sigma^2}}; \end{aligned} \quad (\text{C.4})$$

Here, we have used the approximation  $\sin x \approx x$  which is in principle only valid for frequencies that are not too far away from the carrier. The fact, that the input spectrum decays quickly for larger values of  $f$  ensures that the approximation can be used for all values of  $f$ .

The integral in Eq. (C.4) can be analytically solved using the ‘‘Complex Errorfunction’’ Erfc:

$$\begin{aligned} \int dt \frac{1}{1 + a^2 t^2} e^{-\frac{t^2}{2b^2}} &= \frac{\pi}{a} e^{1/(2a^2 b^2)} \text{Erfc} \left( \frac{1}{\sqrt{2}ab} \right), \\ \text{with} \quad \text{Erfc}(x) &= 1 - \frac{2}{\sqrt{\pi}} \int_0^x e^{-x^2} dx. \end{aligned}$$

Thus, we find for the ratio of the integrated power enhancement attainable with detuned offset frequency to its value given optimal comb parameters:

$$\begin{aligned} \frac{\mathbb{E}_{\text{int}}(\Delta f_{\text{ceo}}, \mathcal{F}, \Delta \nu)}{\mathbb{E}_{\text{int,opt}}} &= \frac{P_{\text{cav}}}{P_{\text{in}} \mathbb{E}_R} = \sqrt{\pi} x \cdot e^{x^2} \text{Erfc}(x), \\ \text{with} \quad x &= \left( \frac{1}{\sqrt{\log 2}} \frac{\Delta f_{\text{ceo}}}{\Gamma_{\text{FWHM}}} \frac{\Delta \nu}{\nu_c} \right)^{-1}. \end{aligned}$$

---

which is Eq. (3.1). In the expression for  $x$  we have introduced the FWHM of the resonance linewidth  $\Gamma_{\text{FWHM}} = \frac{f_{\text{rep}}}{\mathcal{F}}$  and the FWHM of the spectral width  $\Delta\nu = 2\sqrt{2\log 2}\sigma$ .

In a similar way, we can find the FWHM of the intracavity spectrum  $\Delta\nu_{\text{cav}}$ . Using the intracavity power spectral density given as the integrand in Eq. (C.4), one needs to solve the following equation numerically for  $f$ :

$$\frac{1}{1 + \left(\frac{2\mathcal{F}\Delta f_{\text{ceo}}}{f_{\text{rep}}\nu_c}\right)^2 f^2} e^{-\frac{f^2}{2\sigma^2}} \stackrel{!}{=} \frac{1}{2};$$

$$\Rightarrow \Delta\nu_{\text{cav}} = 2|f|.$$



## Appendix D

### Algorithm for phase retrieval

In this section, the algorithm for retrieving the phase from a spatially and spectrally resolved interferogram as described by Eq. (5.11) is given. Both, the development of the algorithm and its numerical implementation were done by M. Trubetskov.

#### Reformulation of the problem

After preprocessing the interferogram (truncation of noisy and unreliable parts), we isolate the oscillating part in the interferogram by considering the separately recorded spectra of the cavity (“sample”) and the input pulse (“reference”) via:

$$A(y, \omega) := \frac{I(y, \omega) - I_r(y, \omega) - I_s(y, \omega)}{2\sqrt{I_r(y, \omega)I_s(y, \omega)}} \quad (\text{D.1})$$

Thus, by comparison with Eq. (5.11) we find, that

$$A(y, \omega) = \cos[\theta(\omega) + \gamma y \omega] \quad \text{with} \quad \gamma = \frac{\sin \alpha}{c} \quad (\text{D.2})$$

should hold in case of a noiseless measurement. Since measurements are always perturbed by various noise sources the exact fulfillment of Eq. (D.2) is impossible. Taking this into account, we rewrite the right-hand side in a form allowing more freedom:

$$\begin{aligned} \cos[\theta(\omega) + \gamma y \omega] &= \sin\left[\left(\theta(\omega) + \frac{\pi}{2}\right) + \gamma y \omega\right] \\ &= \cos\left(\theta(\omega) + \frac{\pi}{2}\right) \sin(\gamma y \omega) + \sin\left(\theta(\omega) + \frac{\pi}{2}\right) \cos(\gamma y \omega) \\ &\rightarrow a(\omega) \sin(\gamma y \omega) + b(\omega) \cos(\gamma y \omega) + c(\omega) \end{aligned} \quad (\text{D.3})$$

The introduction of two arbitrary functions  $a(\omega)$  and  $b(\omega)$  and an arbitrary offset term  $c(\omega)$  improves the ability to approximate the measured interferogram data  $A(y, \omega)$ . The unknown phase  $\theta$  can be obtained as a polar angle of the complex number  $\theta(\omega) = \arg(a(\omega) + ib(\omega))$  (the phase offset  $\pi/2$  can be ignored).

Nevertheless strict equality of the right-hand side of Eq. (D.3) with the data is still impossible and we reformulate the phase retrieval problem in variational form. For this purpose we introduce a functional  $\Phi[a(\omega), b(\omega), c(\omega), \gamma]$

$$\begin{aligned} \Phi[a(\omega), b(\omega), c(\omega), \gamma] &:= \\ &\int_{y_1}^{y_2} \int_{\omega_1}^{\omega_2} |a(\omega) \sin(\gamma y \omega) + b(\omega) \cos(\gamma y \omega) + c(\omega) - A(y, \omega)|^2 d\omega dy \end{aligned}$$

and reformulate the phase retrieval as a problem of minimizing the functional  $\Phi$  with respect to the functions  $a(\omega)$ ,  $b(\omega)$ ,  $c(\omega)$ , and the parameter  $\gamma$ . In numerical implementation, it is natural to substitute the integrals with sums, dropping the constant bin size  $\Delta\omega$  and  $\Delta y$ :

$$\Phi[a, b, c, \gamma] := \sum_{i=i_1}^{i_2} \sum_{j=j_1}^{j_2} |a_j \sin(\gamma y_i \omega_j) + b_j \cos(\gamma y_i \omega_j) + c_j - A_{ij}|^2 \quad (\text{D.4})$$

Here, the function  $a(\omega)$  is sampled at the frequencies  $\omega_j$  resulting in a 1d array  $a$  containing the elements  $a_j = a(\omega_j)$  (and respectively for  $b(\omega)$  and  $c(\omega)$ , and for the 2d array of measured data  $A_{ij}$ ).

## Minimization of the functional

The functional (or double sum)  $\Phi$  in Eq. (D.4) can be represented as a sum over individual functionals  $\Phi_j$  for each frequency  $\omega_j$ . With the additional definition  $\delta_{ij} = \gamma y_i \omega_j$ , this reads:

$$\Phi = \sum_{j=j_1}^{j_2} \Phi_j(\gamma, a_j, b_j, c_j) \quad \text{with} \quad \Phi_j(\gamma, a_j, b_j, c_j) = \sum_{i=i_1}^{i_2} (a_j \sin \delta_{ij} + b_j \cos \delta_{ij} + c_j - A_{ij})^2 \quad (\text{D.5})$$

Since the parameters  $a_j$ ,  $b_j$ ,  $c_j$  are only present in  $\Phi_j$  we can efficiently exclude them in an optimal way using an analytic approach. Note, that the dependency of  $\Phi_j$  on these parameters is quadratic (see Eq. (D.5)). If we assume, that we know the value of the global parameter  $\gamma$  (and thus, all values of  $\delta_{ij}$ ), then we can find optimal values of the parameters  $a_j$ ,  $b_j$  and  $c_j$  using the equations:

$$\frac{\partial \Phi_j}{\partial a_j} = 0, \quad \frac{\partial \Phi_j}{\partial b_j} = 0, \quad \frac{\partial \Phi_j}{\partial c_j} = 0, \quad j = j_1, \dots, j_2. \quad (\text{D.6})$$

These three equations can, however, not be solved independently. Instead, inserting the definition of  $\Phi_j$  from Eq. (D.5) into Eq. (D.6) results in the following system of linear algebraic equations,

$$\mathbf{M}_j \begin{pmatrix} a_j \\ b_j \\ c_j \end{pmatrix} = \mathbf{B}_j, \quad (\text{D.7})$$

where the matrices  $\mathbf{M}_j$  and right-hand sides  $\mathbf{B}_j$  are expressed as:

$$\mathbf{M}_j = \begin{pmatrix} \sum_i \sin^2 \delta_{ij} & \sum_i \sin \delta_{ij} \cos \delta_{ij} & \sum_i \sin \delta_{ij} \\ \sum_i \sin \delta_{ij} \cos \delta_{ij} & \sum_i \cos^2 \delta_{ij} & \sum_i \cos \delta_{ij} \\ \sum_i \sin \delta_{ij} & \sum_i \cos \delta_{ij} & \sum_i 1 \end{pmatrix}, \quad \mathbf{B}_j = \begin{pmatrix} \sum_i A_{ij} \sin \delta_{ij} \\ \sum_i A_{ij} \cos \delta_{ij} \\ \sum_i A_{ij} \end{pmatrix}. \quad (\text{D.8})$$

---

Here, summation over index  $i$  is understood to run from  $i = i_1, \dots, i_2$ . Inserting the solution  $a_j, b_j, c_j$  of the linear system of equations defined in Eqs. (D.7) to (D.8) in the expression for  $\Phi_j$  from (D.5) guarantees that for each value of the (still unknown) parameter  $\gamma$  these parameters are optimal. Therefore, these parameters are excluded from Eq. (D.4) and the functional  $\Phi$  can now be considered to be a function of the single variable  $\gamma$ :

$$\Phi = \Psi(\gamma) \tag{D.9}$$

The dependency of the function  $\Psi$  on  $\gamma$  may be quite complicated due to the oscillating nature of the internal terms. Therefore, we perform a preliminary estimation of the possible optimal value of  $\gamma$  (denoted by  $\gamma^*$ ) using a Fourier analysis of a single  $\omega$ -slice chosen from the central part of the interferogram (see Eq. (D.3)). Subsequently, a search of the global minimum of the function  $\Psi(\gamma)$  is done, assuming that the global minimum is located in the vicinity of the estimated solution, i.e.,  $\gamma \in [0.8\gamma^*, 1.2\gamma^*]$ .



## Appendix E

### Gas expansion with an end-fire nozzle

To simulate the gas jet expansion in the vicinity of the orifice of the gas nozzle, we ran computational fluid dynamics simulations. The results presented in the following paragraphs were obtained with the open-source tool OpenFoam<sup>1</sup> in combinations with the solver rhoCentralFoam. The algorithm solves the Navier-Stokes equations on a specified meshgrid covering the geometry. Rotational symmetry (along the nozzle axis) is assumed and the initial conditions are set to parameters as used in the experiment. The obtained results were crosschecked with simulations employing COMSOL Multiphysics using a steady-state solver<sup>2</sup>.

In Fig. E.1, we present the density, the velocity and the temperature distributions for a nozzle backing pressure of 1 bar and 2 bar. A nozzle diameter of 100  $\mu\text{m}$  was chosen. On the low pressure side a pressure of 1 mbar was assumed (lower pressures led to numerical instabilities). We verified that the nozzle length had no influence on the parameters calculated in the interaction region (i.e., a few tens of micrometers from the nozzle orifice). For increased backing pressure the width of the density distribution barely changes, while the peak density increases approximately linearly. The gas velocity is independent of the backing pressure and depends as  $\sqrt{T_0/m}$  on the temperature  $T_0$  in the backing reservoir and the mass  $m$  of the particles.

In Fig. E.2 the density distribution along the optical axis (i.e. perpendicular to the nozzle axis) is shown. The distance of the optical axis to the nozzle orifice was chosen to be 50  $\mu\text{m}$ , corresponding to  $2w_0$  with a typical focus radius  $w_0 \approx 25 \mu\text{m}$ . At this distance the nozzle induces losses of about 100 ppm for the intracavity light. For the simulations in Chapter 5, we approximate the bell-shaped density distribution by an average density and length. A meaningful average value for the density is half of the peak density. The length of the interaction region is computed such that the total number of gas atoms in a cylinder (radius  $\sim 0.4w_0$ ) along the optical axis is conserved.

Along the nozzle axis, a simple analytical model can be employed [101] to calculate the thermodynamic state variables. At a distance  $x$  from the nozzle orifice, the gas density, the temperature and the velocity component along the nozzle axis can be calculated via:

$$n_{\text{gas}}(x) = n_{\text{gas},0} \times \left(1 + \frac{\kappa-1}{2} M^2(x)\right)^{-1/(\kappa-1)} \quad (\text{E.1})$$

$$T(x) = T_0 \times \left(1 + \frac{\kappa-1}{2} M(x)^2\right)^{-1} \quad (\text{E.2})$$

$$v_x(x) = M(x) \times \left(1 + \frac{\kappa-1}{2} M(x)^2\right)^{-1/2} \times \sqrt{\frac{\kappa k_B T_0}{m}}. \quad (\text{E.3})$$

<sup>1</sup><http://www.openfoam.org>

<sup>2</sup>The simulations were carried out by T. Saule.

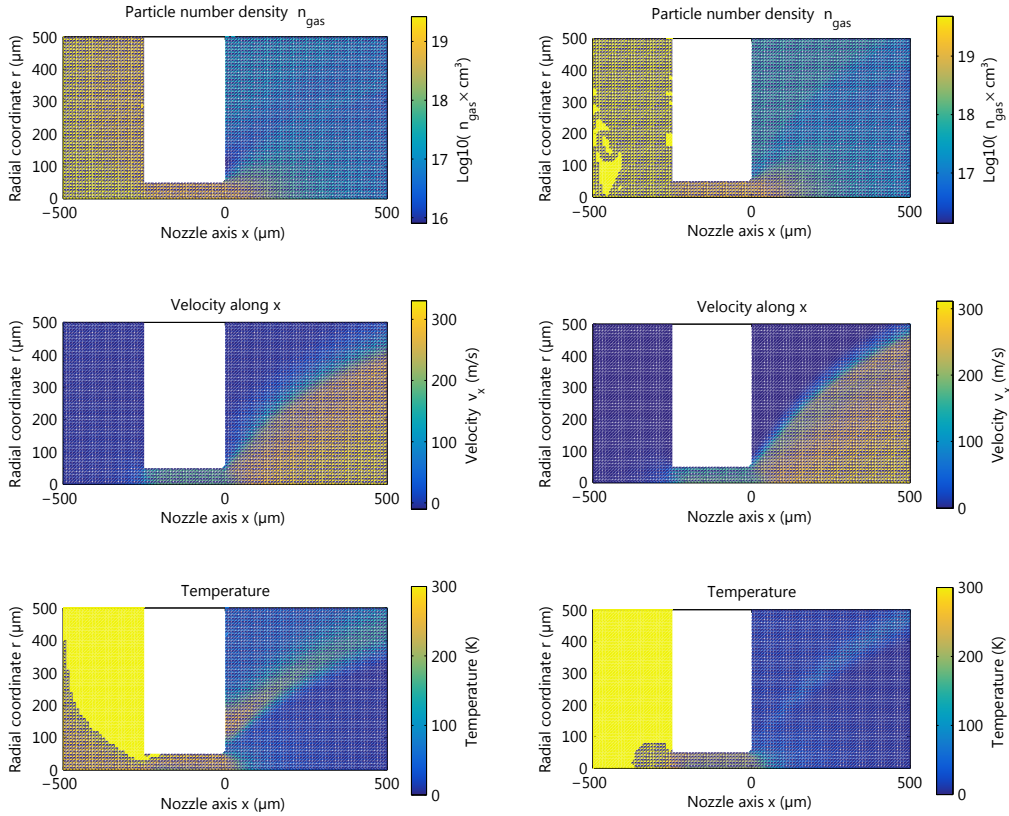


**Figure E.1:** Results of the fluid flow simulations with xenon and a nozzle diameter of  $100\ \mu\text{m}$ . Left panels: backing pressure of 1 bar, right panels: backing pressure of 2 bar.

Here,  $\kappa$  is the adiabatic index ( $\kappa = 5/3$  for a mono-atomic gas),  $M$  denotes the Mach number,  $n_{\text{gas},0}$  the gas density in the reservoir, and  $k_{\text{B}}$  the Boltzmann constant. An approximate expression for the Mach number is given in [102]. It reads

$$M(\xi) = 1 + 3.337\xi^2 - 1.541\xi^3 \quad \text{for } \xi \lesssim 1 \quad \text{and}$$

$$M(\xi) = \xi^{\kappa-1}(3.232 - 0.7563\xi^{-1} + 0.3937\xi^{-2} - 0.0729\xi^{-3}) \quad \text{for } \xi \gtrsim 0.5.$$

Here,  $\xi$  is defined as the ratio of the distance  $x$  from the orifice to the nozzle diameter. We find, that the gas densities predicted by Eq. (E.1) agree reasonably well (within about 50 %) with our numerically obtained results.

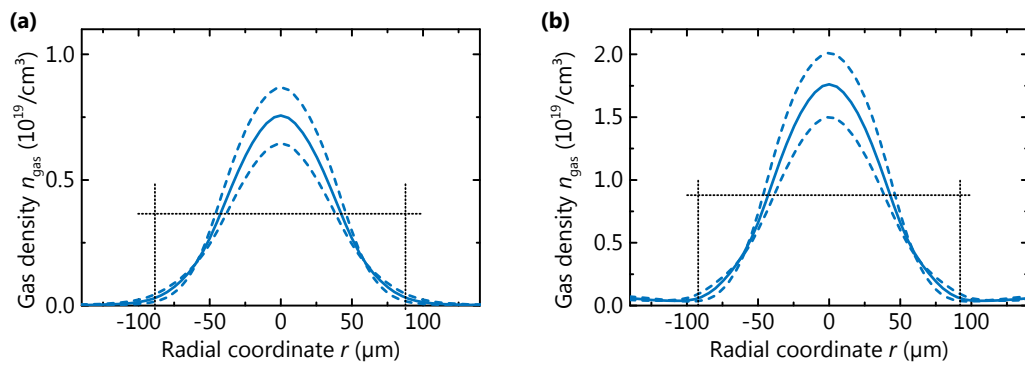


**Figure E.2:** Lineouts of the gas density along the optical axis, i.e., perpendicular to the nozzle axis. A distance of  $50\ \mu\text{m}$  was assumed between the optical axis and the nozzle orifice. The dashed lines correspond to the lineouts taken at a distance of  $10\ \mu\text{m}$  from the optical axis. The dotted lines indicate the length and the average density that enter the intracavity ionization model.



## Appendix F

### Data archiving

The experimental raw data, evaluation files, and original figures can be found on the Data Archive Server of the Laboratory for Attosecond Physics at the Max Planck Institute of Quantum Optics: `/afs/rzg/mpq/lap/publication_archive`

The `/figures` directory relative to the root folder of the data archive, contains subfolders that correspond to the final figure names. It contains the (raw) data of that figure and a text file named `fig_X.X.txt` (where `X.X` is the figure number) which gives detailed information about the organization of the data and the processing performed to obtain the final figure.



## List of scientific publications

### Included publications

S. Holzberger, N. Lilienfein, M. K. Trubetskov, H. Carstens, F. Lücking, V. Pervak, F. Krausz, and I. Pupeza, “Enhancement cavities for zero-offset-frequency pulse trains,” *Opt. Lett.* **40**, 2165 (2015).

I conceived the experiment together with I.P. and N.L. and performed the experiments together with N.L.. I analyzed the data, developed the model, and wrote most of the manuscript.

S. Holzberger, N. Lilienfein, H. Carstens, T. Saule, M. Högner, F. Lücking, M. Trubetskov, V. Pervak, T. Eidam, J. Limpert, A. Tünnermann, E. Fill, F. Krausz, and I. Pupeza, “Femtosecond enhancement cavities in the nonlinear regime,” *Phys. Rev. Lett.* **115**, 023902 (2015).

I conceived the experiment together with I.P. and performed the experiments together with N.L.. I analyzed the data, developed the model together with E.F., and wrote most of the manuscript.

I. Pupeza, M. Högner, J. Weitenberg, S. Holzberger, D. Esser, T. Eidam, J. Limpert, A. Tünnermann, E. Fill, and V. S. Yakovlev, “Cavity-enhanced high-harmonic generation with spatially tailored driving fields,” *Phys. Rev. Lett.* **112**, 103902 (2014).

I was involved in the planning of the project, performed the experiments together with I.P. and J.W. and M.H., and contributed to the manuscript.

I. Pupeza, S. Holzberger, T. Eidam, H. Carstens, D. Esser, J. Weitenberg, P. Rußbüldt, J. Rauschenberger, J. Limpert, T. Udem, A. Tünnermann, T. W. Hänsch, A. Apolonski, F. Krausz, and E. Fill, “Compact high-repetition-rate source of coherent 100 eV radiation,” *Nature Photon.* **7**, 608–612 (2013).

As equally contributing first author, I co-planned the project, performed the experiment together with I.P., analyzed the data, and co-wrote the manuscript.

### Journal publications

N. Lilienfein, H. Carstens, S. Holzberger, C. Jocher, T. Eidam, J. Limpert, A. Tünnermann, A. Apolonski, F. Krausz, and I. Pupeza, “Balancing of thermal lenses in enhancement cavities with transmissive elements,” *Opt. Lett.* **40**, 843–846 (2015).

O. d. Vries, T. Saule, M. Plötner, F. Lücking, T. Eidam, A. Hoffmann, A. Klenke, S. Hädrich, J. Limpert, S. Holzberger, T. Schreiber, R. Eberhardt, I. Pupeza, and A. Tünnermann, “Acousto-optic pulse picking scheme with carrier-frequency-to-pulse-repetition-rate synchronization,” *Opt. Express* **23**, 19586 (2015).

H. Carstens, N. Lilienfein, S. Holzberger, C. Jocher, T. Eidam, J. Limpert, A. Tünnermann, J. Weitenberg, D. C. Yost, A. Alghamdi, Z. Alahmed, A. Azzeer, A. Apolonski, E. Fill, F. Krausz, and I. Pupeza, “Megawatt-scale average-power ultrashort pulses in an enhancement cavity,” *Opt. Lett.* **39**, 2595–2598 (2014).

S. Breilkopf, T. Eidam, A. Klenke, L. v. Grafenstein, H. Carstens, S. Holzberger, E. Fill, T. Schreiber, F. Krausz, A. Tünnermann, I. Pupeza, and J. Limpert, “A concept for multiterawatt fibre lasers based on coherent pulse stacking in passive cavities,” *Light Sci. Appl.* **3**, e211 (2014).

D. Esser, J. Weitenberg, W. Bröring, I. Pupeza, S. Holzberger, and H.-D. Hoffmann, “Laser-manufactured mirrors for geometrical output coupling of intracavity-generated high harmonics,” *Opt. Express* **21**, 26797 (2013).

H. Carstens, S. Holzberger, J. Kaster, J. Weitenberg, V. Pervak, A. Apolonski, E. Fill, F. Krausz, and I. Pupeza, “Large-mode enhancement cavities,” *Opt. Express* **21**, 11606 (2013).

S. Holzberger, T. Schuh, S. Blügel, S. Lounis, and W. Wulfhekel, “Parity effect in the ground state localization of antiferromagnetic chains coupled to a ferromagnet,” *Phys. Rev. Lett.* **110**, 157206 (2013).

## **Conference contributions (selection)**

S. Holzberger, N. Lilienfein, H. Carstens, T. Saule, F. Lücking, M. Trubetskov, V. Pervak, T. Eidam, J. Limpert, A. Tünnermann, E. Fill, F. Krausz, and I. Pupeza, “Femtosecond enhancement cavities in the nonlinear regime,” in *European Conference on Lasers and Electro-Optics* (Optical Society of America, 2015)

S. Holzberger, N. Lilienfein, H. Carstens, T. Saule, M. Högner, F. Lücking, M. Trubetskov, V. Pervak, T. Eidam, J. Limpert, A. Tünnermann, E. Fill, F. Krausz, and I. Pupeza, “Enhancement cavities for intracavity frequency conversion,” in *10th International Conference on Ultrafast Optics* (2015), UFO0091

N. Lilienfein, S. Holzberger, M. Trubetskov, H. Carstens, F. Lücking, V. Pervak, F. Krausz, and I. Pupeza, “Enhancement cavities for pulse trains with fixed offset frequency,” in *10th International Conference on Ultrafast Optics* (2015), UFO0095

T. Saule, O. d. Vries, S. Holzberger, M. Plötner, F. Lücking, J. Limpert, A. Tünnermann, F. Krausz, and I. Pupeza, “Carrier-envelope-phase-stable Ti:sa-master-oscillator-Yb-power-amplifier system,” in *European Conference on Lasers and Electro-Optics* (Optical Society of America, 2015)

N. Lilienfein, H. Carstens, S. Holzberger, C. Jocher, T. Eidam, J. Limpert, A. Tünnermann,

- 
- A. Apolonski, F. Krausz, and I. Pupeza, "Balancing thermal lensing in enhancement cavities," in European Conference on Lasers and Electro-Optics (Optical Society of America, 2015)
- S. Holzberger, M. Högner, J. Weitenberg, D. Esser, T. Eidam, J. Limpert, A. Tünnermann, E. Fill, F. Krausz, V. S. Yakovlev, and I. Pupeza, "Power-scalable and efficient geometric XUV output coupling for cavity-enhanced high-harmonic generation," in Conference on Lasers and Electro-Optics (Optical Society of America, 2014), FTu2D.3
- S. Breitkopf, T. Eidam, L. v. Grafenstein, A. Klenke, H. Carstens, S. Holzberger, I. Pupeza, E. Fill, T. Schreiber, J. Limpert, F. Krausz, and A. Tünnermann, "Approaching TW-peak powers at >10 kHz repetition rate by multi-dimensional coherent combining of femtosecond fiber lasers," in Fiber Lasers XI: Technology, Systems, and Applications, Vol. 8961, edited by S. Ramachandran, Proc. SPIE (2014), p. 896106
- S. Holzberger, T. Schuh, S. Lounis, S. Blügel, and W. Wulfhekel, "Parity effect in ground state localization of antiferromagnetic chains coupled to a ferromagnet," in Verhandlungen der DPG-Frühjahrstagung (Deutsche Physikalische Gesellschaft, 2013), MA 44.3
- H. Carstens, N. Lilienfein, S. Holzberger, C. Jocher, T. Eidam, J. Limpert, A. Tünnermann, A. Apolonski, E. Fill, I. Pupeza, and F. Krausz, "Cavity-enhanced 196 kW average-power infrared pulses," in Advanced Solid State Lasers (Optical Society of America, 2013), JTh5A.3
- I. Pupeza, S. Holzberger, T. Eidam, D. Esser, J. Weitenberg, H. Carstens, P. Rußbüldt, J. Limpert, T. Udem, A. Tünnermann, T. W. Hänsch, F. Krausz, and E. Fill, "Generation of coherent sub-20 nm XUV radiation at 78 MHz via cavity-based HHG," EPJ Web of Conferences **41**, 10023 (2013)
- S. Holzberger, I. Pupeza, J. Kaster, T. Eidam, B. Bernhardt, A. Vernaleken, O. Pronin, V. Pervak, R. Holzwarth, T. Udem, J. Limpert, A. Apolonski, E. Fill, T. W. Hänsch, A. Tünnermann, and F. Krausz, "Power scaling limitations for cavity-assisted high-harmonic generation," in Advanced Solid-State Photonics (Optical Society of America, 2012), AM4A.12
- S. Holzberger, I. Pupeza, D. Esser, J. Weitenberg, H. Carstens, T. Eidam, P. Russbüldt, J. Limpert, T. Udem, A. Tünnermann, T. W. Hänsch, F. Krausz, and E. Fill, "Sub-25 nm high-harmonic generation with a 78-MHz repetition rate enhancement cavity," in Conference on Lasers and Electro-Optics (Optical Society of America, 2012), QTh5B.7
- S. Holzberger, T. Schuh, and W. Wulfhekel, "Antiferromagnetic Mn chains on Ni(110)," in Verhandlungen der DPG-Frühjahrstagung (Deutsche Physikalische Gesellschaft, 2011), MA 50.5
- F. Roux, S. Holzberger, Lampel G., Y. Lassailly, and J. Peretti, "Optical pumping in bulk silicon studied by spin-resolved low-energy photoemission spectroscopy," in 2009 MRS Spring Meeting & Exhibit (Materials Research Society, 2009), FF5.7.

## **Patents**

I. Pupeza, H. Carstens, S. Holzberger, E. Fill, and F. Krausz, "Enhancement resonator including non-spherical mirrors," WO2014111097 A1 (2014)

## Danksagung

Auch wenn die Prüfungsordnung es gebietet, dass eine Dissertationsschrift von einer Einzelperson anzufertigen ist, so ist es dennoch offensichtlich, dass diese Arbeit ohne die Unterstützung einer Vielzahl von Personen nicht möglich gewesen wäre.

Mein erster Dank gebührt dabei meinem Doktorvater Ferenc Krausz dafür, dass er es mir ermöglicht hat diese Arbeit in seiner Gruppe anzufertigen. Die Besprechungen mit dir in kleiner Runde waren geprägt von Effizienz und deine meist passgenauen Vorschläge haben dieses Projekt sehr vorangebracht. Des Weiteren möchte ich mich für den finanziellen Rückhalt bedanken, den du diesem Projekt eingeräumt hast, und für das von dir maßgeblich gestaltete Umfeld, das wissenschaftlichen Diskurs bei vielen internen und externen Veranstaltungen fördert.

Ein großes Dankeschön geht auch an Joachim für die direkte Betreuung dieser Arbeit. Für die Einführung in die bestehenden Systeme im Labor, für deine rund-um-die-Uhr Erreichbarkeit, für deine Bereitschaft über alle möglichen und unmöglichen Experimente (auch mal erbittert) zu diskutieren, für deinen unerschütterlichen Glauben an dieses Projekt und den Erfolg unserer Bemühungen, deine Standhaftigkeit gegenüber Reviewern und für dein Vertrauen in meine Arbeit. Besonderer Dank auch dafür, dass du mit deiner Arbeit die Kontinuität unseres Forschens gesichert hast.

Weiter möchte ich Thomas Udem Danke sagen für die Übernahme des Koreferats dieser Arbeit, für detaillierte Anmerkungen zu unseren Manuskripten und vor allem für viel kritisches Hinterfragen und klärende Diskussionen rund um Cavities, besonders in den ersten beiden Jahren meiner Zeit am MPQ.

Ein großes Danke geht auch an die Faserlaser-Gruppe in Jena. Herzlichen Dank insbesondere an Tino und Jens für eure fortwährende und allzeit gegebene Unterstützung mit dem Lasersystem. Danke auch an unsere "Jenny" für die (mehr oder minder) treuen Dienste in all den Jahren.

Ein weiteres Danke geht ans ILT in Aachen: Dem Team um Dominik, Peter und Johannes für die erfolgreiche Zusammenarbeit bei den XUV Auskopplern und alle Fragen rund um die geometrische Auskopplei. Herzlichen Dank dir, Johannes, für die schöne Zeit des gemeinsamen Experimentierens und Diskutierens – ich durfte viel von dir lernen – nicht nur über Physik. In diesem Zusammenhang geht auch ein herzliches Dankeschön an den Cavity-Club der Hänsch-Gruppe; besonders an den Cavitylosen unter den Cavitisten, Andreas, der uns durch so manch kurzfristige Materialleihgabe das Weiterexperimentieren ermöglicht hat. Herzlich bedanken möchte ich mich auch bei Herrn Fill, dafür dass Sie mich an Ihrem "physikalischen" Erfahrungsschatz (Stichwort: "Dazu gibt es ein Paper von XY aus den 80ern!") immer wieder teilhaben lassen.

Weiter möchte ich Fabian für unsere gemeinsame Zeit bei den Experimenten zur Stabilisierung danken. Es war eine super Zeit mit dir im Labor mit viel Arbeit, Lernen und auch Lachen: deinen geschulten Blick auf das Faserende werde ich nie vergessen!

Besondere Worte des Dankes gehen an meine beiden langjährigen Kollegen Henning und

Nikolai, die mich bei vielen Experimenten mit Rat und Tat unterstützt haben und die mit mir durch wissenschaftliche Höhen (spontane Jubelausbrüche) und Tiefen (stundenlanges Fluchen) gegangen sind. Herzlichen Dank für die super Zusammenarbeit, für uneingeschränkte Hilfsbereitschaft, für die vielen Diskussionen über ALLES, so einige gemeinsame Feierabende und gemütliche Fußballabende. Herzlichen Dank Niko, für die gemeinsame Arbeit bei den SSI und OOF Messungen. Danke auch den jüngeren Mitgliedern des Teams: Maxi, für deine "theoretische" Unterstützung insbesondere in der Endphase; Tobi, für deine unglaubliche Hilfsbereitschaft in und außerhalb des Labors. Euch Vieren und Ioachim auch nochmals herzlichen Dank für die vielen guten Anmerkungen zum Manuskript, und dir, Matt, für den sprachlichen Feinschliff der exponierten Stellen!

Thank you, Michael, for all your support, in particular, with the phase retrieval software and the design of cavity-optics. Thanks for many discussions and explanations—I benefited a lot from them! Danke auch an Vova und sein Spiegelteam für eure Bereitschaft, immer wieder neue Ansätze zu wagen.

Bedanken möchte ich mich auch bei meinen (Ex-)Kollegen Thomas, Olga, Ivan, Daniel, Elena, Yuya für die gute gemeinsame Zeit in unserem cavity-freien Büro! Danke auch vielen weiteren (Ex-)LMU'lern: Friedrich, Stefan, Oleg, Marcus, Jonathan, Matt, Kellie, Catherine, Nora, Dominik, Stephan, Christina, Benedikt, Florian und Waldemar, für das super Arbeits- und Freizeitklima. Danke auch an Jan und Christian für die schöne, wenn auch kurze gemeinsame Zeit der Zusammenarbeit.

Zuletzt möchte ich mich bei meinen Familien und insbesondere bei meinen Eltern für all eure Unterstützung in den vergangenen Jahr(zehnt)en bedanken. Ohne euch und eure Förderung wäre mir dieser Luxus des Forschens und Experimentierens verwehrt geblieben! Und zuallerletzt bedanke ich mich bei dir, Doris, für deine Unterstützung auf diesem Weg. Es ist wunderschön mit dir durchs Leben zu gehen.